Geology and Geophysics
School of Environmental Sciences
University of Liverpool

Seismotectonics of the southern subduction Chilean margin revealed by recent aftershock sequences

Thesis submitted in accordance with the requirements of
the University of Liverpool for the degree of Doctor in Philosophy

by

Hans Agurto Detzel

Liverpool, November 2012

ABSTRACT

Subduction margins, as in the case of south-central Chile, are active seismotectonic environments and locus of the world largest earthquakes. In this thesis, two segments of the south-central Chilean subduction margin are studied: (A) the southernmost portion, at the termination of the Nazca-South America convergence (~46ºS), and (B) the segment located between 34º-38ºS, where the M_W 8.8 Maule Earthquake took place in 2010.

Analysis of data from a local seismic network deployed in 2004-2005 in area A, indicates low levels of background seismicity with magnitudes ranging 0-3.4 M_l. The seismicity corresponds to shallow crustal events, mostly occurring within the upper 10 km. A third of the seismicity is associated to volcanic activity present in the area, while scarce seismicity is associated with a large strike-slip fault, the Liquiñe-Ofqui Fault System (LOFS), that intersects the region along the arc in a N-S-trend.

In 2007, this region was affected by a seismic sequence with a peak of activity associated with a M_W 6.2 earthquake in April that year. A local seismic network was deployed after this main event in order to study its sequence of aftershocks, which provided a unique opportunity to characterise seismotectonically this area that usually lacks intermediate magnitude seismicity, including the calculation of a new local velocity model, accurate aftershock locations and computation of focal mechanisms. The results show P-wave velocities of ~5 km/s for the upper 5 km in accordance with the geology of the area, and low S-wave velocities for the upper 3 km of crust due to rock fracturing and the presence of fluids. An average Vp/Vs ratio of 1.76 was calculated for the region. The alignment of most of the aftershocks within the LOFS plus obtained focal mechanisms, indicate that this sequence had tectonic origin related to the re-activation of the LOFS. Further, a maximum seismogenic depth of about 15 km was determined for the entire region.

Regarding area B, affected by a large megathrust earthquake in 2010, the study of moment tensor solutions for the sequence of aftershocks provided new insight into the distribution of postseismic activity relative to co-seismic slip and the release of seismic afterslip. Thrust aftershocks dominate the postseismic activity, but also normal faulting was detected in the outer-rise area and in the overriding plate near the coastline. The largest seismically released afterslip is located between the two main patches of co-seismic slip. Large aftershocks ($M>4$) occur along the megathrust interface, in zones of intermediate co-seismic slip associated to stress introduced on dislocation tips with high co-seismic slip contrast. On the other hand, smaller events ($M<4$) tend to occur in areas of large co-seismic slip, and might indicate a more diffuse distribution within the damage zone of the megathrust plane. It is likely that these smaller events are associated to secondary processes (fluid release, re-activation of secondary structures).

Although belonging to the same subduction margin, the seismotectonics and earthquake patterns of the two areas investigated here show different underlying tectonic regimes. For the northern area, locus of the 2010 M_W 8.8 Chile earthquake, inter-plate thrust seismicity is dominant both in term of quantity of events and moment release. Conversely, the southern area presents only shallow intra-plate crustal seismicity mainly occurring in the arc, where Quaternary volcanism and the LOFS are present.

RESUMEN

Márgenes de subducción, como en el caso del centro-sur de Chile, corresponden a ambientes sismotectónicos activos donde ocurren los mayores terremotos a nivel mundial. En la presente tesis, dos segmentos del margen subductivo del centro-sur de Chile son estudiados: (A) el segmento más al sur, en la parte terminal de la convergencia entre las placas de Nazca y Sudamérica (~46ºS), y (B) el segmento contenido entre los 34º-38ºS, donde el reciente terremoto de Maule M_W 8.8 tuvo lugar en 2010.

El análisis de datos adquiridos por una red sísmica local instalada en 2004-2005 en el área A, indica bajos niveles de sismicidad de fondo, con magnitudes en el rango 0-3.4 M_l. La sismicidad corresponde a eventos corticales someros, la mayoría localizados en los primeros 10 km de corteza. Alrededor de un tercio de la sismicidad es asociada a actividad volcánica, mientras que eventos dispersos son asociados a un sistema de falla de rumbo de grandes dimensiones, el Sistema de Falla Liquiñe-Ofqui (SFLO), que intersecta esta región a lo largo del arco en dirección N-S.

En el año 2007, esta zona fue afectada por una secuencia de sismos cuyo máximo fue dado por un terremoto M_W 6.2. en abril de ese año. Una red sísmica local fue instalada con el propósito de capturar la secuencia de réplicas del evento principal, siendo una oportunidad única para caracterizar sismotectónicamente esta área que usualmente carece de eventos de magnitud intermedia, incluyendo la obtención de un nuevo modelo de velocidades, mecanismos focales y localización precisa de réplicas. Los resultados indican velocidades de onda P en torno a los 5 km/s para los primeros 5 km de corteza, con bajas velocidades de onda S para los primeros 3 km de corteza debido a la presencia de fracturas y fluidos, y un radio Vp/Vs de 1.76 en promedio para el área. Además, se determinó una profundidad sismogénica máxima de 15 km para la región. La alineación de la mayoría de las réplicas con la traza del SFLO, además de los mecanismos focales obtenidos, indican que esta secuencia tuvo un origen tectónico asociado a la re-activación del SFLO.

Con respecto al área B, el estudio de tensores de momento para la secuencia de réplicas del terremoto de Maule 2010 proporciona un mejor entendimiento de la distribución de actividad postsísmica en relación al desplazamiento cosísmico y postsísmico. La actividad postsísmica es dominada por eventos de fallamiento inverso, pero también se detectó fallamiento normal en el área cercana a la fosa y en la placa continental, cerca de la línea de costa. La mayor parte del desplazamiento postsísmico sismogénico se encuentra entre los dos parches principales de desplazamiento cosísmico. Las mayores réplicas (M>4) ocurren a lo largo del plano de subducción, en áreas de desplazamiento cosísmico intermedio, asociadas a esfuerzos inducidos en bordes de dislocación con altos gradientes de desplazamiento cosísmico. Por otro lado, las réplicas menores (M<4) tienden a ocurrir en áreas de mayor desplazamiento cosísmico y podrían indicar una distribución más dispersa dentro de la zona de fracturamiento de la interfaz subductiva. Es posible que estos eventos menores se encuentren asociados a procesos secundarios (liberación de fluidos, re-activación de estructuras secundarias).

A pesar de pertenecer al mismo margen de subducción, las características sismotectónicas de ambos segmentos estudiados difieren en cuanto a regímenes tectónicos. En el área norte, lugar del sismo M_W 8.8 en 2010, terremotos de subducción de fallamiento inverso dominan en cuanto a cantidad de eventos y momento sísmico liberado. Por otro lado, el área sur presenta solo eventos corticales someros intra-placa, que ocurren principalmente en el arco, donde volcanismo cuaternario y el SFLO están presentes.

CONTENTS

LIST OF FIGURES

LIST OF TABLES

ACKNOWLEDGMENTS

Firstly, I thank CONICYT-Chile and its program of scholarships "Beca Presidente de la República" for the sponsorship of my PhD program.

Secondly, I would like to express my sincere gratitude to all the people who supported me along these four years here in Liverpool. To my supervisor, Andreas Rietbrock, for his trust and continuous support since the day we started to plan this PhD project, back in 2007, during fieldwork in the Patagonian fjord-lands. To my colleagues and co-authors, in particular to Klaus Bataille and Matt Miller. Special acknowledgments to the landowners, colleagues and students that participated in the numerous fieldwork campaigns.

Thanks to my friends, the old ones in Chile and the new ones here in the UK, for their encouragement, friendship and in general for the good moments. A big (apologetic) thank to my family, always supportive and comprehensive despite my prolonged absence.

Lastly, all my love and endless gratitude to Susana, for her patience, dedication and unconditional love. The capricious providence crossed our paths here in Liverpool. To her, the future together.

This work is dedicated to the memory of my former teacher, María Poza Romero, who sadly passed away while I was finishing this manuscript in September 2012.

THESIS OUTLINE

In this thesis I study the seismotectonics of the south-central Chilean margin by analysing two recent aftershock sequences: the 2007 Aysén Fjord seismic sequence and the 2010 Maule earthquake aftershocks.

Chapter 1 offers an introduction to this thesis and the study area. Firstly, it contains a geo-tectonic framework for the studied region. The whole subduction margin is addressed regarding the distribution of several geophysical parameters and seismotectonic differences along strike, with particular emphasis on the seismicity. Then, a broad overview on the occurrence of the 2010 Maule, Chile, megathrust earthquake and its main characteristics is provided, serving as an introduction to the work covered in Chapter 5. Following this, an overview of strike-slip faulting occurring at oblique subduction margins is discussed, citing global examples of this type of tectonic environment, in direct relation with the Liquiñe-Ofqui fault and the southernmost portion of the Chilean subduction margin studied here. Finally, an account of the motivation and aims behind this thesis is provided.

Chapter 2 defines the theoretical concepts that support the present thesis and describes the applied methods and techniques, with special emphasis on the software used. Further, a review of earthquake location methods and seismic source representation is provided.

Chapter 3 describes the regional background seismicity of the area in front of the Chile Triple Junction, based on records from a temporary local network deployed during 2005 and 2006. This chapter provides a detailed seismotectonic framework leading to Chapter 4, in which the seismic sequence of 2007 is discussed. In April of that year, a Mw 6.2 earthquake occurred in the fjord-lands of southern Chile, in the area where the Liquiñe-Ofqui fault starts its development northwards. Little information about the current state of this fault was known until this event, which confirmed the current activity of this fault system. A complete characterization of the aftershock sequence

based on non-linear earthquake locations, focal mechanisms from first motion polarities and a new local velocity model for the area is provided. These results have been recently published in Geophysical Journal International (Agurto *et al.*, 2012a).

In chapter 5, the characterization of the aftershock pattern and seismic afterslip distribution of the Mw 8.8 Maule Chile earthquake is discussed, based on regional moment tensor inversions and a quantitative approach to the aftershock distribution. The 2010 Maule earthquake and its aftershock sequence is one of the best-recorded in modern seismology. The widespread temporary network deployed in the area shortly after the mainshock is used here in order to perform full waveform moment tensor inversions on the largest aftershocks. Furthermore, the relocation and addition of published moment tensor solutions of aftershocks that occurred in absence of the local network enhances and complements a catalogue of largest aftershocks, from the beginning of the sequence until March 2012. Lastly, I discuss the seismic afterslip release and aftershock occurrence relative to the coseismic slip distribution and compare these results to the published coseismic and postseismic models. The main findings of this study have been recently published in Geophysical Research (Agurto *et al.*, 2012b).

Finally, chapter 6 expands on the main points concluded through this thesis, summarising the key findings as well as discussing the different aspects that characterize both of the studied subduction segments and their respective aftershock sequences.

CHAPTER 1

INTRODUCTION

The western margin of South America is characterized by the subduction of the oceanic Nazca plate under the continental South-American plate. With most of this process occurring along the Chilean coast, this country offers a perfect setting to study seismotectonics along different segments of an active subduction margin. Subduction zones are the place on Earth where the largest earthquakes occur, often producing great human and economic losses. Thus the importance of comprehending the involved processes, estimating maximum possible magnitudes and associated hazards, at any given subduction segment.

The present work focuses on two important segments of the Chilean subduction margin. Firstly, the southernmost portion (area A in Figure 1.1.), in front of the Chile Triple Junction (CTJ) where the Nazca, Antarctic and South American plates meet, and the oblique convergence of Nazca relative to South America generates an intra-plate crustal strike-slip fault, the Liquiñe-Ofqui fault, that runs for more than 1000 km in a N-S direction. Recently in 2007, the southern end of this fault re-activated, generating a sequence of seismic events which is studied in this work.

The second segment analysed in this work is the south-central portion of the Chilean margin (area B in Figure 1.1), which in 2010 was affected by a Mw 8.8 megathrust earthquake, the sixth largest earthquake ever recorded. The aim of this thesis is, therefore, to study and comprehend the seismotectonics acting at these two subduction segments by characterising their respective aftershock sequences.

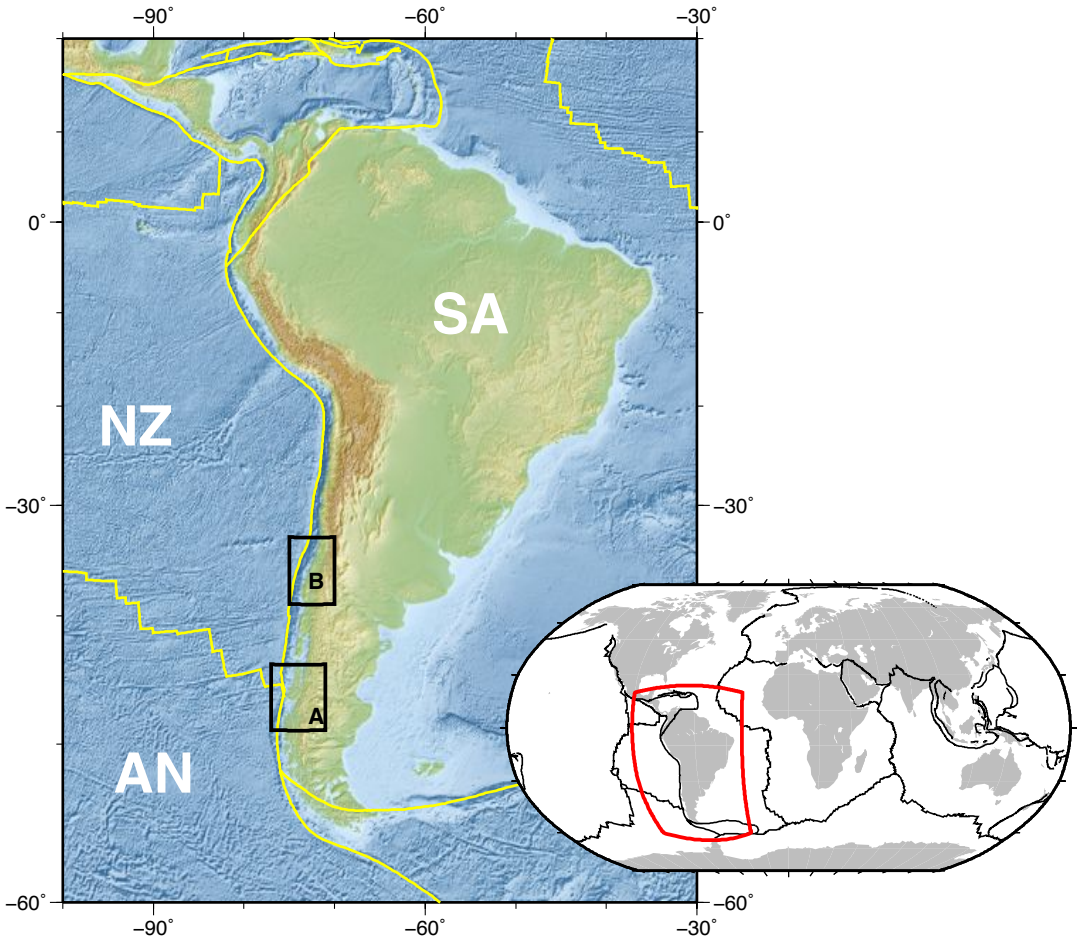

Figure 2.1. Introduction to the study area. Yellow lines delimit major tectonic plates. Area A correspond to the Aysén Region, addressed in Chapters 3 and 4. Area B correspond to the area affected by the 2010 Chile megathrust earthquake addressed in Chapter 5. NZ Nazca plate, AN Antarctic plate, SA South American plate. Topography/Bathymetry ETOPO1.

1.1. Geo-Tectonic Setting Of The Chilean Subduction Margin

The subduction process along western South America produces large earthquakes M>8, often with associated tsunamis (Bilek, 2010). Moreover, the southern segment of this subduction zone generated the largest earthquake instrumentally recorded, the 1960 Mw 9.5 Chile earthquake (Barrientos and Ward, 1990). Recently, in 2010, a Mw 8.8 earthquake ruptured nearly 500 km along the subduction interface in south-central Chile, closing a seismic gap existent since 1835 (Moreno *et al.*, 2012). Besides megathrust earthquakes, the subductive process along western South America creates deformation, volcanism, crustal seismicity and the highest non-collisional orogen, the Andes, which presents altitudes of up to ~7000 m.a.s.l. along more than 8000 km (Ramos, 1999). The morphology of the Central Andes in southern Perú and northern Chile is dominated by the presence of the Altiplano-Puna plateau with average elevations of 4 km (Isacks, 1988). Further south, the mountain system narrows with elevations greater than 3 km down to the Patagonian Cordilleras where the maximum elevations reach 2 km (Figure 1.2a).

Of particular interest is the along-strike segmentation of the Andes. Several authors have investigated and differentiated discretised segments of the Andean margin according to its topography and geotectonics (e.g. Gansser, 1973), seismicity (e.g. Barazangi and Isacks, 1976), geometry of the subducted slab (Pilger, 1981; Jordan *et al.*, 1983; Cahill and Isacks, 1992), geologic history (e.g. Mpodozis and Ramos, 1989), seismotectonics (Dewey and Lamb, 1992), deformation styles (e.g. Kley *et al.*, 1999), rheology (e.g. Tassara *et al.*, 2006) and volcanism (e.g. Stern, 2004).

The subduction of the Nazca plate beneath South America starts at ~4ºN at the Cocos-Nazca spreading centre, and ends at the Chile Triple Junction (CTJ), at ~46ºS, where the Nazca, Antarctic and South American plates collide (Figure 1.1). Convergence rate for Nazca relative to South America north of the CTJ is 66 mm yr^{-1} (Angermann *et al.*, 1999), while south of the CTJ, Antarctica subducts at 20 mm yr^{-1} beneath South America (Chase, 1978).

1.1.1. Geometry and characteristics of the subducting slab

Several bathymetric features are present on the NZ plate, many of them currently colliding with the trench along the subduction margin (Figure 1.2a). In the southern end, an active spreading centre, the Chile Ridge, is being subducted beneath the CTJ at ~46ºS (Herron *et al.*, 1981), while in the north, the aseismic Nazca Ridge intersects the trench at ~15ºS (Beck and Ruff, 1989) constituting the northern end of the Chilean subductive margin. Other bathymetric structures are the Juan Fernandez ridge and several seamounts and fracture zones (FZ). According to Bilek (2010), once subducted these characteristics of the slab may influence the distribution of slip and moment release of subduction earthquakes either by concentrating slip within the feature (asperity) or stopping the rupture (barrier). For example, Barrientos and Ward (1990) recognized the Mocha FZ as the northern limit of the rupture area of the 1960 Great Chile Earthquake, and the Guamblin and Darwin FZs as its southern limit.

Great variability on the amount of sediment entering the trench is observed along-strike (Figure 1.2b). Near the Nazca Ridge, the sediment thickness is about 0.5 km, while the northern Chile trench, between 19-22ºS, is practically devoid of sediments. Further south, from 22º to 30ºS, the thickness is less than 0.5 km, increasing to >1 km from 33ºS southwards (Schweller *et al.*, 1981; Bangs and Cande, 1997).

Figure 1.2c shows the free-air gravity anomaly (Sandwell and Smith, 2009) for south-western South America. Negative anomalies are observed along the trench, with maximum values decreasing southwards until the Mocha FZ, from where less prominent negative values are observed. Offshore, positive anomalies are present in general in the seafloor with strong positive values in the Iquique and Juan Fernández Ridges and at the south-west limit of the Nazca Ridge. Inland, the distribution of anomalies is much more variable. In general, along the Chilean margin, positive values are observed in the Coastal Range and tectonic arc, while slightly negative values are present along the Central Depression.

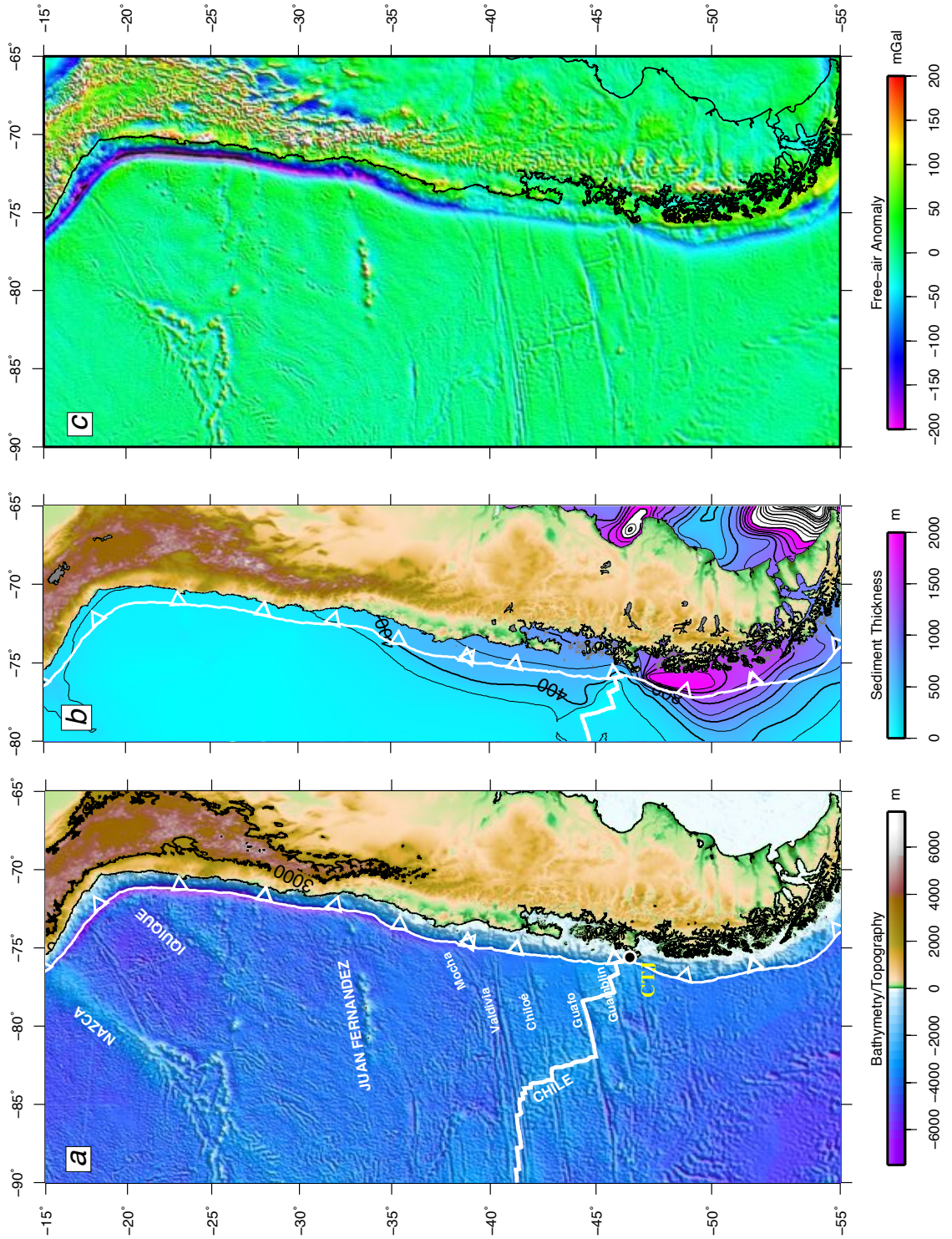

Figure 1.2. Chilean subduction margin. **a)** Topography/Bathymetry and seafloor features. The 3000 m topographic contour is showed in black line. Ridges are shown in UPPER CASE letters, fracture zones in Title Case latters; CTJ Chile Triple Junction. **b)** Sediment thickness along the seafloor of the Chilean subduction margin with contour lines every 200 m thickness (Divins, 2003). **c)** Free-air gravity anomaly map (Sandwell and Smith, 2009).

Recently, the observation of trench-parallel gravity anomalies (TPGA) in the fore-arc has been proposed as an indirect measure to study changes in frictional properties along the megathrust, which in turn might control the rupture dynamics of large megathrust earthquakes (e.g. Song and Simons, 2003; Llenos and McGuire, 2007). For example, for the great 1960 Chile earthquake, Song and Simons (2003) show that the along-strike extent of the rupture area is bounded by regions of increasing TPGA and that high slip regions are concentrated in areas of strong negative anomalies. In general, these authors found that great megathrust earthquakes occur in regions with strong negative TPGA, whilst regions with strongly positive TPGA remain aseismic. They interpret the values of TPGA in terms of variations of shear traction on the megathrust, suggesting an inverse correlation between TPGA and shear traction (i.e. strongly negative TPGA correlates with regions of high shear traction and vice versa). The authors link high slip zones (negative TPGA) with increases in the effective coefficient of friction, proposing that the variations of frictional properties on the megathrust surface (indirectly measured through the TPGA) is an important controlling factor in the occurrence and behaviour of great subduction earthquakes.

The age of the subducting slab (consequently its temperature, density and thickness) varies considerably along the strike of the subductive margin, increasing from virtually 0 Ma at the CTJ to nearly 55 Ma in the north at ~20ºS (Figure 1.3). Along-strike discontinuities on the seafloor age are correlated with offsets in FZs trending with azimuth ~70º (Figures 1.2a and 1.3).

The subduction dip-angle of the Nazca plate also varies along-strike. Segments with low angle ‘flat-slab’ subduction, e.g. beneath central and northern Perú and between 28º and 32ºS in central Chile, are correlated with gaps in the Quaternary volcanism (Figure 1.3; Barazangi and Isacks, 1976). The transitions from a flat segment to a more steepened dip correspond to continuous flexures rather than tears in the slab (Cahill and Isacks, 1992). Except for these flat-slab segments, variable dip angles of 25º to 35º are observed for the subducted slab (Barazangi and Isacks, 1976), down to ~200 km depth, where the inclination increases downwards (Figure 1.3).

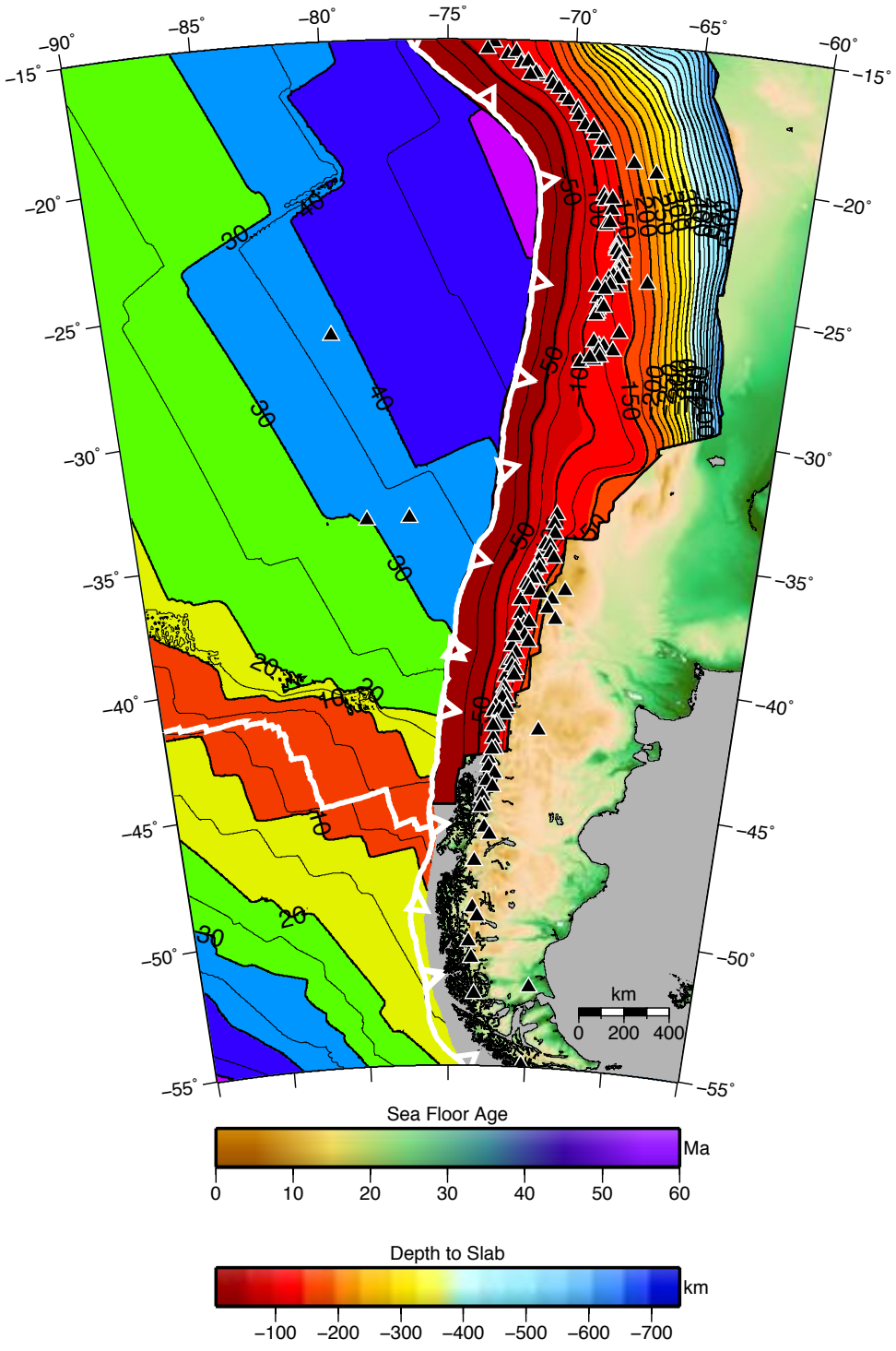

Figure 1.3. Seafloor age and geometry of the subducted slab along the Chilean subductive margin. Seafloor age with isochrones every 5 Ma (Muller *et al.*, 2008). Depth to the top of the subducted slab is shown with contour lines every 25 km (Hayes *et al.*, 2012). Black triangles show Quaternary volcanoes.

1.1.2. Seismicity along the Southern Chilean Subductive Margin

Seismicity along the Chilean margin is related to: subduction zone seismicity on the megathrust, intermediate to deep seismicity in the mantle, and crustal seismicity in the overriding plate and on the Chile Ridge (Figure 1.4). In general, the seismicity along the Chilean subductive margin decreases from north to south towards the CTJ. This pattern is also observed in terms of depth of seismicity, which decreases in the same direction (Figure 1.4).

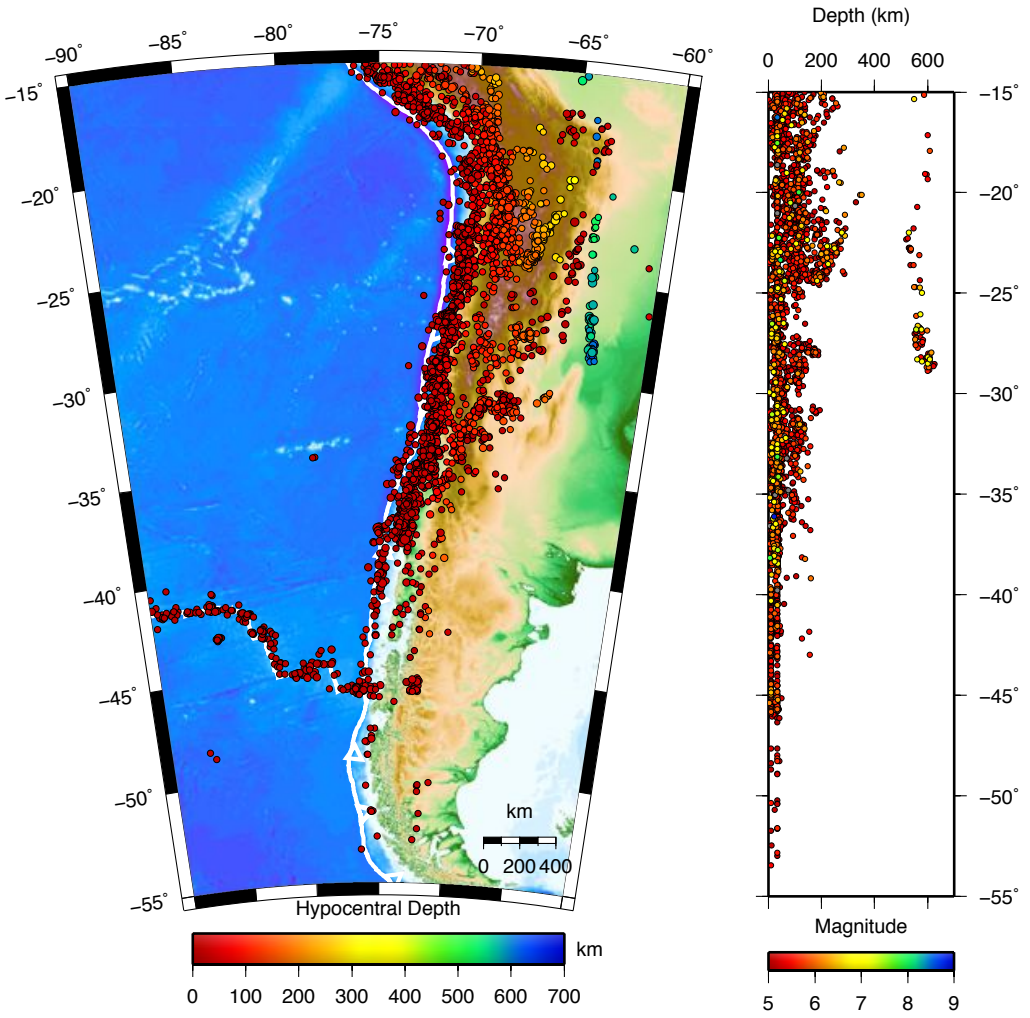

Figure 1.4. Seismicity along the Chilean subduction margin. Left seismicity M≥5 coloured by depth (NEIC catalogue, 1973-2012). Right: depth profile along the margin showing same seismicity of left coloured by magnitude.

Large earthquakes, M>8, have occurred all along the Chilean subductive margin (Bilek, 2010). The largest recorded event, the great 1960 Mw 9.5 Chile earthquake, ruptured circa 900 km along the megathrust, between ~38º and ~46ºS (Barrientos and Ward, 1990). Northwards, the segment between ~35º to ~38ºS ruptured in 1835 with an earthquake magnitude ~8.5 (Lomnitz, 2004). Approximately the same segment ruptured recently in 2010 with an earthquake Mw 8.8 (e.g. Moreno *et al.*, 2012).

The segmented character of the Chilean subduction margin can also be inferred from the distribution of rupture areas of past large megathrust earthquakes, which appear to not overlap and be recurrent in time (e.g. Lomnitz, 2004; Beck *et al.* 1998). The reasons behind the recurrence of large megathrust earthquakes' rupture areas are still not well understood. It has been proposed that incoming seafloor structures such as seamounts and ridges may play a fundamental role in the control of the rupture areas extent (e.g. Cloos, 1992; Bilek, 2010; Sparkes *et al.*, 2010). Nevertheless, Moreno *et al.* (2012) found that no bathymetric feature affected the rupture extent of the 2010 Chile earthquake. Recently, Métois *et al.* (2012) discretised the Chilean subduction margin in 4 segments with a high degree of coupling separated by narrow segments of low coupling which are associated to bathymetric (fracture zones) or coastal features (peninsulas).

1.2. The 2010 Mw 8.8 Maule, Chile, Earthquake

On the early hours of February 27th 2010, a Mw 8.8 earthquake struck the coast of south-central Chile, rupturing nearly 500 km along the subduction interface and generating a widespread tsunami. The occurrence of this event coincided with the occurrence of other great megathrust earthquakes within the last decade: the Mw 9.1 2004 'Boxing Day' Sumatra earthquake and the Mw 9.0 2011 Tohoku-oki, Japan earthquake.

The Chile 2010 earthquake was relocated by Vigny *et al.* (2011) at 36.41ºS and 73.18ºW (see Figure 1.5b), and came to fill a seismic gap present since 1835 (Moreno *et*

al., 2012) when Charles Darwin described an event M~8.5 (Lomnitz, 2004) of similar characteristics with approximately the same rupture area (Beck *et al.*, 1998; Campos *et al.*, 2002).

The 1835 seismic gap or Constitución-Concepción seismic gap, between 35º and 37ºS, was previously reported by Campos *et al.* (2002), who defined seismic gap as a zone where large earthquakes occurred in the past but that has been quiet for decades. It was limited to the south by the rupture area of the 1960 Mw 9.5 Great Chile Earthquake, whilst to the north, the gap was bounded by the 1906 and 1928 Valparaíso earthquakes (Beck *et al.*, 1998; Campos *et al.*, 2002). Beck *et al.* (1998) discarded a major event in this area, the M=7.8 1939 Chillán earthquake, as a megathrust event, instead concluding it was an extensional intra-plate earthquake. Therefore, the Constitución-Concepción seismic gap remained free of large megathrust earthquakes since 1835 up to the recent event in 2010.

Just before the event of 2010, Ruegg *et al.* (2009) concluded that in this segment, the Nazca and South American plates were fully coupled down to a locking depth of 60 km. Given the current rate of convergence, they proposed a slip deficit of more than 10 m since the earthquake of 1835, which, as they suggest, would be enough to produce a large megathrust earthquake Mw=8.0-8.5.

Following the 2010 megathrust earthquake, Moreno *et al.* (2010) showed that the slip distribution of this event correlated closely with the interseismic locking distribution derived from the inversion of GPS observations during the previous decade. This suggests that coseismic slip heterogeneities at the scale of single asperities could indicate the seismic potential of future great earthquakes. Later, Métois *et al.* (2012), based on GPS measurements during the last two decades, found that the segment ruptured in 2010 corresponded to a highly coupled segment bounded by narrow segments of low coupling that would have stopped the rupture.

Figure 1.5 serves as an overview of the seismic activity in this area prior and following the 2010 event. Clearly the detected teleseismic activity increased considerably after the 2010 event, specially in the outer-rise area and in general off-shore. Focal mechanisms

show, as expected, a majority of thrust aftershock events, normal faulting in the outer-rise and a particular concentration of crustal normal faulting in the overriding plate at ~34.5ºS.

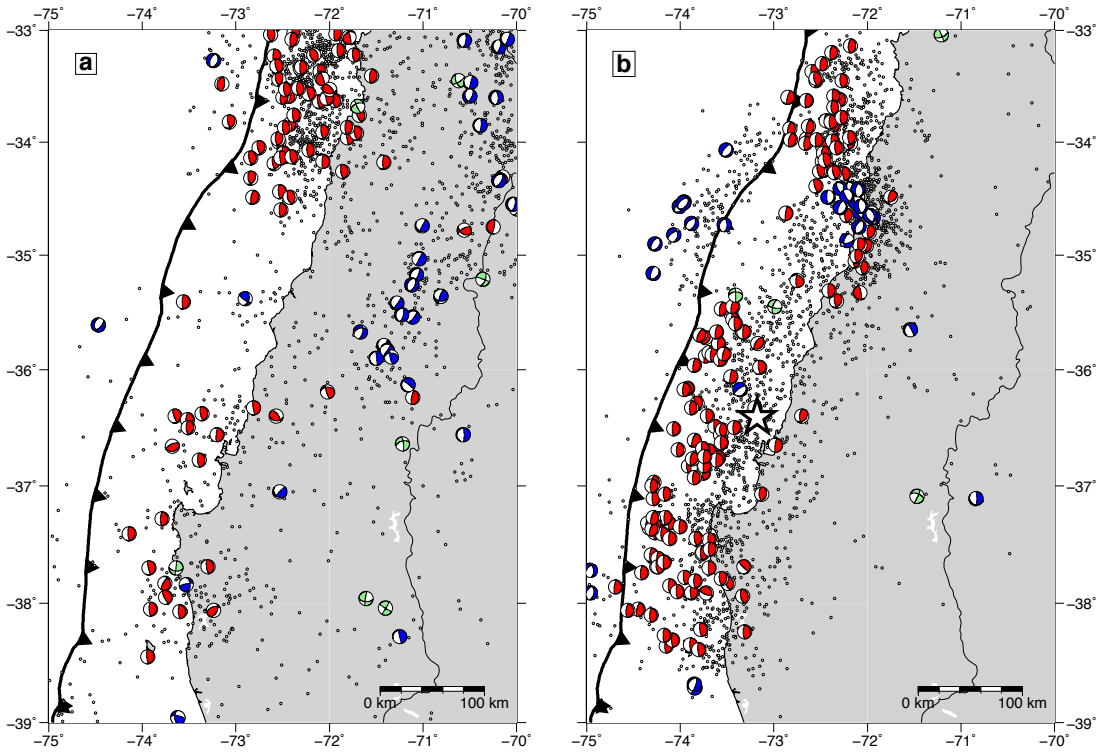

Figure 1.5. Seismicity and focal mechanisms in the area of the 2010 Chile megathrust earthquake prior to the 2010 event (a) and after it (b). Black dots depict events M>4 from the PDE-NEIC catalogue (1973-2012). Focal mechanisms from GCMT catalogue (1976-2012) coloured by faulting mechanism: red thrust, blue normal, green strike-slip. White star indicates epicentre of the 2010 event (Vigny *et al.*, 2011).

The 2010 Chile Earthquake and its series of aftershocks is one of the most well recorded seismic sequences during modern seismology. Several co-seismic slip models have been published to date, based on seismic and GPS observations, satellite interferometry, land-level observations and tsunami data (e.g. Lorito *et al.*, 2011; Vigny *et al.*, 2011; Moreno *et al.*, 2012). Postseismic event distributions have also been published with more than 20,000 aftershocks (e.g. Lange *et al.*, 2012, Rietbrock *et al.*, 2012) recorded by a dense seismic local network deployed by scientific institutions from Chile, France, Germany, USA and the UK.

In the present thesis, specifically in Chapter 5, I characterize the postseismic activity of the 2010 Chile earthquake based on regional moment tensor inversions and a quantitative approach to the distribution of aftershocks relative to published coseismic slip models. The relation between geodetic and seismically measured afterslip is also addressed in this chapter, providing a discussion and methodology that not only applies to this megathrust earthquake, but also to any other earthquake for which slip models have been derived.

1.3. Strike-slip faults in Oblique Subduction Environments

In Chapter 4, I analyse a recent seismic sequence that took place in 2007 on the southern end of the Liquiñe-Ofqui Fault System (LOFS), southern Chile. The LOFS corresponds to a large strike-slip fault that accommodates part of the trench-parallel component of the oblique convergence present between Nazca and South America in its southernmost portion.

Slip vectors of megathrust earthquakes in oblique subduction margins rarely reflect the degree of obliquity: they are neither completely orthogonal to the trench nor aligned with the oblique convergence angle (e.g. McCafrey, 1992). This indicates that the margin-parallel component of the oblique convergence must be absorbed in another way, such as deformation on the overriding plate.

Fitch (1972) was the first to notice the occurrence of trench-parallel strike-slip faulting inland of oblique subduction tectonic environments. He proposed a simple model in which the margin-parallel component of the oblique convergence between two plates is absorbed by inland vertical strike-slip faulting, with the degree of obliquity as the main factor that controls the strike-slip development.

Later, Jarrard (1986) showed that around 50% of modern subduction zones present active margin-parallel strike-slip faulting, often located close to or in the magmatic arc, representing a more common tectonic environment than strike-slip faulting between major plates (transform faults) such as the San Andreas fault and the Alpine fault in

New Zealand. This author proposed three controlling factors for the occurrence of arc-parallel strike-slip faults: the convergence obliquity, the degree of coupling between the overriding and subducting plates, and the strength of the overriding plate. He, therefore, concludes that optimum conditions for the development of strike-slip faulting on subduction zones are: oblique convergence, strong intraplate coupling and a continental overriding plate (an oceanic overriding plate is "too strong" to develop strike-slip faulting due to oblique convergence).

Regarding the large strike-slip faults present in the Chilean margin (see below), Hoffmann-Rothe *et al.* (2006) point out that the sense of slip at the time of formation of these structures is consistent with the convergence obliquity at the respective time, concluding that oblique plate convergence is a necessary prerequisite for the development of margin-parallel strike-slip faults. Nevertheless, temporal variations in the obliquity and/or rate of convergence are not key factors in the reactivation/inactivity of these faults. Instead, these authors suggest that effective rheological weakening of parts of the overriding plate and/or geometries that delimit margin-parallel sliver motion seem to be the primary controlling factors inducing the development of strike-slip strain and fore-arc slivers.

1.3.1. World examples of strike-slip faults in oblique subduction environments

The LOFS belongs to a group of trench-parallel strike-slip faults present in oblique subduction environments. Similar examples within this group are the Philippine Fault (Barrier *et al.*, 1991), the Sumatran Fault (Sieh and Natawidjaja, 2000), the Median Tectonic Line in Japan (Tsutsumi and Okada, 1996), and the Atacama Fault in northern Chile (Scheuber and Andriessen, 1990).

The Philippine Fault is a left-lateral strike-slip fault that transects the whole Philippine Archipelago in a northwest-southeast direction, originated as a consequence of the oblique convergence between the Philippine Sea plate and Eurasia (Barrier *et al.*, 1991; see Figure 1.6). The Philippine Fault also defines the eastern border of a ~NS-oriented fore-arc sliver, the East Philippine block, whose western border correspond to the

Philippine trench. Further, the central portion of this fault is characterized by pure left-lateral strike-slip motion and high seismicity (e.g. Barrier *et al.*, 1991; Besana and Ando, 2005).

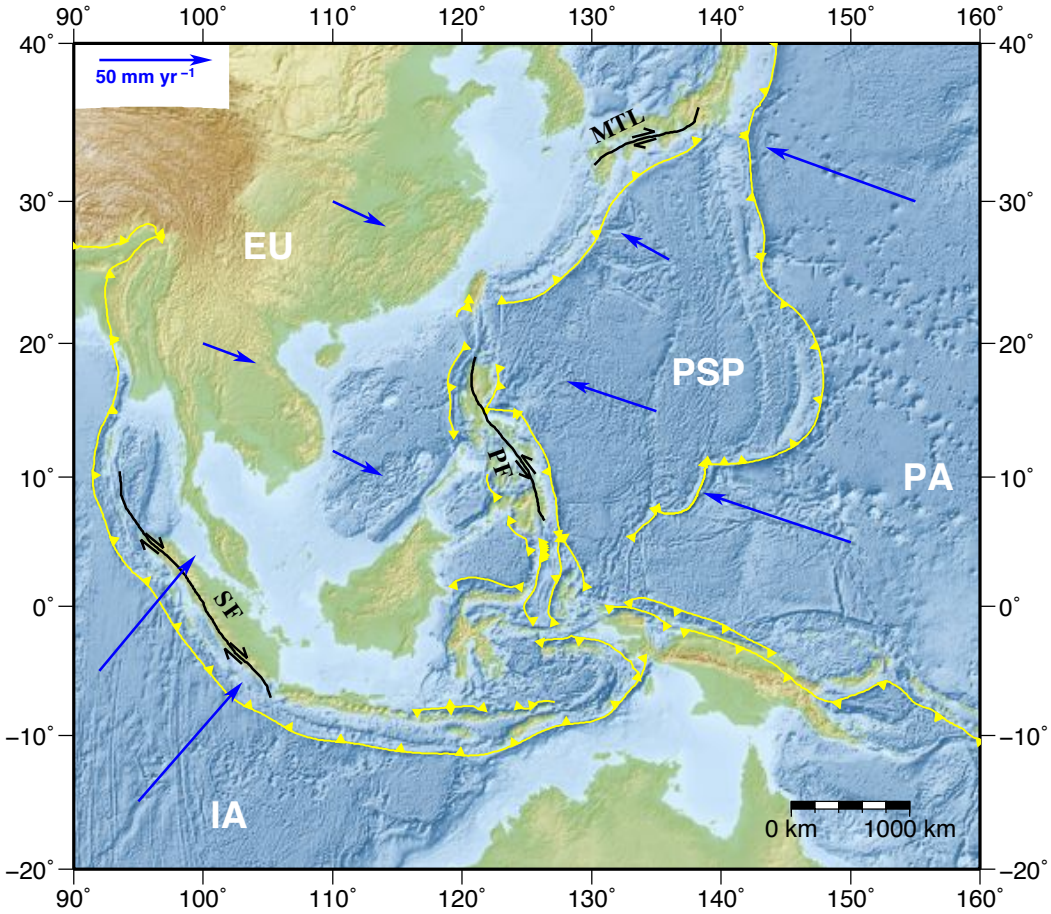

Figure 1.6. Map of southeast Asia showing active subduction zones and large strike-slip faults associated to oblique convergence. EU Eurasian plate, IA Indo-Australian plate, PSP Philippine Sea plate, PA Pacific plate, SF Sumatran Fault, PF Philippine Fault, MTL Median Tectonic Line. Blue arrows indicate plate motion velocities (DeMets *et al.*, 1994).

The Sumatran Fault is located over the active Sumatran volcanic arc, in Indonesia, for more than 1900 km length (Sieh and Natawidjaja, 2000; see Figure 1.6). This large right-lateral strike-slip fault absorbs the trench-parallel component of the oblique convergence between the Indo-Australian plate and Eurasia. As the Philippine Fault, the Sumatran Fault is also the border of a fore-arc sliver plate bounded between this fault and the Sunda (Java) trench (Jarrard, 1986). The highly segmented character of the Sumatran Fault (e.g. Sieh and Natawidjaja, 2000) influences the seismic dimensions of earthquakes along the fault and has limited the magnitudes of large historical

earthquakes to Mw 6.5-7.7 (Natawidjaja and Triyoso, 2007). Recently, Weller *et al.* (2012) collected seismic data in the area, recording crustal events with magnitudes 1.1 to 6.0, and defining a seismogenic depth of 15 km for this strike-slip fault.

The Median Tectonic Line is another classic example of a large strike-slip fault located on an oblique subduction margin. The Median Tectonic Line corresponds to an arc-parallel right-lateral strike-slip fault that runs for more than 300 km along southwest Japan, related to the oblique subduction along the Nankai Trough between the Philippine Sea Plate and Eurasia (Tsutsumi and Okada, 1996; see Figure 1.6). This fault, the longest exposed fault onshore Japan, is also one of the most active faults onshore, with an average slip rate of 5-10 mm yr^{-1} (Research Group for Active Faults of Japan, 1991). Similar to the Sumatran Fault, the Median Tectonic Line has been characterized by discrete sections (Tsutsumi and Okada, 1996) that would limit rupture segments, impeding the rupture of the whole fault during a single event.

The current oblique convergence to the ENE between Nazca and South America has been continuous since the late Cretaceous (Pardo-Casas and Molnar, 1987), preceded by oblique convergence to the SE (Zonenshayn *et al.*, 1984). This configuration has generated the occurrence of two large margin-parallel strike-slip fault systems: the Atacama Fault and the Liquiñe-Ofqui Fault in northern and southern Chile respectively (see Figure 1.7). On the other hand, within the flat-slab segment with no active volcanic arc (28º-33ºS; Figure 1.3), the oblique convergence is accommodated by the subduction zone itself, thus precluding any strain portioning at a lithospheric scale in the overriding plate (Siame *et al.*, 2005).

The Atacama Fault System extends for more than 1000 km between 21º and 30ºS in the fore-arc of northern Chile (Scheuber and Andriessen, 1990; Cembrano *et al.*, 2005). It formed during late Jurassic as a left-lateral strike-slip fault within the Jurassic-early Cretaceous magmatic arc, as a response to the oblique convergence predominant at that time (Scheuber and Andriessen, 1990). Moreover, neotectonic kinematics of the fault are dominated by normal faulting in response to the uplift of the Coastal Cordillera in northern Chile (González *et al.*, 2003).

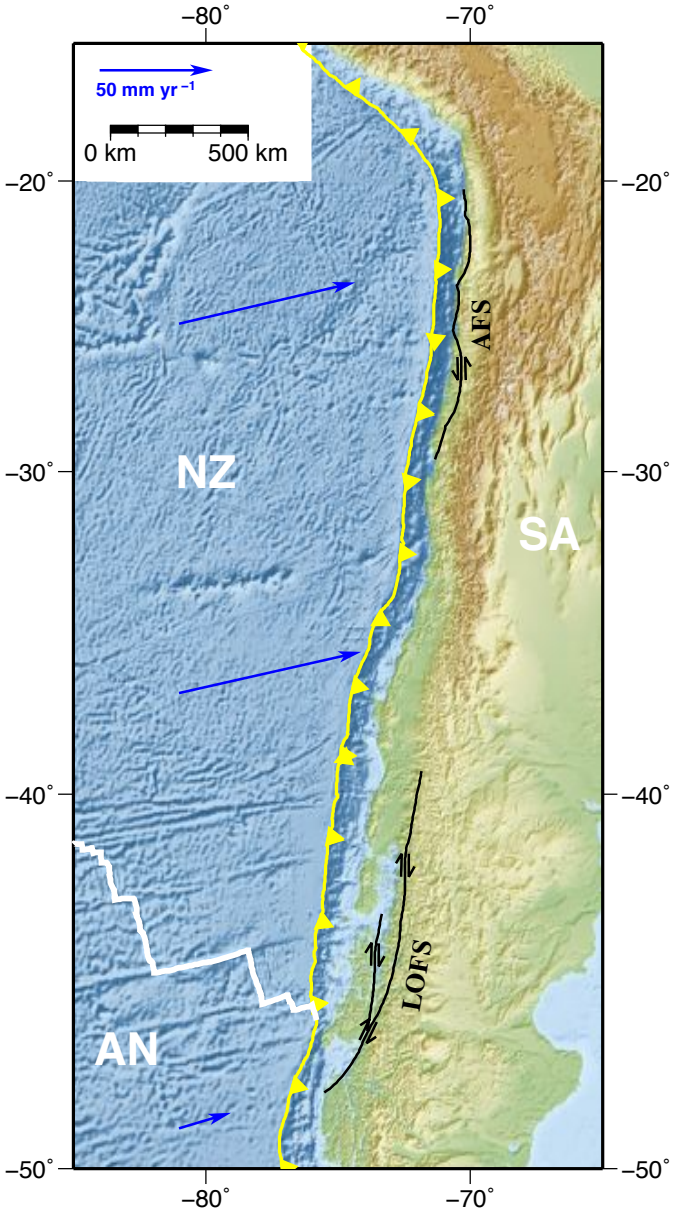

Figure 1.7. Map of the Chilean subductive margin showing location of the Atacama Fault System (AFS) and Liquiñe-Ofqui Fault System (LOFS). NZ Nazca plate, AN Antarctic plate, SA South American plate. Blue arrows indicate plate motion velocities (DeMets *et al.*, 1994).

Last in this group of large strike-slip faults present in oblique subduction environments is the Liquiñe-Ofqui Fault System (LOFS), in southern Chile, which corresponds to an active right-lateral strike-slip fault that runs for more than 1000 km within the arc (Hervé, 1976; Cembrano *et al.*, 1996, 2000, 2002). Cembrano *et al.* (2000) showed evidence of a Mesozoic sinistral predecessor of the LOFS, which might be related to a period of margin-parallel sinistral deformation in the Early Cretaceous, contemporary with that of the Atacama Fault mentioned above. The long- and short-term kinematics of the LOFS though is characterised by dextral strike-slip faulting related to the oblique convergence between Nazca and South America and the partitioning of deformation in a

thermally weakened crust of the overriding plate (Cembrano *et al.*, 2000, 2002). The LOFS is also the eastern border of a fore-arc sliver bounded between this fault and the trench (e.g. Wang *et al.*, 2007). Furthermore, it has been suggested (e.g. Cembrano and Moreno, 1994; Cembrano and Lara, 2009) that this strike-slip structure controls the distribution of Quaternary volcanism along the magmatic arc.

Despite being a common tectonic environment with high levels of seismicity, large strike-slip faults as those mentioned above are still lacking in detailed study, with many questions remaining (e.g. controlling factors, current seismic activity, slip-partitioning, rate of slip, maximum possible earthquake magnitudes, etc.). Chapter 4 of this thesis shows the most recent indications that the LOFS in Southern Chile is at the present seismically active in its southern limit and capable of producing events M>6. Complementarily, Chapter 3 provides a review on the seismotectonics of the Aysén Region, southern Chile, where the LOFS starts its development northwards, based on the seismicity recorded by a local network kept for two years between 2004 and 2005 in the area (Miller *et al.*, 2005).

1.4. Motivation and Thesis Aims

The development of this thesis started with the intent of recording the aftershock sequence of the 2007 Mw 6.2 Aysén Fjord earthquake. The occurrence of this earthquake offered a unique opportunity to study this region, which has been poorly studied whether because of difficulties of fieldwork or lack of teleseismic data. Moreover, this sequence, localised over the main trend of the Liquiñe-Ofqui fault, provided the chance to acquire new knowledge on the current state of deformation of this large strike-slip fault system, that shares similar characteristics with other large strike-slip faults located in oblique subduction margins as the Sumatran fault and the Philippine fault. Consequently, the characterisation of this seismic sequence and associated tectonic processes was one of the primary goals of this PhD work. Further, the inversion of a local velocity model for the area and accurate localisation and estimation of errors, completed the set of goals proposed for the seismotectonic

characterisation of this segment, the southernmost of the subduction margin between Nazca and South America.

Later on, the occurrence of the 2010 Mw 8.8 megathrust earthquake shifted the focus of my PhD project on pursuit of the recording and research of this major seismic event and its sequence of aftershocks. The targets set for this research contemplated the inversion of regional moment tensor solutions for the largest aftershocks and the characterisation of the distribution of postseismic activity relative to published coseismic and postseismic slip models.

By conjugating the research of these two areas of the Chilean subduction margin, the main goal of this thesis is to characterize and comprehend the current seismotectonic state of the subductive process occurring between Nazca and South American plates in southern Chile, expressed and understood as the occurrence of large megathrust earthquakes in the interface and crustal deformation in the overriding plate.

CHAPTER 2

THEORY AND METHODS

2.1. Earthquake Location Methods

An earthquake is a sudden process in the Earth's crust or mantle caused by tectonic stress. The earthquake location specifies the spatial position and time of occurrence for an earthquake. The location may refer to the earthquake hypocentre and corresponding origin time, a mean or centroid of some spatial or temporal characteristic of the earthquake, or another property of the earthquake that can be spatially and temporally localized (Lomax *et al.*, 2009). Thus, the hypocentre or absolute location of an earthquake is defined by:

$$h = (x,y,z,t) \tag{2.1}$$

where x and y are the coordinates in the horizontal plane (epicentre), z is the hypocentral depth and t is the origin time.

Given that earthquakes occur deep in the Earth, earthquake location can be considered as an indirect process involving remote observations. Usually, determining a hypocentral location requires both the identification of seismic phases at several seismometers or seismic stations and knowing the velocity structure of the medium, in this case the Earth, between the hypocentre and the observing stations.

Earthquake location is a classical inverse problem in seismology: given the observations (phases travel times) we must find the model (source location) that "fits" them. This is commonly solved by the match (or misfit) of the observed travel times and the prediction of those arrivals for a source location given a known velocity structure. Predicted arrival times are usually calculated from tracing of seismic waves' ray paths through a medium with known velocity structure, but also from full-waveform inversions and other techniques.

Considering a homogeneous and isotropic medium with seismic wave velocity v, the arrival time at an ith station t_i, is given by

$$t_i = t + \frac{\sqrt{(x_i - x)^2 + (y_i - y)^2 + (z_i - z)^2}}{v} \tag{2.2}$$

with t_i, x_i, y_i and z_i being our observations and t, x, y and z our model or source location that must fit them. Consequently, the earthquake location is ordinarily (see section 2.1.1 below) obtained by reducing the misfit between the predicted and the observed arrival times.

2.1.1. Linearized location method

Although earthquake location is a non-linear problem (see below), direct and iterative linearized inversion methods are commonly used to rapidly obtain hypocentral solutions and error estimates. Most of the computer programs used to obtain earthquake locations are based on linearized methods (e.g. HYPOELLIPSE, HYPO71) developed after the technique proposed by Geiger (1912). Geiger's technique is based on the least-square

method, in which travel-time residuals are iteratively minimized in order to converge to a minimum hypocentral solution.

A travel-time residual corresponds to the difference between the observed travel-time and a predicted or calculated one. Following Equation 2.2, for an observation at the *i*th seismic station, with observed arrival time t_i, the residual travel-time between the predicted and observed time is given by

$$r_i = t_i - c_i \tag{2.3}$$

where r_i is the residual travel-time and c_i is the calculated or predicted travel-time.

Non-zero residual times can be due to (i) incorrect reading of the phase arrivals (noisy signals, experience-related analyst errors, etc), (ii) incorrect assumed velocity model for the prediction of the travel time (including attenuation effects, simplistic assumptions, etc) or (iii) an incorrect choice of earthquake source parameters.

Dismissing reading errors and inaccuracies of the velocity model, the only source of time residuals corresponds to incorrect source parameters. Therefore, the travel-time of a phase would be determined exclusively by the hypocentral coordinates (x,y,z,t). We then find the "correct" source parameters that minimize the residual times such as $r_i = 0$.

In order to do this, we firstly define a trial origin time and hypocentre (x_0, y_0, z_0, t_0) and calculate its residual time. The selection of an initial trial hypocentre is made based on, for example, the location of the closest station (smallest travel time), approximate depth range of the seismicity, etc. We then calculate the residual time for a new hypocentral location ($x_0+\Delta X$, $y_0+\Delta Y$, $z_0+\Delta Z$, $t_0+\Delta T$), with Δ being small perturbations on each one of the spatio-temporal coordinates (X,Y,Z,T). The residual time for this new location can be calculated from the partial derivatives of the travel-time evaluated at the new hypocentral parameters. This is solved through a Taylor series expansion:

$$r_i = \sum_{j=1}^{4} \frac{\partial t_i}{\partial h_{ij}} \Delta h_{ij} \tag{2.4}$$

where h_j are the estimated (not true) hypocentral parameters and Δh represents the variations or perturbations on the hypocentral parameters with respect to the initial trial hypocentre. The partial derivatives of travel time with respect to the hypocentral parameters ($\partial t/\partial h$) express the relative influence of each one of the spatio-temporal coordinates on a given travel time datum (Thurber, 1993). The usage of partial derivatives linearizes the location problem as seen in Equation 2.4.

Geiger's least-squares method implies that the perturbations on the hypocentral parameters are selected such as the root-mean-square (RMS) of the residual is minimized. We then repeat this process iteratively until the perturbations Δ on the hypocentral parameters (smaller after every iteration) do not reduce the RMS of the residuals anymore, hopefully reaching a minimum solution.

2.1.2. Simultaneous inversion of travel time data for hypocentral and velocity structure parameters – The minimum 1-D velocity model

As seen above, misfits between calculated and observed travel times are produced by timing errors, hypocentre location errors, inaccurate and/or simplistic assumed velocity model or, most likely, a combination of all the above. Accurate location of earthquakes requires the most reliable possible information about the velocity structure of the study region, and the simultaneous solution of the **coupled hypocentre velocity model problem** (e.g. Kissling, 1988; Kissling *et al.*, 1994).

Though, for simplicity, in Section 2.1.1 the importance of an accurate velocity model was dismissed, the evident reciprocal dependency of hypocentral and velocity model parameters requires the simultaneous and correct determination of them. The determination of the unknown hypocentral parameters and velocity model from a set of arrival times is called the coupled hypocentre velocity model problem (Kissling, 1988).

In matrix notation, the coupled hypocentre velocity model parameter relation can be written as (Kissling *et al.*, 1994):

$$\mathbf{r} = \mathbf{H}\,\boldsymbol{\Delta}\mathbf{h} + \mathbf{M}\,\boldsymbol{\Delta}\mathbf{m} + \mathbf{e} \qquad (2.5)$$

where

r is the vector of travel time residuals

H is the matrix of partial derivatives of travel time with respect to hypocentral parameters

Δh is the vector with adjustments to hypocentral parameters

M is the matrix of the partial derivatives of travel time with respect to velocity model parameters

Δm is the vector with adjustments to velocity model parameters

e is the vector containing travel time errors

The determination of Δm, and therefore, of our 1-D minimum velocity model can be obtained through a least-squares solution for a system of linear equations:

$$\Delta m = (M^T M)^{-1} M^T r \quad (2.6)$$

where M^T is the transposed matrix M.

Further, following the method introduced by Aki *et al.* (1977), the least squares solution can be solved using damped parameters, which allow the stabilization of the solution avoiding underestimated parameters:

$$m = (M^T M + L)^{-1} M^T r \quad (2.7)$$

where L is the diagonal matrix containing the damping parameters.

The damped least squares solution shown in equation (2.7) is implemented in the program VELEST (Kissling *et al.*, 1994; Kissling *et al.*, 1995) in order to find the **minimum 1-D velocity model**. The concept of minimum 1-D velocity model (Kissling *et al.*, 1994) is used to describe a preferred initial 1-D velocity model that can be used for earthquake location and 3-D seismic tomography. For areas in which little information is known about the velocity structure, the calculation of such a velocity model is fundamental in order to address correctly the earthquake location problem.

In this thesis, the program VELEST was used to invert simultaneously for both hypocentral and velocity structure parameters including station corrections for the aftershock dataset recorded in the Aysén Fjord area, obtaining in this way a new 1-D velocity model for earthquake location purposes for this area (see Chapter 4).

2.1.3. The problem of earthquake location: nonlinearity

Equation 2.2 is inherently nonlinear even for a simple homogeneous medium: t does not depend linearly on either x, y or z, and therefore, we cannot find a solution by using standard methods of solving a system of linear equations as, for example, a linear least-squares solution. As seen in Sections 2.1.1 and 2.1.2 this issue is most commonly solved by approximating a hypocentral solution (x,y,z,t) through a Taylor series expansion around a prior solution or estimate. However, this method does not guarantee convergence to the absolute minimum or, in our case, the correct earthquake location (Lay and Wallace, 1995).

In order to deal with the nonlinearity of the earthquake location problem, Tarantola and Valette (1982) proposed to consider the data and parameters of the nonlinear inversion as *probability density functions* (pdf). A pdf is a function of a variable X that describes the probability or likelihood of occurrence of a given value for that variable. The method of Tarantola and Valette (1982) produces a comprehensive hypocentral solution that offers a 4-dimensional, posterior pdf over all possible solutions (spatial locations and origin times). This posterior pdf quantifies the agreement between predicted and observed travel times in relation to all uncertainties, and forms a complete, probabilistic solution.

With linearized methods we obtain a single 'best-fit' hypocentral location and linearly estimated uncertainties, which are often a poor representation of the complete *pdf* solution. Moreover, a linearly-estimated location may be unstable when the *pdf* is irregular, or presents multiple solutions due to insufficient data, outliers, velocity model complexities, and/or other causes (Lomax *et al.*, 2009). On the positive side, linearized methods do not involve large-scale searches and therefore do not require great computational power.

2.1.4. Nonlinear location methods

In non-linearized location techniques, explicit use of partial derivatives is not performed. Instead, they are based on deterministic or stochastic searches, which may be exhaustive or directed and evolutionary (Lomax *et al.*, 2009). It is because of that that these methods are known as direct-search location methods.

For example, a simple direct-search method that uses graphical analysis is the well-known *method of the circles* (e.g. Lay and Wallace, 1995), nowadays typically used for educational purposes, in which at least three stations around the source are needed to estimate an earthquake location.

An illustrative comparison is presented in Figure 2.1 that shows a hypothetic location obtained by a linearized method (red circle) and a direct-search (nonlinear) method (green star). In this case, because of the source is located at the limits of the seismic network and near to a sharp velocity interface, the linearized optimal hypocentre is located on the secondary local maximum of the complete *pdf* obtained from the direct-search method. The linearized error ellipsoid does not even take in account the primary location *pdf* maximum located above the sharp interface. Instead, the maximum-likelihood hypocentre obtained by the direct-search method is correctly located at the primary maximum of the complete location *pdf*.

Direct-search methods perform a sampling of either the partial or total solution space, estimating the complete location *pdf* and, therefore, providing more stable solutions with more accurate estimation of uncertainties. Furthermore, they do not rely on the quality of initial guesses as linearized methods do. The negative side however is the great computational power usually required in order to perform searches over large solution spaces in particular for cases with many unknowns.

Conclusively, it has been proved (e.g. Lomax *et al.*, 2000; Husen *et al.*, 2003) that linearized location methods provide stable and complete location and uncertainty estimations when the source is within the seismic network, except near strong gradients in the velocity structure. For sources outside the network, instead, the linearized methods present inconsistencies in determination of hypocentres and reliable uncertainties. On the other hand, direct-search methods are always stable and provide a complete solution even for cases when the source is located outside the seismic network or near a strong velocity gradient.

2.1.5. Used nonlinear location method: NonLinLoc

In order to obtain the complete posterior earthquake location *pdf* and estimate reliable location uncertainties, in the present work was used the software NonLinLoc (henceforward NLL; Lomax *et al.*, 2000). NLL performs a search of the solution space in a 3-D model and estimates the posterior location *pdf* for the spatial (*x, y, z*) coordinates of the hypocentre and the maximum likelihood origin time. It benefits from a probabilistic nonlinear approach to the earthquake location problem, thus producing more consistent estimation of uncertainties.

Following there is a brief description of how NLL works and its 3 options of search algorithms:

Firstly, given an input velocity model, the program creates a 3-D model grid considering previously defined parameters like grid spacing, number of nodes and origin of the grid. Then, NLL generates travel-time and take-off angle grids for each

phase type (i.e. P, S) at each one of the stations considered in the seismic network. These travel-time grids will then be used when searching for an optimum solution. Lastly, the code locates the event(s) defined by phase picks, by using a preferred direct-search algorithm over the 3-D volume. The chosen sampling algorithm in NLL can be (i) nested grid-search, (ii) Metropolis-Gibbs or (iii) Oct-tree.

(i) **Nested grid-search algorithm:** the nested grid-search algorithm performs a systematic search over the 3-D volume obtaining a misfit function, an optimal hypocentre and the posterior location *pdf*. The algorithm searches successively finer from an initial grid into subsequent 'nested' grids located within the previously searched grid until reaching an optimum solution. Unfortunately this method requires great computer power and is highly time-consuming. Moreover, it requires a careful selection of the grid size and node spacing: if the final sampled grid is too large in relation with the size of the pdf, then the resolution would be too low; instead, if the final grid is too small, it would not contain the totality of the space used by the *pdf*, thus truncating it.

It is convenient now to introduce the concept of **importance sampling**. An importance sampling algorithm is a sampling algorithm that increases its efficiency in targeting a function by choosing a sampling density which follows the function as closely as possible. Although in our case the target function (earthquake location pdf) is unknown, the efficiency of the search can still be improved by adjusting (or adapting or evolving) the sampling by incorporating information gained from previous samples, so that the sampling density tends towards the target function, reducing the required computer power and processing time (Lomax *et al.*, 2000). The Metropolis-Gibbs and Oct-tree sampling algorithms are examples of importance sampling.

(ii) **Metropolis-Gibbs sampling algorithm:** The Metropolis-Gibbs sampling performs a guided random search over the 3-D volume obtaining a set of samples that follow the location *pdf*. These samples contain an estimate of the optimal hypocentre and an image of the posterior location *pdf*. Therefore, the search is directed over the spatial solution towards regions of high likelihood for the location *pdf*. This algorithm is much faster (around 100 times faster) than the grid-search, although its downside is that being a

stochastic search it may provide inconsistent recovery of a very irregular *pdf* with multiple maxima, missing important features of the *pdf*'s space (Lomax *et al.*, 2000). Further, it also requires careful selection of sampling parameters.

(iii) **Oct-tree sampling algorithm:** the Oct-tree importance sampling method (Lomax and Curtis, 2001) provides a complete estimation of the earthquake location *pdf* over a 3-D volume in a more efficient way than the previous two algorithms. It takes its name from being a hierarchical tree data structure in which each node has exactly eight child-cells or children nodes.

The Oct-tree algorithm performs a recursive subdivision and sampling of rectangular cells over the 3-D volume converging to a cascade of oct-tree structures that contain *pdf* values. The higher the *pdf* values in a sampled region (low misfit) the larger the number of smaller cells around that region. In this way, the method provides an importance sampling of the true *pdf*, representing it in a consistent manner.

The relative probability (P_i) that an earthquake location is in a given cell i is approximately given by

$$P_i = v_i \times pdf(x_i) \qquad \text{(2.8; Lomax and Curtis, 2001)}$$

where v_i is the volume of the cell i and x_i is the centre of the cell i. The algorithm starts sampling the full search space on an initial crude regular grid obtaining the misfit value at the centre of each grid cell and calculating its probability P_i. Then, the cell with the highest probability is divided into eight new children cells and the process is repeated recursively.

The advantages of the Oct-tree sampling method in comparison with the previous two algorithms are its simplicity, speed, stability and completeness. Because of this, the Oct-tree sampling method was chosen to perform direct-search earthquake location on the seismic sequence analysed in Chapter 4 and in Chapter 3, providing in this way complete and accurate hypocentral solutions and reliable estimations of uncertainties.

2.2. Calculation of magnitudes

Richter (1958) defined the scale of local magnitude as the logarithm of the maximum zero-to-peak amplitude A, recorded at an epicentral distance of 100 km on a standard Wood-Anderson torsion seismograph. For general epicentral distances, the following formula can be applied:

$$M_l = \log A - \log A_0 \tag{2.9}$$

where A_0 is the empirically obtained correction factor for different epicentral distances and is scaled so that for $M_l = 3$, A = 1mm at epicentral distance = 100km.

Later, Bakun and Joyner (1984) determined the factor A_0 from Wood-Anderson instruments in the area of central California and rewrote Richter's equation considering a new distance correction factor as:

$$M_l = log\ A + [n\ log(R/100) + K\ (R-100) + 3] \tag{2.10}$$

where the terms contained within the square brackets correspond to the distance correction factor composed by R = hypocentral distance, n = geometrical spreading factor = 1, and K = attenuation coefficient = 0.00301 for central California.

Equation (2.10) is implemented in the automated magnitude calculation tool in the GIANT software package (Rietbrock and Scherbaum, 1998), which was used for the calculation of local magnitudes shown in Chapter 4. The same values for K and n from Bakun and Joyner (1984) were used in this work, as little information is available regarding the area of this study. Nevertheless, these differences are likely to be small.

2.3. Seismic Source Representation

Seismic sources can be differentiated into two categories: faulting sources and volume sources (Aki and Richards, 2002). A volume source is an event associated with an internal volume, such a sudden volumetric expansion or shrinkage (e.g. nuclear explosions, changes in mineral phases, etc.). A faulting source is an event associated with an internal surface involving shear dislocation on a plane, and is the most common source type for an earthquake.

In physical terms, a seismic source can be defined as a system of equivalent forces over a point source. For a faulting source, these forces correspond to force couples, in which opposing point forces act separated by a small distance. Moreover, a faulting source is defined by a system of two force couples called double couple in which no net torque occurs (Figure 2.2).

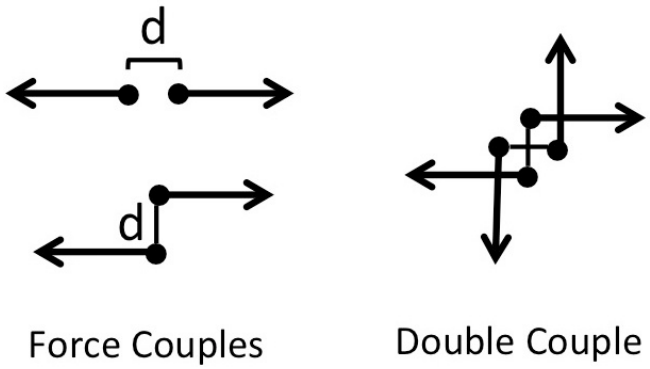

Figure 2.2. Force couples and double couple system.

Given that seismogram signals are the result of both propagation and source effects, once the propagation effects have been isolated, seismograms contain valuable information on the earthquake source. Among this information is the radiation pattern. The radiation pattern is a geometric description of the amplitude and sense of initial motion distributed over the P and S wavefronts around a source (Lay and Wallace, 1995). The geometry of a fault can be constrained from this radiation pattern of the point source (Figure 2.3).

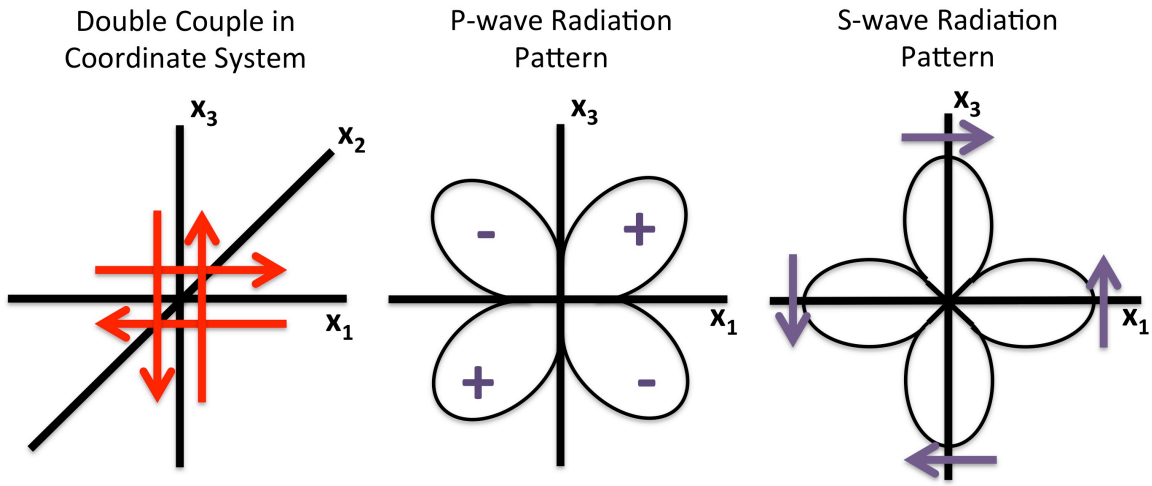

Figure 2.3. Double couple force system. The double couple on the plane x_1x_3 produces a shear rupture in the plane x_1x_2 (auxiliary plane x_3x_2). The correspondent radiation patterns for P-wavefront (+ compressional, - dilatational quadrant) and S-wavefront is shown to the left. Modified from Lay and Wallace (1995).

If enough coverage of seismic stations around a seismic source is present, the radiation pattern of each one of the seismograms can be used to constrain the geometry of the seismic source (see section 2.3.1 below). In this way, the radiation pattern of the P-wavefront defines 4 quadrants separated by two perpendicular nodal planes between them. One nodal plane corresponds to the fault plane, while the other corresponds to the auxiliary plane. Moreover, the fault plane defines a pair of orthogonal dipoles without shear located at 45º from the fault plane. These dipoles or principal axes correspond to the compressional or P-axis and the tensional or T-axis. A third principal axis, the null or B-axis, is located orthogonally to the previous two. With the information of the P-wave radiation pattern we can estimate the fault geometry of the seismic source by obtaining focal mechanisms (see below).

Before continuing on how to represent a seismic source, we shall define the standard nomenclature used to describe a rupture plane. This contains three parameters (see Figure 2.4):

Strike (ϕ), which is the azimuth angle measured clockwise between the north and the projection of the fault onto the surface. It ranges from 0º to 360º.

Dip (δ), which is the angle measured from the horizontal to the plane of the fault in a vertical plane perpendicular to the strike. It ranges from 0º to 90º.

Rake or slip (λ), which is the angle measured in the fault plane from the strike direction to the slip vector and indicates the movement of the hanging wall relative to the footwall. It ranges from -180º to +180º.

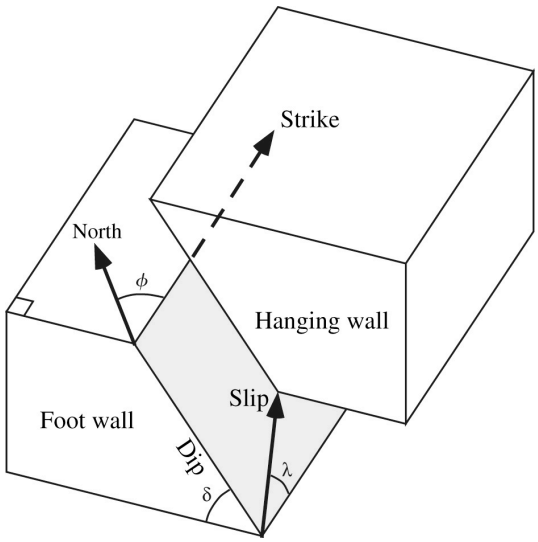

Figure 2.4. Representation of strike, dip and rake defining a fault plane.

2.3.1. Focal mechanisms

In the present thesis, the earthquake source is characterised through focal mechanisms. A focal mechanism is a geometric representation of the source inelastic deformation, equivalent to a force model, in order to characterize the processes that act during an earthquake. Moreover, focal mechanisms are graphically depicted by "beach ball" diagrams, in which four quadrants are present, namely two compressive and two dilatational (Figure 2.5).

The method of first motion polarities is based on the radiation pattern of P-waves. Specifically, on the first movement, up (compressional) or down (dilatational), of an onset of P-waves radiated from the seismic source. "Up" first motion polarities indicate that the first particle motion is towards the station (compressional), whilst "down" polarities indicate that the first particle motion is away from the station (dilatational). Now, provided that there is enough coverage of seismic stations around the source, P-

wave first motion polarities can be identified for each one of the stations and plotted according to their station azimuth and incident angle in an stereographic projection defining 4 quadrants: two compressional comprised by up polarities and two dilatational with down polarities (Figure 2.5). The incident angle is obtained through the ray-tracing of the signal from the source to the seismic station.

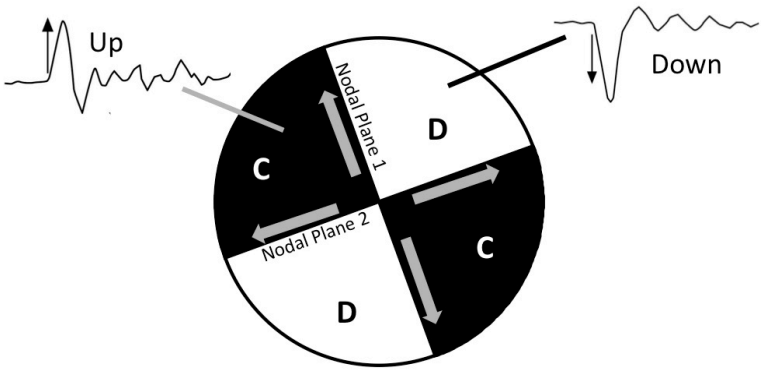

Figure 2.5. First motion polarities from P-waves and focal mechanism. First motions define 4 quadrants separated by two nodal planes. One nodal plane is the actual fault plane and the other is the auxiliary plane. C=compressional, D=dilatational.

The stereographic lower hemisphere projection of the 4 quadrants mentioned before result in a focal mechanism or "beach ball" diagram in which shaded areas represent the compressional quadrants while non-shaded areas are the dilatational quadrants (Figures 2.5 and 2.6). Differentiation of the fault plane from the auxiliary plane cannot be inferred directly from the focal mechanism and must be addressed considering additional geological, geodetic or seismic information as fault and ground motion observations, alignment of earthquakes, present structures, directivity of the rupture, etc.

In addition to first motion P-wave polarities, S-wave/P-wave amplitude ratios provide a supplementary datum in order to constrain focal mechanisms from the radiation pattern. This method is based on the premise that S-waves amplitudes are large near the nodal planes while P-wave amplitudes are large near the P and T axes and smaller near the nodal planes, establishing systematic variations of S/P amplitude ratios on the focal sphere. Thus, by considering the distribution of S/P amplitude ratios on the focal sphere it is possible to constrain the position of the nodal planes and therefore complement the

information acquired from P-wave first motion polarities (e.g. Snoke *et al.*, 1984; Hardebeck and Shearer, 2003).

In this work, focal mechanisms shown in Chapter 4 were obtained from first motion polarities and S/P amplitude ratios by using the software FOCMEC (Snoke *et al.*, 1984; Snoke, 2009).

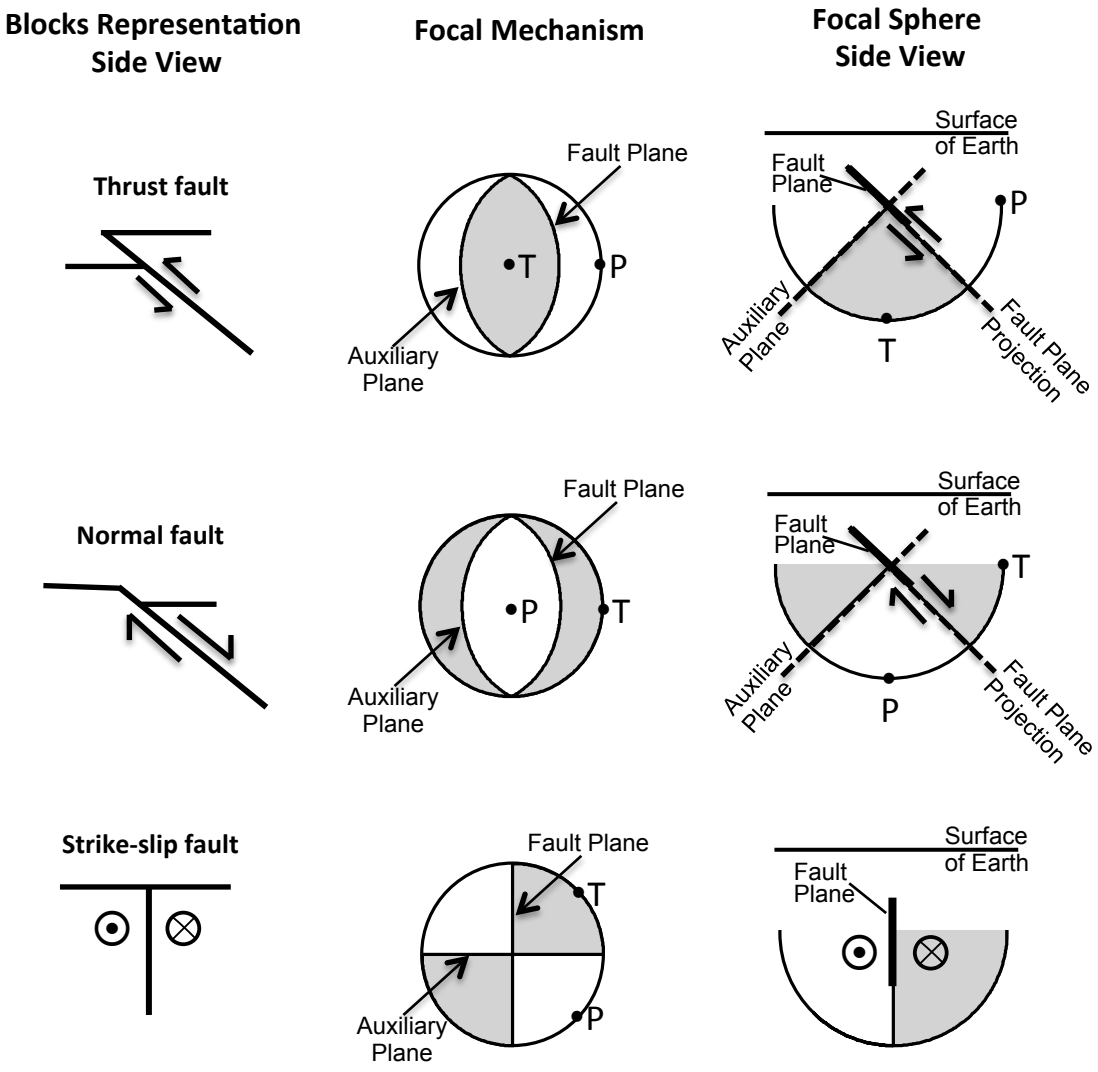

Figure 2.6. Basic types of focal mechanism. The three basic types of faulting, thrust, normal and strike-slip, are shown together with their focal mechanism and focal sphere on side view. P and T axes are also shown. Shaded regions in focal mechanisms and focal spheres indicate compressional P-wave motions.

2.3.2. The seismic moment tensor

The moment tensor is a mathematical representation of the seismic source, considered as an equivalent forces representation. The moment tensor quantifies the 9 possible force couples on a coordinate system (Figure 2.7), and is defined by the matrix:

$$M = \begin{pmatrix} \mathbf{M_{11}} & \mathbf{M_{12}} & \mathbf{M_{13}} \\ M_{21} & \mathbf{M_{22}} & \mathbf{M_{23}} \\ M_{31} & M_{32} & \mathbf{M_{33}} \end{pmatrix}. \quad (2.11)$$

Because the moment tensor is always symmetric, M can be characterized with only 6 independent elements (elements in bold font in Equation (2.11)).

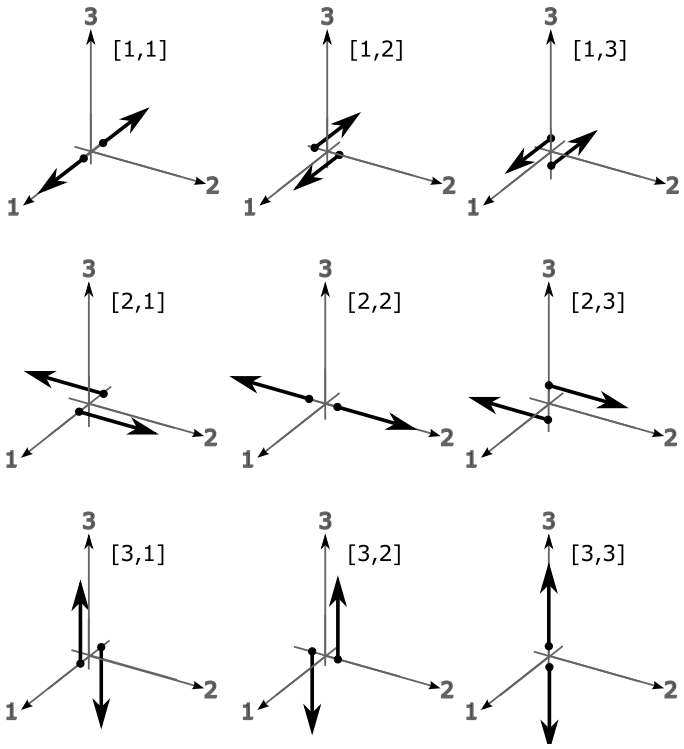

Figure 2.7. The nine possible force couples components of the moment tensor. Modified after Aki and Richards (2002).

For example, a pure right-lateral strike-slip vertical fault would have force couples only in the elements M_{12} and M_{21} and its moment tensor would be:

$$M = M_0 \begin{pmatrix} 0 & M_{12} & 0 \\ M_{21} & 0 & 0 \\ 0 & 0 & 0 \end{pmatrix} \quad (2.12)$$

where the scalar M_0 correspond to the seismic moment with unit dyne-cm or N-m.

The seismic moment M_0 defines the strength of an earthquake and can be related to the dimensions of the rupture as (Aki and Richards, 2002):

$$M_0 = \mu \bar{u} A \quad (2.13)$$

where μ is the rigidity or shear modulus of the medium, $\bar{u}$ is the average slip on the fault, and A is the fault area.

In turn, the moment magnitude (M_W) scale is defined by (Kanamori, 1977) as:

$$M_W = \frac{2}{3}(\log M_0 - 16.1). \quad (2.14)$$

The seismic moment tensor elements can be also related to the strike, dip and rake angles with the following formulae (Aki and Richards, 2002):

$M_{11} = -M_0(\sin\delta \cos\lambda \sin 2\phi + \sin 2\delta \sin\lambda \sin^2\phi)$
$M_{22} = M_0(\sin\delta \cos\lambda \sin 2\phi - \sin 2\delta \sin\lambda \cos^2\phi)$
$M_{33} = M_0(\sin 2\delta \sin\lambda) = -(M_{11} + M_{22})$
$M_{12} = M_0(\sin\delta \cos\lambda \cos 2\phi + \frac{1}{2}\sin 2\delta \sin\lambda \sin 2\phi)$
$M_{13} = -M_0(\cos\delta \cos\lambda \cos\phi + \cos 2\delta \sin\lambda \sin 2\phi)$
$M_{23} = -M_0(\cos\delta \cos\lambda \sin\phi - \cos 2\delta \sin\lambda \cos 2\phi)$

2.3.2.1. Decomposition of the moment tensor

In general, a seismic moment tensor does not necessarily correspond to a pure *double couple* source. For instance, if all three diagonal elements of the moment tensor are nonzero and equal, then that tensor describes an explosion or an implosion, for which the body force system is a *triple vector dipole* composed by three equal and orthogonal

force couples. Thus, the seismic moment tensor might as well describe an *isotropic* or 100% volume seismic source.

The trace of a moment tensor is a measure of volume changes occurring during the event. For an isotropic source, the trace will always be nonzero, while for a pure double couple the trace is equal to 0.

Another possible non-double couple source are *compensated linear vector dipoles* (CLVD). These are sets of three force dipoles that are compensated, with one dipole -2 times the magnitude of the others (Stein and Wysession, 2003):

$$\mathrm{M} = \begin{pmatrix} -\lambda & 0 & 0 \\ 0 & \lambda/2 & 0 \\ 0 & 0 & \lambda/2 \end{pmatrix}. \qquad (2.15)$$

The trace for such a tensor is 0, hence there is no isotropic component.

Furthermore, we can decompose any moment tensor M into an isotropic (M^0), double-couple (M^{DC}) and CLVD (M^{CLVD}) parts:

$$\mathrm{M} = \mathrm{M}^0 + \mathrm{M}^{DC} + \mathrm{M}^{CLVD}.$$

First we isolate the isotropic part as:

$$\mathrm{M}^0 = \tfrac{1}{3}(\mathrm{tr\ M})\mathrm{I}$$

where tr M is the trace of the moment tensor M, and I is the inverse matrix.
Consequently, M is decomposed into an isotropic part and a *deviatoric moment tensor* (M'):

$$\mathrm{M} = \mathrm{M}^0 + \mathrm{M'}$$

M' is free of isotropic sources and can be decomposed into a best double couple and a CLVD part as:

$$\mathrm{M}' = M^{DC} + M^{CLVD} = \begin{pmatrix} \tfrac{1}{2}(\sigma_1 - \sigma_3) & 0 & 0 \\ 0 & 0 & 0 \\ 0 & 0 & -\tfrac{1}{2}(\sigma_1 - \sigma_3) \end{pmatrix} + \begin{pmatrix} -\frac{\sigma_2}{2} & 0 & 0 \\ 0 & \sigma_2 & 0 \\ 0 & 0 & -\frac{\sigma_2}{2} \end{pmatrix}$$

(2.16)

where σ1, σ2 and σ_3 are the eigenvalues of M'.

A measure of the misfit between M' and a pure double-couple source (i.e. the size of the CLVD part relative to the double-couple part) is provided by the value:

$$\varepsilon = \frac{|m_{min}|}{|m_{max}|} \tag{2.17}$$

where m_{min} and m_{max} are the smallest and largest eigenvalues of the deviatoric part of the moment tensor, respectively, both in absolute terms. For a pure double-couple source, ε=0; while for a pure CLVD source ε=0.5. The contribution of the double-couple part is expressed in percentage as

$$DC\% = (1-2\varepsilon)\times 100 \tag{2.18}$$

CLVD sources can be related to simultaneous rupture of faults with different orientations, or curved faults. Moreover, magma injection would produce a source with both volumetric (isotropic) and CLDV parts.

2.3.2.2. Moment tensor inversion

Seismograms can be used to obtain moment tensor solutions through waveform inversion. Being *m* a vector containing the 6 independent components of the moment tensor and $G_{ij}(t)$ the Green's function at the i^{th} station due to the moment tensor component m_j, the i^{th} seismogram is the sum of the Green's functions weighted by the moment tensor components (Stein and Wysession, 2003):

$$d_i(t) = \sum_{j=1}^{6} G_{ij}(t) m_j \tag{2.19}$$

In matrix notation equation (2.19) would be:

$$d = Gm \tag{2.20}$$

where d is our data vector composed of the seismograms at *n* stations, G is the Green's function matrix with as many rows as seismometers and as many columns as moment tensor components (6), and m is our vector of moment tensor's components.

The linear inverse problem d=Gm is then solved for m by the least-square method:

$$m = (G^T G)^{-1} G^T d \tag{2.21}$$

where G^T is G transposed and $()^{-1}$ is the inverse of the so called system matrix ($G^T G$).

2.3.3. ISOLA software

In order to obtain moment tensors solutions, in this work, specifically in Chapter 5, the software ISOLA (Sokos and Zahradnik, 2008) is used, which considers full waveform inversions. Following equation (2.19) and the method proposed by Kikuchi and Kanamori (1991), ISOLA approximates the data seismograms as a combination of elementary seismograms (e_j) corresponding to 6 elementary moment tensors (see Figure 2.8):

$$d_i(t) = \sum_{j=1}^{6} G_{ij}(t) e_{j.} \tag{2.22}$$

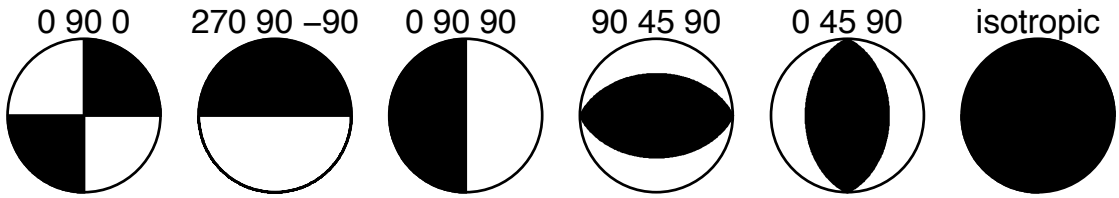

Figure 2.8. The 6 elementary focal mechanisms used in ISOLA. Strike, dip and rake are shown above each focal mechanism.

The advantage of this method is that calculations of moment tensor can be solved for:

1) Full moment tensor including isotropic part (e_1-e_6): DC + CLVD + VOL
2) Deviatoric moment tensor (e_1-e_5): DC + CLVD
3) Pure double-couple solution: DC with CLVD=0%, VOL=0%.

2.3.3.1. ISOLA procedure

The procedure in ISOLA starts with the import of the data and input of a velocity model and event information such as preliminary hypocentral location, magnitude (if available), and the seismograms' information such as starting time and duration. Next, it is necessary to select the stations to use for the inversion. In this thesis, the selection of stations around the events was made considering in one hand the signal/noise ratio and in the other the sufficient distance to maintain the assumption of a point source.

Following, the next step is to define the trial approach for the source position search. In ISOLA, this option can be **single source** or **multiple source**. For single source, this can be either the hypocentral position or a search over several positions (depths) below the (fixed) epicentre, given a starting depth, depth step and number of sources. The grid search over depth provides the optimum source position characterised by the best fit between the waveform data and the synthetics. The multiple source option allows to search for several positions over a plane or the strike or dip of a given fault. The single source search method over depth below a fixed epicentre was used in this thesis, given the good accuracy of epicentral locations from the local catalogue and lesser processing time required.

Next step in the procedure is to calculate the Green's functions, selecting the maximum frequency to be computed. Finally, for the inversion itself, it is necessary to establish the filtered frequencies to be inverted, the time steps for the search over centroid time, and the type of inversion: full moment tensor, deviatoric moment tensor or pure double couple (see above).

After a first inversion, it is recommended to refine the inversion and repeat it, considering finer searches over the centroid depth and time. Also, to visually check the correlation between the data and synthetic seismograms and discard any station with low correlation. In general it is always good to visually check the data in order to avoid clipped seismographs and other failures.

CHAPTER 3

REGIONAL SEISMICITY OF THE AYSEN REGION

Abstract

The Aysén Region, southern Chile, is the area located at the southern end of the Nazca-South America subduction zone, to the east of the Chile Triple Junction. This area has historically presented low levels of seismicity mostly associated to volcanism. Nevertheless, a seismic sequence occurred in 2007, related to the reactivation of the strike-slip Liquiñe-Ofqui fault, confirmed that this region is not exempt from major seismic activity M>6. Here we present results from local earthquake locations of two years preceding the sequence of 2007. Event magnitudes range between 0.5-3.4 M_l and seismicity occurs at shallow depths, mostly within the upper 10 km of crust, in the overriding South American plate. No events were detected in the area locus of the 2007 sequence, and the Wadati-Benioff plane is not observable given the lack of subduction inter-plate seismicity in the area. A third of the seismicity is related to the Hudson volcano activity, and sparse crustal events can be spatially associated with the trace of the Liquiñe-Ofqui fault. Other minor sources of seismicity correspond to glacial calving in the terminal zones of glaciers and explosions due to mining activities.

3.1 Introduction

The Aysén Region, southern Chile, is located in the vicinity of the Chile Triple Junction (CTJ), where the active Chile Ridge is currently being subducted beneath South America. This region has presented historically low levels of seismicity in comparison with the northward segments of the Chilean subduction margin, where some of the world's largest recorded megathrust earthquakes have occurred in the past (e.g. Chile 1960, Maule 2010). Nonetheless, this area remains an interesting seismotectonic environment, as it is bisected by a large strike-slip fault system, the Liquiñe-Ofqui fault system (LOFS), which absorbs the trench-parallel component of the oblique convergence between the Nazca and South American plates. Moreover, the subduction of an active spreading centre, the Chile Ridge, has generated the presence of an asthenospheric slab window beneath the overriding plate.

In this study, data from an extensive local network deployed during 2004-2005 is analysed to obtain accurate earthquake locations and magnitude estimations in order to characterise the background seismicity of the area and establish its main sources of activity.

3.1.1 Location and Geo-Tectonic Setting

The Aysén Region is located at the southern end of the convergent margin between the Nazca and South American plate (Figure 3.1). It is also the place where the Liquiñe-Ofqui Fault System (LOFS) starts its development northwards. Furthermore, the active Chile Ridge is currently subducting offshore of the Aysén Region (Herron *et al.*, 1981; Cande *et al.*, 1987) at the so-called Chile Triple Junction (CTJ) where the Nazca, Antarctic and South American plates meet. This tectonic configuration corresponds to the only present-day active ridge-trench collision in which the overriding plate represents continental lithosphere.

The CTJ is located off the Taitao Peninsula and has been migrating northwards since 14 Ma when the ridge collided against the trench for the first time near Tierra del Fuego

(~53ºS) (Bangs and Cande, 1997). North of the CTJ the Nazca plate is being subducted at a rate of 6.6 cm/yr (Angermann *et al.*, 1999; Wang *et al.*, 2007), while to the South, the Antarctic plate is being subducted at 2 cm/yr below South America (Chase, 1978).

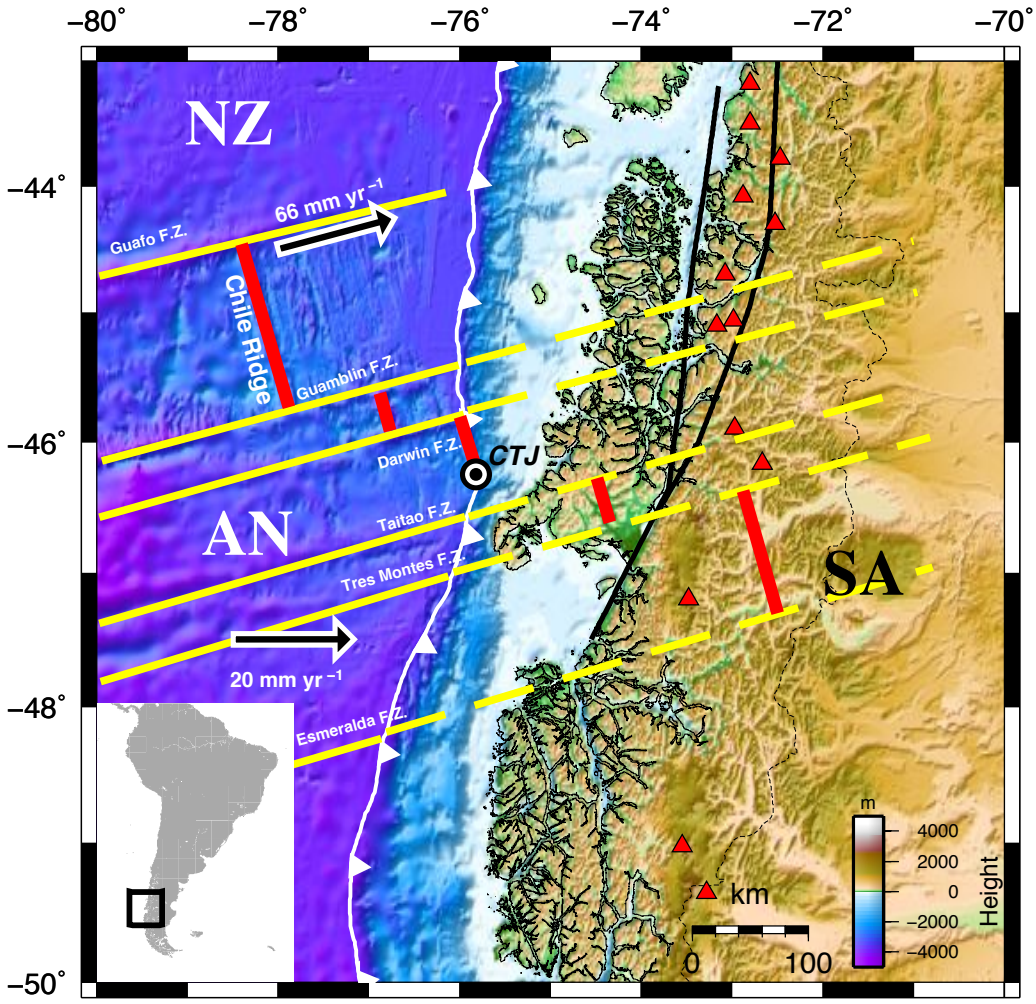

Figure 3.1. Location and tectonic settings of the Aysén Region. NZ Nazca Plate; AN Antarctic Plate; SA South American Plate; CTJ Chile Triple Junction. White line with triangles indicates the trench. Red segments show spreading centres of the Chile Ridge and their projection after subduction. Yellow lines indicate fracture zones (solid yellow lines) and their projection (dashed yellow lines). Black line depicts the Liquiñe-Ofqui Fault System (LOFS), while red triangles indicate Quaternary volcanoes. Bathymetry/Topography: GTOPO30; convergence NZ: Angermann *et al.* (1999); convergence AN: Chase (1978).

Several consequences of the Chile Ridge subduction beneath the CTJ have been observed including: tectonic erosion, plutonism near the trench and uplift during the Upper Cretaceous in the Taitao Peninsula (Cande and Leslie, 1986), emplacement of an ophiolitic complex in the Taitao Peninsula (Forsythe *et al.*, 1986) and the displacement of a fore-arc sliver (Forsythe and Nelson, 1985; Wang *et al.*, 2007). Another important consequence is the occurrence of a 350 km long volcanic gap within the arc (Ramos and Kay, 1992) whilst in the back-arc zone widespread basaltic-plateau volcanism takes place (e.g. Ramos and Kay, 1992; Gorring *et al.*, 1997). Ramos and Kay (1992) argue that the most intense periods of this basaltic volcanism are related to the passage of a slab window (subducted ridge) below the plateau.

The geology of the Aysén Region is most simply defined by three predominantly N-S trending domains: a western coastal domain, a central plutonic belt and an eastern back-arc volcano-sedimentary domain (see Figure 3.2). The morpho-structural setting is controlled by NE–SW and NW–SE structures related to the LOFS (D'Orazio *et al.*, 2003).

The coastal domain is mainly characterized by Palaeozoic and Triassic metamorphic rocks located on the archipelago islands. Additionally, an ophiolite complex was emplaced within the fore-arc about 3 Ma in the Taitao Peninsula (Forsythe *et al.*, 1986). This ophiolite accretion and anomalous near-trench magmatism are most likely related to the passage of the CTJ at the latitude of the Taitao Peninsula ~3 Ma (Behrmann *et al.*, 1994).

A granitic plutonic belt of Meso-Cenozoic age, the North Patagonian Batholith, is located within the tectonic arc between 39º and 47º lat. S (Pankhurst *et al.*, 1999) and includes the highest altitudes in the area (up to 2000 m.a.s.l.). Quaternary volcanism is also present in the area with strato-volcanoes Hudson, Maca, Cay and several monogenetic cones, which occur over the main range (D'Orazio et al, 2003). The active Hudson volcano had its last major eruption on August 1991, producing more than 4 km of pyroclastic material (Naranjo and Stern, 1998).

To the east, the back-arc zone is composed mainly of Meso-Cenozoic volcano-sedimentary rocks and the eastern outcrop of the Paleozoic basement (Niemeyer *et al.*, 1984, SERNAGEOMIN, 2003).

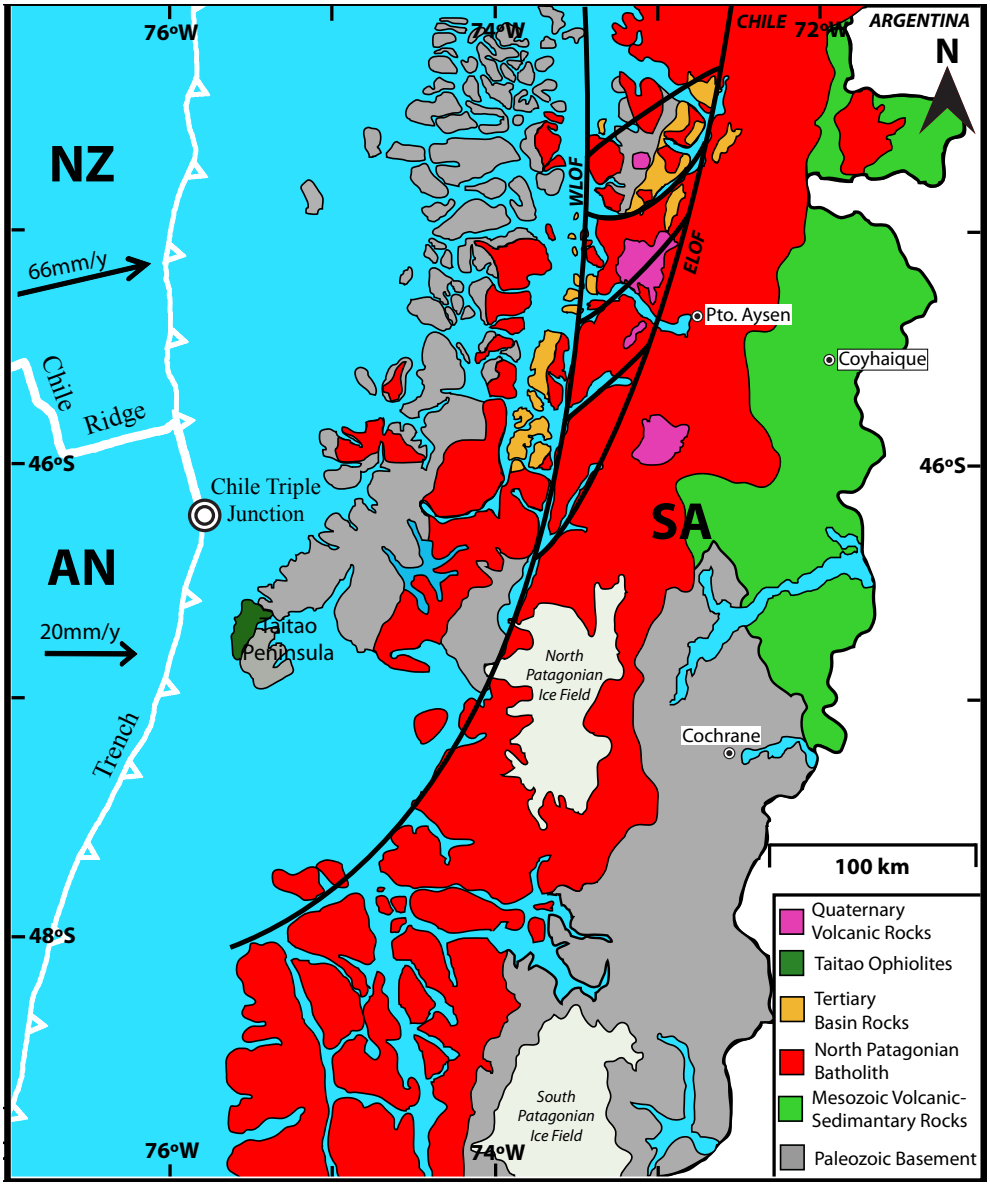

Figure 3.2. Simplified geology of the Aysén Region. NZ Nazca plate; AN Antarctic plate; SA South American plate. Modified from SERNAGEOMIN (2003).

3.1.2. The Liquiñe-Ofqui Fault System

The LOFS is located within the active arc in southern Chile and corresponds to a dextral strike-slip NNE-trending fault system that extends for more than 1000 km. It is formed by two main NNE-trending parallel lineaments, the western and eastern Liquiñe Ofqui Fault (henceforward WLOF and ELOF, respectively), connected by at least four NE-trending *en échelon* lineaments that define a strike-slip duplex (Cembrano *et al.*, 1996, Figure 3.2). This fault system accommodates part of the strike-parallel component of the oblique convergence between the Nazca and South American plate and it is thought to control the distribution of quaternary volcanism in the area (Cembrano and Moreno, 1994; Cembrano and Lara, 2009).

Whilst some authors consider oblique subduction as the driving mechanism of the displacement along the LOFS (e.g. Hervé, 1976; Beck, 1988; Cembrano *et al.*, 1996, 2000, 2002), others add the indenter effect of the ridge's subduction (e.g. Forsythe and Nelson, 1985; Cembrano *et al.*, 2002). The indenter effect would cause the detachment of a fore-arc sliver, the Chiloé block, from the continental margin along the LOFS. According to Cembrano *et al.* (2002), both oblique subduction and the indenter effect of the ridge subduction generate transpressional deformation along the subduction margin. The same authors add that long-term dextral transpression appears to be driven by oblique subduction, while short-term deformation is in turn controlled by ridge collision (from 6 Ma to the present day). Cembrano *et al.* (2000) also propose that strong intra plate coupling resulting from the subduction of young and buoyant oceanic lithosphere north of the CTJ plus a thermally weak continental crust appear to be the key factors for the strain accumulation along the LOFS.

Most of the information on the current deformation state of the LOFS comes from structural and thermo-chronological evidence (e.g. Cembrano *et al.*, 1996; 2000; 2002) which suggest that this fault has been active since Late Mesozoic as a sinistral strike-slip fault, while the dextral strike-slip motion is dated to begin about Middle Miocene. Strike-slip brittle deformation during the Pliocene to post-Pliocene and high rates of uplift during the Holocene characterise the recent tectonics of the LOFS (Cembrano *et al.*, 1996).

Based on structural field work and fault kinematic analysis, Rosenau *et al.* (2006) determined intra-arc shear rates for the Pliocene to recent period of 32±6 mm/yr for the portion of the LOFS between 40º-42ºS and of 13±3 mm/yr for the northern portion between 38º-40ºS. These rates indicate that about half of the convergence obliquity is absorbed in the arc by the LOFS in the northern segment of their study (38º-40ºS), while complete partitioning occurs in the southern portion (40º-42ºS). Furthermore, these authors suggest that where partitioning is incomplete, the convergence obliquity is accommodated by oblique interplate thrusting and fore-arc transpression.

Wang *et al.* (2007) exposed the first geodetic evidence on the current dextral shear of the LOFS, finding a trench-parallel slip rate of 6.5mm/a between 42° and 44°S, which accommodates about 75% of the current margin-parallel component of the Nazca-South America relative plate motion. They attribute this displacement to the whole width of the fault system with the consequent northward translation of the Chiloé block located to the West of the LOFS.

Recently, Lange *et al.* (2008) observed local crustal seismicity along a 130 km long segment of the fault at ~42°S. At this latitude, the Chiloé block mentioned above has been decoupled from South America by the action of the LOFS (Forsythe and Nelson, 1985; Wang *et al.*, 2007; Melnick *et al.*, 2009). While the northern portion of this fault system has been intensely investigated (e.g. Rosenau *et al.*, 2006; Lange *et al.*, 2008; Haberland *et al.*, 2007; Haberland *et al.*, 2009; Melnick *et al.*, 2009), the southern portion remains more elusive. The present study therefore aims to provide a better characterization and understanding of this intra-arc fault system and the region in general.

3.2. Background seismicity

The background seismicity of the area between 36ºS and 50ºS (Figure 3.3) is directly linked to the present major tectonic processes: the subduction of the Nazca plate under South America and the ocean floor spreading along the Chile Ridge. Additionally,

intraplate seismicity in the overriding plate can be associated with deformation on the LOFS and active volcanism in the arc (Figure 3.3).

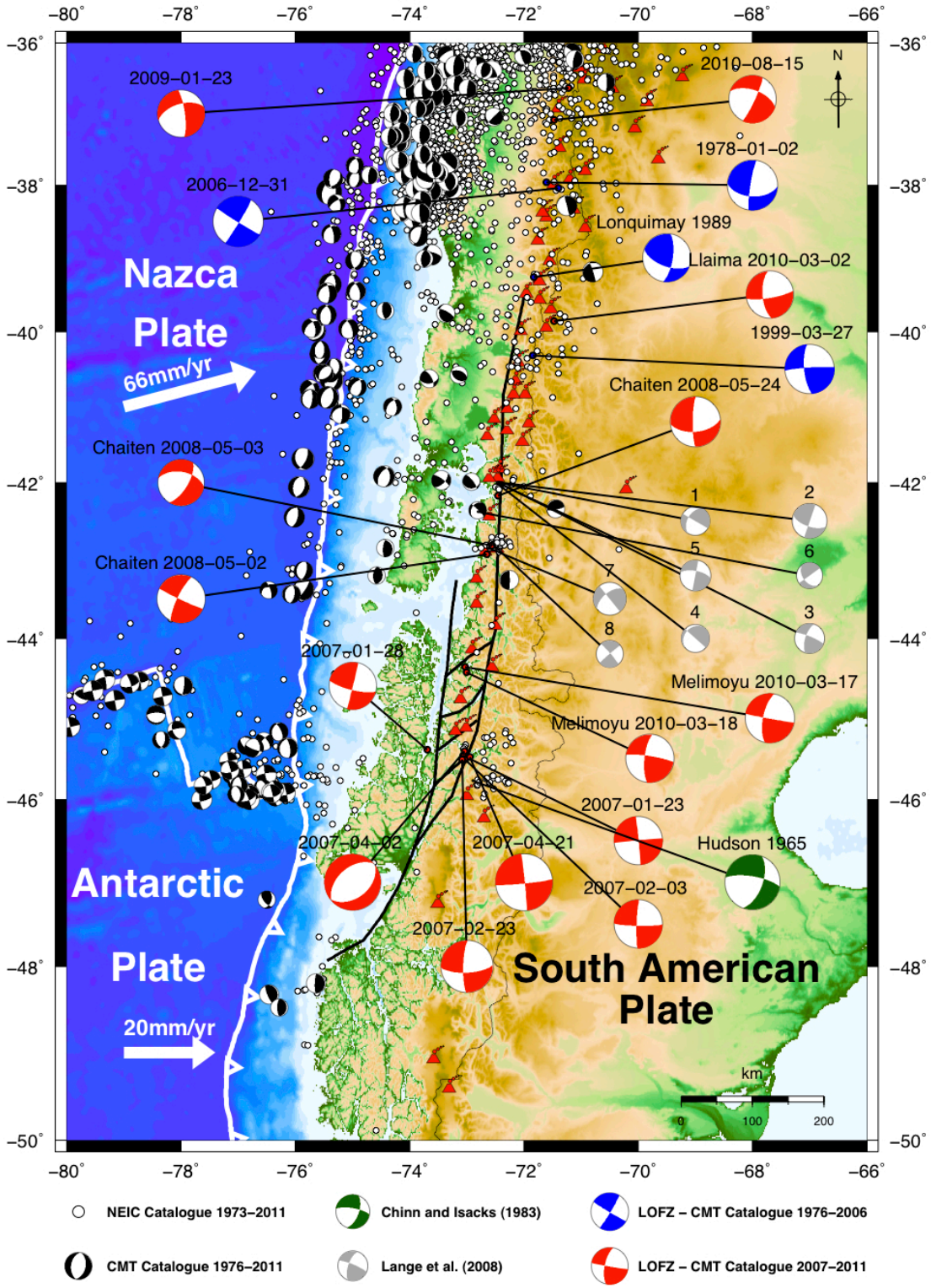

Figure 3.3. Seismicity and focal mechanisms of the South America Western Margin between 36º-50ºS. Non-black focal mechanisms have been associated to LOFS events.

The inter-plate thrust seismicity due to the subduction of the Nazca plate becomes shallower in north-south direction until reaching the CTJ where only shallow events are observed. The same directional tendency is observed in terms of number of subduction events, which decreases in direction north-south until practically disappear at the CTJ. Further south, scarce thrust events associated with the subduction are observed probably caused by the slow convergence of the Antarctic plate under South America.

Shallow normal-fault events are observed in the outer-rise, while shallow normal and strike-slip faulting is observed in the spreading axis and fracture zones of the ridge respectively.

Approximately north-south right-lateral strike-slip crustal faulting occurs in the arc, along the trace of the LOFS. Some of these events are associated to the presence of Quaternary volcanoes, which in turn are disposed and oriented according to this fault system. Teleseismically recorded events related to the LOFS seem to have increased after the 2007 Aysén Seismic Sequence (Chapter 4), with recent activity on the Chaitén and Melimoyu volcanoes in 2008 and 2010 respectively.

3.3. Previous Seismic Studies in the Aysén Region

Considering the available information, the Aysén Region has a poor catalogue of seismic events because of the lack of local studies and/or the low rates of seismicity. According to the Chilean Seismological Survey (http://sismologia.cl), only one historical event M>7 has been observed in the time period from 1570 to 2005. This event, magnitude 7.1, occurred on November 21, 1927, (Greve, 1964) to the West of the Aysén Fjord causing a local tsunami. Other minor seismicity in the region is directly linked to the volcanic activity of Hudson volcano.

In terms of seismo-tectonic studies, the Aysén Region is still not well investigated. This is mainly due to the difficulties of conducting fieldwork (accessibility, climate) and the lack of major seismicity that could be used for teleseismic (remote) studies. Only a few local seismic networks have been installed in the Aysén Region. Murdie *et al.* (1993)

deployed nine seismometers in the Taitao Peninsula between February and March 1992, locating around 50 events with magnitudes from 0 to 4 close to the CTJ. Miller *et al.* (2005) maintained the first local seismic network throughout the whole Aysén Region between January 2004 to February 2006 detecting only minor crustal seismicity.

Comte *et al.* (2007) deployed a dense seismic network in the region allowing them to capture the initial phases of the Aysén seismic sequence of 2007 and to determine the background seismicity pattern in this area for the two years preceding the sequence. Using the same local network, Russo *et al.* (2010a) produced body-wave travel-time tomography, imaging and confirming the existence of an asthenospheric slab window beneath the overriding plate, produced by the subduction of the Chile active spreading centre. Gallego *et al.* (2010) produced seismic noise tomography for the region, obtaining high crustal shear-wave velocities in outcrop areas of the North Patagonian Batholith and highly compacted metamorphic rocks, while low shear-wave velocities were found along the volcanic arc and the trace of the LOFS.

Using teleseismic arrivals of S-waves radiated from six of the largest events of the 2007 Aysén seismic sequence (see Chapter 4), Russo *et al.* (2010b) studied the shear wave splitting and upper mantle flow of this region. Their results show a transition from the generally N-S-trending fast shear wave azimuths north of the CTJ, to ENE-trending azimuths in the area of the asthenospheric slab window mentioned before. They interpreted this ENE-trend as the flow of Pacific Basin upper mantle from the west, eastward beneath South America. This flow then interacts with the mantle wedge present above the asthenospheric window to produce the extensive basaltic plateau present east of Chile and Argentina in this region.

3.4. Regional Seismicity

During 2004 and 2005 a local seismic network (Miller *et al.*, 2005) of more than 60 stations, broadband and short-period seismometers, was kept continuously recording in the Aysén Region (Figure 3.4). Data from this network was obtained and analysed for

the present thesis in order to address the regional seismicity in the whole of the Aysén Region.

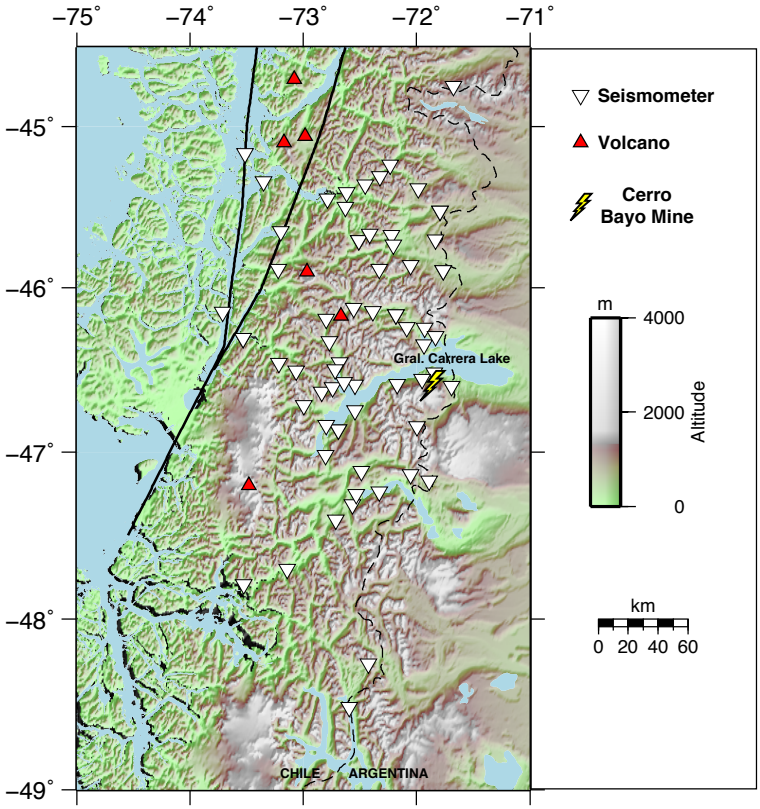

Figure 3.4. Stations network. Set of seismic stations used for the characterization of the regional seismicity in this study. Black line depicts trace of LOFS.

P- and S-phases were hand-picked for a total of 519 events. In order to obtain event locations, arrival times were processed with the software NonLinLoc (Lomax *et al.*, 2000), which provides non-linear probabilistic locations with a complete determination of the posterior probabilistic density function (pdf), therefore providing reliable location uncertainties. The local 1-D velocity model proposed by Agurto *et al.* (2012a; see Chapter 4) was used for this instance. The complete catalogue of 519 events is shown in Figure 3.5.

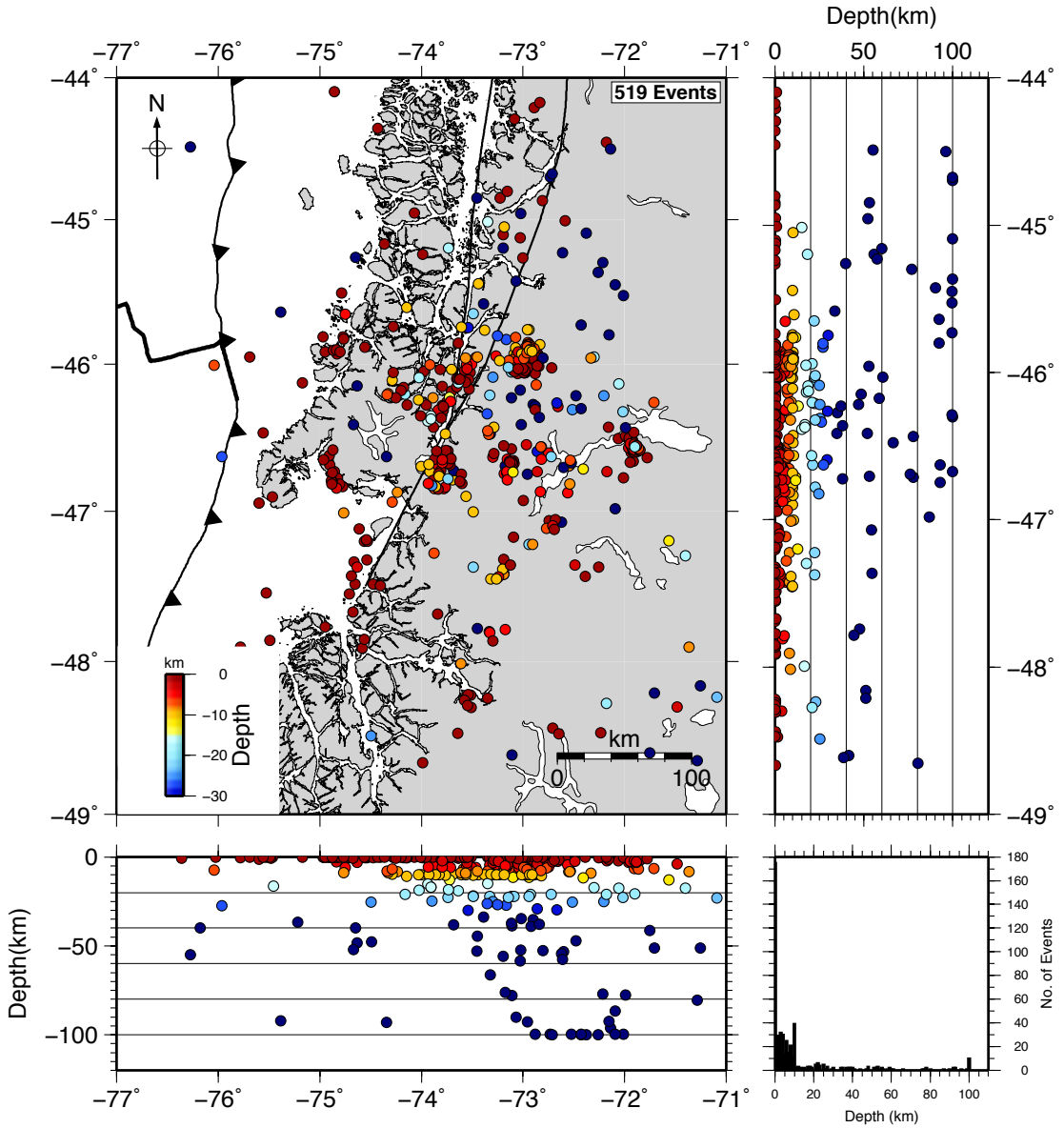

Figure 3.5. Locations of all the processed events coloured by depth.

Only events with uncertainty ellipsoid semi-axes smaller than 20 km were considered for the following analyses, reducing the number of events to 276. Uncertainty estimations are shown in Figures 3.6 and 3.7. As expected, the smallest location errors are found for those events located within the network, while larger errors are present for events outside and away the seismic network. The orientation of the 68% confidence ellipsoids do not show any particular orientation except for those events located near the Taitao Peninsula (~ 47ºS, 75ºW), which show ellipses with major axes NW-orientated (see Figure 3.6).

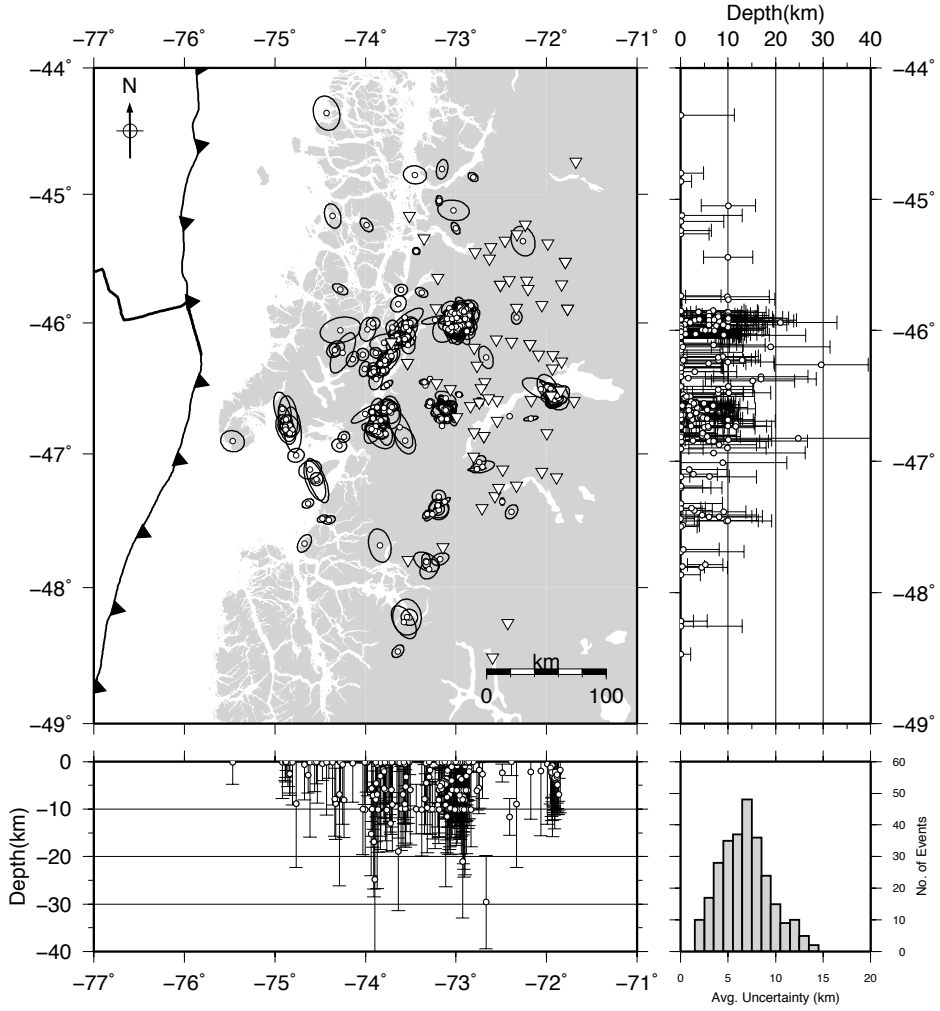

Figure 3.6. Location uncertainty estimations of events with NonLinLoc uncertainty ellipsoids' semi-axes lesser than 20 km (276 events). Ellipses in plan view and error bars in profiles correspond to 68% confidence location uncertainties. Histogram shown in lower right corner indicates averaged values of the three semi-axes of the uncertainty ellipsoids.

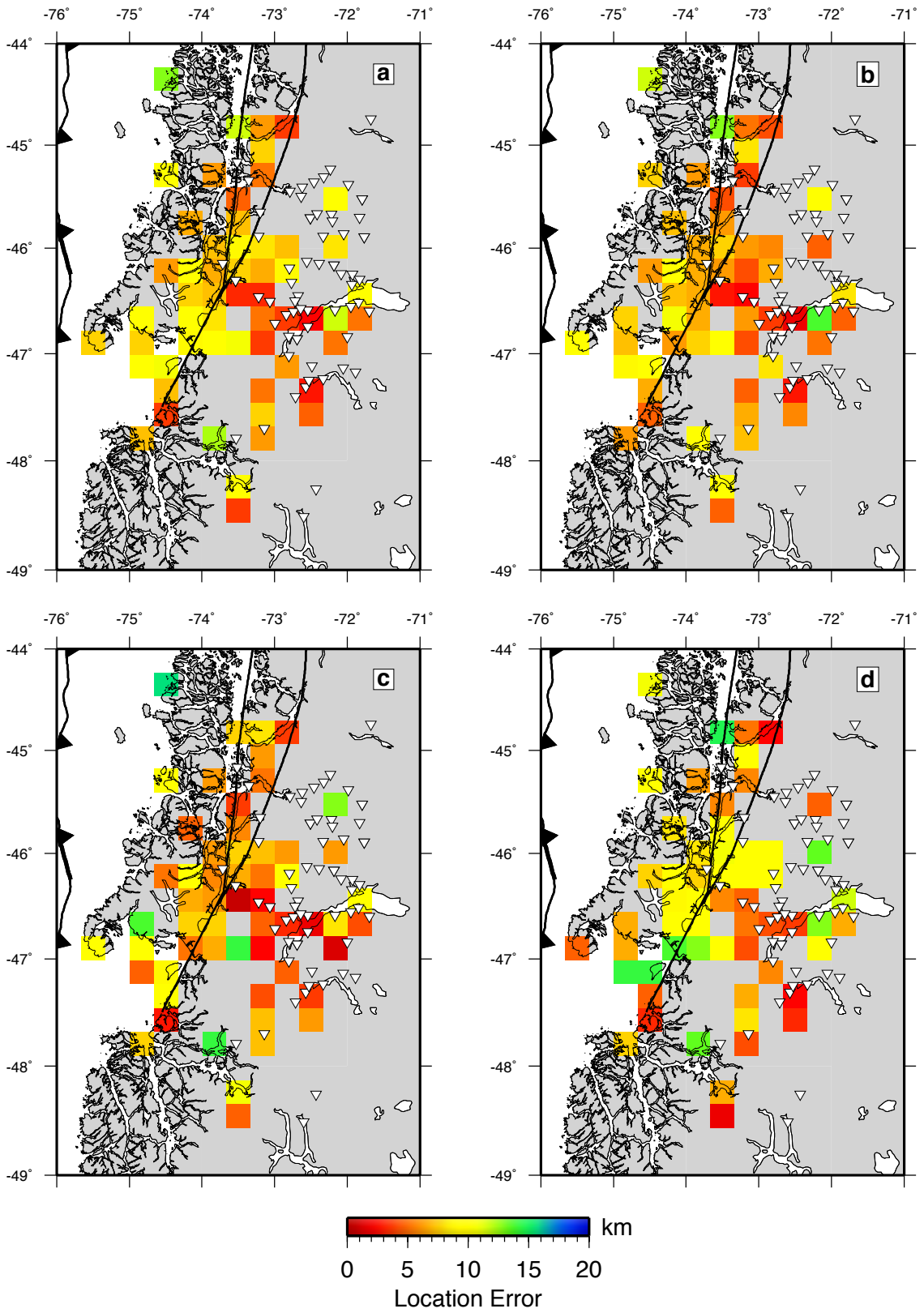

Figure 3.7. Mean location uncertainties. Averaged uncertainties calculated on a grid of tiles 25x25 km for events with error ellipsoids' semi-axes less than 20 km (276 events). Error values were calculated from the events' error covariance of latitude, longitude and vertical directions considering a 68% confidence. Inverted white triangles indicate station seismic locations. **a)** averaged latitude, longitude and depth directions error; **b)** latitude error; **c)** longitude error; **d)** vertical error.

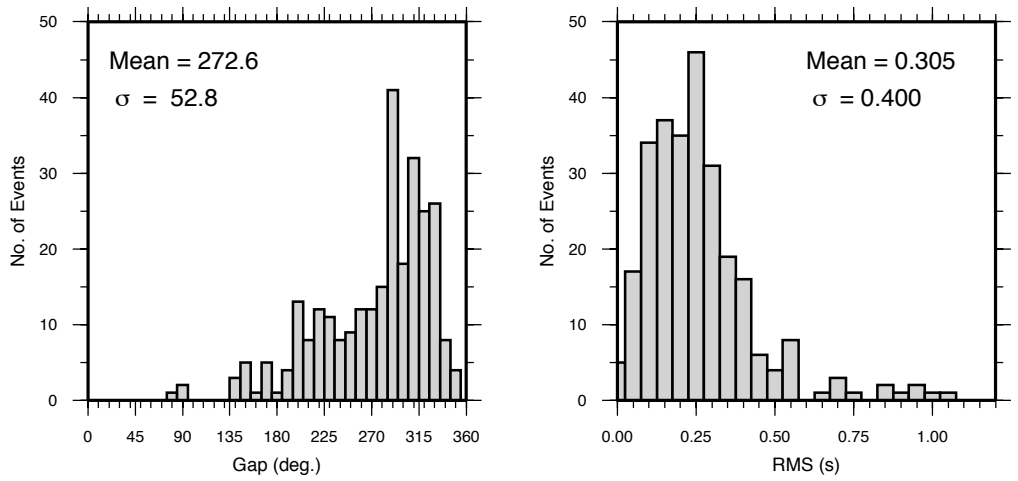

Figure 3.8. Histograms for gap angle and RMS of events in Figure 3.6.

Considering all detected events, i.e. 519, an average of 1.35 seismic events per day occur in the Aysén Region. The temporal distribution (Figure 3.9) shows for most of the days the occurrence of 1 to 2 events, with a slightly greater concentration of events during the first months of study (January-May 2004).

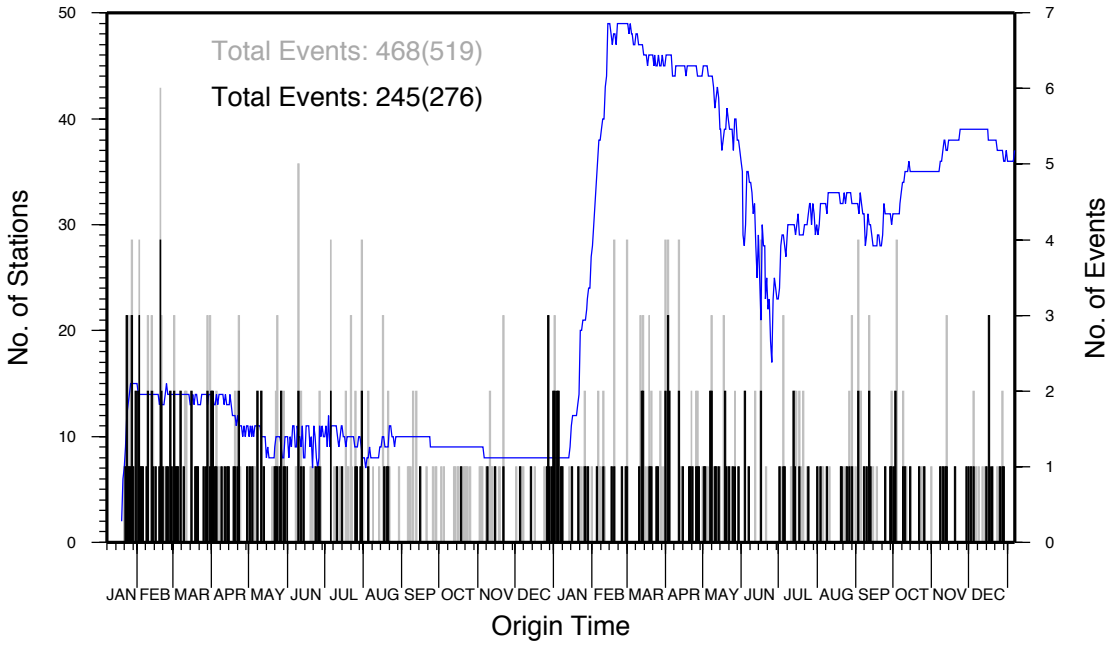

Figure 3.9. Events occurrence and active stations per day during the experiment (2004-2005). Events associated to mining activities have been filtered out. Grey bars show total events processed, black bars show events in Figure 3.6 (right axis). Blue thin line shows number of active stations (left axis).

Local magnitudes (M_l) were obtained in the range of 0.5-3.4. The largest magnitudes are observed in the vicinity of the CTJ and the southern end of the LOFS, while the smallest magnitudes are present in clusters B and D.

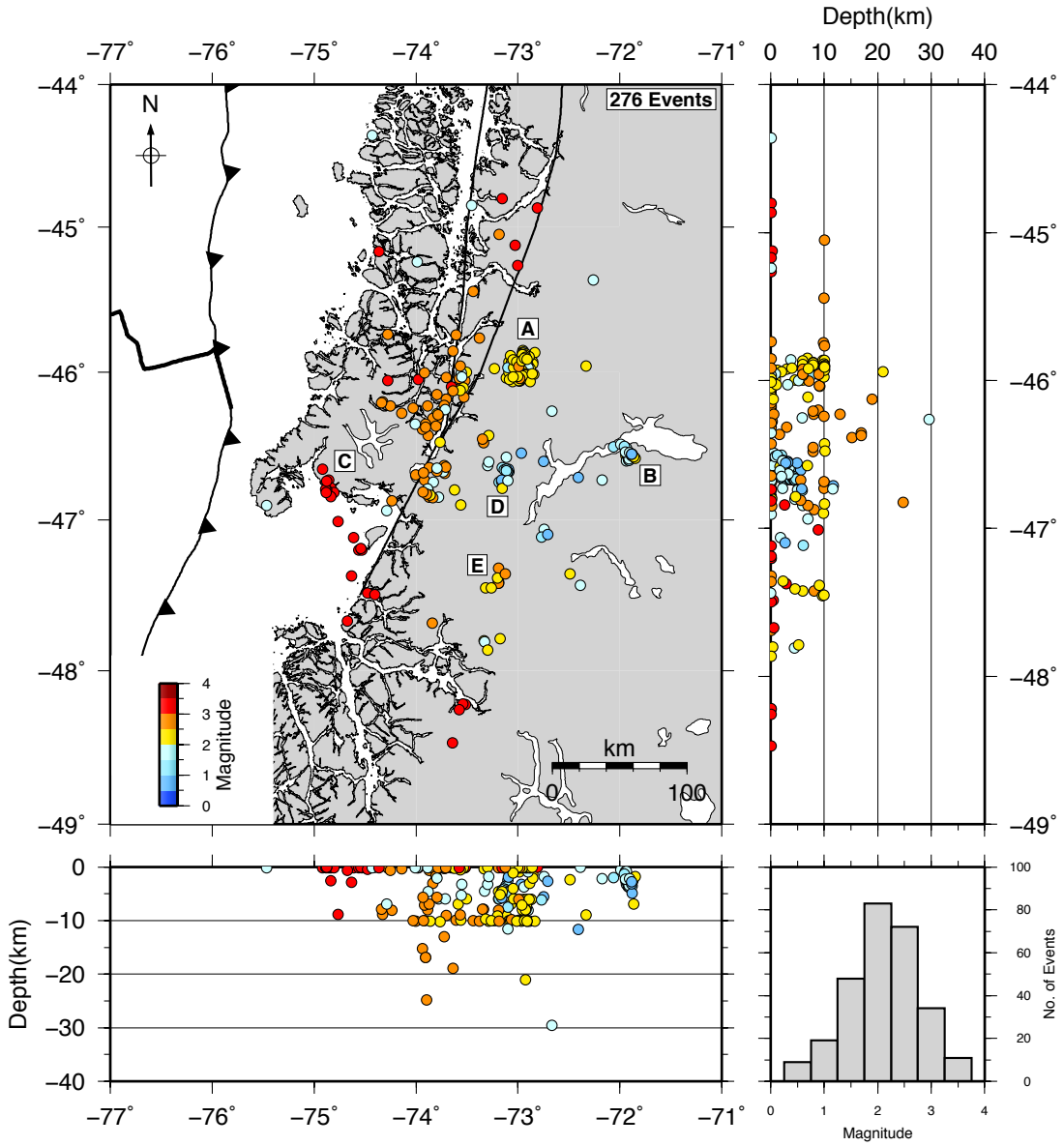

Figure 3.10. Events shown in Figure 3.6 coloured by local magnitude. Uppercase letters indicate associated cluster (see text and Figure 3.11).

Most of the seismicity nucleates at crustal depths, shallower than 10 km, with events occurring predominantly in clusters, in particular associated with activity at Hudson

volcano. Maximum hypocentral depths of 30 km were located, which constrains the seismogenic depth of the region to this value. For the Aysén Fjord seismic sequence (Chapter 4), the seismogenic depth is constraint to the upper 15 km. This difference might be due to the uncertainty range of the locations in this chapter and/or to the nature of the seismicity analysed in the Aysén Fjord area, exclusively related to the LOFS.

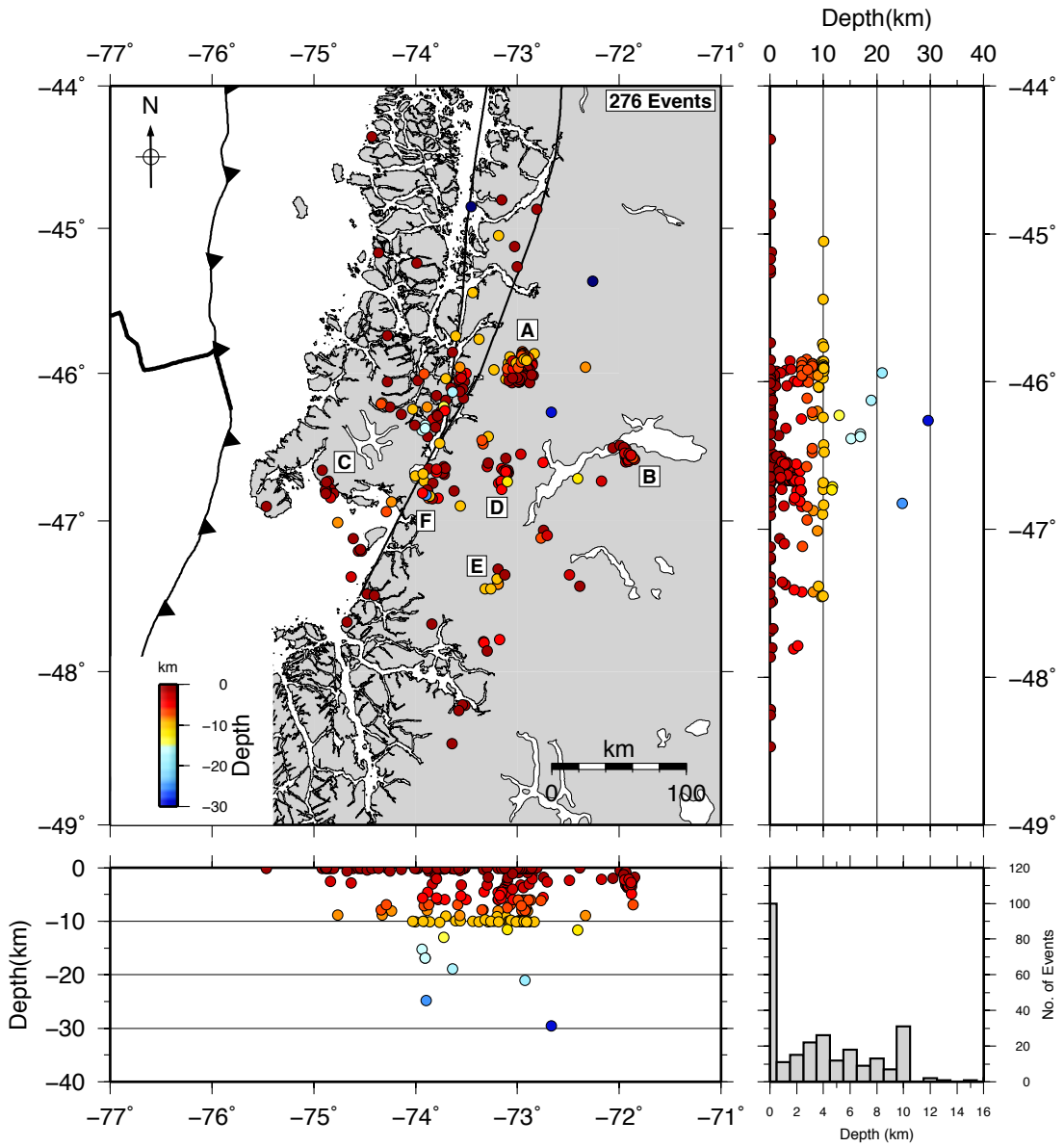

Figure 3.11. Locations of selected events (error ellipsoids' semi-axes lesser than 20 km) coloured by depth. Uppercase letters indicate associated seismic cluster: A Hudson volcano, B Cerro Bayo mine, C CTJ vicinity, D-F glacier events.

The distribution of seismicity tends to occur in clusters, as shown in Figure 3.11 which displays the selected 276 events with uncertainty ellipsoids' semi-axes smaller than 20 km, which are distributed according to clusters A-F. The rest of the events not associated to any cluster seem to be mostly associated to shallow crustal activity on the LOFS, and to events sparsely located, at shallow depths and unrelated to any known regional seismic source.

Shallow crustal events down to depths of 10 km are located in spatial concordance with the trace of the LOFS, in particular in the area where both the East and West main branches meet at ~46.3ºS. This seems to be a highly active seismic zone, with maximum observed magnitudes up to 3.4 M_l.

Cluster A is associated to seismic activity at Hudson volcano, representing nearly a third of the total seismicity (85 events out of 276). The events occur mostly within the caldera of the volcano and to the south of it, down to depths of 10 km (Figure 3.12). The events that occur within the caldera are located at depths between 6-10 km, while the events located to the south of the caldera occur at shallower depths. Regarding the magnitudes, these fluctuate between 1.4 to 2.9 M_l.

In terms of the temporal distribution of the Hudson events, frequencies of 0-10 events per month are observed for the period of study, except for February 2004, when up to 33 events related to the volcanic activity were recorded (Figure 3.13).

Cluster B contains events associated to mining activities in the Cerro Bayo Mine, nearby General Carrera Lake. The hypocentres, 31 in total, are located at shallow depths and present magnitudes between 0.6 to 2.3 M_l. They occur at regular times of the day, between 15 and 24 hours GMT (11-20 hours Local Time) as depicted in Figure 3.14. Although these events correspond to mine explosions occurring on the surface, the hypocentral depth range observed is 0-7 km (Figure 3.11), providing an independent measure of the vertical uncertainty for this set of locations.

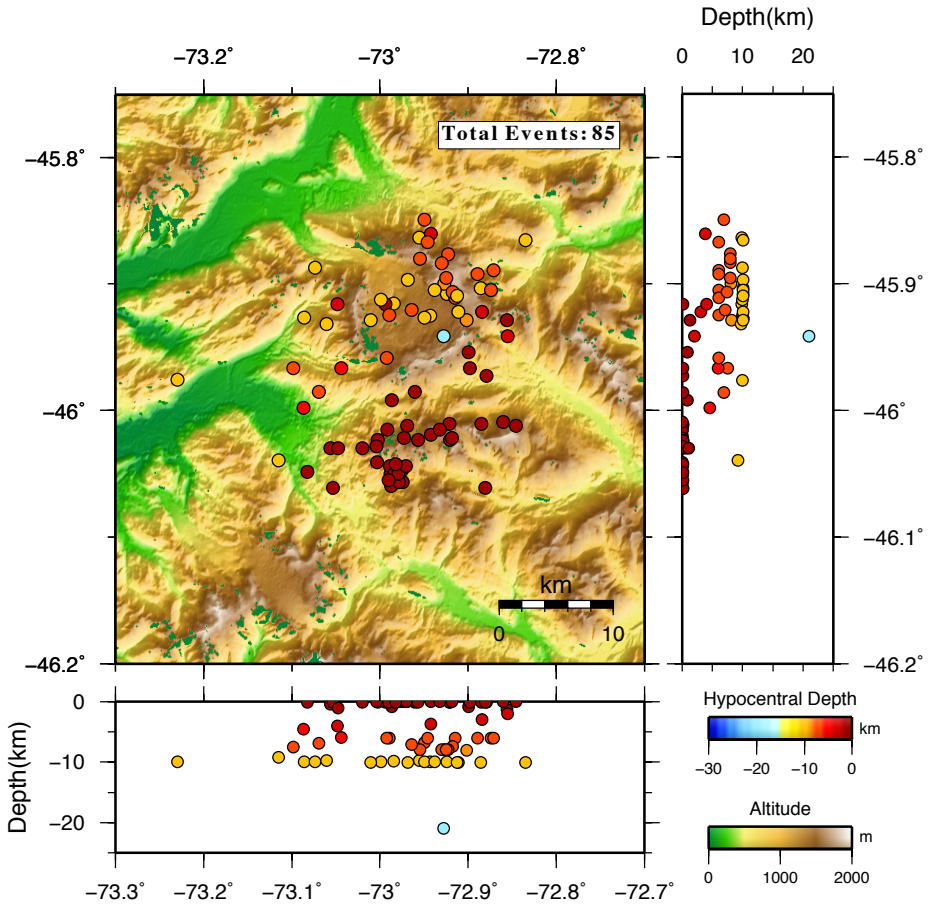

Figure 3.12. Hudson volcano related events coloured by depth.

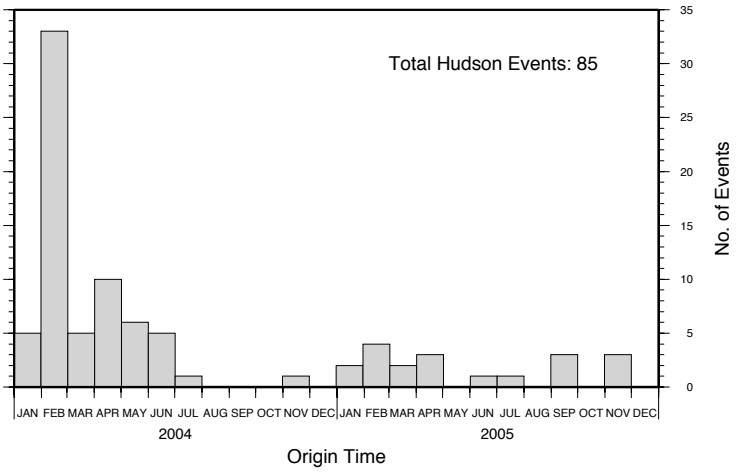

Figure 3.13. Histogram of time occurrence of events associated to the Hudson volcano distributed in monthly bins.

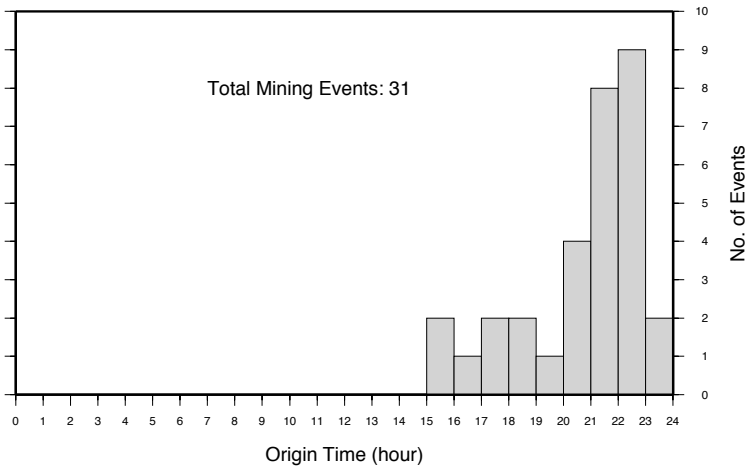

Figure 3.14. Histogram of time occurrence of mining related events distributed in hourly bins.

Cluster C correspond to events located in the vicinity of the CTJ. These events, including the biggest located in the present study, occur at depths shallower than 5 km and present magnitudes of up to 3.4 M_l. This seismicity might be associated with activity on the slab-window of the subducted ridge (Murdie *et al.*, 1993), but given its shallow depth, it might as well correspond to activity on some shallow crustal structure not recognised previously.

Clusters D-F correspond to events that coincide spatially with the presence of glaciers and their terminal zone ending in lakes. Cluster D occurs nearby Fiero Glacier, cluster E in the proximity of Colonia Glacier and cluster F close to Quintín and San Rafael Glaciers; all of them part of the North Patagonian Ice Field. Furthermore, these events present a slight tendency to occur in the summer months (Dec-Feb) as shown in Figure 3.15. All this suggests the possibility that these epicentres are related to ice calving and avalanches in the mentioned glaciers.

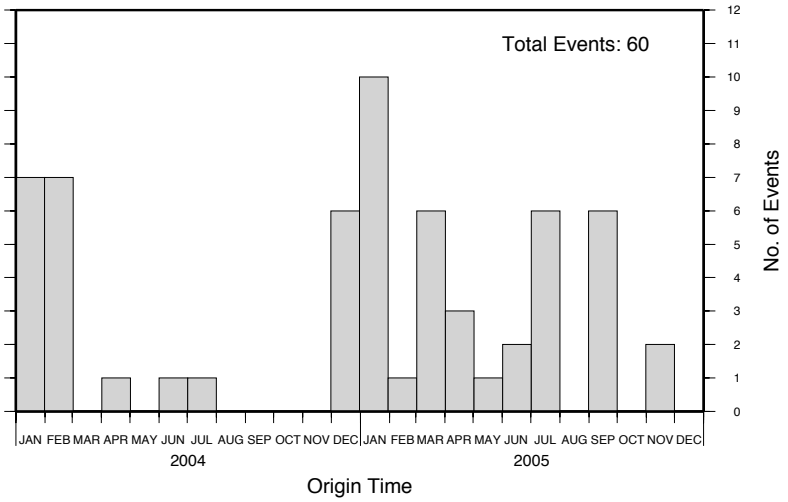

Figure 3.15. Histogram of time occurrence of glacier related events distributed in monthly bins.

3.5. Discussion

The regional seismicity in the Aysén Region corresponds mostly to shallow crustal events located in the overriding South American plate at depths shallower than 30 km, mostly within the upper 10 km of crust. It was not possible to identify the Wadati-Benioff plane of the subducted Nazca and Antarctic plates given that no seismicity due to subduction was identified. Instead, the seismicity in the region is related mainly to activity at Hudson volcano, which represents a third of the levels of seismicity in the area. These events occur within the caldera of the volcano and in a cluster ~5 km to the south of it, at depths between 0-10 km. In this regard, these results partially disagree with Naranjo *et al.* (1993), who reported hypocentral depths clustered between 2-20 km for seismic events occurring during the Hudson eruptive sequence of 1991.

The second source of seismicity in the region is related to the LOFS, which represents an active fault system during the time of this study (2004-2005) with magnitudes of up to 3.4 M_l, but as seen bellow in Chapter 4, is capable of generating earthquakes of at least Mw=6.2, representing a significant seismic hazard for the nearby populated areas. The activity on the LOFS is particularly intense in the area of convergence of the two main branches of the fault at ~46.3ºS. During the period of this experiment (2004-2005),

no seismicity was observed in the area of the Aysén Fjord where the sequence of 2007 took place.

Focal mechanisms would be necessary to associate with more certainty some of the events either to the LOFS or other seismotectonic sources in the area, as well as to address the distribution of stress and faulting geometries in the region. Unfortunately, given the low magnitudes of the processed events it was impossible to perform moment tensor inversions from seismic waveforms. Neither was it possible to compute focal mechanisms from first motion polarities given that, although the azimuthal coverage was smaller than 180º for some events, the shallow occurrence of these events together with relatively large hypocentral distances only contributed to a very narrow range of observed incidence angles.

Seismic activity was recorded on the Taitao Peninsula and nearby area (cluster C). This zone was previously studied by Murdie *et al.* (1993), who inferred that this seismicity was caused by the subduction of the active ridge below South America. In particular, they managed to constrain focal mechanisms obtaining for all of them extensional faulting associated with the subducted spreading centre. Therefore, the seismicity observed in that area (cluster C) in the present study might also correspond to activity on the subducted ridge that would prove to continue active after subduction in the CTJ.

Minor seismicity was also observed spatially related to several glaciers within the North Patagonian Ice Field. These events would be associated to ice calving on the terminal zones of the glaciers or/and avalanches in the areas of steep slopes. Given the small magnitudes, these events were only detectable given the presence of nearby seismic stations.

On the other hand, no seismicity is observed in the outer-rise area, nor at the ridge. This could be due to the lack of proximal stations and the insufficient magnitudes of events in this area to be recorded for stations located mainly further inland.

The regional seismicity in the Aysén Region is, therefore, concentrated in the arc, at depths shallower than 10 km and related to the LOFS and the Hudson volcano activity.

No seismicity is observed in the back arc, while little activity occurs in the ridge and outer-rise areas, although teleseismic catalogues show these areas are seismic active sources. Magnitudes in the region range from 0 to 4, but recent activity on the LOFS in the Aysén Fjord area presented magnitudes of up to 6.2 M_W.

Future seismic research in the area should be aimed at obtaining focal mechanisms and the collection of offshore data which would allow a better seismic coverage. Furthermore, additional geological mapping of structures and re-estimation of geological hazards is necessary in order to obtain a complete picture of the seismotectonics of this region both at a local level and as a unique example of an area in which young crust and an active triple junction is subducted under continental crust.

3.6. Conclusions

We have recorded and characterised the local seismicity for the area in the vicinity of the Chile Triple Junction between 44ºS and 49ºS during the years 2004-2005. A total of 519 events were detected, with a high quality subset of 276 events with error ellipsoid semi-axes lesser than 20 km. Magnitudes vary in the range of 0.5 to 3.4 M_l.

Earthquake clustering seems to be the characteristic type of occurrence in this region. Only intra-plate crustal events were detected with shallow depths mostly down to 10 km. No Wadati-Benioff plane could be determined from the observed seismicity.

The main source of seismic activity in the region correspond to the Hudson volcano with approximately a third of the total seismicity with depths 0-10 km. Sparse events are associated to the LOFS activity, in particular a high concentration is observed where the two main branches meet, at ~46.2ºS. Other clustered shallow events, with low magnitude, were spatially associated to the terminal parts of glaciers, probably related to glacier calving during the summer months. Few events occur in the area nearby the subduction of the CTJ, although the location resolution in this area is too poor to be determinant.

In conclusion, the 'normal' background seismicity of this region presents crustal events shallower than 15 km and maximum magnitudes up to 4. Episodically, during eruptive phases of the Hudson volcano or reactivation of the LOFS as in 2007, maximum magnitudes can reach M>6, representing a critical source of hazard for industry and populated areas.

CHAPTER 4

SEISMO-TECTONIC STRUCTURE OF THE AYSEN REGION, SOUTHERN CHILE, INFERRED FROM THE 2007 MW 6.2 AYSEN EARTHQUAKE SEQUENCE

Abstract

On 2007 April 21, a Mw 6.2 earthquake shook the Aysén Fjord, Southern Chile, in an unprecedented episode for this region characterized by low seismicity. The area is intersected by the Liquiñe-Ofqui Fault System (LOFS), a +1000-km-long strike-slip fault that absorbs part of the oblique convergence motion between Nazca and South American plates. To study the aftershock sequence of this main event, we installed a seismic network of 15 stations in the area for a period of nearly 7 months. We characterized the seismogenic structure of the zone by calculating a minimum 1-D local velocity model and obtaining precise hypocentral coordinates and uncertainty estimates by using a non-linear probabilistic approach. We also obtained fault plane solutions based on first motion polarities and SV/P amplitude ratios. The velocity model shows an average Vp/Vs ratio of 1.76 for the area and low shear wave velocity values for the upper 3 km of crust. The aftershock seismicity was located mainly between 4 and 10 km

depth and disposed in (1) a ~N-S trending alignment that follows the trace of the LOFS and (2) an E-W alignment at the East of the main fault. Furthermore, we re-analysed the previously published foreshock and early aftershock activity of the sequence including four of its largest events, improving considerably previous location estimates. Selected focal mechanisms show a strong strike-slip component that coincides with the nature of the LOFS. Based on our new analysis, we conclude that the 2007 Aysén seismic sequence had a tectonic origin related to activity on the southern end of the LOFS, however not discarding the presence and potential action of fluids on the aftershock activity.

4.1. Introduction

The world largest recorded earthquakes have all taken place along subduction margins (e.g. Chile, 1960; Andaman-Sumatra, 2004; Chile, 2010; Japan, 2011). In order to fully comprehend the stress distribution involved in these tectonic environments, it is essential to gain a better understanding of occurrence and maximum possible magnitudes of earthquakes at any given segment of a subduction zone. Moreover, oblique subduction zones as in the case of Southern Chile commonly feature large strike-slip faults parallel to the trench that accommodate the oblique convergent motion; e.g. the Atacama fault in northern Chile (Cembrano *et al.*, 2005), Philippine fault (Barrier *et al.*, 1991), the Sumatran fault (Sieh and Natawidjaja, 2000), and the Liquiñe-Ofqui fault (Cembrano *et al.*, 1996, 2000, 2002), which is subject of study in the present work. Up to now not many geophysical studies have been carried out on these major trench-parallel strike-slip fault systems that, as in the case of the Sumatran fault, have generated many historical earthquakes with magnitudes M≥7 (Sieh and Natawidjaja, 2000). Therefore, more observations are needed in order to address possible maximum earthquake magnitudes, variability of slip rates, segmentation along strike and also their interplay with the subduction thrust.

Due to the low seismicity of the Aysén Region in Southern Chile, the 2007 Aysén fjord earthquake sequence represents a unique opportunity to study the seismo-tectonic structure of this area in detail. Precise earthquake locations, estimation of uncertainties

and fault plane solutions are required in order to characterize this poorly studied zone and, in general, to understand the processes involved in zones of oblique subduction in which bulk transpressional deformation is expected. Additionally, we have re-analysed the fore- and early aftershock data presented by Legrand *et al.* (2010) to give a complete overview of the seismicity in this region. We also carried out new relocations of the major events of the sequence by using local stations, improving in this way significantly previous locations (Russo *et al.*, 2010c) and providing an in-depth study of the whole seismic sequence of 2007.

The results of this study allow us to determine a local velocity model and to define the seismogenic zone for this area, giving a starting point for future geophysical investigations in the region. Moreover, our research adds new information on these types of intra-arc strike-slip fault systems that are not very well studied so far.

4.2. The 2007 Aysén Seismic Sequence

The seismic calmness of the Aysén Region (see previous chapter) was dramatically interrupted in 2007 when the zone was shaken by a series of earthquakes that took place during the first half of that year. The seismic sequence started on January 10 with a single small shock (M_L<3) at shallow depth beneath the Aysén Fjord after which more events occurred on January 14, 18, 19 and 21, until the 23rd of January when a magnitude 5.2 earthquake shook the area releasing a sequence with more than 20 events per hour detected immediately afterwards (Barrientos *et al.*, 2007; Russo *et al.*, 2010c). Initially several hypotheses about the origin of the earthquakes were discussed, including a volcano-magmatic origin (e.g. Lara, 2008) and a tectonic origin (e.g. Cembrano *et al.*, 2007). According to the NEIC Catalogue (http://earthquake.usgs.gov/earthquakes/eqarchives/epic/), after this initial event 5 major earthquakes M>5 occurred on January 28 (M_w 5.2), February 3 (M_w 5.3), February 23 (M_w 5.7), April 1 (M_w 6.1) and finally April 21 (M_w 6.2; see Table 4.1 and Figure 4.1).

Using a temporary local seismic network, Mora *et al.* (2010) recorded the initial events of the sequence (January 2007) inferring a tectonic origin to the seismicity related to

activity on the LOFS based on earthquake locations and focal mechanisms. Legrand *et al.* (2010) maintained a local seismic network in the epicentral area from late February to mid June 2007, deducing that the origin of the Aysén seismic sequence of 2007 may have been related to a combined fluid-driven mechanism and intra-arc tectonic activity based on the distribution of the earthquakes, published focal mechanisms, geology of the area and other geophysical parameters. Russo *et al.* (2010c) relocated 6 of the largest events of the sequence (M>5) by using joint hypocentral determination (JHD; Douglas, 1967) and the event M_w=5.3 of the 23rd of February as master event (this event was locally recorded by them). They relocated all of the events at shallow depths (1-12 km) with five of them placed very proximal to the Eastern Liquiñe-Ofqui Fault (ELOF). By modelling the Coulomb stress generated by these events, they also argue the possible connections between events.

The seismic sequence of the Aysén Fjord culminated (at least in its critical phase) on the 21st of April with a M_w=6.2 earthquake (the largest of the sequence; see Figure 4.1) that produced damage to salmon farms, several landslides and a landslide-induced tsunami in the fjord that caused ten reported casualties (three dead and seven still missing people). The effects of this earthquake have been studied in several publications (e.g. Naranjo *et al.*, 2009; Sepúlveda and Serey, 2009; Sepúlveda *et al.*, 2010). Although the temporary local seismic network (5 seismometers and 5 GPS stations) installed by Chilean efforts at the beginning of the sequence was almost completely destroyed by the tsunami, the exact location of this earthquake was constrained and re-located by Legrand *et al.* (2010) within the Aysén Fjord at a depth of 4 km. According to the NEIC-USGS Catalogue the focal mechanism for this event shows dextral strike-slip faulting NNE-trending and it was located exactly on the trace of the ELOF (Figure 4.1).

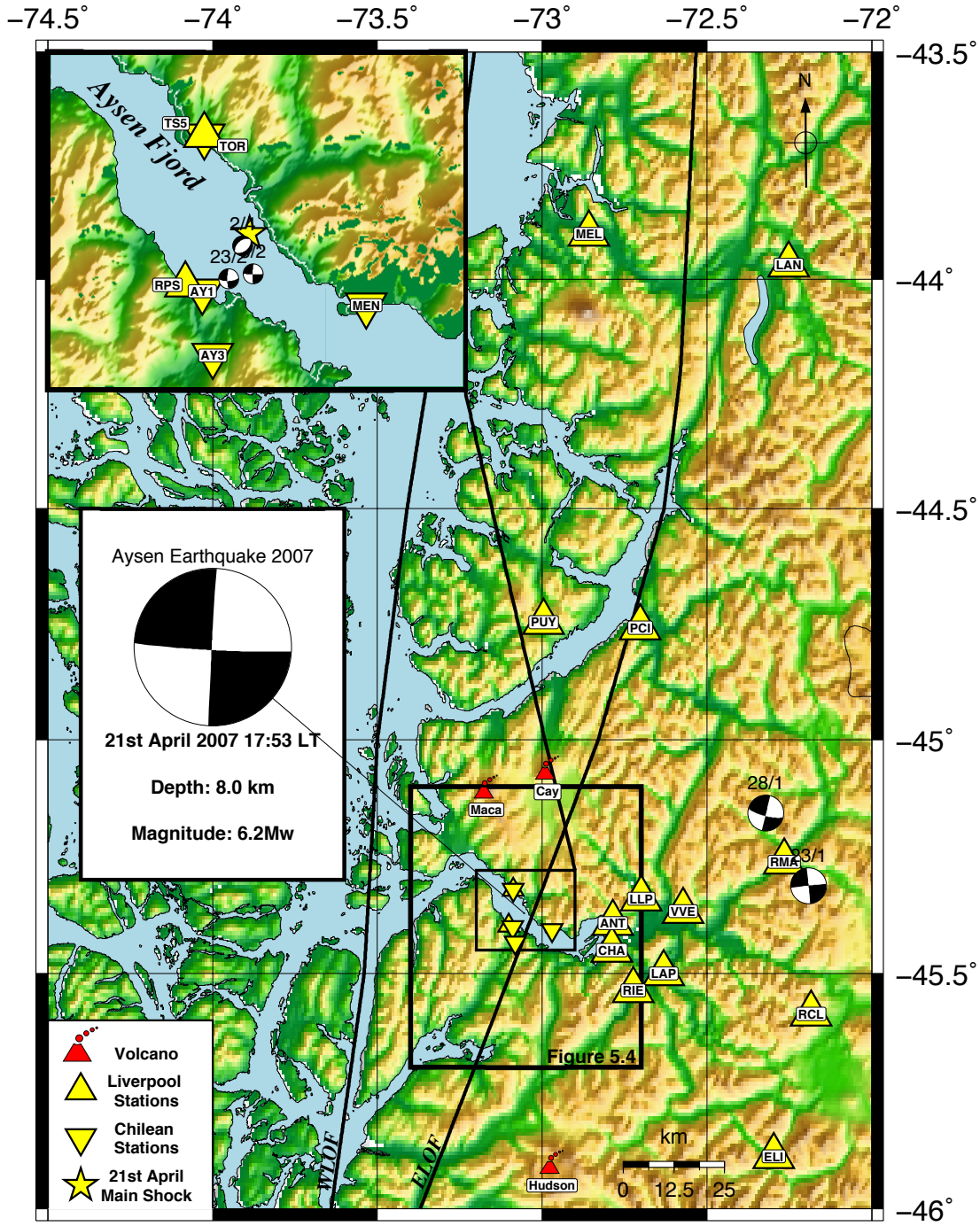

Figure 4.1. Study area and distribution of seismic network around Aysén Fjord including largest events (M>5) of the 2007 seismic sequence. Focal mechanisms from GCMT Catalogue except main shock from USGS Catalogue. Location of largest events from this work except events 23 and 28 of January from NEIC catalogue. WLOF Western Liquiñe-Ofqui Fault; ELOF Eastern Liquiñe-Ofqui Fault.

4.3. Liverpool Aftershocks Network and Data Processing

During July 2007 to February 2008 we deployed a network of 15 three-component short-period seismic stations in the area around the Aysén Fjord (see Figure 4.1 and Table 4.2). Five of the stations were installed between July-August 2007 and due to the severe weather conditions and restrictions on navigation within the fjord the remaining stations could only be deployed in September and late October 2007. The stations were continuously recording at a sampling rate of 50 Hz for a period of nearly seven months. Data could be acquired from 13 stations, although one of them also presented timing problems. The deployment was especially difficult due to weather conditions, accessibility, and the closure of the fjord to vessels other than Navy/Police boats during the whole deployment period. Navy/Police boats, zodiac boats and 4x4 vehicles were used in order to reach some of the sites. Additionally, part of the data recorded by the local seismic network deployed by Chilean institutions (e.g. Barrientos *et al.*, 2007; Legrand *et al.*, 2010; see Figure 4.1) was used in the present study in order to complement and enhance the coverage of our stations during the first part of the recording period (July-October 2007).

Once the data were collected, a visual examination of the continuous recording was carried out using the software PQL (PASSCAL Quick Look), finding a total of 236 aftershocks. These events were processed using the GIANT software package (Rietbrock and Scherbaum, 1998) including bandpass filtering the data between 0.5Hz and 15Hz, manually picking both P and S arrival times (1535 P- and 1429 S-phase picks), and assigning weights to each pick according to its quality. We used a standard weighting system in which each weight has an assigned time-window error or uncertainty for the pick. In this case we used 0=0.04s, 1=0.08s, 2=0.2s, 3=0.8s and 4=1.5s based on the given data quality (proximity of stations, very good signal/noise ratio, three components stations, sampling frequency), which allowed us to pick also S-wave arrivals very accurately.

Data from the Chilean local network were processed with the program SDX (http://pcwww.liv.ac.uk/~aeh/Software.htm) adding 170 P- and 170 S-picks to our data set. The combined data set consisted then of 1705 P- and 1599 S-arrivals, which were

used to obtain preliminary hypocentral locations using the HYPO-71 software (Lee and Lhar, 1972). Due to limited available information about this region, a velocity model from the Chiloé area (Lange *et al.*, 2007), ~700 km northwards of the study zone, was used in this preliminary instance.

Date	Time	Lat.S	Lon.W	Depth (km)	Magnitude	Source / No. Fig.4.10	gCMT FM (str/dip/slip)
23/01/2007	20:40:16.30	-45.3130	-72.1920	32	5.3Mw	NEIC	264/89/-1
23/01/2007	20:40:11.30	-45.4067	-73.0996	1-10		Russo *et al.*	
28/01/2007	02:53:20.85	-45.1570	-72.3210	49	5.2Mw	NEIC	104/76/1
28/01/2007	02:53:14.00	-45.4029	-73.1198	1-12		Russo *et al.*	
31/01/2007	08:06:14.69	-45.1940	-72.3270	15	4.8Mw	NEIC	
31/01/2007	08:06:11.08	-45.3876	-73.0591	8.46		This work	
03/02/2007	09:00:15.79	-45.2390	-72.2360	10	5.3Mw	NEIC	91/84/-6
03/02/2007	09:00:13.50	-45.3601	-73.1709	1-10		Russo *et al.*	
03/02/2007	09:00:11.92	-45.4156	-73.1017	5.43		This work**(1)**	
21/02/2007	00:23:23.00	-45.3300	-73.0240	8	4.7Mw	NEIC	
21/02/2007	00:23:23.05	-45.4017	-73.0613	6.01		This work	
23/02/2007	19:55:48.60	-45.3370	-72.3190	25	5.7Mw	NEIC	87/70/-12
23/02/2007	19:55:41.90	-45.3468	-72.9873	1-10		Russo *et al.*	
23/02/2007	19:55:44.08	-45.4004	-73.0668	9.71		This work**(2)**	
23/02/2007	22:38:56.75	-45.3340	-72.5880	35	4.6Mw	NEIC	
23/02/2007	22:38:51.06	-45.4855	-73.1037	11.03		This work	
24/03/2007	00:45:34.50	-45.3590	-73.0410	6	4.5Mw	NEIC	
24/03/2007	00:45:34.13	-45.3770	-73.0482	8.34		This work	
02/04/2007	02:49:35.90	-45.3820	-73.0580	4	6.1Mw	NEIC	53/43/-86
02/04/2007	02:49:31.10	-45.4472	-73.6762	1-10		Russo *et al.*	
02/04/2007	02:49:35.47	-45.3830	-73.0657	7.19		This work**(3)**	
02/04/2007	09:04:52.31	-45.4190	-72.7190	58	4.7Mw	NEIC	
02/04/2007	09:04:44.75	-45.4672	-73.1103	9.60		This work	
19/04/2007	14:36:30.33	-45.2120	-72.5500	59	4.7Mw	NEIC	
19/04/2007	14:36:21.10	-45.4463	-73.1079	9.81		This work	
21/04/2007	17:53:46.31	-45.2430	-72.6480	36	6.2Mw	NEIC	84/86/2
21/04/2007	17:53:38.60	-45.3293	-73.2073	1-10		Russo *et al.*	93/87/-1**
21/04/2007	17:53:39.86	-45.3716	-73.0551	8.00		This work**(4)**	
19/08/2007	07:42:24.49	-45.7140	-72.5380	35	5Mw	NEIC	
19/08/2007	07:42:16.97	-45.9165	-72.9267	0.12	4.4(ML)	This work*	
08/12/2007	13:24:32.79	-45.7880	-72.7910	35	4.8Mw	NEIC	
08/12/2007	13:24:26.51	-45.9203	-73.0449	3.43	4.4(ML)	This work*	

Table 4.1. Comparison of location of the largest events during the Aysén sequence. Focal mechanisms from GCMT catalogue except those indicated. *Hudson volcano related event. **NEIC Catalogue focal mechanism.

Name	Latitude	Longitude	ID	Installed/Removed	Name	Latitude	Longitude	ID	Installed/Removed
ANT	45.3926ºS	72.7855ºW	6030	27/06/07–16/02/08	RIE	45.5366ºS	72.7228ºW	6071	04/07/07-16/02/08
CHA	45.4505ºS	72.7890ºW	6102	30/06/07-16/02/08	RMA	45.2617ºS	72.2654ºW	6097	16/09/07-17/02/08
ELI	45.8890ºS	72.2971ºW	6188	No data	RPS	45.3979ºS	73.1020ºW	6140	27/10/07-17/02/08
LAN	43.9686ºS	72.2525ºW	6161	No data	TOR	45.3212ºS	73.0883ºW	6160	29/10/07-22/02/08
LAP	45.4999ºS	72.6317ºW	6051	01/07/07-01/02/08	VVE	45.3672ºS	72.5726ºW	6088	11/09/07-17/02/08
LLP	45.3411ºS	72.6993ºW	6217	12/09/07-16/02/08	TS5*	45.3217ºS	73.0883ºW		Used between
MEL	43.9009ºS	72.8583ºW	6178	24/07/07-19/02/08	AY1*	45.4013ºS	73.0897ºW		14-08-07
PCI	44.7580ºS	72.7023ºW	6165	03/07/07-18/02/08	AY3*	45.4342ºS	73.0822ºW		to
PUY	44.7460ºS	72.9951ºW	6044	09/09/07-19/02/08	MEN*	45.4083ºS	72.9703ºW		29-10-07
RCL	45.5862ºS	72.1839ºW	6093	10/09/07-17/02/08					

Table 4.2. Seismic stations used for the present study. *Chile stations.

4.3.1. 1-D Velocity Model

In standard earthquake locations, velocity parameters remain fixed to *a priori* values taken from previously available information (previous seismic studies, refraction profiles, etc.) which is considered to be correct and thus, final solutions are obtained minimizing the travel time error (RMS) by only perturbing the hypocentral parameters. Nevertheless, precise earthquake locations and meaningful error estimates require the solution of all the parameters contained in the inversion problem, i.e. hypocentral parameters and velocity structure. The program VELEST (Kissling *et al.*, 1995) allows the calculation of a minimum 1-D layered velocity model by simultaneously inverting for both earthquake hypocentres and velocity parameters including station corrections, solving in this way the coupled hypocentre-velocity model problem (Crosson, 1976; Kissling, 1988).

Based on Wadati diagrams we determined an average Vp/Vs ratio of 1.76 in the Aysén Fjord area. A selection of best events was made based on number of observations (>6 P-wave picks) and GAP or angle of stations coverage (<180º) for the inversion. Additionally, the average Vp/Vs ratio was used in order to reject those observations with a Vp/Vs value larger than 1.80 seconds off the main trend. Observations from stations with timing problems were also removed leading to a final selection of 79 high quality events (out of 214) including 785 P- and 749 S-phases. The average pick uncertainty for P-phases of this subset is 0.062s (weight 0 representing 77% of the picks) and for the S-phases is 0.067s (weight 0 representing 65% of the picks).

Regarding the spatial distribution of the subset, the events are located within the fjord area and further North including a northern cluster (see below) at depths down to 15 km but mostly around 5 km.

Subsequently, this selection was used as input for the simultaneous inversion. The velocity model proposed by Lange *et al.* (2007) for the Chiloé area was used as the base model for the processing. It is important to notice that the inverted velocity structure depends decisively on the initial guess, as it tends to maintain the overall shape of the starting model (Langer *et al.*, 2007).

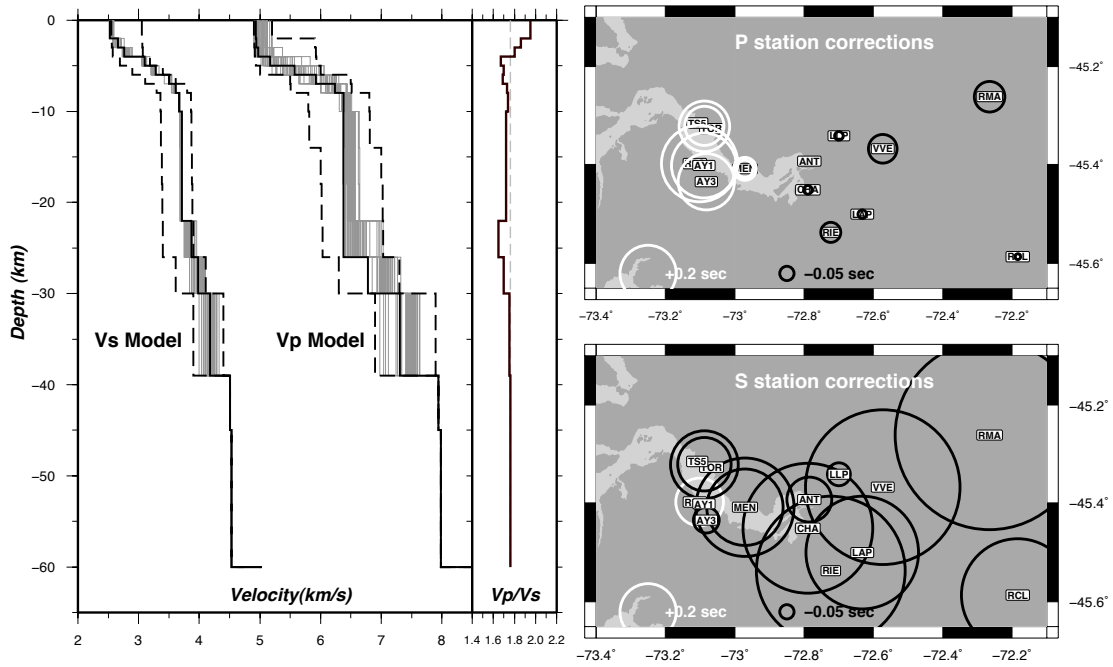

Figure 4.2. (Left) Final 1-D velocity model for P and S velocities as well as Vp/Vs ratio. Dashed lines indicate range of starting models, grey lines indicate final models (best 5%) and the bold black line represents the best final model with the lowest overall RMS. **(Right)** P and S station corrections.

The inversion in VELEST was performed following the procedure proposed by Kissling *et al.* (1994). A first approach was carried out testing different configurations of the layers' properties and parameters (e.g. number of iterations, damping, etc.) involved in the simultaneous inversion. Finally, a thousand initial velocity models were randomly created for both P and S waves inversions and only the best 5% (lowest RMS) of the final models were considered for plotting (Figure 4.2). This process could be considered

as a Monte Carlo-approach type method since we randomly searched for initial models in order to get a best final model with the lowest RMS. The simultaneous inversion looks for the best velocity model (lowest RMS) according to the given travel time dataset, keeping the layer thickness and depths of the initial model constant and changing only layer velocity, hypocentre location and station corrections. By adopting such an approach we are also relaxing the dependency of the starting model as mentioned above.

Figure 4.2 displays the final 1-D velocity model obtained for both P- and S-waves, as well as the Vp/Vs ratio. Final RMS for P-model is 0.068s and for the S-model 0.080s, reducing in ~0.05s the initial RMS. Due to the lack of deep hypocentres, reliable velocity information was obtained only for the upper ~20 km, and hence the velocities from 39 km depth downwards were fixed to those provided for the Chiloé area.

For the upper 5 km depth, P-wave velocities around 5 km/s were calculated. These values show agreement with velocities expected for this area based on its geology, which consists mostly of granitic rocks from the North-Patagonian Batholith. At 5 km depth a rise in P-wave velocities from 5.17 km/s to 5.57 km/s is observed and from this depth velocities increase gradually to 6.38 km/s at 8 km depth. From 8 to 26 km depth, P-wave velocities keep constant at 6.38 km/s. Elevated Vp/Vs ratios of 1.80 to 1.95 were found for the upper 3 km, while for greater depths Vp/Vs ratios in the range of 1.65 to 1.76 were obtained.

The station ANT was chosen as the fixed reference station since its central location and number of observations. Noticeable, P-wave station corrections indicate negative values at the East of the area whilst to the West of the ELOF positive values are observed (see Figure 4.2) despite the fact that the geology is mostly uniform in the whole study area. The opposite sign of station corrections at both sides of the ELOF could be attributed to a structural difference on both sides of the fault; however, more detailed geological/structural mapping would be necessary to assess this point with a degree of certainty.

In order to check the robustness and location stability of the final 1-D velocity model,

we performed a series of tests by randomly shifting both latitude and longitude of the original hypocentre spatial coordinates by ±3-5 km and depth by ±0-3 km. The new shifted hypocentres were then introduced to VELEST for a relocation keeping the velocity and station parameters fixed so the program looks for a solution only by changing the hypocentral parameters. This operation was repeated a hundred times for each event, therefore we obtained a representative average of the events' new relocations. If the final minimum 1-D velocity model presents a robust minimum in the solution space, no significant changes in the hypocentre locations are expected (e.g. Husen *et al.*, 1999). Figure 4.3 shows the results obtained from this stability test.

The test was applied to the whole dataset of 214 events, including those events that were not used for the simultaneous inversion. Except for a few hypocentres, most of them were relocated very close to their original position. The population of differences between the original and the new relocated position of the events exhibits a normal distribution for the three coordinate directions. In the latitude and longitude directions the calculated σ value corresponds to 212.18 and 275.25 m respectively. It is possible to observe both, in the latitude and longitude directions that there is a particularly small dispersion of relocations between events 85 and 129 (see Figure 4.3). This is due to the combined use of Chilean and Liverpool stations during that period (2-September to 29-October 2007; see Table 4.2 and Figure 4.7), whilst for the rest of the events only our stations (Liverpool) were available. In the depth direction the calculated σ value corresponds to 468.94 m. As expected, a higher dispersion and therefore, a higher sigma value on the depth direction was obtained in comparison with the horizontal components despite the smaller shift applied in the vertical component (0-3 km vs. 3-5 km for the horizontal components). Specifically, for the subset of 79 events used in the simultaneous inversion (black crosses in Figure 4.3), the greatest misfits obtained are 66.7, 306.3 and 679 m for the latitude, longitude and depth directions respectively. Overall, 96% and 89% of the events were relocated within 500 m from their original position for the horizontal and vertical components correspondingly.

We also performed stability tests addressing the coupled inversion problem based on our best subset of events (used for the simultaneous inversion) by introducing randomly perturbed hypocentral locations and inverting simultaneously for velocity model, station

corrections and hypocentral locations. The results indicate average variations in velocity of 0.04 km/s for the upper 4 km of crust, 0.25 km/s for the next couple of kilometres, and 0.04 km/s down to 30 km depth where the standard deviation and averaged variation of velocity increases due to the lack of hypocentres at this depth. The standard deviations for the hypocentral relocations are 1.7, 1.3 and 2.6 km for the N-S, E-W and vertical directions respectively.

4.3.2. Events Location

The final location of events was carried out by using the software NonLinLoc (Lomax *et al.*, 2000) that computes non-linear probabilistic locations by producing an estimate of the spatial probability density function and the maximum likelihood origin time. Out of 214 events processed, 182 correspond to seismicity localized within the Aysén Fjord area, 17 earthquakes are spatially related to the Hudson volcano (~46º lat. S) and 15 events could not be associated to any known source. No seismicity related to the Wadati-Benioff Zone was detected in the study area during the observation period.

Figure 4.4 shows the final locations for the 182 events in the Aysén Fjord area whilst location uncertainties (68% confidence limit) are shown in Figure 4.5. The final locations show intra-arc seismicity at shallow depths, mostly between 4-10 km, that can be described as two main features: (1) an alignment of events NNE-trending that crosses the Aysén Fjord extending for more than 50 km coinciding with the ELOF and including a cluster of 19 very concentrated events observed to the North of the area (~45.15º lat. S); and (2) an arrangement of events located to the East of the main trend and distributed as a nearly W-E-trending alignment. Location uncertainties are particularly small in the area near by the fjord and for the northern cluster of events whilst locations placed at the South of the seismic network show the greatest uncertainties. For the horizontal directions 80% of the events present uncertainty ellipses smaller than ±2 km whilst in the vertical direction this percentage decreases to 57%.

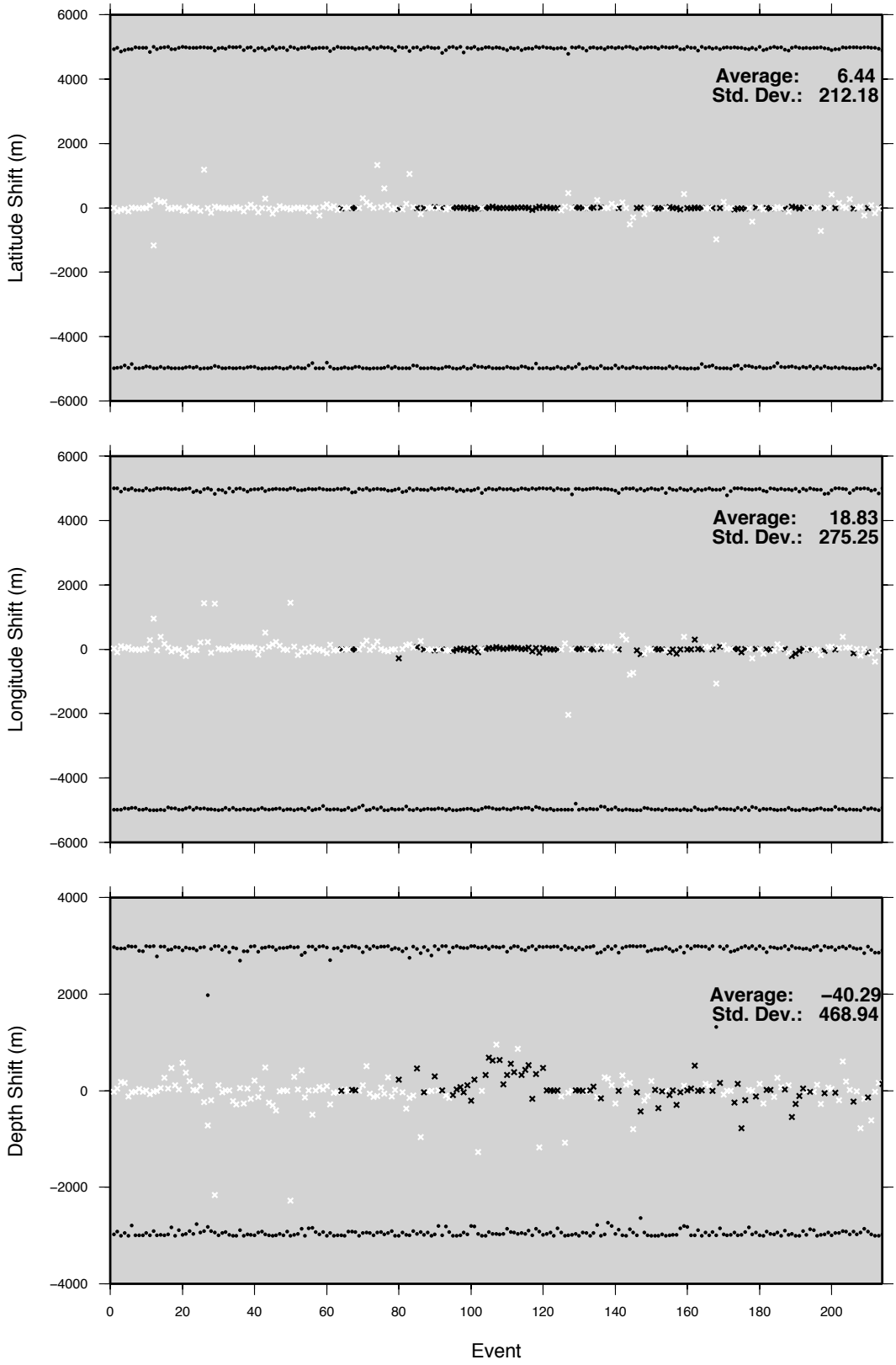

Figure 4.3. Hypocentre stability tests. Black dots show maximum negative and positive random shifting for each event. Black and white crosses represent the average relocation for each event used (79) and not used (135) in the simultaneous inversion respectively. See text 4.3.1 for more details.

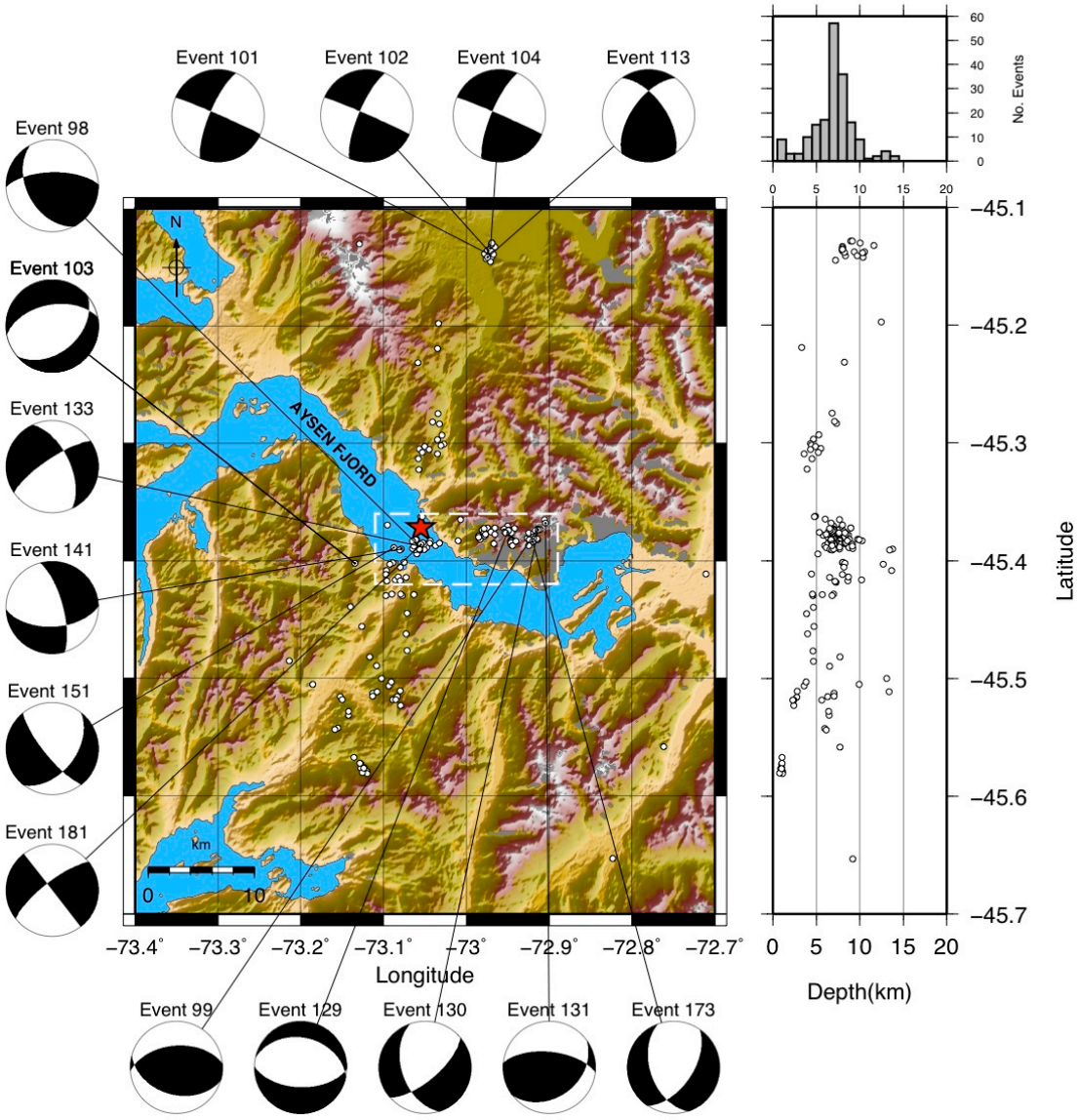

Figure 4.4. Final location of aftershocks and focal mechanisms calculated in this work. Rectangle in white dashed line indicates events on Figure 4.6. Red star indicates location of 21st April main shock.

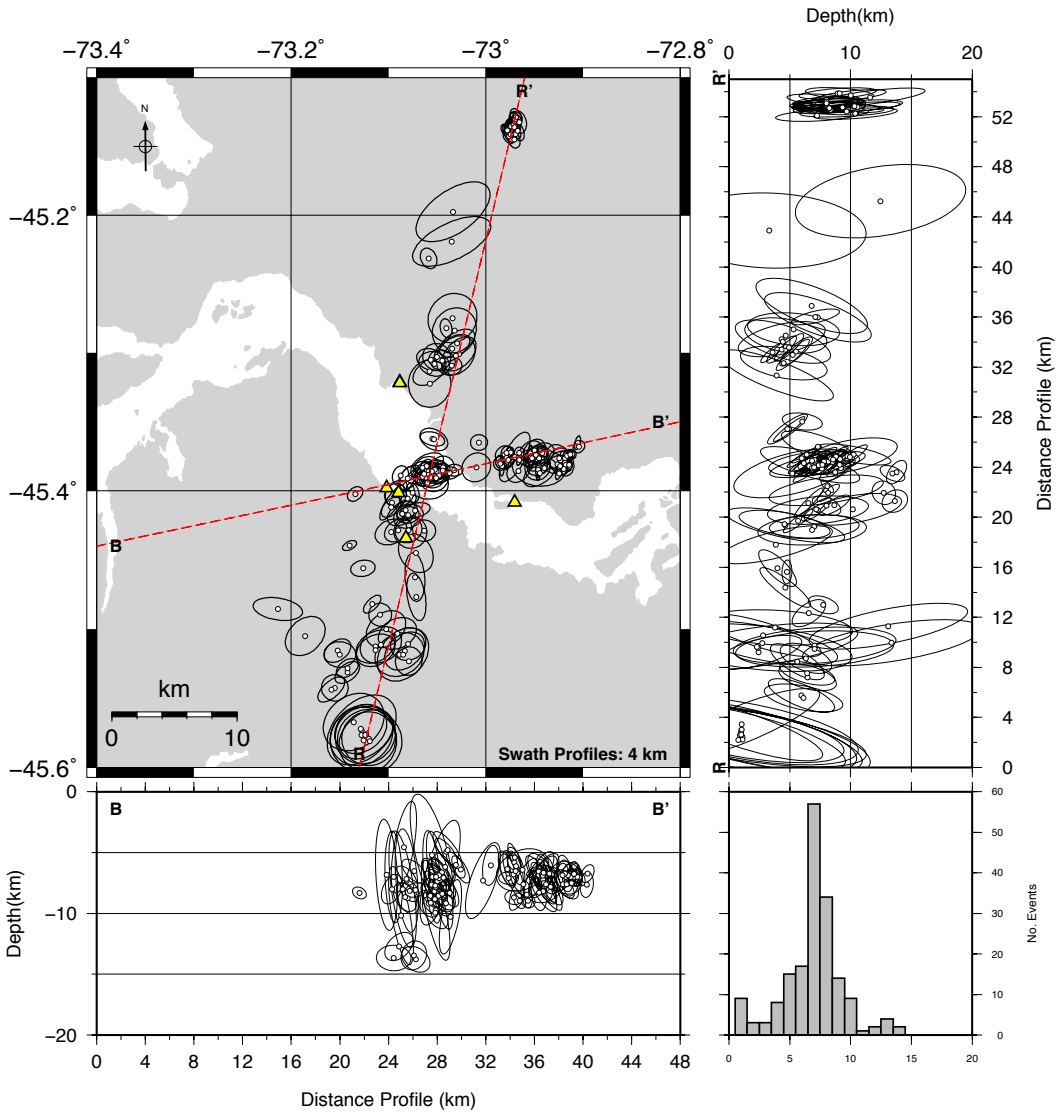

Figure 4.5. Final location uncertainties. Error ellipses represent 68% confidence limit. Yellow triangles show local network in the area nearby.

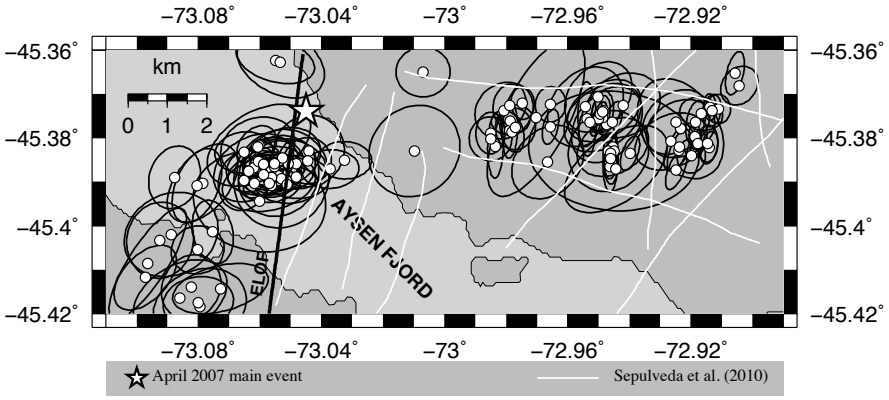

Figure 4.6. Detail of events within the Aysén fjord area showing seismicity and present structures. See text for more details.

Figure 4.6 shows in detail the area highlighted in Figure 4.4. It is possible to observe that both seismicity related to the main NNE-trending alignment and seismicity related to the W-E alignment occur mostly at depths between 5 and 10 km within the Aysén fjord adjacent area.

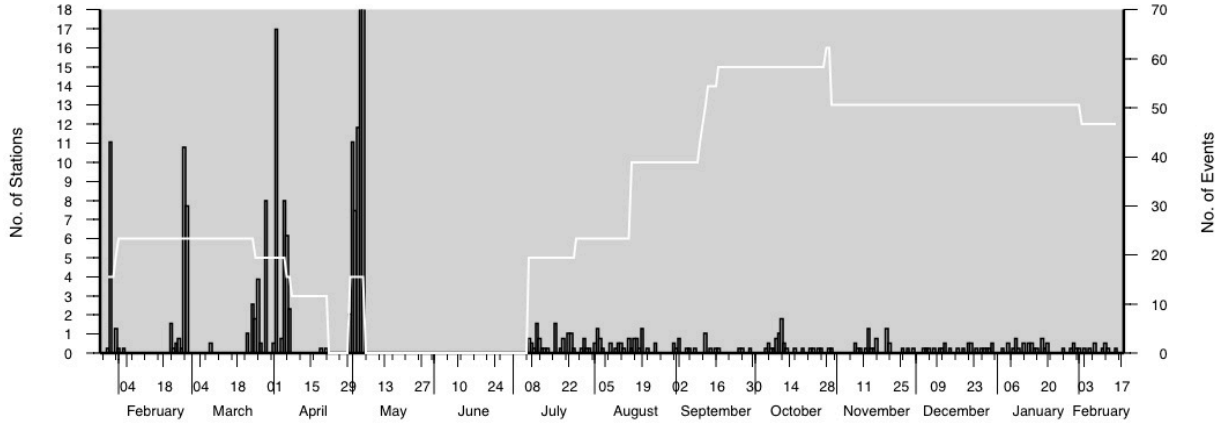

Figure 4.7. Histogram showing frequency of events during the period of the experiment in grey bars and stations availability in white line.

Regarding the chronological occurrence of the events, no clear time-dependent pattern was observed, neither an increase nor a decrease in the late Aysén fjord aftershock seismicity during the time of our deployment and moreover, no spatial migration of the epicenters was detected. The only temporal characteristic to highlight is the occurrence of an event cluster located to the North of the area, which spanned only one week in October 2007 (see Figures 4.4 and 4.7).

4.3.3. Local Magnitudes

Local magnitudes (M_L) were calculated by using the automated magnitude calculation included in the GIANT software package (Rietbrock and Scherbaum, 1998). Maximum peak-to-peak amplitudes were selected manually from a time window of 2 seconds after the arrival of the S-wave in both of the horizontal components for each event. These amplitudes were then transformed into the corresponding amplitude of a Wood-

Anderson seismometer and computed by GIANT following the equations from Bakun and Joyner (1984). Finally the magnitude of the event is calculated from the average of the magnitudes for each used station.

Magnitudes were found in a range between 1.2 and 4.4 with most of the events concentrated between 1.6 and 2.6 M_L (Figure 4.8). The geographic distribution shows bigger magnitudes on the main ~NS-alignment while the events located at the East of the main fault show smaller ones. The highest magnitudes are related to the Hudson volcano activity. No special distribution of magnitudes is appreciated either in depth or in time.

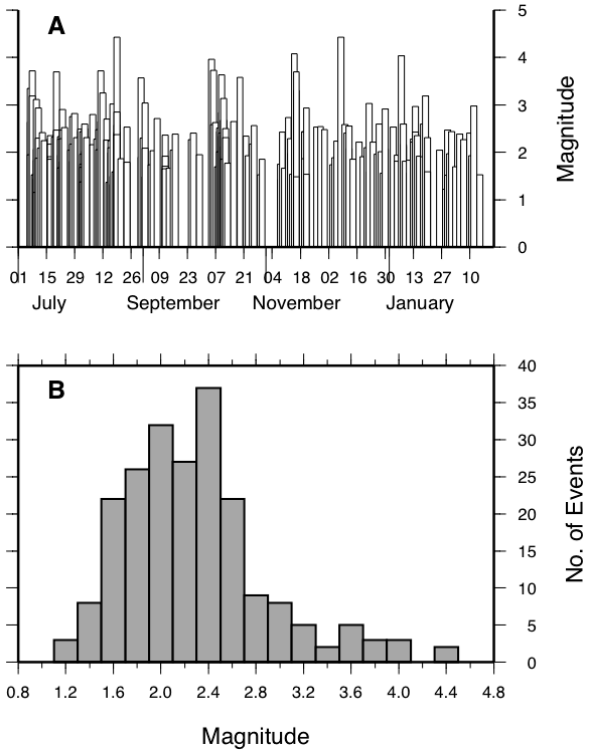

Figure 4.8. Local magnitudes calculated in this work. **A**. Magnitudes per event on time. **B**. Histogram of frequencies of magnitudes

During the observation period, two of our detected events were also listed in the NEIC catalogue and two in the Servicio Sismológico de la Universidad de Chile catalogue (GUC; www.sismologia.cl). Differences with the NEIC catalogue were 0.57 and 0.38, whilst differences with the GUC catalogue were 0.14 and 0.43. It is important to notice here that the NEIC catalogue is based on a different magnitude scale.

4.3.4. Focal Mechanisms

Focal mechanisms were constrained for selected events using the software FOCMEC (Snoke *et al.*, 1984; Snoke, 2009). FOCMEC performs a search of the focal sphere and reports acceptable solutions based on selection criteria for the number of polarity errors and errors in amplitude ratio.

Obtaining focal orientations was particularly difficult due to the failure of some stations during the recording period and consequently, the lack of optimal station coverage around the events. In total, 15 focal mechanisms were successfully calculated from first motion P-wave polarities and SV/P amplitude ratios (Figure 4.4). The method used by FOCMEC is explained in Snoke *et al.* (1984) and Snoke (2009), whilst the usage of S/P amplitude ratio for focal mechanisms determination has been widely explained in several publications (e.g. Kisslinger, 1980; Hardebeck and Shearer, 2003). Take-off angles were computed from the final location in the 1D velocity model. In order to calculate amplitude ratios, we used the maximum peak-to-peak amplitude of the P- and S-wave arrival. Since the waveforms of S-wave arrivals are usually more complicated than P-wave arrivals, we selected the peak-to-peak maximum amplitude contained within a window of 1 second after the S-wave arrival. In the case of the P-wave, we used the first impulse.

The solutions shown in this paper are presented by equal area, lower hemisphere projection. Table 4.3 shows the parameters obtained for the focal mechanisms. No error for first motion polarity was allowed in the processing. In case of multiple solutions, the focal mechanism with the smallest RMS was chosen for plotting. Even though we obtained multiple solutions for most of our focal mechanisms (11 out of 15 events), these solutions differed only by few degrees, therefore not affecting considerably the faulting geometry of each of the mechanisms shown in Figure 4.4.

Event	Errors/ Polarities	Errors/ Ratios	Fault Solution Strike/Dip/Rake	Auxiliary Plane Strike/Dip/Rake
98	0/10	0/6	268.46/65.82/51.04	151.59/44.81/144.47
99	0/10	0/5	265.51/50.73/77.04	105.49/41.03/105.34
101	0/15	2/11	293.49/87.42/14.78	202.81/75.23/177.34
102	0/15	1/10	293.49/87.42/14.78	202.81/75.23/177.34
103	0/10	0/8	259.11/51.62/-70.72	49.71/42.27/-112.63
104	0/14	1/11	293.49/87.42/14.78	202.81/75.23/177.34
113	0/12	2/8	324.74.79/60.00/35.26	222.32/60.00/144.74
129	0/6	1/6	282.10/35.31/-81.33	91.51/55.15/-96.10
130	0/9	0/9	49.82/67.48/-45.90	161.38/48.44/-149.21
131	0/8	0/7	54.06/35.53/53.95	275.88/61.98/112.80
133	0/12	6/10	236.03/75.97/-32.40	334.77/58.68/-163.52
141	0/7	2/7	344.73/71.25/-36.01	56.17/87.87/-157.24
151	0/10	1/10	38.06/48.36/-18.88	140.86/76.00/-136.78
173	0/7	0/7	34.37/56.17/-53.00	160.82/48.44/-131.93
181	0/10	0/10	232.11/75.00/-0.00	90.00/142.11/165.00

Table 4.3. Parameters of focal mechanisms calculated in this study.

Four of the 15 focal solutions calculated (events 101, 102, 104 and 113) are spatially related to the cluster of earthquakes located to the North of the study area (~lat. 45.15°S). These focal mechanisms show strike-slip faulting and are strongly similar among them indicating either right-lateral strike-slip faulting NNE-trending or left-lateral strike-slip faulting NW-trending. The remaining focal mechanisms show a more diverse variety of solutions with no clear common pattern.

4.4. Foreshocks and Aftershocks previous to Liverpool network

In order to obtain a better understanding of the whole Aysén seismic sequence we re-located the data published by Legrand *et al.* (2010), containing the foreshock activity (28th of February to 21st of April 2007) and early aftershock activity (30th of April to 5th of May 2007) of the sequence using our new velocity model.

The dataset consists of manual picks (P- and S-arrivals) of 344 foreshocks and 615 aftershocks. Firstly, we used our new local 1-D velocity model to perform a simultaneous inversion for station corrections and hypocentres on a selection of the best 225 events in terms of number of observations and GAP from the foreshocks data. We

used only foreshocks for the simultaneous inversion given the better seismic network used for their location. The station corrections show negative values (~0.3 seconds) for the S-wave, which suggests that our velocity model might underestimate the S-wave velocity for this dataset. It is important to notice that when inverting with fixed velocity parameters, changes needed in the velocity model might not be completely absorbed by the station correction terms, therefore introducing a bias into hypocentral locations. However this, 92, 69 and 72% of the events were relocated within 2 km from the original locations by Legrand *et al.* (2010) in latitude, longitude and depth directions, respectively, suggesting the robustness of the obtained locations The largest discrepancies between the different locations approaches are found for the early aftershock data predominantly caused by the changes of the seismic network and less number of observations after the main shock of the 21st of April (Legrand *et al.*, 2010; see discussion below).

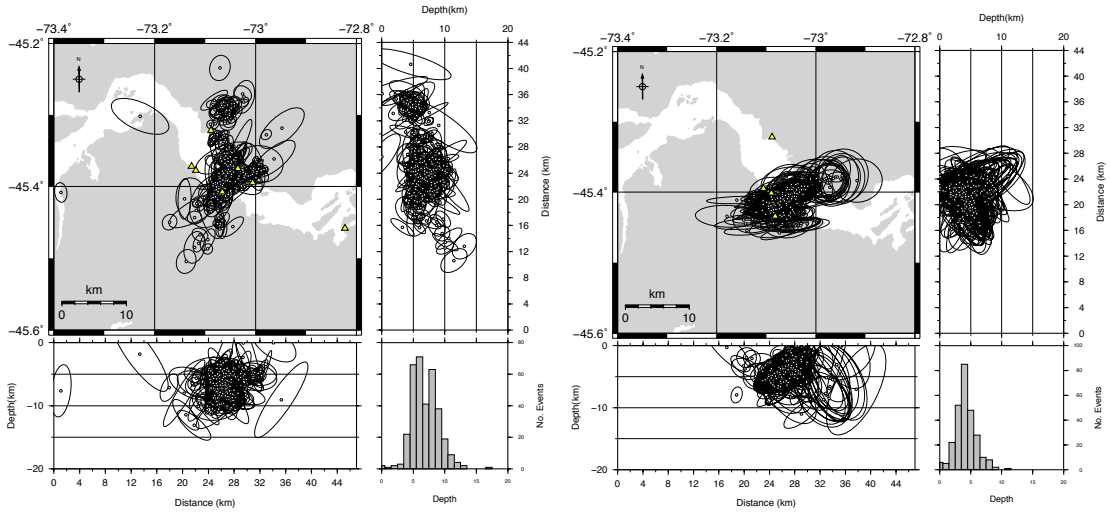

Figure 4.9. Re-location of foreshocks (left) and early aftershocks (right) previous to Liverpool deployment including 68% location confidence limit. Only events with horizontal ellipses' semi axes smaller than 5 km have been plotted.

Figure 4.9 shows our relocation of these events including 68% confidence limits. For our further interpretation we will only use events with uncertainty ellipses' semi-axes smaller than ±5 km, comprising in the case of the foreshocks 316 events out of 344 and for the early aftershocks 267 out of 615. The foreshock activity is located following the main trend of the ELOF along 26 km, mostly at depths between 4-10 km with also some

incipient activity at the East of the main alignment. Early aftershock seismicity shows instead less reliable locations due to lack of appropriate stations coverage. These events are located mostly within ~6 km to the South of the 21st April main shock in the Aysén fjord.

5.5. Discussion and Conclusion

The present study focuses on the Aysén seismic sequence of 2007 and in particular on the late aftershock activity of the 21st of April main shock, recorded between July 2007 and February 2008. Additionally we present for the first time a 1-D local velocity model for this area. Previous studies (e.g. Mora *et al.*, 2010) focused on the foreshock activity and located it exclusively within the Aysén Fjord inferring a tectonic origin for the whole seismic sequence, whilst Legrand *et al.* (2010) attribute the seismicity in the Aysén Fjord to a combined volcano-tectonic activity.

Here we show that seismicity was not exclusively constrained to the Aysén Fjord nearby area but it extends for ~50 km in a NNE-trending alignment that coincides with the trace of the ELOF. Furthermore, the development of aftershock activity to the east of the main fault indicates that the sequence of 2007 and its main event, the 21st of April Aysén earthquake, re-activated subsidiary faults located to the East of the main fault that belong to the same structural system. These subsidiary faults could correspond to NE- and NW-trending structures recognized by Sepúlveda *et al.* (2010), although given our location resolution we can not support this hypothesis conclusively (see Figure 4.6). Another possible approach to the eastern seismicity is to take it as a single W-E-trending alignment subordinated to the main fault; however, such a structure has not been identified in previous studies in the Aysén area. The occurrence of aftershock activity is exclusively constrained within and to the eastern side of the main fault, whilst to the west no events were detected. Sepúlveda *et al.* (2010) also found that a large number of landslides induced by the April 2007 Aysén earthquake were located to the east and north of the main event, which in turn is related to the presence of these secondary faults and higher topography at this side of the main fault. The W-E-trending seismicity zone extends for ~15 km east of the main fault giving an idea of the width of

deformation across the main fault. It is important to note that it is our belief that these events occur on re-activated subsidiary faults. Certainly, better geological mapping of structures in the area is also necessary in order to address the spatial distribution of the aftershocks in relation to these structures.

By using empirical equations from Wells and Coppersmith (1994) we calculated a subsurface rupture length of 18 km for the M_w=6.2 strike-slip fault of the main shock. Although we observe seismicity along ~50 km, the bulk of the aftershock seismicity that occurs in the Aysén fjord is contained in a 20 km long segment which coincides with the above estimate. The only seismicity occurring outside this 20 km segment is the northern cluster of events (~45.15 lat. S), which might or might not be related to the 2007 sequence and its 21st April main shock, but it is certainly aligned with the ELOF.

Additionally, the relocation of the foreshock and early aftershock activity contributes significantly to understanding the whole seismic sequence. Unfortunately the disruption of the local seismic network by the landslide-induced tsunami of the 21st of April led to greater uncertainties in locations of the early aftershock activity. Nevertheless, it is possible to conclude that the seismic activity immediately after the main shock was concentrated in the area around the 21st April event (instead of along the trace of the main fault) with up to 400 events per day on the 5th of May 2007. The smaller Vp/Vs ratio of 1.69 calculated by Legrand at al. (2010) in comparison with the ratio calculated by us for the latter part of the sequence (1.76) could suggest a change in time (pre- and after- main shock) of the Vp/Vs ratio in the area. However, it is important to notice that our value is the average over a much larger area including stations further North in comparison with the network of Legrand *et al.* (2010).

Given the depth of the located events, it is possible to suggest a seismogenic zone restricted to the first 15 km of crust for the study area, which agrees with numbers postulated by Tassara and Yañez (2003) who calculate a maximum crustal thickness of 40 km for the segment between 39° S and 47° S.

We also correlated 14 of the biggest events during the sequence of 2007 that were located by the USGS and by Russo *et al.* (2010c), with our relocations (see Table 4.1).

We found noticeable differences with previous locations, in particular in terms of depth provided by the NEIC catalogue. Figure 4.10 shows differences in the epicentres of 4 of the biggest events proposed by Russo *et al.* (2010c) and relocated in the present work. Again, differences in locations are considerable, with all of our relocations placed within the Aysén fjord. Specifically regarding the main shock of the sequence, the M_w=6.2 event of the 21st of April 2007, our relocation indicates that it was placed within the Aysén fjord at a depth of 8 km. Our relocations improve considerably previous locations by using local stations and a new 1-D local velocity model as well as the employment of a non-linear probabilistic location approach on the estimation of uncertainties.

From the six largest events of the sequence, two could not be relocated by our local network (January 23 and 28) as this was not yet installed. These events were located to the East of the Aysén fjord by the USGS-NEIC (see Figure 4.1 and Table 4.1) but we believe they were mislocated given the high uncertainties on teleseismic locations especially for this remote area of the world. Instead, we believe these earthquakes occurred very close to the other large events relocated by us within the Aysén fjord.

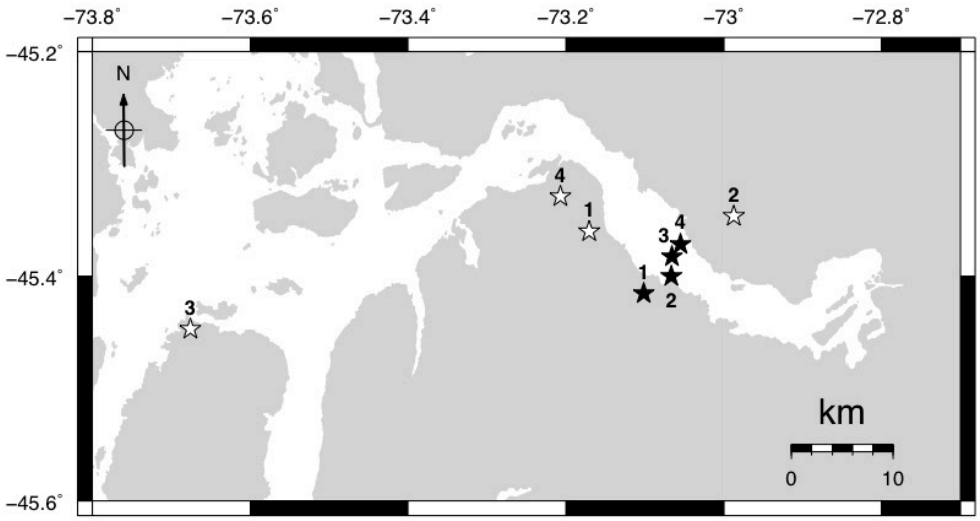

Figure 4.10. Location of 4 of the biggest events of the Aysén sequence by Russo *et al.* (2010c; white stars) and our relocations (black stars). 1: February 3; 2: February 23; 3: April 2; 4: April 21. See Table 4.1 for details.

The two available focal mechanisms for the 21st April 2007 main shock are those from the USGS-NEIC and GCMT catalogues (see Table 4.1). They differ slightly (9 deg.) regarding strike of the fault plane but agree well in the dip and slip angles. Therefore, both solutions show dextral strike-slip faulting orientated either NNW (GCMT, 84/86/2) or NNE (USGS-NEIC, 93/87/-1). The other 5 focal mechanisms of the sequence are only available from the GCMT catalogue and are shown in Figure 4.1. Except for the event on the 4th of February that exhibits normal faulting, all of them show right lateral strike-slip faulting, most likely related to the activity on the ELOF. The normal faulting solution could be associated to activity on the *en échelon* faults that join both of the main traces of the LOFS. Regarding the focal mechanisms computed in this work, they clearly indicate for the Northern cluster right-lateral strike slip faulting trending NNE, just as for the LOFS-related focal mechanisms calculated in previous publications (e.g. Lange *et al.*, 2008) and also supported by the focal mechanism obtained from the GCMT and USGS-NEIC catalogues for the main shock of the 2007 sequence. On the other hand, the situation to the east of the ELOF is rather more complex as depicted by the diversity of rupture geometries obtained for these events.

The aftershock sequence of the 21st April 2007 Aysén earthquake was successfully recorded by our temporary seismic network. The seismicity analysed is clearly aligned with the ELOF and the event distribution suggests that this fault is currently seismically active in its southern end. Based on our findings, we infer that the Aysén seismic sequence of 2007 had a tectonic origin, with activity on the ELOF as its main driving force. However, it is not possible to dismiss the potential action of hydrothermal fluids that could re-activate secondary structures and migrate along them generating minor seismicity that occurs besides the main tectonic events, especially to the East of the main fault. The presence of hydrothermal fluids and rock fracturing is also suggested by the high Vp/Vs ratio varying from 1.80 to 1.95 for the upper 3 km as observed in this study and the existence of several monogenetic cones and hydrothermal activity in the area described by D'Orazio *et al.* (2003). We also demonstrated that teleseismically determined hypocentre locations can still have large associated errors in remotely located regions, even for the case of a joint hypocentre determination.

The whole Aysén fjord earthquake sequence of 2007 and its effects including hundreds of landslides and a tsunami reveals that it is imperative to re-estimate the geologic hazards for this region that was formerly believed a "seismically quiet" region in Chile.

Acknowledgments

We thank the valuable comments and suggestions of Dr. Stephan Husen and an anonymous reviewer. We also thank the support of the Chile National Emergency Office (ONEMI), Chilean Navy and CONICYT, Chile through its program of scholarships 'Beca Presidente de la República'. This project was partially funded by NERC grant NE/F001703/1. The seismic instruments and data management facilities were provided by SEIS-UK at the University of Leicester. The facilities of SEIS-UK are supported by the Natural Environment Research Council under Agreement No. R8/H10/64. Data collected will be available through the IRIS Data Management Center.

Note Added In Proof

Recently, on 2012 May 8, Chilean authorities approved the construction of a hydroelectric power dam on the Cuervo River, in the northern side of the Aysén Fjord. This structure will be built on the area of the 2007 Aysén seismic sequence, over the Liquiñe-Ofqui Fault System and next to the Macá volcano. The dam therefore will be clearly exposed to a significant geological hazard including volcanic activity, earthquakes on the active fault system and landslides with potential induced local tsunamis, which could all affect nearby populated areas. Another project (Central Cóndor), contemplating the construction of a dam in the southern side of the fjord, is in the pipeline exposed to similar conditions.

CHAPTER 5

SEISMIC-AFTERSLIP CHARACTERIZATION OF THE 2010 M_W8.8 MAULE, CHILE, EARTHQUAKE BASED ON MOMENT TENSOR INVERSION

Abstract

On February 27th 2010, a M_W8.8 earthquake struck the coast of south-central Chile, rupturing ~500 km along the subduction interface. Here we estimate the amount of seismically-released afterslip (SRA) and the mechanisms underlying the distribution of aftershocks of this megathrust earthquake. We employ data from a temporary local network to perform regional moment tensor (RMT) inversions. Additionally, we relocate global centroid-moment-tensor (GCMT) solutions, assembling a unified catalogue covering the time period from the mainshock to March 2012. We find that most (70%) of the aftershocks with M_W>4 correspond to thrust events occurring on the megathrust plane, in areas of moderate co-seismic slip between 0.15 and 0.7 fraction of the maximum slip (S_{max}). In particular, a concentration of aftershocks is observed between the main patches of co-seismic slip, where the highest values of SRA are

observed (1.7 m). On the other hand, small events, M_W<4, occur in the areas of largest co-seismic slip (>0.85 S_{max}), likely related to processes in the damage zone surrounding the megathrust plane. Our study provides insight into the mechanics of the seismic afterslip pattern of this large megathrust earthquake and a quantitative approach to the distribution of aftershocks relative to coseismic slip that can be used for similar studies in other tectonic settings.

5.1. Introduction

Subduction zones, in which vast interplate strain is generated by the subduction of an oceanic plate under another plate, are the areas where the world's largest earthquakes occur, often resulting in great human and economic losses (e.g. Chile 1960, 2010; Sumatra 2004; Japan 2011). The M_W 8.8 2010 Chile megathrust earthquake, the sixth largest seismic event ever recorded, ruptured nearly 500 km along the interface between the down-going Nazca plate and the overriding South American plate. The earthquake was responsible for large economic costs and, in conjunction with the subsequent tsunami, killed more than 525 people (http://www.interior.gob.cl/filesapp/listado_fallecidos_desaparecidos_27Feb.pdf).

The segment that ruptured in 2010 was previously identified as a mature seismic gap (Campos *et al.*, 2002; Ruegg *et al.*, 2009) and coincides with the region affected by a major earthquake (M~8.5) described by Darwin in 1835 (Lommitz, 2004). Since the 1835 event, major megathrust earthquakes have occurred within the area of the 2010 event in 1906, 1928, 1960 and 1985 (Campos *et al.*, 2002; Bilek, 2010), only partially rupturing the Darwin seismic gap (Figure 5.1).

Several co-seismic slip models for the 2010 rupture have been published to date (e.g. Lorito *et al.*, 2011; Vigny *et al.*, 2010; Moreno *et al.*, 2012; and references therein), showing as a first order feature two high-slip patches located roughly to the north and south of the epicentre. Published aftershock distributions (e.g. Lange *et al.*, 2012; Rietbrock *et al.*, 2012) show seismicity concentrated between 10-35 km depth on the interface and then a second group at 40-45 km depth. Increased outer-rise seismicity is

observed at the northern part of the rupture, whilst crustal events occur in the Pichilemu area (Ryder *et al.*, 2012).

Previous studies on aftershock distributions, mainly of strike-slip faults (e.g. Mendoza and Hartzell, 1988), show that most of the aftershocks occur outside or near the edges of the areas of large slip. For a limited data set of subduction zone earthquakes, Das and Henry (2003) did not find a correlation between regions of high or low slip and aftershock occurrence, but argued that regions of high slip have fewer and smaller aftershocks. For the 2010 Maule earthquake, Rietbrock *et al.* (2012) analysed three months of aftershocks and concluded that aftershocks are located preferentially in regions of rapid transition from high to low slip. In a recent study based on the analysis of aftershock focal mechanisms of the 2011 Tohoku-Oki, Japan, earthquake, Asano *et al.* (2011) found that interplate aftershocks with thrust faulting do not occur within the area of large co-seismic slip, but instead were localized in the surrounding regions.

Here we present aftershock focal mechanisms (FMs) and corresponding centroid depths based on full waveform regional moment tensor (RMT) inversions of the largest aftershocks recorded on the International Maule Aftershock Dataset (IMAD) network. We also relocated focal solutions from the global centroid-moment-tensor (GCMT) project by using mislocation vectors derived from local observations. In this way, we assemble a catalogue of FMs covering the whole time period since the mainshock (2010 February 27) up to March 2012. Utilizing this comprehensive catalogue we produce a model of seismically-released afterslip (SRA) and discuss its relationship with published co-seismic and post-seismic slip models. Finally, we investigate the relationship of co-seismic slip and number of aftershocks using a quantitative approach.

We aim to quantitatively describe the source characteristics and distribution of the 2010 aftershock sequence relative to the distribution of coseismic and postseismic slip, by employing a methodology that can be used to study any other subduction earthquake or, in general, any earthquake for which its sequence of aftershocks and a slip model are available.

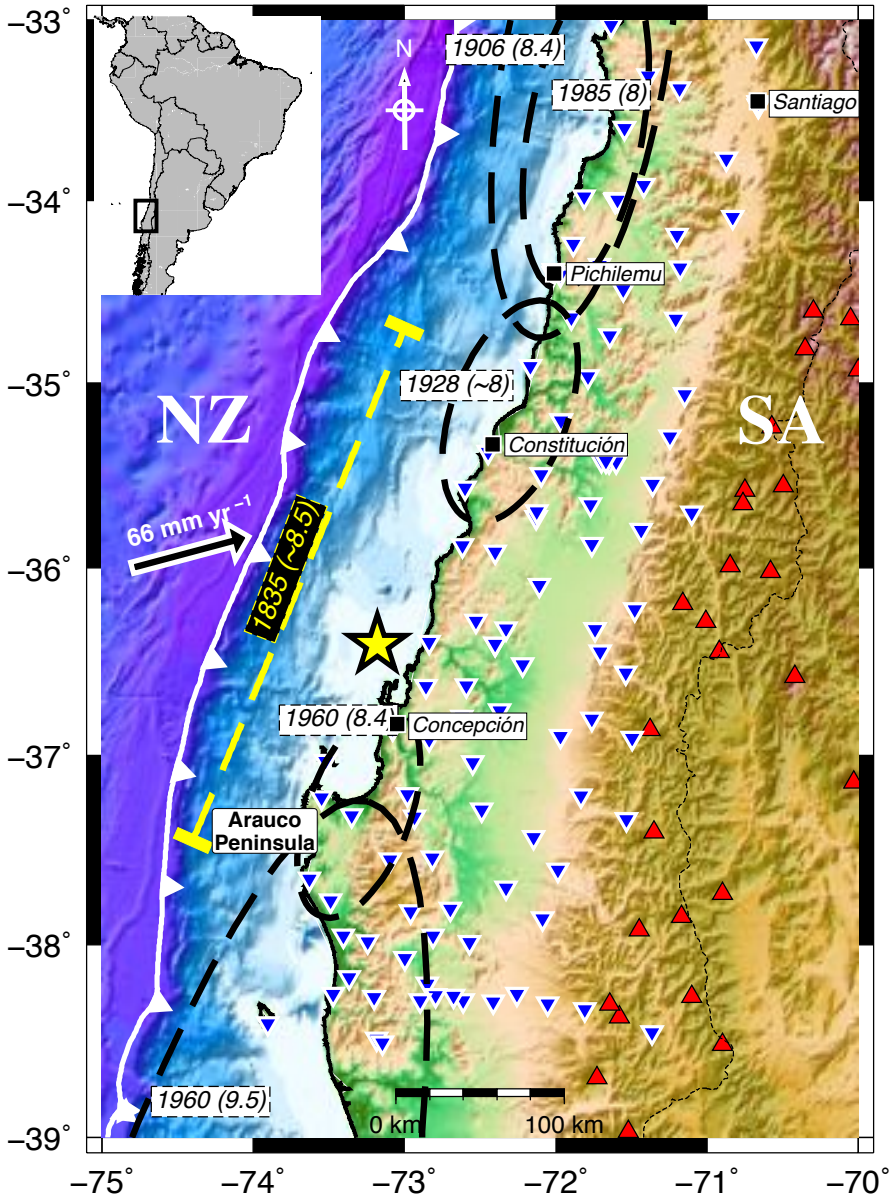

Figure 5.1. Location map. Yellow star indicates main shock (Vigny *et al.*, 2011); inverted blue triangles show IMAD network and red triangles active volcanoes. Dashed black lines show approximate rupture areas of past megathrust earthquakes, including rupture extent of 1835 earthquake (dashed yellow line) (Campos *et al.*, 2002; Bilek, 2010). NZ=Nazca Plate; SA=South American Plate. Topography/bathymetry GTOPO30.

5.2. Data and Methods

We obtained RMT solutions for 125 earthquakes, from full waveform inversions, between March 18th and December 1st 2010. We employed data from the International

Maule Aftershock Dataset (http://www.iris.edu/mda/_IMAD; Figure 5.1) and used the software package ISOLA (Sokos and Zahradnik, 2008) to derive the RMT solutions. For each event we used its epicentral coordinates from an expanded version of the catalogue of aftershocks published by Rietbrock *et al.* (2012), following their procedure. These authors used gap and number of observations criteria (≤270º gap and more than 12 P-phase observations), and a 2-D velocity model (Haberland *et al.*, 2009) to build their catalogue of aftershocks. We then selected the bigger events (M>4.5) with a minimum of 20 P-phase observations (usually more than 60 P-wave observations) to invert for the RMT solutions.

Additionally, we relocated 145 events from the GCMT catalogue covering the aftershock sequence until March 2012. Earthquake relocations were calculated by averaging the differences in epicentral location for those events included in both the GCMT and our local catalogue (Sup. Fig. D.1). The averaged mislocation vector (16 km in SE direction) is then used to relocate the GCMT events that occurred in absence of the local network.

In order to calculate the amount of slip for each aftershock, we used the scaling relationships for subduction zones proposed by Blaser *et al.* (2010). We obtained the associated slip by solving the equation for seismic moment (Aki, 1966), considering an average shear modulus μ=39 GPa, which corresponds to an average S-wave velocity of 3.58 km/s (Haberland *et al.*, 2009) and a density of 3050 kg/m^3 (Tassara *et al.*, 2006) at megathrust seismogenic depths. Further details on methods and data processing are discussed in the Supplementary Information in Appendix D.

5.3. Results and Discussion

Thrust aftershocks occur mostly within ±5 km depth of the subduction interface, except for those located north of the northern co-seismic slip patch, which are located at greater depth (Figures 5.2 and 5.3a). Notably, a high concentration of thrust events occurs north and south of the 8 m co-seismic slip contour of the northern co-seismic slip patch. P-axes of thrust interface events show a homogeneous distribution of azimuths

concentrated in an ~E-W direction, orthogonal to the trench, with nearly all of them contained between 260º and 290º (Sup. Fig. D.3).

The absence of major thrust aftershocks near the trench in front of the northern patch of co-seismic slip might indicate complete strain release during the mainshock's rupture, reaching shallow depths up-dip the megathrust as suggested by Vigny *et al.* (2011).

Normal fault events tend to occur at shallower depths: (i) events in the Pichilemu area are located close to the coastline in the overriding plate at depths less than 20 km; (ii) increase of outer-rise seismicity occurs near the trench in front of the main co-seismic slip patch (34º-35ºS) and in front of the Arauco peninsula (~37.6 S) at shallow depths.

Crustal normal-fault events in the Pichilemu area have been attributed to faulting induced by the Maule mainshock (Farías *et al.*, 2011; Ryder *et al.*, 2012), in a similar setting to the crustal normal-fault seismicity described for the 2011 Tohoku-Oki earthquake by Kato *et al.* (2011). Regarding the outer-rise normal fault events, it is widely accepted that outer-rise tensional events generally follow interplate ruptures in subduction zones, as demonstrated by Lay *et al.* (1989). Slab bending and slab pull forces transmitted to the outer rise region due to the strain released by the mainshock can explain the increase in outer-rise seismicity observed in front of the northern and southern main slip patches.

Strike-slip events are sparsely distributed in the overriding plate at shallow depths close to the coastline in the Pichilemu area and within the volcanic arc. Noteworthy is the strike-slip event M_W5.1 that occurred on 15th of August 2010, located at ~37ºS/71ºW, which corresponds to a NW left-lateral strike-slip fault associated with activity on the Nevados de Chillán volcano (Cembrano and Lara, 2009).

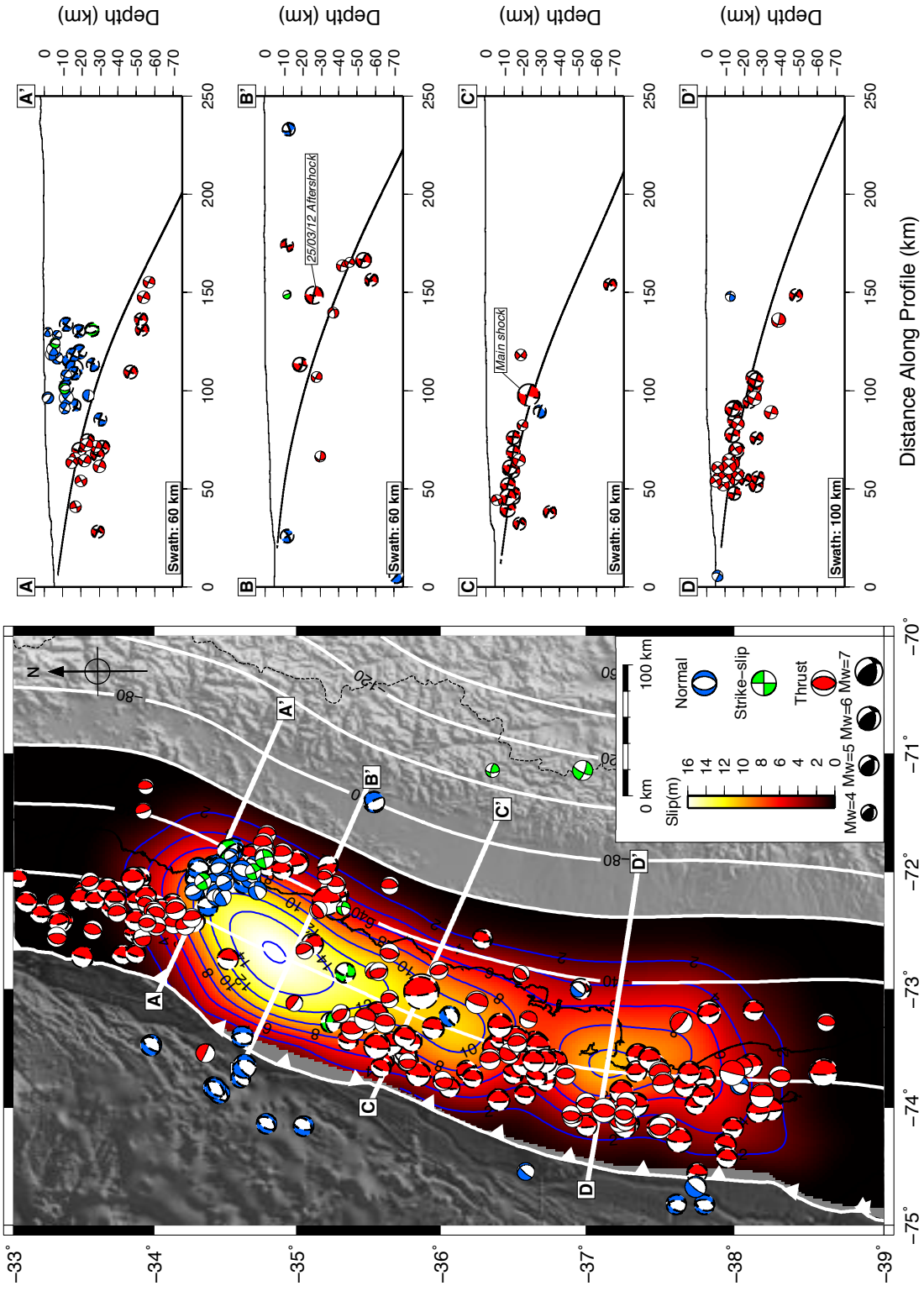
Depth (km)
Distance Along Profile (km)
Swath: 60 km
Swath: 100 km
25/03/12 Aftershock
Main shock
Normal
Strike−slip
Thrust
Slip(m)
100 km
0 km
Mw=4 Mw=5 Mw=6 Mw=7
A
A'
B
B'
C
C'
D
D'
N

Figure 5.2 (previous page)**.** Distribution of FMs. **Left**, FMs are shown as lower half-sphere projection; colour indicates fault type. FMs with solid outline are from this work; with dashed outline are relocated GCMT solutions. White contour lines show depth of the top of the slab (Hayes *et al.*, 2012). Co-seismic slip model (Moreno *et al.*, 2012) is shown with blue contour lines every 2 m. White lines and uppercase letters indicate profiles shown in the right panel. **Right**, FMs are shown as far half-sphere projection on a vertical section. Solid thick black line indicates the top of the slab (Hayes *et al.*, 2012); top black line shows topography/bathymetry.

Figure 5.3 (next page)**.** Interface thrust events and SRA model. Interface events were defined as those located at depths within 13 km (GCMT) and 6 km (this work) from the top of the slab respectively. Other features same as Figure 2. **a)** Coseismic slip model (Moreno *et al.*, 2012) and interface thrust events coloured by vertical distance from the top of the slab. Inset: histogram of frequency of thrust events according to their nodal planes' dip angles; dashed blue line indicates dip angle of mainshock (megathrust plane). **b)** Cumulative SRA. Inset: exponential relationship between calculated M_W and slip. **c)** Cumulative SRA model for the 12-day period following the mainshock. Red contour lines show the 12-day postseismic afterslip model proposed by Vigny *et al.* (2011) every 0.1 m. Inset: same as 5.3b, including 1σ of slip from scaling relationships (blue and red dots).

Assuming that aftershocks occur in areas of rapid transition between high and low slip, surrounding high-slip regions of the mainshock (Rietbrock *et al.*, 2012), we compared our distribution of moment tensors with published co-seismic slip models. Our distribution of events correlates well with the key features of published slip models (Sup. Fig. D.4), although we favour the model proposed by Moreno *et al.* (2012) since we find an absence of aftershock thrust faulting within the two coseismic slip maxima (in particular in the northern patch, which presents the largest slip values) and aftershocks occurrence surrounding and delineating the zones of high co-seismic slip (Figures 5.2 and 5.3a). A similar distribution pattern has been reported for the aftershocks of the M_W=9.0 2011 Tohoku-Oki earthquake by Asano *et al.* (2011), and therefore might be characteristic of large megathrust earthquakes.

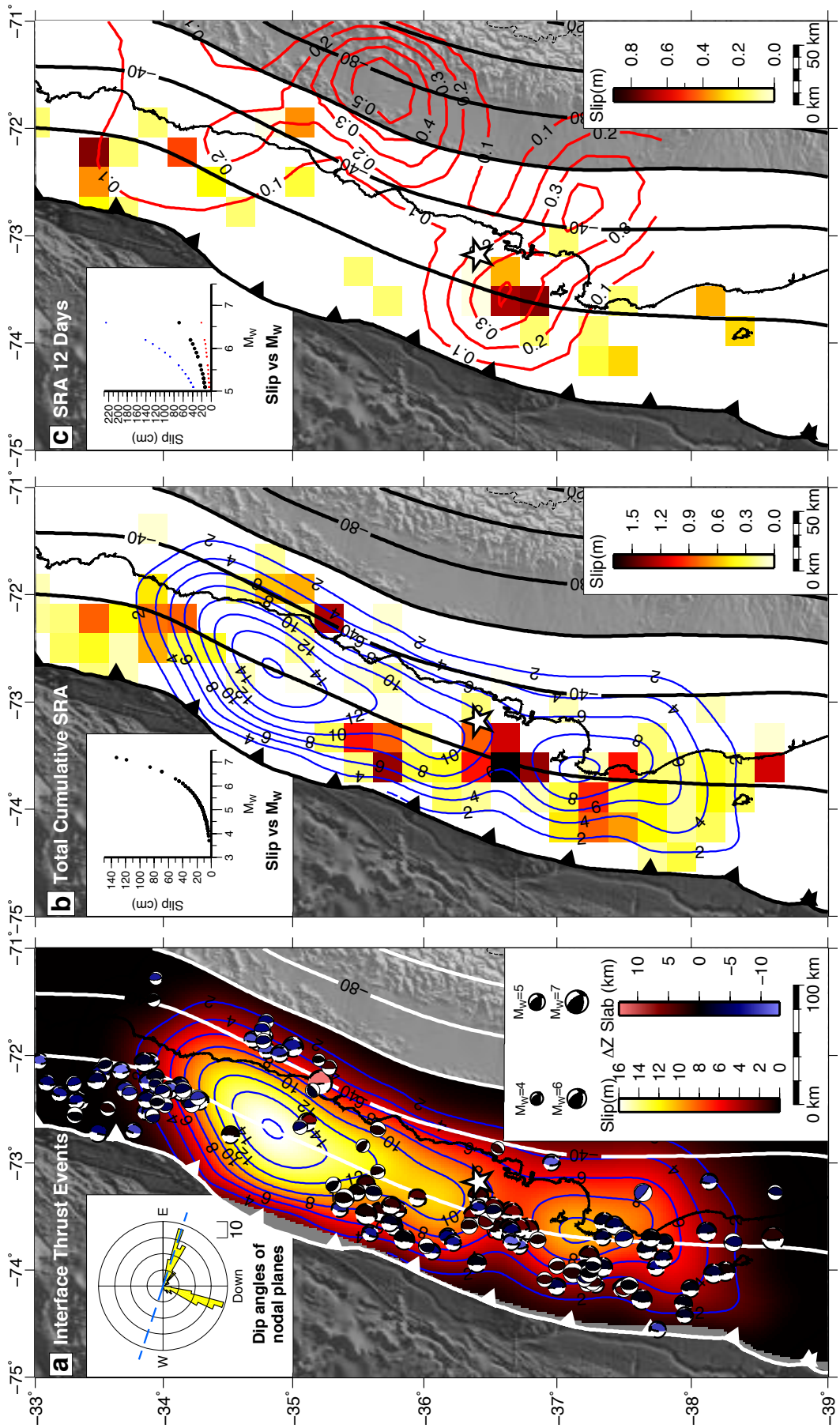
a Interface Thrust Events
Dip angles of nodal planes
Down
10
E
W
Slip(m)
ΔZ Slab (km)
0 km
100 km
b Total Cumulative SRA
Slip vs Mw
Slip (cm)
Mw
Slip(m)
0 km
50 km
c SRA 12 Days
Slip vs Mw
Slip (cm)
Mw
Slip(m)
0 km
50 km
−33°
−34°
−35°
−36°
−37°
−38°
−39°
−71°
−72°
−73°
−74°
−75°

Although aftershock studies of the 2010 Chile earthquake (e.g. Lange *et al.*, 2012; Rietbrock *et al.*, 2012) do show aftershock seismicity in the areas of high co-seismic slip, this corresponds mostly to small (M<4) events, while there is a striking absence of major seismicity. All this indicates that most of the interplate stress was released during the mainshock, and therefore no major slip can occur postseismically on the main patches of co-seismic slip. On the other hand, stress introduced on dislocation tips in areas with high slip contrast, surrounding high-slip patches, will promote thrust faulting on the megathrust, as observed in our data set (Figure 5.3a).

Figure 5.3b shows the SRA model based on the cumulative seismic moment of thrust aftershocks located on the interface. The bulk of the afterslip (up to 1.7 m) is released offshore, between the two main patches of co-seismic slip at ~36.8ºS, followed by the afterslip due to the two largest aftershocks to date at 38.7ºS (M_W7.1) and 35.3ºS (M_W7.2), which occurred on the 2nd of January 2011 and 25th of March 2012, respectively. No afterslip is observed in the area of the two main co-seismic slip patches. Onshore, smaller afterslip is observed mainly in the Arauco peninsula and south of the Pichilemu area at ~35ºS.

To our knowledge, the only afterslip model published to date is that of Vigny *et al.* (2011) based on GPS measurements for 12 days of postseismic deformation. In order to compare this afterslip with ours, we calculated the SRA for the first 12 days of postseismic activity (Figure 5.3c). Although the model by Vigny *et al.* (2011) shows two prominent patches of afterslip occurring onshore at ~35.7 and ~37.2ºS, we do not observe such features, which indicates that the geodetically-measured afterslip might occur aseismically along deeper parts of the subduction interface. Offshore, both models show general agreement in the distribution of afterslip, in particular in the area between the two main patches of co-seismic slip (36º-37ºS). However, for the significant afterslip patch at ~73.7ºW/36.8ºS, the SRA of 0.7 m is larger than the 0.4 m of afterslip inferred from geodetic observations. This discrepancy might be caused by uncertainties in the scaling relationships (Figure 5.3c inset) or the applied smoothing in the geodetic slip inversion.

It is important to highlight the release of most of the seismic afterslip by several aftershocks with M_W<6.8 (cumulative equivalent M_W = 6.92) in between the two main patches of co-seismic slip (~36.8ºS; Figures 5.3a and 5.3b), as opposed to the possible occurrence of an event M_W 7.5-8.0 in this area suggested by Lorito *et al.* (2011). The afterslip in this zone is a persistent feature observed throughout the whole first year of postseismic activity.

In order to quantify the correlation between the spatial patterns of aftershock locations and the distribution of co-seismic slip, we normalized the seismicity occurring in a given range of slip (e.g. 4-5m) relative to the areal density of aftershocks for this slip range using a quantitative approach (Hauksson, 2011). Thus, we define the ratio $R_{ds}=(N_{ds}/N_t)/(A_{ds}/A_t)$, where N_{ds} is the number of aftershocks occurring within a given range ds of slip, N_t is the total number of aftershocks, A_{ds} is the corresponding area covered by the range ds of slip, and A_t is the total area covered by the co-seismic slip (i.e. the area covered by the 0 m slip contour line). If $R_{ds} > 1$, the seismicity rate is considered to be greater than average rate, while if $R_{ds} < 1$, the seismicity rate is smaller than the average rate. The utilization of an areal normalization takes into account the inhomogeneous areal distribution of co-seismic slip models, as opposed to simply quantifying the cumulative distribution of aftershocks relative to co-seismic slip (e.g. Woessner *et al.*, 2006).

Figure 5.4a shows the obtained R_{ds} values for aftershocks located at interface depths (within 10 and 15 km above and below the top of the slab respectively) from the full catalogue of aftershocks published by Rietbrock *et al.* (2012) as a fraction S of maximum slip. We observe that most of the aftershocks occur in areas with slip $S > 0.3$. A high rate of aftershocks in the fractional slip range $0.4 < S < 0.75$ is observed and another peak is seen for areas with high slip ($S > 0.85$). On the other hand, the normalized distribution of large interface thrust aftershocks (Figure 5.4b) shows that nearly 80% of these events occur in areas of moderate slip $0.15 < S < 0.7$ (i.e. slip between 2 and 11 m) rather than in areas of high and low slip.

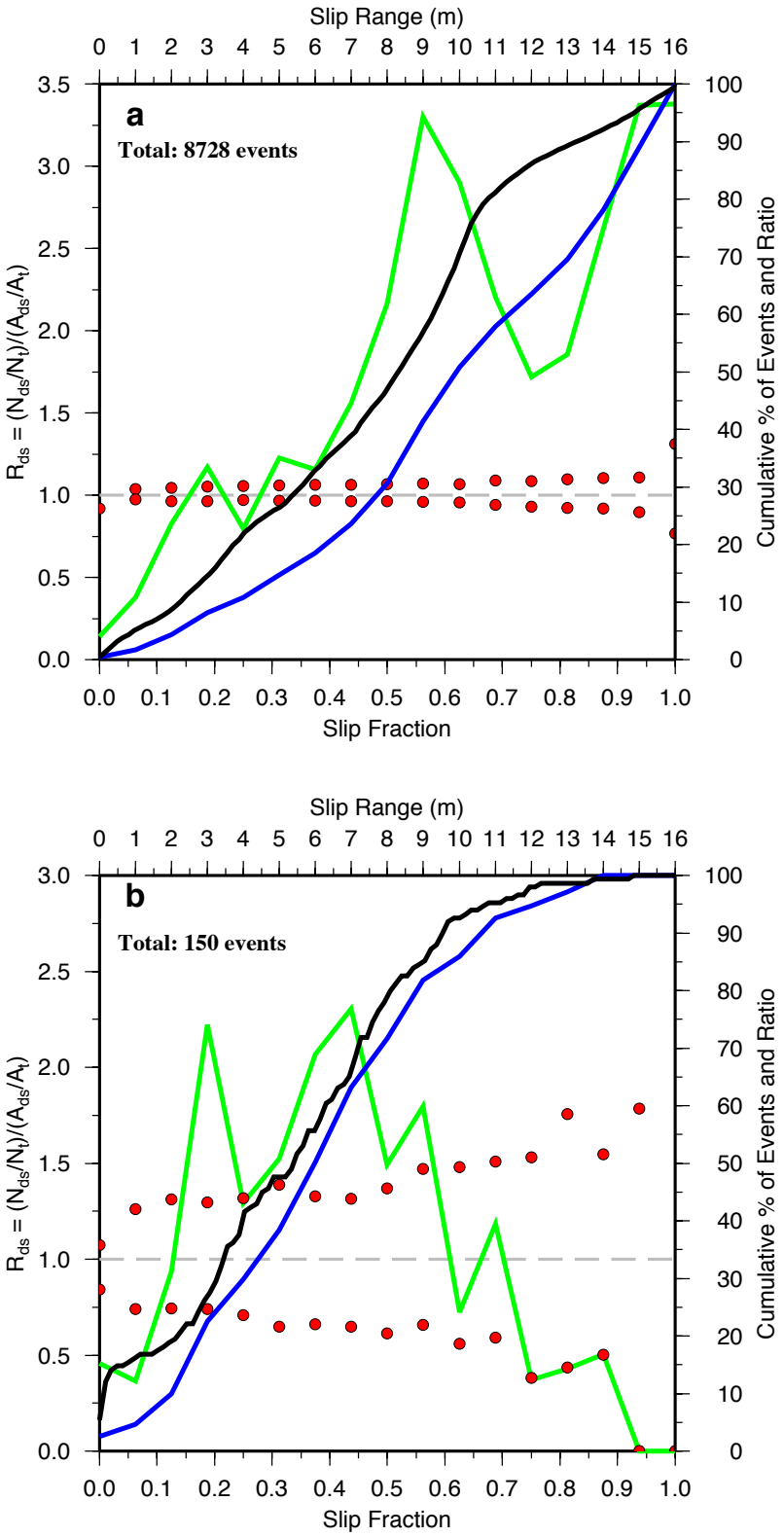

Figure 5.4. Histograms of aftershock distribution for **a)** interface events from expanded catalogue published by Rietbrock *et al.* (2012), **b)** largest interface thrust events (as shown in Figure 5.3a). Green line shows R_{ds} values (left axis), blue line corresponds to the cumulative percentage of R_{ds} values (right axis), black line is the cumulative percentage of events (right axis). Red dots indicate one standard deviation values of R_{ds} for randomly distributed events test (see Supplementary Information in Appendix D).

Our results show that the largest (M_W>4) thrust aftershocks occur along the megathrust plane in areas of intermediate fractional slip (~0.2-0.7), around patches of largest slip, accommodating stress increases resulting from the earthquake rupture process. Taking into account the whole magnitude range of aftershocks, a slightly different picture emerges. Smaller magnitude aftershocks (M<4) occur predominantly in areas of larger co-seismic slip, and are more loosely distributed laterally and in depth. Consequently, they might be associated with processes in the damage zone surrounding the megathrust plate interface, and could be triggered by coseismically released fluids (e.g. Nippress and Rietbrock, 2007).

5.4. Conclusion

We determined RMT solutions from regional seismograms based on a full waveform inversion technique. Additionally, we re-located GCMT solutions leading to a combined catalogue of 270 aftershock events. Thrust faulting dominates the postseismic seismicity, with also increased normal faulting in the outer-rise and Pichilemu area. SRA values obtained from scaling relations indicate up to 1.7 m of afterslip at ~36.8º S in the area between the two main co-seismic slip patches. Most of the SRA is observed offshore, with only marginal values observed inland.

The distribution of the largest thrust aftershock events suggests that they occur at intermediate ranges of fractional co-seismic slip between 0.15-0.7. Small aftershocks are located in areas of high co-seismic slip (> 0.85 S_{max}) and are likely linked to processes in the damage zone surrounding the megathrust plane (e.g. fluids release and re-activation of pre-existent secondary structures).

The present catalogue of moment tensor solutions, derived SRA model, and histograms of aftershock distribution can be used as a reference for future afterslip studies, providing constraints on the spatio-temporal aftershock distribution of the 2010 Chile megathrust earthquake. Our comparison of SRA and published geodetic afterslip models provides insight into the mechanisms underlying the occurrence of afterslip recorded by geodetic/seismic networks. Moreover, our study offers a quantitative

measure of the distribution of aftershocks relative to coseismic slip that can be applied to other large subduction earthquakes.

Acknowledgments

HA thanks J. Zahradnik and E. Sokos for their support in the usage of ISOLA; and CONICYT, Chile, through its program of scholarships 'Beca Presidente de la República'. We received funding from NERC (NE/I005420/1). Seismic instruments were provided by CNRS-INSU, IRIS/PASSCAL, GIPP(GFZ), GEF/Seis-UK (Loan 922). Figures were done with GMT software (Wessel and Smith, 1998).

CHAPTER 6

CONCLUSIONS

In this thesis I have studied two important segments of the Chilean subduction margin: (i) the southernmost segment in front of the Chile Triple Junction (CTJ), and (ii) the segment recently ruptured by the Mw8.8 Maule earthquake between ~34º-38ºS. Through the characterisation of recent aftershock sequences occurred in these two segments, I provide new insights into the seismotectonic processes that take place currently in this subduction zone.

I have participated in the collection of data through the organisation and execution of fieldwork campaigns in both the southern and northern regions reviewed here. Besides, during the development of this research, I have used several seismic processing techniques, namely, linearized and non-linear earthquake location, 1-D travel-time tomography, computation of focal mechanisms from first motion polarities, full waveform inversion for the calculation of regional moment tensor solutions, etc.

The following conclusions can be extracted from the three studies performed during this thesis:

Regional Seismicity of the Aysén Region

For the southern area, the Aysén Region, we analysed seismic data collected by a temporal local network kept continuously recording during 2004 and 2005. We performed non-linear earthquake locations and magnitude estimations for this dataset. A total of 519 events were detected during the experiment. A high quality subset (based on location uncertainty) of 276 events was then used for further analysis. The hypocentral locations show shallow intra-plate seismicity occurring in the overriding South American plate, at depths down to 30 km, with the majority located within the first 10 km of crust, and magnitudes ranging between 0.5 to 3.4 M_l.

The events seem to occur mainly in clusters, but also some disperse activity can be spatially related to the LOFS. Around a third of the seismicity is associated with the Hudson volcano, with depths varying between the surface down to 10 km depth, and magnitudes of up to 2.9 M_l. Other minor sources of seismicity in the region are mining activity and glacial calving, particularly in the summer months.

Although determination of focal mechanisms for this dataset was not possible, the locations suggest that some of the crustal seismicity, particularly at the intersection of the two main branches of the LOFS at ~46.2ºS, is spatially related to the trace of this fault system. This may indicate that the LOFS is currently active at its southern end. Magnitudes associated with LOFS events during the period of this study (2004-2005) are ≤3.4, but the occurrence of events with magnitudes up to 6.2 in 2007, and historical records of an event M~7 in 1927, indicate that this fault represents an important source of hazard for both industry and population in the area.

2007 Aysén Seismic Sequence

An unprecedented sequence of seismic events took place in early 2007 in the Aysén Region, specifically in the Aysén Fjord, with a peak of activity given by the occurrence of an event Mw 6.2 that produced a local landslide-induced tsunami, killing 10 people. Shortly after this earthquake, we deployed a local seismic network of 15 stations in

order to capture the aftershock activity in this area. 1-D travel-time tomography, nonlinear earthquake locations and inversion of focal mechanisms from first motion polarities was performed on the acquired dataset.

The calculated local velocity model presents and average Vp/Vs ratio of 1.76 for the area, with low S-wave velocities for the upper 3 km probably due to rock fracturing and the presence of hydrothermal fluids. P-wave velocities for the upper 5 km show values around 5 km/s, in agreement with expected values from the geology present in this area (granitic rocks). The seismicity and focal mechanisms observed during the 2007 sequence suggest a tectonic origin for the series of events, in direct relation with a reactivation of the LOFS in this area. The location of aftershocks to the east of the trace of the LOFS, and diversity of obtained focal mechanisms, suggest the presence of a complex structural setting associated with the major strike-slip structure. Furthermore, obtained seismogenic depths indicate a maximum of 15 km for the Aysén Fjord zone.

2010 Chile Earthquake Area

The Mw 8.8 earthquake occurred in south-central Chile in 2010 ruptured circa 500 km along the megathrust interface, filling a seismic gap present since 1835. As part of an international effort for the recording and analysis of the aftershocks of this major event, we determined regional moment tensor solutions from full waveform inversions for the largest aftershocks. Additionally, we addressed quantitatively the distribution of postseismic activity in relation to geodetic coseismic and postseismic models. Our method of quantitative analysis of distribution of aftershocks can be easily implemented for the analysis of other earthquakes, while our results provide a reference study for comparison with other megathrust events or any earthquake in general for which a coseismic slip model is known.

We found that most of the aftershocks correspond to thrust events occurring on the interface, with homogeneous distribution of P-axes' azimuths perpendicular to the trench, and similar faulting geometry to the mainshock. Normal faulting events are

observed in the overriding plate in the Pichilemu area, and increased normal faulting activity is present in the outer-rise area.

The largest thrust events (Mw≥4) occur in areas of moderate coseismic slip, 0.15-0.7 S_{max}, with a high concentration of events between the main patches of coseismic slip, at ~36.8ºS, where the highest value (1.7 m) of seismically released afterslip is observed. On the contrary, smaller events (Mw<4) tend to occur preferably in areas of large coseismic slip, S > 0.85 S_{max}, likely related to processes occurring in the damage zone surrounding the megathrust interface.

Final Remarks

Although belonging to the same subduction margin, the seismotectonics and earthquake patterns of the two areas researched here show different underlying deformation mechanisms. For the northern area, locus of the 2010 Mw 8.8 Chile earthquake, inter-plate thrust seismicity is dominant both in terms of quantity of events and moment release. On the other hand, the southern area close to the subduction of the CTJ presents only shallow intra-plate crustal seismicity, mainly occurring in the arc, where Quaternary volcanism and the LOFS are present.

It seems then, that there is a gradual change in terms of prevailing seismotectonics from the area affected by the 2010 megathrust earthquake southwards to the area proximal to the CTJ. This transition goes from the northern area, where the interface seismicity absorbs the obliquity of the plate convergence and large megathrust events dominate the released tectonic strain, towards the southernmost portion of the subduction margin, where the seismicity becomes gradually shallower, no large interface events occur, and the obliquity of the convergence is absorbed by the strike-slip LOFS.

Outlook

This thesis offers new insight into the seismotectonic processes governing the two studied segments. Nonetheless, further studies are still necessary to satisfactorily comprehend and quantify these processes.

For the southern region, in front of the subduction of the CTJ, determination of focal mechanisms for the regional background seismicity is necessary, but as shown in this work, this is a task of difficult implementation given the small magnitudes recorded. The continuous monitoring of this region is indispensable in order to address the evolution of seismicity patterns in time, specially given that historical records of this region date back only from the 20th century on.

Although the occurrence of the 2007 seismic sequence provided a unique opportunity to study this region that usually lacks of seismicity M>4, further geological and geophysical studies are still required. In particular, the Aysén Fjord area proved to be a complex geo-tectonic environment, where a large strike-slip fault system interacting with the volcanic arc, presence of hydrothermal fluids, and glacial relief modelling, have configured an spectacular landscape not exempt of geologic hazards for the nearby populated areas.

Much more studied is the northern region researched in this study, which in 2010 suffered the occurrence of the sixth largest earthquake instrumentally recorded. However, this event and its sequence of aftershocks came to produce new questions regarding the controlling factors in the distribution of coseismic slip (asperities/barriers), the evolution of the aftershock sequence, stress transfer during the mainshock, and in particular, the agreement (or disagreement) of geodetically- and seismically-obtained slip models. These issues should be addressed in future works in the area, and concern not only this earthquake, but in general all large megathrust earthquakes occurring in subduction zones as in the south-central Chilean margin.

BIBLIOGRAPHY

Agurto, H., Rietbrock, A., Barrientos, S., Bataille, K. and Legrand, D. (2012a), Seismotectonic structure of the Aysén Region, Southern Chile, inferred from the 2007 Mw= 6.2 Aysén earthquake sequence. *Geophys. J. Int.*, 190, 116–130.doi: 10.1111/j.1365-246X.2012.05507.x.

Agurto, H., Rietbrock, A., Ryder, I. and Miller, M. (2012b), Seismic Afterslip Characterization of the 2010 Mw 8.8 Chile earthquake based on moment tensor inversions, *Geophys. Res. Lett.,* 39, L20303, doi:10.1029/2012GL053434.

Aki, K. (1966), 4. Generation and propagation of G waves from the Niigata earthquake of June 14, 1964. Part 2. Estimation of earthquake moment, released energy and stress strain drop from G wave spectrum, *B. Earthq. Res. I Tokyo* , 44, 73–88.

Aki, K., Christoffersson, A., and Husebye, E.S. (1977), Determination of the three-dimensional seismic structure of the lithosphere, *J. Geophys. Res.*, 82, 277-296.

Aki, K. and Richards, P.G. (2002), Quantitative Seismology - Theory and Methods. Second edition, *University Science Books*, Sausalito, California.

Angermann, D., Klotz, J. and Reigber, C. (1999), Space-geodetic estimation of the Nazca-South America Euler vector, *Earth Planet. Sci. Lett.*, 171(3), 329–334.

Asano, Y., Saito, T., Ito, Y., Shiomi ,K., Hirose, H., Matsumoto, T., Aoi, S., Hori, S. and Sekiguchi, S. (2011), Spatial distribution and focal mechanisms of aftershocks of the 2011 off the pacific coast of Tohoku earthquake, *Earth Planets and Space*, 63(7), 669, doi:10.5047/eps.2011.06.016.

Bakun, W.H. and Joyner, W.B. (1984), The ML scale in central California, *Bull. Seism. Soc. Am.*, 75(5), 1827–1843.

Bangs, N.L. and Cande, S.C. (1997), Episodic development of a convergent margin inferred from structures and processes along the southern Chile margin, *Tectonics*, 16, 489–503.

Barazangi, M. and Isacks, B. (1976), Spatial distribution of earthquakes and subduction of the Nazca plate beneath South America, *Geology*, 4(11), 686–692.

Barrientos, S.E., and Ward, S.N. (1990), The 1960 Chile earthquake: Inversion for slip distribution from surface deformation, *Geophys. J. Int*., 103, 589–598, doi:10.1111/j.1365-246X.1990.tb05673.x.

Barrientos, S., Bataille, K., Aranda, C., Legrand, D., Báez, J.C., Agurto, H., Pavez, A., Genrich, J., Vigny, C. and Bondoux, F. (2007), Complex sequence of earthquakes in Fjordland, Southern Chile, *in Proceedings Geosur 2007*, 21, Santiago.

Barrier, E., Huchon, P. and Aurelio, M. (1991), Philippine Fault: a key for Philippine kinematics, *Geology*, 19, 32–35.

Beck, M.E. (1988), Analysis of Late Jurassic-Recent paleomagnetic data from active plate margins of South America, *J. S. Am. Earth Sci*., 1, 39–52.

Beck, S.L. and Ruff, L.J. (1989), Great earthquakes and subduction along the Peru trench. *Phys. Earth Planet. Inter.*, 57, 199-224.

Beck, S., Barrientos, S., Kausel, E. and Reyes, M. (1998), Source characteristics of historic earthquakes along the central Chile subduction zone, *J. S. Am. Earth Sci*., 11(2), 115–129.

Behrmann, J., Lewis, S. and Cande, S. (1994), Tectonics and geology of spreading ridge subduction at the Chile triple junction: a synthesis of results from leg 141 of the ocean drilling program, *Geol. Rundsch*, 83(4), 832–852.

Besana, G. and Ando, M. (2005), The central Philippine fault zone: Location of great earthquakes, slow events, and creep activity, *Earth Planets, and Space*, 57(10), 987–994.

Bilek, S. (2010), Invited review paper: Seismicity along the South American subduction zone: Review of large earthquakes, tsunamis, and subduction zone complexity, *Tectonophysics,* 495, 2–14, doi: 10.1016/j.tecto.2009.02.037.

Blaser, L., Kruger, F., Ohrnberger, M. and Scherbaum, F. (2010), Scaling relations of earthquake source parameter estimates with special focus on subduction environment, *Bull. Seismol. Soc. Am.*, 100(6), 2914–2926, doi:10.1785/0120100111.

Cahill, T. and Isacks, B. (1992), Seismicity and shape of the subducted nazca plate, *J. Geophys. Res.*, 97(B12), 17503–17529.

Campos, J., Hatzfeld, D., Madariaga, R., Lopez, G., Kausel, E., Zollo, A., Iannacone, G., Fromm, R., Barrientos, S. and Lyon-Caen, H. (2002), A seismological study of the 1835 seismic gap in south-central Chile, *Phys. Earth Planet. In.*, 132(1), 177–195, doi:10.1016/S0031-9201(02)00051-1.

Cande, S. and Leslie, R. (1986), Late Cenozoic tectonics of the southern Chile trench, *J. geophys. Res.*, 91, 471–496.

Cande, S., Leslie, R., Parra, J. and Hobart, M. (1987), Interaction between the Chile Ridge and Chile Trench: geophysical and geothermal evidence, *J. geophys. Res.*, 92, 495–520.

Cembrano, J. and Moreno, H. (1994), Geometría y naturaleza contrastante del volcanismo cuaternario entre los 38ºS y 46ºS: Dominios compresionales y tensionales en un régimen transcurrente, *in Congreso Geologico Chileno*, 7, 17–21, Concepción.

Cembrano, J., Hervé, F. and Lavenu, A. (1996), The Liquine–Ofqui fault zone: a long-lived intra-arc fault system in southern Chile, *Tectonophysics*, 259, 55–66.

Cembrano, J., Schermer, E., Lavenu, A. and Sanhueza, A. (2000), Contrasting nature of deformation along an intra-arc shear zone, The Liquiñe-Ofqui Fault System, Southern Chilean Andes, *Tectonophysics*, 319, 129–149.

Cembrano, J., Lavenu, A., Reynolds, P., Arancibia, G., López, G. and Sanhueza, A. (2002), Late Cenozoic transpressional ductile deformation north of the Nazca-South America-Antarctica triple junction, *Tectonophysics*, 354, 289–314.

Cembrano, J., Gonzalez, G., Arancibia, G., Ahumada, I., Olivares, V. and Herrera, V. (2005), Fault zone development and strain partitioning in an extensional strike-slip duplex: a case study from the Mesozoic Atacama fault system, Northern Chile, *Tectonophysics*, 400(1–4), 105–125, doi:10.1016/j.tecto.2005.02.012.

Cembrano, J., Lara, L., Lavenu, A. and Hervé, F. (2007), Long-term and short- term kinematic history of the Liquiñe Ofqui fault zone, southern Chile: a review and implications for geologic hazard assessment, *in Proceedings Geological Society of América Annual Meeting*, 39(6), 231, Denver.

Cembrano, J. and Lara, L. (2009), The link between volcanism and tectonics in the southern volcanic zone of the Chilean Andes: A review, *Tectonophysics*, 471(1-2), 96–113, doi:10.1016/j.tecto.2009.02.038.

Chase, C. (1978), Plate kinematics: the Americas, East Africa, and the rest of the world, *Earth Planet. Sci. Lett.*, 37, 355–368.

Cloos, M. (1992), Thrust-type subduction zone earthquakes and seamount asperities: a physical model for seismic rupture. *Geology*, 20, 601–604.

Comte, D., Gallego, A., Russo, R., Murdie, R. and VanDecar, J. (2007), The Aysen (Southern Chile) 2007 seismic swarm: volcanic or tectonic origin?, *EOS Trans. Am. Geophys. Un.,* 88(23), Jt Assem. Suppl., Abstract S43C-04.

Crosson, R.S. (1976), Crustal structure modeling of earthquake data, 1, simultaneous least squares estimations of hypocenter and velocity parameters, *J. geophys. Res.*, 81 (17), 3036–3046.

Das, S. and Henry, C. (2003), Spatial relation between main earthquake slip and its aftershock distribution, *Rev. Geophys*., 41(3), 1013-1036, doi:10.1029/2002RG000119.

DeMets, C., Gordon, R.G., Argus, D.F. and Stein, S. (1994), Effect of recent revisions to the geomagnetic reversal time scale on estimates of current plate motions, *Geophys. Res. Lett.*, *21*, 2191-2194.

Dewey, J. and Lamb, S. (1992), Active tectonics of the Andes, *Tectonophysics*, 205(1), 79–95.

Divins, D.L. (2003), Total Sediment Thickness of the World's Oceans & Marginal Seas, *NOAA National Geophysical Data Center*, Boulder, CO.

D'Orazio, M., Innocenti, F., Manetti, P., Tamponi, M., Tonarini, S., Gonzalez-Ferran, O., Lahsen, A. and Omarini, R. (2003), The Quaternary calc-alkaline volcanism of the Patagonian Andes close to the Chile triple junction: geochemistry and petrogenesis of volcanic rocks from the Cay and Maca volcanoes (~45ºS, Chile), *J. S. Am. Earth Sci.*, 16(4), 219–242, doi:10.1016/S0895-9811(03)00063-4.

Douglas, A. (1967), Joint epicenter determination, *Nature*, 215, 47–48.

Farías, M., Comte, D., Roecker, S., Carrizo, D. and Pardo, M. (2011), Crustal extensional faulting triggered by the 2010 Chilean earthquake: The Pichilemu seismic sequence, *Tectonics*, 30(6), TC6010, doi:10.1029/2011TC002888.

Fitch, T.J. (1972), Plate convergence, transcurrent faults, and internal deformation adjacent to Southeast Asia and the western Pacific. *J. Geophys. Res.,* 77, 4432–4460.

Forsythe, R. and Nelson, E. (1985), Geological manifestations of ridge collision: evidence from the Golfo de Penas-Taitao basin, southern Chile, *Tectonics*, 4(5), 477–495.

Forsythe, R., Nelson, E., Carr, M., Keading, M., Hervé, M., Mpodozis, C., Soffia, J. and Harambour, S. (1986), Pliocene near trench magmatism in Southern Chile: a possible manifestation of ridge collision, *Geology*, 14, 23–27.

Gallego, A., Russo, R. M., Comte, D., Mocanu, V. I, Murdie, R. E. and Vandecar, J. C. (2010), Seismic noise tomography in the Chile ridge subduction region, *Geophys. J. Int.*, 182(3), 1478–1492, doi:10.1111/j.1365-246X.2010.04691.x.

Gansser, A. (1973), Facts and theories on the Andes, *J. Geol.Soc.Lond*., 129, 93–131.

Geiger, L. (1912), Probability method for the determination of earthquake epicenters from the arrival time only, (translated from Geiger's 1910 German article), *Bull. St. Louis Univ.*, 8(1), 56-71.

González, G., Cembrano, J., Carrizos, D., Macci, A., and Schneider, H. (2003), Link between forearc tectonics and Pliocene-Quaternary deformation of the Coastal Cordillera, Northern Chile*, J. S. Am. Earth Sci.,* 16, 321–342.

Gorring, M., Kay, S., Zeitler, P., Ramos, V., Rubiolo, D., Fernandez, M. and Panza, J. (1997), Neogene Patagonian plateau lavas: continental magmas associated with ridge collision at the Chile Triple Junction, *Tectonics*, 16(1), 1–17.

Greve, F. (1964), Historia de la Sismología en Chile, Instituto de Geofísica y Sismología, Universidad de Chile, 138. [unpublished].

Haberland, C., Rietbrock, A., Lange, C.D., Bataille, K. and Hofmann, S. (2006), Interaction between continental forearc and oceanic plate at the South-Central

Chilean margin as seen in local earthquake data, *Geophys. Res. Lett.*, 33, L23302, doi:10.1029/2006GL028189.

Haberland, C., Rietbrock, A., Lange, D., Bataille, K. and Dahm, T. (2009), Structure of the seismogenic zone of the south-central Chilean margin revealed by local earthquake travel-time tomography, *J. Geophys. Res*., 114(B1), B01317, doi:10.1029/2008JB005802.

Hardebeck, J.L. and Shearer, P.M. (2003), Using S/P amplitude ratios to constrain the focal mechanisms of small earthquakes, *Bull. seism. Soc. Am.*, 93, 2434–2444.

Hauksson, E. (2011), Crustal geophysics and seismicity in southern California, *Geophys. J. Int.*, 186, 82-98, doi:10.1111/j.1365-246X.2011.05042.x.

Hayes, G., Wald, D. and Johnson, R. (2012), Slab1.0: A three-dimensional model of global subduction zone geometries, *J. Geophys. Res.*, 117(B1), B01302, doi:10.1029/2011JB008524.

Herron, E., Cande, S. and Hall, B. (1981), An active spreading center collides with a subduction zone: a geophysical survey of the Chile Margin Triple Junction, in Nazca Plate: Crustal Formation and Andean Convergence, *Geol. Soc. Am. Mem.*,154, 683–702.

Hervé, M. (1976), Estudio geológico de la falla Liquiñe-Reloncaví en el área de Liquiñe; antecedentes de un movimiento transcurrente (Provincia de Valdivia), *Primer Congreso Geológico Chileno*, Actas, l, B39– B56.

Hoffmann-Rothe, A., Kukowski, N., Dresen, G., Echtler, H., Oncken, O., Klotz, J., Scheuber, E. and Kellner, A. (2006), Oblique convergence along the Chilean margin: Partitioning, margin-parallel faulting and force interaction at the plate interface *in* the Andes active subduction orogeny, 125–146, Springer, Berlin.

Husen, S., Kissling, E., Flueh, E. and Ash, G. (1999), Accurate hypocenter determination in the seismogenic zone of the subducting Nazca plate in north Chile using a combined on/offshore network, *Geophys. J. Int.*, 138, 687–701.

Husen, S. (2003), Probabilistic earthquake location in complex three-dimensional velocity models: Application to Switzerland, *J. Geophys. Res*., 108(B2), 2077-2097, doi:10.1029/2002JB001778.

Isacks, B. (1988), Uplift of the Central Andean Plateau and bending of the Bolivian Orocline, *J. Geophys. Res*., 93(B4), 3211-3231.

Jarrard, R. (1986), Terrane motion by strike-slip faulting of forearc slivers, *Geology*, 14(9),780–783.

Jordan, T., Isacks, B., Allmendinger, R., Brewer, J., Ramos, V. and Ando, C. (1983), Andean tectonics related to geometry of subducted nazca plate, *Geol. Soc. Am. Bull*., 94(3), 341–361.

Kanamori, H. (1977), The energy release in great earthquakes, *J. Geophys. Res.*, 82(20), 2981–2987.

Kato, A., Sakai, S. and Obara, K. (2011), A normal-faulting seismic sequence triggered by the 2011 off the pacific coast of Tohoku earthquake: Wholesale stress regime changes in the upper plate, *Earth Planets and Space*, 63(7), 745-748, doi:10.5047/eps.2011.06.014.

Kikuchi, M., and Kanamori, H. (1991), Inversion of complex body waves – III, *Bull. Seismol. Soc. Amer.*, 81, 2335-2350.

Kissling, E. (1988), Geotomography with local earthquakes, *Rev. Geophys.*, 26, 659–698.

Kissling, E., Ellsworth, W.L., Eberhart-Phillips, D. and Kradolfer, U. (1994), Initial reference models in local earthquake tomography, *J. Geophys. Res.*, 99, 19635–19646.

Kissling, E., Kradolfer, U. and Maurer, H. (1995), VELEST User's Guide: Short Introduction, *Institute of Geophysics and Swiss Seismological Service*, ETH, Zurich.

Kisslinger, C. (1980), Evaluation of S to P amplitude ratios for determining focal mechanisms from regional network observations, *Bull. Seism. Soc. Am*., 70, 999–1014.

Kley, J., Monaldi, C. and Salfity, J. (1999), Along-strike segmentation of the Andean foreland: causes and consequences, *Tectonophysics*, 301(1-2), 75–94.

Lange, D., Rietbrock, A., Haberland, C., Bataille, K., Dahm, T., Tilmann, F. and Flüh, E. (2007), Seismicity and geometry of the south Chilean subduction zone (41.5ºS-43.5ºS): implications for controlling parameters, *Geophys. Res. Lett*., 34, L06311, doi:10.1029/2006GL029190.

Lange, D., Cembrano, J., Rietbrock, A., Haberland, C, Dahm, T. and Bataille, K. (2008), First seismic record for intra-arc strike-slip tectonics along the Liquiñe-Ofqui fault zone at the obliquely convergent plate margin of the Southern Andes, *Tectonophysics*, 455, 14–24, doi:10.1016/j.tecto.2008.04.014.

Lange, D., Tilmann, F., Barrientos, S. E., Contreras-Reyes, E., Methe, P., Moreno, M., Heit, B., Agurto, H., Bernard, P., Vilotte, JP. and Beck, S. (2012), Aftershock seismicity of the 27 February 2010 *Mw* 8.8 Maule earthquake rupture zone, *Earth Planet. Sci. Lett.*, 317–318, 413-425, , doi: 10.1016/j.epsl.2011.11.034

Langer, H., Raffaele, R., Scaltrito, A. and Scarfi, L. (2007), Estimation of an optimum velocity model in the Peloritani Mountains: assessment of the variance of model parameters and variability of earthquake locations, *Geophys. J. Int.*, 170(3), 1151-1164, doi:10.1111/j.1365-246X.2007. 03459.x.

Lara, L. (2008), Holocene submarine volcanoes in the Aysén fjord, Patagonian Andes (44◦ S): relations with the Liquiñe-Ofqui Fault Zone, *in Proceedings of 7th*

International Symposium on Andean Geodynamics, ISAG 2008, Extended Abstracts, 285–288, Nice.

Lay, T., Astiz, L., Kanamori, H. and Christensen, D. (1989), Temporal variation of large intraplate earthquakes in coupled subduction zones, *Phys. Earth Planet. In.*, 54(3-4), 258–312.

Lay, T. and Wallace, T. C. (1995), Modern global seismology, Volume 58 in International geophysics series, *Academic Press*, San Diego.

Lee, W.H.K. and Lhar, J.C. (1972), HYP071: A computer program for determining hypocenter, magnitude, and first motion pattern of local earthquakes (Open File Report), *U. S. Geological Survey*.

Legrand, D., Barrientos, S., Bataille, K., Cembrano, J. and Pavez, A. (2010), The fluid-driven tectonic swarm of Aysen Fjord, Chile (2007) associated with two earthquakes (Mw = 6.1 and Mw = 6.2) within the Liquiñe Ofqui Fault Zone, *Cont. Shelf Res.*, 31, 151–154, doi:10.1016/j.csr.2010.05.008.

Llenos, A. L., and McGuire, J. J. (2007), Influence of fore-arc structure on the extent of great subduction zone earthquakes, *J. Geophys. Res.*, 112(9).

Lomax, A., Virieux, J., Volant, P. and Berge, C. (2000), Probabilistic earthquake location in 3D and layered models: introduction of a Metropolis–Gibbs method and comparison with linear locations *in* Advances in Seismic Event Location, 101–134, *Springer*, Amsterdam.

Lomax, A. and Curtis, A. (2001), Fast, probabilistic earthquake location in 3D models using oct-tree importance sampling, *Geophys. Res. Abstr.,* 3:955.

Lomax, A., Michelini, A., Curtis, A. (2009), Earthquake Location, Direct, Global-Search Methods, *in* Encyclopedia of Complexity and System Science, Part 5, 2449-2473, *Springer*, New York, doi:10.1007/978-0-387-30440-3.

Lomnitz, C. (2004), Major earthquakes of Chile: a historical survey, 1535-1960, Seismol. Res. Lett., 75(3), 368–378.

Lorito, S., Romano, F., Atzori, S., Tong, X., Avallone, A., McCloskey, J., Cocco, M., Boschi, E. and Piatanesi, A. (2011), Limited overlap between the seismic gap and coseismic slip of the great 2010 Chile earthquake, *Nature Geosci.*, 4(3), 173–177, doi:10.1038/ngeo1073.

McCaffrey, R. (1992), Oblique plate convergence, slip vectors, and forearc deformation, *J. Geophys. Res.,* 97(B6), 8905–8915.

Melnick, D., Bookhagen, B., Strecker, M.R. and Echtler, H. (2009), Segmentation of megathrust rupture zones from forearc deformation patterns over hundreds to millions of years, Arauco Peninsula, *J. geophys. Res.*, 114, B01407, doi:10.1029/2008JB005788.

Mendoza, C., and Hartzell, S. (1988), Aftershock patterns and main shock faulting, *Bull. Seismol. Soc. Am.*, 78(4), 1438–1449.

Métois, M., Socquet, A. and Vigny, C. (2012), Interseismic coupling, segmentation an mechanical behavior of the central Chile subduction zone, *J. Geophys. Res.*, 117(B3),
B03406, doi:10.1029/2011JB008736.

Miller, M., Bataille, K., Priestley, K., Iwamori, H. and Calisto, I. (2005), Seismic imaging of a subducted ridge, southern Chile, *EOS Trans. Am. Geophys. Un.*, 86(52), Fall Meet. Suppl., Abstract S51A-0982.

Mora, C., Comte, D., Russo, R., Gallego, A. and Mocanu, V. (2010), Aysén seismic swarm (January 2007) in southern Chile: analysis using joint hypocentral determination, *J. Seismol.*, 14(4), 683–691, doi:10.1007/s10950-010-9190-y.

Moreno, M., Rosenau, M. and Oncken, O. (2010), 2010 Maule earthquake slip correlates with pre-seismic locking of Andean subduction zone. *Nature,* 467, 198–202. doi:10.1038/ nature09349.

Moreno, M., Melnick, D., Rosenau, M., Baez, J., Klotz, J., Oncken, O., Tassara, A., Chen, J., Bataille, K., Bevis, M., Socquet, A., Bolte, J., Vigny, C., Brooks, B., Ryder, I., Grund, V., Smalley, B., Carrizo, D., Bartsch, M. and Hase, H. (2012), Toward understanding tectonic control on the M_W 8.8 2010 Maule Chile earthquake, *Earth Planet. Sci. Lett.*, 321, 152–165, doi:10.1016/j.epsl.2012.01.006.

Mpodozis, C. and Ramos, V.A. (1989), The Andes of Chile and Argentina *in* Geology of the Andes and its relation to hydrocarbon and mineral resources, 59-89, Earth Science Series, *Circum-Pacific Council of Energy and Mineral Resources*, Houston.

Müller, R.D., Sdrolias, M., Gaina, C. and Roest, W.R. (2008), Age spreading rates and spreading asymmetry of the world's ocean crust, *Geochem. Geophys. Geosyst.*, 9, Q04006, doi:10.1029/2007GC001743.

Murdie, R., Prior, D., Styles, P., Flint, S., Pearce, R. and Agar, S. (1993), Seismic responses to ridge-transform subduction: Chile triple junction, *Geology*, 21(12), 1095–1098.

Naranjo, J.A., Moreno, H. and Banks, N. (1993), La erupción del volcán Hudson en 1991 (46°S), Región XI, Aisén, *Servicio Nacional de Geología y Minería,* 44, Santiago.

Naranjo, J.A., and Stern, C. (1998), Holocene explosive activity of Hudson volcano, southern Andes, *Bull. Volcanol.*, 59(4), 291–306.

Naranjo, J.A., Arenas, M., Clavero, J. and Muñoz, O. (2009), Efectos de la crisis sísmica de Aisén 2007, *Andean Geol.*, 36(1), 137–145.

Natawidjaja, D. H. and Triyoso, W. (2007), The Sumatran Fault Zone- From Source To Hazard, *J. Earthq.Tsunami*, 1(1), 21–47.

Niemeyer, H., Skármeta, J., Fuenzalida, R., Espinosa, W. (1984), Hojas Península de Taitao y Puerto Aisén, Carta Geológica de Chile, 60–61, 1 mapa escala 1:500.000. *Servicio Nacional de Geología y Minería*, Santiago.

Nippress, S.E.J. and Rietbrock, A. (2007), Seismogenic zone high permeability in the Central Andes inferred from relocations of micro-earthquakes, *Earth Planet. Sci. Lett.*, 263(3-4), 235-245, doi:10.1016/j.epsl.2007.08.032.

Pankhurst, R.J., Weaver, S.D., Hervé, F. and Larrondo P. (1999), Mesozoic-Cenozoic evolution of the North Patagonian batholith in Aysén, Southem Chile, *J. Geol. Soc. London*, 156, 673-694.

Pardo-Casas, F., and Molnar, P. (1987), Relative motion of the Nazca (farallon) and South American plates since late cretaceous time, *Tectonics*, 6(3), 233–248.

Pilger, R. (1981), Plate reconstructions, aseismic ridges, and low angle subduction beneath the Andes. *Bull. Geol. Soc. Am.,* 92, 448-456.

Ramos, V. and Kay, S. (1992), Southern Patagonian Plateau basalts and deformation: back-arc testimony of ridge collision, *Tectonophysics*, 205, 261–282.

Ramos, V.A. (1999), Plate tectonic setting of the Andean Cordillera, *Episodes*, 22(3), 183-190.

Research Group for Active Faults of Japan (RGAFJ). (1991), Active Faults in Japan: Sheet Maps and Inventories (Revised Edition), *University of Tokyo Press*.

Richter, C.F. (1958), Elementary Seismology, *Freeman and Co*., San Francisco.

Rietbrock, A. and Scherbaum, F. (1998), The GIANT analysis system (graphical interactive aftershock network toolbox), *Seism. Res. Lett.*, 69, 40–45.

Rietbrock, A., Ryder, I., Hayes, G., Haberland, C., Comte, D., Roecker, S. and Lyon-Caen, H. (2012), Aftershock seismicity of the 2010 Maule M_W=8.8, Chile, earthquake: Correlation between co-seismic slip models and aftershock distribution?, *Geophys. Res. Lett*., 39(8), L08310, doi:10.1029/2012GL051308.

Rosenau, M., Melnick, D. and Echtler, H. (2006), Kinematic constraints on intra-arc shear and strain partitioning in the Southern Andes between 38ºS and 42ºS latitude, *Tectonics*, 25(4), TC4013, doi:10.1029/2005TC001943.

Ruegg, J., Rudloff, A., Vigny, C., Madariaga, R., Chabalier, J. D., Campos, J., Kausel, E., Barrientos, S. and Dimitrov, D. (2009), Interseismic strain accumulation measured by GPS in the seismic gap between Constitución and Concepción in Chile, *Phys. Earth Planet. In.*, 175(1-2), 78–85, doi:10.1016/j.pepi.2008.02.015.

Russo, R. M., Gallego, A., Comte, D., Mocanu, V. I., Murdie, R. E. and Vandecar, J. C. (2010a), Source-side shear wave splitting and upper mantle flow in the Chile ridge subduction region, *Geology*, 38(8), 707–710, doi:10.1130/G30920.1.

Russo, R., Vandecar, J. C., Comte, D., Mocanu, V. I. Gallego, A. and Murdie, R. E. (2010b), Subduction of the Chile ridge: Upper mantle structure and flow, *GSA Today*, 4–10, doi:10.1130/GSATG61A.1.

Russo, R.M., Gallego, A., Comte, D., Mocanu, V.I., Murdie, R.E., Mora, C. and VanDecar, J.C. (2010c), Triggered seismic activity in the Liquiñe-Ofqui fault zone, Southern Chile, during the 2007 Aysen seismic swarm, *Geophys. J. Int.*, 184, 1317-1326, doi:10.1111/j.1365-246X.2010.04908.x.

Ryder, I., Rietbrock, A., Kelson, K., Bürgmann, R., Floyd, M., Socquet, A., Vigny, C. and Carrizo, D. (2012), Large extensional aftershocks in the continental forearc triggered by the 2010 Maule earthquake, Chile, *Geophys. J. Int*., 188, 879–890, doi:10.1111/j.1365-246X.2011.05321.x.

Sandwell, D.T. and Smith, W.H.F. (2009), Global marine gravity from retracked Geosat and ERS-1 altimetry: Ridge Segmentation versus spreading rate, *J. Geophys. Res.*, 114, B01411, doi:10.1029/2008JB006008.

Scheuber E. and Andriessen, P.A.M. (1990), The kinematic and geodynamic significance of the Atacama Fault Zone, Northern Chile, *J. Structural Geology* 12(2):243–257.

Schweller, W.J., Kulm, L.D. and Prince, R.A. (1981), Tectonics, structure, and sedimentary framework of the Peru–Chile Trench *in* Nazca plate: crustal formation and Andean convergence, 323–349, *Memoir. Geol. Soc. Am.*, Boulder, CO.

Sepúlveda, S. and Serey, A. (2009). Tsunamigenic, earthquake-triggered rock slope failures during the 21st of April 2007 Aysén earthquake, southern Chile (45.5ºS), *Andean Geol.*, 36(1), 131–136.

Sepúlveda, S., Serey, A., Lara, M., Pavez, A. and Rebolledo, S. (2010). Landslides induced by the April 2007 Aysén Fjord earthquake, Chilean Patagonia, *Landslides*, 7, 483–492.

SERNAGEOMIN. (2003), Mapa Geológico de Chile: versión digital, 4 (CD-ROM, versión1.0, 2003), 1 mapa geológico de Chile escala 1:1.000.000, *Servicio Nacional de Geología y Minería*, Santiago.

Siame,L.L., Bellier, O., Sébrier, M. and Araujo, M. (2005), Deformation partitioning in flat subduction setting: Case of the Andean foreland of western Argentina (28°S–33°S), *Tectonics*, 24, TC5003, doi:10.1029/2005TC001787.

Sieh, K. and Natawidjaja, D. (2000), Neotectonics of the Sumatran fault, Indonesia, *J. geophys. Res.*, 105, 28295–28326.

Snoke, J.A. (2009), FOCMEC: FOCal MEChanisms Determinations. FOCMEC Software Manual, Available at: http://www.iris.edu/software/downloads/processing/ (last accessed 2012 February 25).

Snoke, J.A., Munsey, J.W., Teague, A.C. and Bollinger, G.A. (1984), A program for focal mechanism determination by combined use of polarity and SV-P amplitude ratio data, *Earthq. Notes*, 55(3), 15.

Sokos, E., and Zahradnik, J. (2008), ISOLA a Fortran code and a MATLAB GUI to perform multiple-point source inversion of seismic data, *Computers & Geosciences*, 34(8), 967–977, doi:10.1016/j.cageo.2007.07.005.

Song, T.R.A. and Simons, M. (2003), Large trench-parallel gravity variations predict seismogenic behavior in subduction zones, *Science,* 301 (5633), 630–633.

Sparkes, R., Tilmann, F., Hovius, N. and Hillier, J. (2010), Subducted seafloor relief stops rupture in South American great earthquakes: Implications for rupture behaviour in the 2010 maule, Chile earthquake, *Earth Planet. Sci. Lett*., 298(1-2), 89–94, doi:10.1016/j.epsl.2010.07.029.

Stein, S. and Wysession, M. (2003), An Introduction to Seismology, Earthquakes and Earth Structure, *Blackwell Publishing*, Oxford.

Stern, C. (2004), Active Andean volcanism: its geologic and tectonic setting, *Rev. geol. Chile*, 31(2), 161-206.

Tarantola, A. and Valette, B. (1982), Inverse problems = quest for information. *J. Geophys. Res.,* 50:159–170.

Tassara, A. and Yañez, G. (2003), Relación entre el espesor elástico de la litósfera y la segmentación tectónica del margen andino (15–47ºS), *Rev. Geol. Chile*, 30(2), 159–186.

Tassara, A., Gotze, H., Schmidt, S. and Hackney, R. (2006), Three-dimensional density model of the Nazca plate and the Andean continental margin, *J. Geophys. Res.*, 111, B09404, doi:10.1029/2005JB003976.

Thurber, C. H. (1993), Local earthquake tomography: velocities and Vp/Vs theory *in* Seismic Tomography: Theory and practice, 20, 563-583. *Chapman and Hall*, London.

Tsutsumi, H., and Okada, A. (1996), Segmentation and holocene surface faulting on the median tectonic line, Southwest Japan, *J. Geophys. Res.*, 101(B3), 5855–5871.

Vigny, C., Socquet, A., Peyrat, S., Ruegg, J.C., Mtois, M., Madariaga, R., Morvan, S., Lancieri, M., Lacassin, R., Campos, J., Carrizo, D., Bejar-Pizarro, M., Barrientos, S., Armijo, R., Aranda, C., Valderas-Bermejo, M.-C., Ortega, I., Bondoux, F., Baize, S., Lyon-Caen, H., Pavez, A., Vilotte, J.P., Bevis, M., Brooks, B., Smalley, R., Parra, H., Baez, J.-C., Blanco, M., Cimbaro, S. and Kendrick, E. (2011). The 2010 Mw 8.8 Maule mega-thrust earthquake of Central Chile, monitored by GPS, *Science*, 332, 1417–1421. doi:10.1126/ science.1204132.

Wang, K., Hu, Y., Bevis, M., Kendrick, E., Smalley, R. Jr., Vargas, R. and Lauría, E. (2007), Crustal motion in the zone of the 1960 Chile earthquake: detangling

earthquake-cycle deformation and forearc-sliver translation, *Geochem. Geophys. Geosyst.*, 8, Q10010, doi:10.1029/2007GC001721.

Weller, O., Lange, D., Tilmann, F., Natawidjaja, D. Rietbrock, A., Collings, R. and Gregory, L. (2012), The structure of the Sumatran fault revealed by local seismicity, *Geophys. Res. Lett.*, 39(1), L01306, doi:10.1029/2011GL050440.

Wells, D.L. and Coppersmith, K.J. (1994), New empirical relationships among magnitude, rupture length, rupture width, rupture area, and surface displacement, *Bull. Seism. Soc. Am.*, 84, 974–1002.

Wessel, P., and Smith, W. (1998), New, improved version of generic mapping tools released, *EOS Trans. Am. Geophys. Un*., 79, 579–579, doi:10.1029/98EO00426.

Woessner, J., Schorlemmer, D., Wiemer, S. and Mai, P. (2006), Spatial correlation of aftershock locations and on-fault main shock properties, *J. Geophys. Res.*, 111, B08301, doi:10.1029/2005JB003961.

Zonenshayn, L. P., Savostin, L. and Sedov, A. (1984), Global paleogeodynamic reconstruction for the last 160 million years, *Geotectonics*, 18, 181–195.

APPENDIX A

Catalogue of events processed in Chapter 3. Column headers: **Date** of event occurrence; **Origin Time** of event occurrence in GMT time; **Latitude South** coordinates of epicenter in degrees; **Longitude West** coordinates of epicenter in degrees; **Dep** hypocentral depth in km; **Ml** local magnitude; **No** number of observations; **Gap** angle of non-coverage; **RMS** in seconds; **Columns 10-16: azimuth** and **dip** angles, and **length** (km) of semi-axis 1, 2 and 3 of 68% confidence error ellipsoids.

Date	Time	Lat. S	Lon. W	Dep	Ml	No	Gap	RMS	AZ1	DIP1	LEN1	AZ2	DIP2	LEN2	LEN3
040123	04:24:16.98	46.0108	72.8849	0.1	2.3	10	327	0.26	338.6	-31.3	5.14	245.4	-5.3	8.04	9.13
040124	02:12:06.77	46.0393	73.1147	9.2	2.1	6	345	0.12	296.8	-6.6	9.76	21.2	40.2	12.61	19.94
040124	07:42:40.02	46.8461	73.7774	6.0	1.5	8	325	0.25	260.4	-19.7	5.86	350.2	0.4	9.78	11.2
040124	15:13:40.87	46.6610	73.1257	4.0	0.8	6	290	0.03	79.4	-58.8	4.82	356.4	4.2	7.52	11.6
040125	14:12:29.42	45.8494	72.9497	6.8	2.3	18	296	0.35	57.1	-2.5	3.43	323.8	-51.8	5.9	7.41
040126	14:32:09.65	46.6642	73.1070	4.4	1.6	8	259	0.07	192	9.5	2.25	284.4	14	4.7	7.98
040127	11:34:00.82	46.6681	73.1032	4.3	1.3	10	259	0.1	197.3	2	1.7	293.7	72.3	2.9	3.93
040128	05:16:56.61	46.6665	73.1171	3.8	1.6	16	248	0.14	185.1	-7.9	1.44	271.6	23.8	2.95	3.28
040128	06:20:18.22	45.9079	72.9239	10.0	2.1	24	199	0.32	7.6	0.1	1.63	277.6	-5.9	3.07	5.42
040128	06:46:43.45	46.5479	72.9667	3.2	0.6	8	226	0.09	207.2	-13.5	1.38	289.3	29.4	3.46	3.87
040129	10:50:12.14	46.6736	73.0968	4.4	1.1	10	260	0.11	196.4	-3.6	1.69	266.1	79.8	2.67	4.08
040131	14:45:20.11	45.9918	72.9868	0.9	2.3	10	247	0.14	112.8	8.8	5.92	208.1	31.2	9.83	12.85
040131	15:28:29.47	46.6800	73.1009	2.5	1.4	8	289	0.06	5.5	1.2	2.32	275.7	-11.2	4.43	8.55
040202	06:13:40.54	46.6681	73.1123	3.5	1.2	12	262	0.1	191.1	-10.4	1.53	249.6	70.7	2.61	3.3
040202	11:45:29.13	45.8636	72.9552	9.8	2.2	18	213	0.37	13.1	-1.7	1.83	281.9	-33.4	5.57	6.87
040203	07:34:10.32	45.9253	72.9428	10.0	2.2	12	246	0.27	193.2	-1.4	3.25	103.1	-0.4	6.05	9.51
040203	13:46:43.04	46.6673	73.1159	4.3	1.2	10	286	0.14	25.8	-4.2	2.13	76.8	83.4	3	4.13
040203	19:23:08.76	46.3146	73.7819	0.1	2.6	10	322	0.41	146.7	27	7.18	277.1	51.8	10.3	18.67
040204	14:25:56.50	46.6641	73.1208	3.6	1	8	315	0.12	13.1	34.8	2.71	336	-48.9	3.92	5.15
040205	17:27:44.44	46.0566	72.9741	0.1	2.1	14	233	0.26	105.1	21.4	5.45	210	33.4	6.39	15.38
040206	17:46:33.72	46.6562	74.9170	0.1	3.3	12	335	0.36	269.6	-45	4.9	244	42	8.96	14.79
040209	02:34:40.69	45.9000	72.9269	8.0	2.2	22	231	0.49	19.8	-9.4	3.48	285	-26.6	4.56	5.8
040210	01:20:22.03	45.9158	72.9846	9.9	2.1	18	250	0.34	42	-11.7	4.15	304.8	-30.8	4.88	8.22
040210	01:23:16.21	46.0566	72.9878	0.1	2.2	14	235	0.27	341.4	-55.9	4.81	263.9	8.3	7.03	14.32
040213	05:00:42.97	45.9032	72.8857	10.1	1.9	10	255	0.19	201.9	0	2.47	291.9	6.3	5.02	9.36
040213	12:47:56.78	45.9412	72.9277	21.0	2.3	15	244	0.3	154.9	-6.1	6	243.6	12.2	9.25	12.09
040214	13:51:55.66	47.1182	74.6114	0.1	3.2	12	326	0.36	75.1	32.1	6.57	162.9	-3.4	7.44	18.26
040216	05:12:13.05	46.6341	73.7248	0.2	2.8	12	279	0.29	31.2	16.9	4.18	316.7	-41.3	5.45	9.02
040219	05:11:05.71	45.9048	72.8742	6.0	2.1	18	201	0.31	346.5	-7.2	3.25	254.6	-14.5	5.2	6.41

040219	15:47:10.61	46.5059	72.0639	2.0	1.4	6	208	0.1	38.6	21.3	3.04	335.6	-49.3	10.82	19.97
040220	02:19:14.62	45.2656	73.0041	0.1	3	16	291	0.39	50.8	-12.4	2.83	307.7	-45.6	4.61	7.39
040220	07:11:47.67	45.8890	72.8711	6.0	2.2	12	213	0.26	9.1	0.1	1.6	279.1	-10.7	4.56	8.11
040220	07:27:50.68	45.9285	72.9016	8.1	1.8	6	256	0.15	358.1	-1.4	7.97	267.5	-24	13.94	16.02
040220	15:18:31.79	46.0598	72.9875	0.1	1.9	16	278	0.19	70.5	5.6	3.83	163.7	29.9	4.99	13.16
040221	00:54:47.46	46.0503	72.9792	0.1	2.1	14	322	0.24	325.3	-47	4.25	238.8	3.3	5.24	10.85
040221	00:55:35.45	46.0503	72.9883	0.1	1.5	16	312	0.2	66.5	4.1	3.54	159.5	36.5	4.49	11.65
040222	02:02:26.85	45.8605	72.9419	3.8	1.9	15	204	0.25	188.8	1.5	1.62	278.8	1.2	4.21	9.97
040225	09:36:08.30	45.8653	72.8347	10.1	2.3	14	238	0.28	33.1	-21.3	4.55	293.4	-23	6.74	8.6
040226	15:34:59.54	45.8668	72.9458	6.0	2	17	204	0.28	17.1	0.2	1.5	287.1	-5.4	2.87	6.86
040228	16:25:29.32	46.0124	72.8460	0.1	2	14	285	0.27	356.1	-41.4	4.29	249.8	-17.5	5.41	9.57
040228	17:07:08.01	45.9111	72.9146	6.0	2.1	17	269	0.31	45.7	-0.7	1.82	315.3	-22.9	4.59	9.39
040228	22:18:27.42	46.5621	71.8817	3.5	1.4	14	136	0.13	66.2	-7.1	1.19	338.5	18.2	1.83	5.55
040229	21:16:05.68	45.9064	72.9173	7.4	2.2	8	311	0.22	328.7	-4	7.4	235.1	-42	11.8	15.71
040302	02:47:18.40	46.6697	73.1168	4.3	1.4	14	260	0.1	188.3	-9.1	1.36	258	65.2	2.82	3.25
040302	23:50:16.50	45.8763	72.9223	8.0	2	14	213	0.31	41.2	0.6	2.38	311.4	-15.1	4.2	6.9
040303	07:39:21.33	45.9269	72.9495	10.0	2	19	201	0.34	55.8	-0.1	2.5	325.7	-24.5	4.72	6.64
040304	20:36:56.53	45.9285	72.8561	1.3	2.3	8	270	0.09	45.6	0.2	2.1	315.6	-6.8	6.15	12.31
040305	01:31:44.62	45.9269	73.0859	10.0	2	15	216	0.26	20.2	-1.4	2.18	290	-9.8	4.3	9.54
040307	01:06:23.75	45.9222	72.8839	3.0	2.1	11	266	0.29	46.8	2.5	2.51	317.8	-21.6	4.92	7.78
040307	02:16:12.67	45.9412	72.8549	2.1	2.3	6	269	0.08	67.4	-20.8	8.38	2.8	48.3	9.77	10.89
040309	22:02:44.05	46.5756	71.8675	2.4	1.5	15	206	0.16	13.2	-2.7	1.89	282.9	-5.5	3.4	6.01
040310	04:23:18.33	45.9222	72.9112	10.1	2.2	8	281	0.16	315.5	-7.1	7.41	223.4	-16.3	8.38	14.79
040316	02:48:09.01	47.4220	73.1890	6.0	2.3	7	315	0.27	116.3	-11.3	8.15	213.6	-32.4	9.5	12.07
040316	04:06:27.40	45.9538	72.8992	0.9	1.8	12	271	0.3	44.2	-0.4	3.88	314	-21.5	5.66	8.61
040319	14:51:42.79	46.0566	72.9787	0.1	2.2	13	289	0.23	326.7	-51.8	4.22	232.1	-3.6	7.78	10.65
040320	23:12:47.73	46.0408	73.0029	0.1	2.1	16	257	0.29	288.3	-42.5	4.9	221.1	22.9	5.57	11.81
040321	01:29:18.70	46.5756	73.1149	0.3	1.5	7	296	0.04	200.4	-3.1	2.59	287.1	46.5	7.23	12.63
040326	01:13:38.04	45.9855	73.0694	6.9	2.1	14	292	0.22	102.8	7.4	4.81	194.1	9.5	5.97	11.15
040328	02:30:20.32	46.0234	72.9202	0.1	2.3	8	327	0.2	341.3	-11.6	5.9	248.9	-11.5	9.24	13.1
040329	08:30:08.88	46.7306	72.1731	2.2	1.6	8	203	0.1	350.6	-3.6	1.82	260.1	-7.8	6.15	10.01
040329	13:15:30.43	46.2829	73.7752	0.1	2.7	12	319	0.23	104	29.3	5.07	197.2	5.7	5.91	9.71
040331	14:36:48.07	45.9728	72.8793	0.1	2	14	304	0.28	299.9	-28.4	4.76	221.1	19.7	5.49	9
040401	04:09:27.08	45.1248	73.0277	0.3	3.2	12	343	0.27	352.1	-27.7	5.49	225.4	-48.6	13.3	15.63
040401	10:59:44.54	46.2576	73.7497	0.1	1.9	14	296	0.26	13.9	-1.8	3.65	282.8	-30.6	4.99	9.53
040401	22:34:50.62	46.5676	71.9398	2.6	2	7	290	0.09	182.3	7.8	4.22	284.8	57.5	9.51	10.8
040402	07:29:08.98	46.1817	73.7008	0.1	2.6	12	323	0.18	67.6	8.9	5.24	162.6	29.5	5.7	9.72
040402	08:01:30.65	46.0298	73.0198	0.1	2.3	9	295	0.13	279.4	-10.9	6.79	216.3	66.8	10.89	15.04
040404	07:06:40.81	46.2829	73.7935	0.1	2.4	12	320	0.29	103.3	33	5.35	196.7	5.2	6.23	9.68
040405	21:54:01.75	45.8874	73.0736	10.0	2.4	13	270	0.35	326.4	-28.2	6.4	238.1	3.2	7.12	9.15
040409	20:34:38.87	45.8921	72.8890	6.0	2.4	16	269	0.26	40.3	0.1	2.41	310.3	-23.6	4.74	6.92
040412	01:18:28.01	47.6877	73.8413	0.1	2.9	8	334	0.19	213	-39.2	6.2	280.4	25.2	9.97	18.41
040414	01:21:13.38	46.2291	73.8845	8.0	2.9	10	301	0.25	23.8	-2.3	3.66	292.6	-27.5	5.65	9.53

040415	13:47:27.67	46.0487	73.9755	0.1	3.3	8	329	0.27	123.4	50.6	5.75	273.4	35.4	8.39	10.67
040419	08:51:25.31	45.9665	72.8981	0.1	1.9	8	310	0.14	245.6	18	5.97	152.1	10.5	7.04	12.88
040420	03:05:11.74	45.9855	72.9601	0.1	2.2	9	305	0.26	234	6.6	5.32	322.5	-12.8	5.88	12.02
040422	18:00:51.64	45.8526	73.6354	0.1	2.7	8	332	0.1	310.6	-16.7	6.45	217.5	-10.1	7.55	16.87
040423	06:34:07.13	45.9570	72.3301	9.0	2.3	8	325	0.09	95.3	0.1	4.55	5.3	-9.3	5.86	13.5
040423	11:23:31.14	45.7450	73.6075	9.9	2.5	14	319	0.28	351	-24.1	5.32	256.4	-10.1	5.77	9.5
040424	21:57:14.95	46.5945	71.9206	3.7	1.7	10	285	0.13	190.2	-8.7	2.98	279.4	4.9	4.32	5.73
040426	21:50:08.59	46.5946	71.9161	3.7	1.9	10	319	0.11	88.4	-23.9	4.08	356.8	-3.6	4.49	6.31
040430	05:02:19.70	47.2005	74.5595	0.1	3	10	345	0.27	243.1	-57.3	4.85	252.9	32.3	8.53	17.44
040502	23:03:06.66	46.0108	72.9214	0.1	2	11	287	0.2	90.1	10.9	5.6	182.3	11.9	5.74	10.63
040504	07:18:54.05	46.6467	73.8713	0.6	2.5	10	332	0.25	290.3	-20.6	5.71	14.9	14	8.04	10.34
040508	08:02:10.65	46.0218	72.9180	0.1	1.9	14	285	0.22	5.2	-33.5	4.55	259.5	-22.2	5.06	11.35
040508	10:57:56.16	46.0195	72.9422	0.0	1.8	12	300	0.14	43	-13.6	3.28	302.4	-37	4.15	10.14
040511	08:38:39.83	46.0472	72.9750	0.1	1.9	11	312	0.16	68.5	6.3	4.5	162.2	30.8	5.59	14.08
040511	18:04:10.45	46.0440	72.9889	0.1	1.9	11	312	0.15	63.3	3.9	4.14	155.6	30.9	5.75	14.25
040513	10:25:15.77	46.0298	73.0563	0.5	2.2	10	314	0.21	76.9	2.1	4.51	167.3	13	5.96	12.39
040514	22:52:37.00	46.5930	71.9093	3.4	2.3	8	319	0.11	142.6	-11	5.36	228.8	18.6	5.63	9.22
040517	21:53:52.98	46.5471	71.9351	2.4	1.5	7	335	0.05	82.3	-27.2	4.91	20.7	42.8	5.09	7.83
040522	16:31:24.49	46.1690	73.5281	0.1	2.6	8	326	0.16	84.2	10.8	5.89	175.2	5.7	7.51	13.15
040523	16:06:39.40	46.0124	72.9690	0.1	2.1	11	313	0.17	70.4	3.8	4.35	162.7	32	6.09	14.37
040524	01:16:59.78	46.0155	72.9323	0.1	2	11	313	0.14	95.3	20.1	4.87	195.9	26.9	5.16	12.93
040526	04:30:44.37	46.7322	74.8573	0.1	3.2	12	336	0.53	265.1	-66.8	4.19	266.4	23.2	8.78	19.4
040527	06:01:16.22	46.1120	73.5875	6.9	2.2	12	310	0.26	290.4	-15.8	5.26	23.6	-10.6	7.41	11.3
040527	09:38:56.53	46.0440	72.9798	0.1	1.9	13	312	0.2	57.2	0.5	4.2	147.5	35.6	5.05	13.23
040529	21:28:37.13	47.2005	74.5316	0.1	3.2	10	345	0.34	241.7	-42.8	6.05	258.7	45.8	9.74	19.79
040530	11:03:59.31	46.0503	72.9838	0.1	2.1	10	312	0.17	66.5	4	4.12	158.9	31.7	5.6	14.61
040601	22:37:35.72	46.0155	72.9915	0.1	2.1	9	314	0.18	316.7	-31.2	5.9	229.5	4.5	6.94	13.54
040606	21:55:28.01	46.6009	71.9337	3.3	1.7	8	300	0.05	335.4	-21.9	3.12	244.3	-2.8	6.28	13.47
040610	03:08:19.10	46.0218	72.9727	0.1	2.3	12	313	0.2	61	1.2	4.46	151.6	30.3	6.02	13.36
040610	06:48:41.60	46.0614	73.0535	0.1	2.3	11	313	0.32	286.5	-11.7	4.96	20.1	-16.5	6.12	10.71
040612	11:04:51.93	46.1120	73.5692	0.1	2.7	8	324	0.23	82.7	20.8	5.98	172.9	0.6	7.07	13.8
040614	04:40:18.71	45.9317	73.0605	9.8	2.8	11	319	0.39	83	5.6	4.79	175.1	20.7	6.48	10.27
040614	21:19:19.26	46.5882	71.9121	3.0	1.5	6	305	0.06	342.5	-26.2	4.92	247.5	-10	7.59	12.34
040617	16:48:04.65	46.5629	71.9242	2.6	1.4	7	291	0.02	117.8	-8.3	3.99	29.6	11.8	5.35	6.89
040618	21:59:05.15	46.5661	71.9239	3.1	1.6	6	307	0.08	345.9	-31.2	5.32	258.5	4.4	6.69	8.35
040620	22:26:43.11	46.5819	71.9082	3.7	1.9	10	291	0.08	153	7.3	2.56	244.4	10.9	4.45	7.2
040624	12:31:12.69	46.0551	73.5191	0.1	2.6	8	325	0.38	119.3	30.4	7.13	102.4	-58.4	9.83	10.94
040626	11:03:37.22	46.0234	73.0022	0.1	2.5	7	326	0.21	283	-16.2	6.87	197.3	14.7	9.39	10.21
040627	18:33:17.58	46.0614	72.8802	0.1	2.3	12	325	0.43	339.6	-39.7	5.44	239.7	-11.7	7.05	11.12
040706	17:49:33.97	46.7828	74.8358	0.1	3	12	328	0.31	263.1	-49.8	4.77	218.8	31.1	8.61	10.39
040706	21:19:16.90	46.0503	72.9792	0.1	2.1	12	311	0.15	68	6.3	4.16	162	33	4.82	12.68
040708	18:57:51.25	46.5819	71.9174	3.6	1.4	7	319	0.05	144	-4.1	4.36	234.1	-0.7	5.24	7.61
040711	10:06:04.04	46.0440	72.9707	0.1	2	14	281	3.61	57.4	-2.6	4.87	322.5	-62.4	8.51	17.78

040715	10:31:29.17	46.1500	73.7945	0.1	2.5	14	302	0.87	166.6	48.8	7.3	171.5	-41	9.26	12.14
040725	22:01:44.79	46.5914	71.9026	3.5	1.8	8	290	0.05	156.3	6.7	2.39	247.8	12.3	5.1	6.74
040726	20:19:07.56	45.9159	72.9937	0.1	2.5	10	330	0.26	357	-36.2	6.08	247.3	-24.7	7.58	8.68
040727	08:46:50.22	46.0551	72.9902	0.1	2.1	8	325	0.25	320.4	-16.7	6.27	33.4	44.2	10.12	10.76
040730	23:53:00.94	47.4093	73.1901	4.6	2.1	7	314	0.29	256.8	-5.5	8.43	163.2	-33.2	9.49	12.12
040731	12:00:25.54	46.0234	72.9566	0.1	2.4	8	326	0.23	343.2	-29.7	5.75	251.6	-2.7	6.85	9.7
040731	12:16:14.97	46.0994	73.6524	0.1	3.1	8	325	0.3	105.5	27.8	6.19	43.3	-41.4	8.44	10.02
040804	17:32:49.51	46.5945	71.9160	3.8	1.8	9	290	0.06	339	-9.2	2.48	69.6	-3.4	4.67	7.65
040805	05:05:50.38	46.0424	73.5748	0.1	2.6	8	335	0.13	127.8	15.9	6.57	44.4	-21.6	9.6	12.88
040807	22:01:42.98	46.5977	71.9111	3.8	1.3	7	319	0.07	140.3	-6.1	4.35	229.1	11.6	5.49	6.46
040811	17:27:34.94	46.5882	71.9121	3.5	1.8	9	290	0.07	151.5	3.1	2.36	242	9.7	4.93	6.79
040818	17:19:32.16	46.6942	74.0014	10.1	2.8	12	295	4.53	147.4	2.9	3.78	215.7	-82.1	9.84	13.78
040820	01:13:13.01	45.9981	73.0864	4.6	2	10	173	0.2	326.9	-17	2.4	213.6	-52.3	9.41	10.17
040821	15:19:17.64	46.6056	72.7461	5.6	0.8	8	205	0.15	3.4	-17.1	3.65	263.3	-29.5	4.35	5.86
040831	22:46:45.15	46.4901	71.9921	0.5	1.5	6	218	0.06	50.2	-12.4	4.12	306.6	-46.5	11.05	14.92
040907	23:08:56.40	46.5123	71.9436	0.8	1.4	10	222	0.18	224.2	-4.9	1.59	309.5	43.7	5.1	8.19
040916	08:13:36.78	46.4284	73.8833	0.1	2.5	10	325	0.27	290.9	-22.9	6.08	14	15.9	9.83	11.13
040927	22:04:40.42	46.5154	71.9341	0.8	1.6	11	223	0.13	222.9	-3.5	1.32	309.8	42.4	4.69	7.97
041003	21:52:20.32	46.5044	71.9560	1.3	1.3	8	220	0.15	215.6	-7.4	1.59	252.6	80.7	7.73	11.22
041019	12:37:21.20	46.8714	74.2382	8.1	2.6	12	308	0.23	309.9	-10	4.49	33.4	32.5	5.22	8.85
041109	21:39:49.20	46.5661	71.8824	2.9	1.8	7	232	0.13	85.5	-80.9	6.88	238.1	-8	9.54	11.59
041109	23:21:10.16	45.9127	72.9985	10.0	1.8	9	169	0.22	320.9	-16.1	3.54	231.1	0.7	5.96	7.94
041115	08:46:59.14	45.9981	73.5055	6.0	2.1	9	272	0.21	175.4	20.8	3.93	269.1	9.8	6.5	12.42
041118	23:08:00.13	46.5677	71.8754	2.6	2.1	7	232	0.11	318.4	14.1	7.3	104.8	73.2	8.51	12.08
041122	23:49:07.08	46.8145	74.8063	0.1	3.2	10	344	0.33	255.9	-44.2	6.6	275.3	44.1	10.05	19.53
041205	01:03:43.31	47.3207	73.1888	0.1	2.5	12	330	0.23	16.4	31.9	5.11	291.2	-7.7	5.75	9.83
041214	02:43:06.91	44.8464	73.4535	53.0	1.5	12	319	0.13	9.9	-3.9	7.25	277.6	-29.5	11.6	15.88
041227	17:25:48.47	46.0551	74.2759	0.1	3	8	343	0.16	229	81.1	8.01	347	4.2	10.78	17.74
041228	05:41:31.55	46.6736	73.1015	4.4	0.9	8	289	0.13	204.4	-55.6	3.41	247.6	26.5	5.42	9.39
041228	14:57:03.72	46.6674	73.1021	3.7	1.2	8	289	0.11	201.9	-51	3.03	252.7	27.1	5.14	8.66
041228	23:42:52.83	46.6578	73.1306	4.2	0.6	6	318	0.01	228.7	62.2	5.54	334.2	8	5.89	12.52
041229	19:23:26.63	46.6736	73.0876	4.5	0.7	7	287	0.12	225.3	-38.3	3.52	265.6	44	6.2	14.8
041231	17:09:59.70	46.6562	73.0915	1.9	0.5	6	281	0.05	234.8	-38	4.07	247.3	51.2	7.66	13.3
050101	12:23:44.62	46.6483	73.1545	4.3	1.1	8	295	0.12	7.5	15.8	2.74	98.5	3.6	5.21	5.29
050101	21:29:36.89	46.6736	73.1015	4.4	1.1	8	289	0.12	212.2	-51.1	3.33	249.4	32.7	5.37	9.94
050102	04:47:14.48	46.6705	73.1017	4.4	1.1	8	289	0.12	209.3	-49.2	3.14	253.6	31.6	5.3	9.56
050102	22:29:48.51	46.6736	73.1015	4.7	1.1	8	289	0.11	202.3	-50.7	3.06	248.3	29.6	5.05	7.84
050104	04:00:07.09	46.6642	73.1162	4.4	1.1	8	291	0.16	211.2	-57.3	3.36	243.6	28.4	5.48	9.62
050104	13:24:47.79	46.6594	73.1327	4.1	1	6	318	0.01	71.5	-62.9	5.76	337.6	-1.9	5.9	13.09
050105	23:01:55.39	46.6578	73.1121	4.3	1.1	8	289	0.19	221.1	-46.4	3.44	246.2	40.7	5.77	10.6
050105	23:41:02.74	47.0629	72.7407	1.8	1.9	8	313	0.13	325.4	13.9	4.84	246.6	-38.1	5.87	9.34
050107	01:54:47.30	46.6736	73.1061	4.5	1.1	8	290	0.1	190.8	-52.7	2.91	247.7	22.5	4.96	7.23
050108	11:18:47.00	46.6673	73.1159	4.7	1.1	8	291	0.15	212.1	-52.1	3.21	245.4	33	5.28	9.4

050110	20:38:35.31	46.5835	71.8505	1.8	2.1	11	236	0.18	192	-2.2	3.02	281.2	21.6	5.97	9.41
050113	20:29:55.97	46.5408	71.9451	2.3	1.5	8	319	0.02	65.8	13	6.4	173.4	52.8	7.64	12.2
050116	16:41:40.25	45.9665	73.0984	7.5	1.4	6	197	0.06	152.5	19.4	2.64	247.4	13.4	7.64	9.53
050121	10:34:52.01	47.4219	73.1889	8.1	2.7	14	298	0.26	320	-0.1	4.07	229.9	-38.6	4.99	7.93
050126	02:18:51.00	45.4428	73.4394	10.0	2.8	34	271	0.38	31.3	-5.8	2.65	297.6	-31.7	3.99	5.64
050127	02:01:17.40	46.0361	73.7029	9.1	2.8	14	292	0.55	99.7	25.7	5.98	185.9	-7.7	6.47	10.32
050129	01:23:41.60	45.8969	72.9681	10.1	2.3	30	215	0.33	20.4	1.9	1.5	290.5	-3	3.02	5.82
050131	20:46:55.11	46.5439	71.9033	2.2	1.7	24	198	0.17	221.2	-0.6	1.02	310.9	32.1	3.14	5.35
050205	01:01:56.77	47.1894	74.5393	0.1	3.2	18	288	0.16	245.7	-55.1	3.32	341.8	-4.2	5.49	6.49
050210	14:57:03.65	45.9760	73.2296	10.0	2	15	202	0.38	346.4	-6.9	2.8	239.9	-67	7.46	12.67
050211	19:05:39.71	46.5574	71.8776	4.9	0.7	10	152	0.08	141.8	-13.1	1.46	231.9	-0.3	1.69	6.35
050213	18:51:16.74	46.5732	71.8620	6.9	2	55	93	0.21	211.2	1.6	0.76	301.5	10.2	1.13	3.39
050215	15:32:29.11	46.5542	71.8826	3.2	0.7	10	150	0.09	140.9	-13.5	1.48	231.1	-1.1	1.57	7.69
050217	08:57:13.17	48.2209	73.5156	0.1	3	28	318	0.34	204.8	-77.3	2.28	224.4	11.9	6.69	6.84
050217	20:06:47.86	46.5566	71.8835	2.8	0.6	8	152	0.13	69.5	-9.1	1.66	341	9.7	2.18	7.33
050219	07:55:05.99	48.2193	73.5419	0.1	3.3	15	284	0.39	176.8	-83.9	5.34	266.4	0	11.65	14.84
050225	01:09:17.43	46.7306	73.9180	10.0	2.5	32	207	0.24	329.5	-1.9	1.85	239.2	-7.9	3.41	8.14
050228	06:46:42.80	45.8834	72.9296	8.0	2.1	53	78	1.45	17.7	1.6	1.12	287.9	-8.2	1.79	4.04
050301	02:56:10.33	46.8967	73.5604	9.9	2.2	9	326	0.22	184.8	-59.6	5.9	251.6	13	7.89	13.44
050311	08:47:48.55	46.0044	73.9149	7.1	2.5	12	285	0.48	356.2	-31.4	5.52	251.5	-22.4	6.37	7.92
050313	17:57:58.17	47.1134	72.7682	6.1	1.4	9	174	0.12	353.1	-4.2	1.3	249	-73.3	3.65	7.94
050313	19:03:54.43	46.4284	73.2865	10.1	2.2	40	136	0.27	357	-3.6	1.72	266.9	-1.3	1.78	5.3
050314	15:37:00.87	45.7387	74.2790	0.1	2.9	14	306	0.3	26.6	-2.2	3.6	294.5	-42.8	5.29	10.34
050314	18:04:30.12	46.4791	73.3373	7.9	2.5	46	147	0.39	332.4	-0.2	1.15	242.4	-2.2	1.66	5.38
050319	06:59:58.43	45.9246	72.9895	6.0	2.9	59	88	1.81	5.4	-1.7	1.3	275.1	-8.5	1.89	3.46
050320	09:45:35.65	46.9030	75.4678	0.1	1.5	60	281	0.96	250	-71.5	3.68	198.8	11.8	8.91	10.41
050321	20:05:51.64	47.0976	72.7093	2.7	0.7	6	317	0.02	343.5	54.1	4.76	348.8	-35.7	5.5	10.4
050325	10:02:54.21	45.9665	73.0437	6.0	2.3	16	249	0.4	114.3	6.8	2.96	207.1	22.4	6.81	9.78
050326	09:15:53.30	47.0106	74.7667	8.9	3.4	13	267	0.36	351.5	-11.1	5.08	257.3	-20.4	7.45	14.32
050401	04:45:44.79	46.1057	73.5332	0.1	2.3	10	226	0.23	91	23	2.65	352.3	19.5	8.94	13.11
050401	21:43:39.01	47.8032	73.3304	0.3	2.2	15	222	0.18	232.2	-43.8	2.89	286	31.6	4.34	7.12
050403	09:00:39.14	46.8461	73.8699	6.9	2.8	9	264	0.2	32.8	-2.6	3.42	302.5	-6.3	7.11	19.89
050403	09:58:33.79	46.7448	73.8315	0.1	1.5	10	316	0.7	179.7	13.5	4.34	270.1	1.8	7.13	16.02
050403	10:30:55.97	46.8492	73.8372	0.2	2.6	8	333	0.3	227.1	2.4	9.7	317.4	6.5	14.27	18.36
050404	09:08:49.46	46.0013	73.5553	5.3	1.8	6	285	0.12	312.7	-19.9	6.83	357.9	62.8	11.27	19.48
050404	09:10:10.34	46.0298	73.5485	3.2	1.5	8	260	0.1	90.5	11.6	4.41	181.8	6.2	6.77	11.76
050412	03:46:56.89	45.8803	72.9548	8.0	2.3	61	153	0.4	25.2	2.5	1.1	295.8	-14.9	2.18	3.55
050412	06:45:56.57	47.3729	74.6347	2.9	3.2	25	269	0.43	62.3	62.4	2.97	335.7	-1.8	3.59	5.78
050415	10:01:20.41	46.3145	73.8369	3.0	2.7	30	242	0.29	355.2	-8.9	1.69	261.2	-24.2	3.36	7.71
050420	15:02:33.21	46.2267	73.7258	13.0	2.7	73	190	1.25	194.5	5.5	1.28	303.7	73.7	1.82	2.47
050421	19:44:28.45	47.8095	73.3251	4.4	1.5	9	227	0.18	230.5	-60.1	3.93	202.8	27	7.61	11.73
050423	01:41:23.63	46.6847	73.7208	0.2	2.6	8	339	0.2	261.6	-3.9	7.23	166.6	-51.7	13.43	17.5
050426	02:48:36.65	46.7433	73.1829	5.9	1.2	10	287	0.14	18.6	-6.5	2.19	60.3	81.4	4.4	4.66

050427	02:17:02.84	46.8018	73.8826	4.6	1.5	22	241	0.92	351.2	-5.5	3.55	5.6	84.3	7.1	9.29
050428	20:14:58.96	46.0424	72.9822	0.1	2.5	38	163	0.54	343.2	-58.9	3.71	235.6	-10.3	7.84	9.08
050502	03:55:52.43	46.8413	74.8347	2.6	3.2	27	281	0.26	272	-55.9	2.94	359.9	1.4	3.42	5.68
050503	10:18:02.52	48.4709	73.6415	0.1	3.4	37	276	0.57	42.7	80.6	1.83	310.1	0.4	4.08	5.86
050507	10:24:07.30	46.2529	73.7112	5.9	1.7	11	229	0.21	298.5	-24.3	5.13	25.8	6.1	6.16	8.31
050507	23:34:03.73	46.4759	73.7649	10.2	2.2	12	251	0.23	326.2	-5.3	2.63	234.8	-14.1	6.05	9.04
050508	02:21:04.30	46.7892	73.8835	0.1	1.5	13	313	0.69	120.5	53.8	6.73	296.8	36.1	9.12	15.87
050508	06:41:35.97	46.6752	73.7354	0.1	1.5	12	321	0.41	70.1	7.2	8.04	157.3	-20.8	11.36	12.72
050511	04:46:17.96	46.2766	74.1419	0.3	2.8	16	333	0.2	293.9	-30.8	4.71	208.5	7.6	6.87	9.2
050512	06:04:22.47	46.0282	73.0040	0.1	2.1	13	224	0.25	85.5	12.3	4.42	176.8	6.3	7.35	13.7
050514	16:11:56.22	46.3651	73.8055	1.7	2.5	16	244	1.68	342.6	-5.3	2.26	249.2	-33.1	5.45	9.41
050519	12:39:56.87	46.1247	73.5682	0.5	2.1	14	219	0.21	280.7	-27.6	1.97	194.4	7	6.38	11.09
050519	21:32:01.50	45.9159	73.0483	4.0	2.1	24	189	0.95	292.6	-1.8	2.24	202.4	-5.5	7.94	9.63
050520	20:38:14.56	47.8633	73.2966	0.1	2.2	20	169	1.05	114.5	77.7	3.96	307.2	12	6.87	8.9
050522	10:39:30.48	46.7116	72.4058	11.7	0.7	11	179	0.15	226.4	-0.3	1.45	316.3	5.8	1.91	3.88
050525	10:41:42.57	46.7970	74.8743	0.1	3.3	40	283	1	244.5	-81.1	1.64	197	6	3.87	5.57
050527	20:11:02.22	46.0488	73.0820	0.1	2.1	10	253	0.13	59.5	8.3	4.28	331.1	-10.7	6.28	14.04
050530	15:36:24.82	46.8334	73.8616	10.1	2.4	16	218	0.25	320.5	-0.8	2.42	230.5	-4.7	4.62	9.1
050604	15:08:06.10	47.6720	74.6743	0.6	3.1	22	293	0.27	36	49.6	4.29	303.3	2.3	4.83	10.46
050604	18:35:34.27	47.4868	74.4729	0.4	3.4	32	285	0.51	60.6	56.7	2.39	336.4	-3.8	2.83	5.43
050607	07:12:19.69	45.2387	73.9883	0.1	1.5	16	290	0.54	36.3	-19.7	4.57	282.1	-48.6	5.22	8.36
050617	05:40:51.45	46.2639	72.6691	29.6	1.5	8	295	0.06	76.8	-12	5.63	6.5	57.5	9.45	11.46
050617	20:45:44.29	46.6721	73.7956	5.7	2.8	11	275	0.26	358.4	24.5	3.35	271.8	-7.2	5.72	7.99
050702	15:11:13.97	46.1278	73.6364	19.0	2.7	10	280	0.38	327.9	-9.3	6.57	232.4	-30.4	10.9	13.14
050705	13:57:27.37	46.4537	73.3486	7.9	2.5	27	252	0.42	2.7	4.6	2.52	274.1	-17.4	4.33	7.51
050706	04:28:13.99	45.8953	72.9251	8.0	2.3	35	200	0.56	19.3	4.1	1.61	290	-10.7	2.84	4.62
050713	06:01:38.53	45.7640	73.3792	10.1	2.6	14	278	0.32	25.1	2.6	3.68	295.8	-15.5	5.91	10.03
050713	18:28:53.51	46.6831	73.9262	10.0	2.8	44	256	0.3	1.5	21.9	2.62	278.2	-16.4	3.26	6.26
050714	14:31:20.00	46.8239	73.8947	24.8	2.5	7	309	0.1	202.2	9.5	5.26	291.8	-2.7	11.71	19.73
050718	04:09:53.08	44.8021	73.1537	0.1	3.2	32	303	0.57	192.7	69.5	3.61	281.7	-0.4	4.88	9.28
050725	02:57:36.03	47.4963	74.4020	0.1	3	38	286	0.43	48.4	60.8	2.43	339.3	-11.2	3.43	5.92
050801	07:19:10.17	46.8113	73.9327	5.7	2.6	14	286	0.34	41.2	10.5	3.75	321	-42.6	5.32	8.29
050804	03:43:19.70	46.6325	73.2987	3.3	1.8	18	306	0.12	3.9	4.4	2.03	275.1	-15.1	3.51	7.43
050809	11:06:46.16	46.7401	73.1601	5.0	1.5	12	299	0.09	175.8	-18	2.62	87	3.5	3.88	4.01
050820	13:43:13.01	46.7322	73.1585	5.8	0.8	7	288	0.07	45	-66	3.25	13.1	20.6	3.97	5.11
050821	08:28:58.48	46.0298	73.0472	1.1	2.4	8	314	0.21	62.9	3.2	4.25	333.4	-10.7	6.5	15.26
050825	16:34:19.48	47.3856	73.1992	9.1	2.4	34	198	0.34	346.9	3	1.48	257.4	-8.7	2.75	4.67
050827	08:26:38.64	46.6088	73.2846	1.8	1.5	17	291	0.14	6.8	2.7	1.97	278.2	-27.8	3.5	7.63
050829	16:04:20.28	46.7939	74.8883	0.1	3.3	22	309	0.32	264.6	-64.4	3.06	244.7	24.2	6.3	7.34
050903	05:20:18.04	47.3579	72.4883	2.4	2.3	47	138	0.43	123.3	-56.6	1.49	258.9	-25.1	1.96	3.32
050903	17:55:27.85	46.7868	73.1547	4.6	2.1	45	205	0.29	355.7	0.9	1.19	266.2	-27.9	2.27	2.9
050908	06:59:28.64	46.2006	74.3301	8.9	2.9	12	309	0.29	276.8	-44.9	5.45	339.6	24.6	6.65	10.17
050910	23:52:13.65	46.7338	73.1006	11.6	1.5	10	255	0.19	168	-1.5	2.45	257.1	29.3	4.52	8.34

050912	01:11:51.62	46.7986	73.6193	0.2	2.1	9	327	0.37	242.3	-15.5	7.37	255.2	74	11.84	19.09
050912	17:37:50.15	46.2291	74.2504	0.6	2.7	8	346	0.23	292.2	-19.6	8.26	321.5	67.7	12.81	18.98
050913	09:50:13.69	46.2069	74.3388	7.9	2.9	16	308	0.26	68.7	30	4.67	164.2	9.6	5.58	8.71
050925	09:30:25.11	47.4536	73.3170	9.7	2.3	16	296	0.22	315.6	0.8	2.42	225.8	-16.3	4.95	9.81
050929	01:35:12.00	46.3525	73.9073	16.9	2.6	14	279	0.24	231	-1.8	5.04	321.5	-16.9	5.74	10.25
050930	05:57:40.13	46.2417	74.0300	10.0	2.6	16	285	0.32	243.7	-4.1	4.63	335.9	-28.6	5.94	10.56
051002	03:26:11.39	45.9285	73.0107	10.1	2.2	25	236	0.36	31.1	-1.1	2.31	300.5	-27.1	4.55	6.21
051003	11:42:11.65	45.9586	72.9921	6.0	2.5	31	249	0.43	33.7	-6.9	2.71	298.6	-36.4	3.75	6.76
051003	23:22:31.26	47.7890	73.1739	5.2	2.1	13	332	0.2	119.9	70.9	3.38	340.4	14.8	4.84	7.59
051009	12:07:17.64	45.9206	72.9637	7.1	2	16	218	0.37	28.6	-1	1.7	297.2	-54.6	5.38	9.32
051011	22:30:29.70	47.4520	73.2587	10.0	2.2	16	216	0.24	319.3	2.4	2.22	234.2	-64.1	5.46	9.15
051015	09:49:53.97	46.3873	73.9368	15.2	2.7	28	288	0.25	37	5.1	3.41	308	-11.6	3.87	8.96
051022	01:35:12.97	47.3602	73.1221	0.1	2.5	36	185	0.25	321.3	-1.4	1.69	229.6	-48.5	3.02	7.11
051026	10:13:58.57	46.8144	74.8802	0.1	3.2	13	314	0.49	255.7	-76.7	3.88	248	13.1	7.54	13.04
051108	22:54:08.72	46.3525	74.0082	0.1	1.5	18	297	0.33	289.4	-25.5	4.3	197.2	-4.6	6.67	9.74
051110	16:55:22.31	45.9570	73.5680	9.0	2.7	56	192	0.39	2.8	-3.9	1.49	272.4	-4.5	2.27	3.9
051112	02:27:10.92	45.3653	72.2590	99.9	1.5	25	173	0.4	50.8	-78.6	4.41	249.7	-10.7	10.1	13.24
051113	06:04:32.37	44.8638	72.8115	0.1	3.1	51	202	0.65	351.7	-74.1	1.98	220.1	-10.6	3.4	4.93
051120	10:27:07.46	46.2893	73.7839	0.1	2.6	14	319	0.29	304.7	-28.8	5.05	209.9	-8.6	6.58	9.84
051129	07:14:25.65	45.9048	72.9378	10.0	2.2	24	201	0.32	14.9	-0.7	1.41	284.8	-3.1	3.31	5.69
051201	04:05:24.10	46.6436	73.7102	0.1	2.5	20	283	0.44	325.8	-18.9	4.4	229	-19	4.74	9.56
051203	18:45:29.87	46.0092	72.8600	0.1	2.1	19	232	0.28	108.9	35.6	4.31	226.2	32.6	4.74	11.99
051205	00:55:20.51	44.3591	74.4296	0.1	1.5	31	314	0.86	330.8	-56.6	6.38	250.8	6.5	11.42	18.17
051215	23:28:58.08	46.7369	74.8778	0.1	3.4	20	309	0.76	254.4	-65.9	2.78	249.9	24	4.98	13.01
051217	04:50:34.29	45.9095	72.9124	10.1	2.3	10	271	0.24	335.8	-6	6.15	242.7	-27.1	8.85	13.54
051217	20:33:03.91	46.3715	73.9060	16.9	2.5	12	318	0.16	23.8	-10	4.84	291.3	-13.5	5.49	12.06
051217	21:48:45.49	45.0489	73.1866	10.1	2.6	19	229	0.32	273	-2.5	1.89	185.1	40.3	3.76	6.84
051218	12:46:01.44	45.1692	74.3613	0.1	3.4	16	297	0.56	27.1	-44.9	4.72	271.5	-23.3	7.33	13.42
051220	22:37:14.56	47.4354	72.3866	0.0	1.5	20	228	0.35	326.3	64.7	2.09	300.3	-23	4.9	6.53
051226	06:14:04.87	48.2573	73.5766	0.1	3.4	14	333	0.38	206.4	-36.8	7.02	268.4	32	9.39	18.52
051228	08:12:28.99	46.6499	73.7927	2.1	1.5	12	286	0.68	138.9	-16	6.76	53.4	15.1	9.41	10.13
051229	15:43:19.71	46.9347	74.2894	6.9	1.5	10	319	0.21	18.5	6.7	5.42	290.1	-13.2	6.49	19.85

APPENDIX B

Catalogue of events processed in Chapter 4. Column headers: **Date** and **Origin Time** of event occurrence GMT time; **Lat.** and **Lon.** coordinates of epicentre in degrees; **Dep.** hypocentral depth in km; $\mathbf{M_L}$ local magnitude; **NO** number of observations; **DM** minimum distance to nearest station in km; **GAP** angle of non-coverage; **RMS** in seconds; **Columns 12-16:** strike and dip angles, and length (km) of semi-axis of 68% confidence error ellipsoids.

Date ymmdd	Origin Time	Lat. S (deg)	Lon.W (deg)	Dep. (km)	M_L	NO	DM	GAP	RMS	STK/DIP Axis1	LEN Ax1	STK/DIP Axis2	LEN Ax2	LEN Ax3
70707	05:46:17.42	45.3738	72.9807	6.8	2.640	10	15.35	246	0.03	320.5/-0.5	0.63	050.7/-18.9	0.82	2.08
70707	14:06:59.48	45.5127	73.1132	7.04	3.342	10	26.27	286	0.05	328.9/0.1	1.16	058.9/-4.3	1.71	6.71
70707	23:57:47.38	45.5153	73.1132	7.04	1.951	9	26.35	287	0.04	331.2/-1.5	1.18	061.3/-2.9	1.65	6.51
70708	00:21:21.53	45.5001	73.1026	13.1	3.717	10	25.12	283	0.04	321.7/1.8	1.28	051.4/-10.4	1.78	6.68
70708	07:00:59.56	45.5115	73.1078	13.39	3.183	10	25.83	286	0.06	329.4/0.1	1.34	059.4/-8.9	1.77	7.44
70709	06:30:45.10	45.695	72.6283	18.68	1.529	8	18.96	337	0.02	238.7/3.0	1.44	320.1/-70.7	4.01	17.4
70710	00:26:39.11	45.3726	72.942	7.81	1.440	9	12.38	238	0.03	328.2/2.8	0.64	056.4/-31.2	0.9	1.88
70710	01:01:31.85	45.377	72.9473	6.8	2.066	10	12.72	240	0.04	259.4/25.1	0.75	160.4/18.5	0.8	2.03
70710	01:02:32.91	45.7443	72.6253	5.94	1.832	8	24.18	342	0.01	241.0/-5.0	1.92	339.0/-58.2	8.23	24.8
70710	19:17:10.85	45.4298	73.0775	4.63	1.543	8	22.58	326	0.03	222.7/3.9	1.3	131.9/11.4	1.36	5.05
70710	20:56:31.09	45.5159	73.0834	2.76	3.108	10	24.15	285	0.05	140.2/6.2	1.29	049.2/8.9	1.83	6.3
70710	23:34:06.57	45.5064	73.0934	3.61	1.151	6	24.6	338	0.03	279.5/60.6	8.03	151.0/19.3	9.39	14.7
70711	07:43:26.65	44.6255	73.719	19.44	2.927	10	81.51	317	0.09	317.0/-10.4	3.62	050.7/-19.7	8.27	17
70711	08:18:50.68	45.9114	72.9195	0.12	2.299	8	44.57	344	0.11	179.0/-3.0	4.15	089.9/16.3	11.9	14.8
70711	11:13:24.36	45.5232	73.0792	2.43	1.876	10	24.1	286	0.03	289.1/-13.0	1.09	017.4/7.5	1.16	3.66
70712	04:29:47.31	45.5184	73.0887	2.42	2.081	10	24.63	286	0.04	151.3/2.6	1.66	061.1/5.0	2.05	7.76
70713	07:17:25.27	45.2969	73.0347	4.69	2.413	10	22.05	246	0.01	146.6/8.4	0.84	055.9/4.6	1.63	3.42
70714	00:47:11.06	45.5184	73.0851	2.3	2.246	10	24.37	286	0.05	311.4/-3.8	1.77	041.0/7.0	2.4	8.38
70717	03:39:31.96	45.2931	73.0294	5.33	2.284	10	21.89	245	0.02	147.3/4.9	0.88	057.2/0.7	1.59	3.8
70717	04:01:53.22	45.3007	73.0275	4.34	2.274	10	21.35	245	0.03	133.8/10.0	1.02	225.2/8.1	1.68	3.74
70717	04:06:45.44	45.2837	73.0323	7.33	2.347	8	22.62	342	0.01	307.5/-2.9	1.23	218.5/20.1	2.02	4.86
70717	05:22:56.04	45.5032	73.0908	3.81	2.171	10	24.31	283	0.04	152.6/3.4	1.17	062.5/0.8	1.61	6.36
70717	06:10:13.35	45.3808	72.9265	7.61	1.908	10	11.06	237	0.03	334.7/0.9	0.56	064.0/-37.2	0.83	1.59
70717	08:24:52.29	45.3779	72.9234	7.6	1.853	10	10.86	236	0.04	349.9/-9.5	0.7	086.2/-33.0	0.81	1.59
70719	06:45:45.21	45.3868	73.062	7.01	2.322	10	21.58	260	0.01	329.3/-1.8	0.77	059.5/-6.1	1.09	3.76
70720	04:56:57.84	45.4115	72.711	4.48	3.693	10	6.15	273	0.05	099.6/33.1	7.68	100.9/-56.9	14.7	72.9
70720	05:35:18.64	45.3817	73.0603	9.75	2.440	10	21.46	259	0.04	329.2/1.3	0.84	058.9/-11.6	1.47	4.18
70720	09:11:46.78	45.3887	73.0539	7.28	2.465	10	20.94	259	0.04	314.8/-2.5	0.97	045.3/-10.3	1.09	4.04
70722	01:27:33.75	45.6469	72.6838	23.11	1.940	8	12.58	332	0	239.1/2.4	1.46	321.1/-73.5	3.62	17.8
70722	02:06:06.87	45.5792	73.1203	1.13	2.330	10	29.65	299	0.05	152.3/1.8	1.79	061.8/14.2	2.22	8.72
70722	03:03:11.17	45.5729	73.1276	1.02	2.280	8	29.82	330	0.04	135.1/6.6	2.21	044.2/7.4	3.29	9.74
70722	09:54:44.00	45.6975	72.6355	17.52	1.670	8	19.02	338	0	239.3/-2.3	1.69	332.4/-53.5	7.05	22
70723	04:47:07.62	45.3893	73.053	6.66	1.802	8	20.87	328	0.03	119.5/7.0	1.12	031.2/-13.9	1.31	4.38
70723	10:29:53.56	45.576	73.1231	0.99	2.897	10	29.67	298	0.06	141.3/0.2	1.63	051.3/9.5	2.46	8.66

70723	11:33:55.58	45.4184	73.0795	7.3	2.466	10	22.88	267	0.03	337.4/-3.3	0.92	067.7/-4.3	1.22	4.19
70723	11:45:59.06	45.3944	73.0601	5.21	2.285	8	21.43	328	0.03	007.5/-13.2	1.31	098.2/-3.2	1.69	5.06
70724	09:23:34.75	45.4286	73.0902	7.01	2.517	12	23.58	254	0.03	147.1/1.8	0.81	237.1/1.0	1.18	3.69
70727	18:14:10.38	45.445	73.0719	3.87	2.043	8	22.05	324	0.04	238.6/-3.3	1.27	329.4/-13.9	1.72	4.85
70728	13:22:35.65	45.5811	73.1194	1.11	1.805	8	29.7	330	0.03	206.0/-1.2	2.54	116.2/10.4	2.63	9.54
70728	14:43:30.27	45.5766	73.1276	0.9	2.755	8	30.02	330	0.04	140.2/5.1	2.29	049.5/7.5	2.67	10.5
70728	19:22:33.08	45.5804	73.1257	0.79	2.173	8	30.09	330	0.05	162.6/1.0	2.66	072.4/9.6	2.69	11
70729	19:01:39.18	45.5722	73.1285	1.05	2.811	11	29.85	284	0.06	138.6/1.4	1.4	048.2/18.3	1.86	7.12
70730	06:55:39.80	45.5766	73.1239	1.02	2.312	9	29.77	285	0.05	150.6/4.9	2.18	059.6/11.7	2.52	10.2
70801	13:44:21.72	45.6937	73.46	0.12	2.447	8	59.04	344	0.11	071.4/-0.8	3.41	161.4/1.3	7.17	15.2
70801	16:39:15.42	45.5672	73.1358	1.05	2.488	11	30.11	283	0.05	310.0/-4.5	1.37	038.2/21.2	2.25	7.05
70802	00:32:06.82	45.3821	72.9454	7.76	2.434	12	12.52	228	0.04	331.7/1.1	0.56	061.0/-31.1	0.79	1.85
70802	01:17:20.79	45.402	73.0888	8	1.957	10	23.7	265	0.02	331.6/-3.9	1.02	062.0/-6.8	1.24	4.77
70802	04:14:56.80	45.383	72.9468	6.72	1.750	8	12.61	320	0.03	013.2/-29.2	0.82	110.3/-12.5	1.01	1.98
70802	19:35:24.17	45.3779	72.9234	7.07	1.687	8	10.86	319	0.02	244.7/36.0	0.69	327.1/-10.4	1.4	1.53
70802	19:58:58.71	45.3764	72.9248	7	1.373	8	11	320	0.01	234.4/36.3	0.63	143.2/1.7	0.72	1.59
70803	01:14:19.83	45.4286	73.0794	4.57	2.017	12	22.74	253	0.04	147.5/6.7	0.96	056.6/7.1	1.13	3.8
70803	06:33:28.19	45.5051	73.1856	9.95	2.495	12	31.56	273	0.07	315.8/4.3	1.31	045.5/-4.2	1.82	6.35
70803	08:40:43.48	45.3134	73.0578	4.51	2.594	12	22.9	232	0.05	144.2/9.6	0.89	053.5/4.5	1.51	3.64
70804	22:03:54.37	45.383	73.0098	7.3	2.311	10	17.52	237	0.04	312.7/-2.3	0.94	223.5/19.3	1.29	3.28
70807	10:52:23.50	45.4298	73.0974	6.84	2.795	12	24.12	254	0.05	335.0/-2.7	0.96	065.1/-1.8	1.34	4.47
70807	18:06:36.70	45.302	73.031	4.45	2.162	10	21.53	227	0.01	130.7/9.5	1.1	043.4/-15.6	1.85	4.3
70809	23:00:59.56	45.383	72.945	7.65	2.279	8	12.47	319	0.01	220.6/43.1	1.19	163.2/-30.0	1.74	2.56
70810	04:43:09.41	45.3223	73.0577	3.93	2.478	8	22.55	337	0	296.0/-8.0	1.33	208.8/19.2	1.8	5.33
70810	11:50:02.63	45.3707	72.9501	7	2.058	8	13.04	324	0.01	265.1/22.2	0.68	167.1/18.8	0.77	2.01
70811	04:15:38.50	45.8962	72.9416	0.12	2.642	8	43.65	343	0.1	009.4/4.4	3.28	099.2/-2.4	5.37	12.3
70811	08:13:28.36	45.3738	72.9483	7.44	3.712	12	12.84	227	0.04	326.2/1.1	0.62	055.5/-30.3	0.78	2.01
70812	13:51:05.16	45.5583	72.7618	7.74	3.248	10	3.91	293	4.72	106.3/-78.8	7.99	109.2/11.2	13	26.5
70814	14:46:09.95	45.2748	73.0342	6.81	2.261	8	23.28	343	0.02	308.8/-5.9	1.3	221.0/20.5	2.19	5.19
70814	17:21:00.75	45.3866	73.0555	8.55	2.704	18	3.14	127	0.04	269.7/-36.2	0.27	336.7/28.1	0.65	0.95
70814	20:46:59.28	45.3835	72.9461	7.27	2.253	14	3.36	194	0.02	091.4/10.9	0.18	084.4/-79.0	0.47	0.65
70815	17:14:19.88	45.3819	72.9835	7.08	1.366	13	3.1	198	0.03	269.9/-19.3	0.21	275.4/70.6	0.51	0.81
70816	08:47:52.79	45.3865	72.9462	7.26	1.987	15	3.08	101	0.03	091.8/11.7	0.18	060.5/-76.4	0.49	0.65
70816	13:02:58.38	45.4014	73.0753	8.09	2.248	15	1.12	96	0.04	091.0/41.2	0.27	062.8/-45.1	0.71	0.84
70816	20:40:27.38	45.2821	73.0408	7.12	2.097	14	13.83	285	0.03	080.3/12.1	0.47	169.4/-4.1	0.77	2.05
70817	00:36:06.68	45.4624	73.0729	4	1.323	12	3.21	240	0.06	135.4/36.3	0.31	062.1/-21.4	0.84	2.82
70817	01:28:51.61	45.4767	73.0714	4.63	1.488	12	4.78	246	0.05	138.4/32.2	0.29	058.8/-16.0	0.75	3.21
70817	12:59:34.20	45.3847	72.9461	7.22	3.017	14	3.25	193	0.03	092.0/9.0	0.19	028.1/-70.1	0.56	0.68
70818	20:33:49.67	45.3855	72.9665	7.6	1.587	10	14.14	231	0.03	312.1/0.3	0.8	222.0/25.4	0.85	2.4
70819	07:42:16.97	45.9165	72.9267	0.12	4.426	10	45.29	335	0.13	186.4/-11.1	3.32	096.8/2.1	4.9	11.3
70819	08:50:29.55	45.8608	72.9641	0.12	2.571	10	40.84	336	0.09	030.2/5.8	2.93	119.6/-5.9	4.4	10.9
70819	09:24:31.88	45.8912	72.9199	0.12	2.409	10	42.47	334	0.12	200.8/-10.7	3.18	110.4/-2.1	5.41	10.8
70819	11:29:14.63	45.2191	73.0351	3.32	2.850	12	27.24	220	0.06	154.4/1.8	1.48	064.3/0.5	3.42	7.95
70819	15:38:09.31	45.1976	73.0337	12.46	2.374	10	28.89	218	0.03	324.5/-2.7	1.72	054.9/-8.9	3.47	7.14
70821	00:23:19.25	45.3871	72.9444	7.52	1.865	8	12.41	318	0.01	014.0/-25.3	0.68	112.8/-18.0	0.87	2.83
70824	07:51:44.73	44.6673	72.7419	7.97	2.530	12	10.51	171	0.13	002.7/-31.9	2.22	157.0/-55.3	3.17	6.65

70824	15:32:05.00	45.3754	72.9487	8.18	1.787	10	12.85	227	0.03	323.5/1.5	0.74	052.5/-31.0	0.84	2.09
70831	03:22:35.20	45.3792	72.673	13.94	1.893	8	8.93	328	0.02	182.3/8.1	1.03	085.8/38.5	2.76	10.1
70831	19:56:36.80	45.6532	72.8231	9.2	3.569	7	15.23	318	0.03	110.9/-9.1	2.86	329.1/-78.5	5.8	19.6
70901	13:27:02.06	45.3729	72.9542	6.84	2.296	10	13.31	227	0.04	243.7/27.5	0.78	148.3/10.3	0.85	2.25
70902	00:50:41.06	45.3789	72.9851	6.42	1.478	14	8.56	147	0.03	091.2/15.0	0.22	182.4/4.5	0.53	1.37
70902	17:24:32.47	45.4165	73.0859	10.19	3.035	12	23.4	251	0.04	329.4/3.6	0.83	058.8/-9.4	1.31	4.06
70902	23:34:22.14	45.3653	72.9057	7.65	2.089	15	9.82	97	0.04	283.4/1.1	0.21	193.3/6.0	0.56	1.04
70905	12:07:16.07	45.3783	72.9788	8.69	1.739	14	3.4	202	0.02	268.2/-13.7	0.2	312.2/71.3	0.58	0.72
70906	16:23:22.95	45.4561	73.1263	4.76	2.033	15	4.23	277	0.04	165.4/59.5	0.26	171.0/-30.4	0.75	0.99
70908	19:48:03.88	45.3764	72.9185	7.49	2.705	18	10.51	103	0.05	280.8/-0.3	0.21	190.8/12.3	0.57	1.07
70912	01:23:57.30	45.4396	73.1401	4.7	2.355	17	4.56	259	0.05	358.9/-55.0	0.25	143.8/-29.8	0.38	0.64
70912	03:39:27.96	45.3787	72.9781	5.81	1.917	23	3.33	110	0.05	258.8/-23.1	0.22	345.1/8.4	0.53	0.67
70912	04:35:46.81	45.3757	72.9537	6.56	1.708	13	3.86	183	0.03	261.3/-22.3	0.25	122.4/-61.4	0.47	0.98
70912	06:29:00.67	45.3724	72.9656	8.97	1.650	17	4.01	188	0.03	083.4/12.6	0.21	161.4/-42.9	0.53	0.63
70914	23:30:14.39	45.3859	73.0481	9.15	1.657	17	3.69	110	0.05	098.3/29.9	0.28	179.1/-15.7	0.63	0.84
70916	01:06:59.57	45.3734	72.9111	7.04	2.046	17	6.07	88	0.03	089.0/9.6	0.2	175.0/-22.5	0.4	0.74
70917	23:23:03.44	45.3904	73.0617	7.65	2.378	25	2.51	104	0.04	263.6/-34.1	0.23	345.5/11.8	0.36	0.68
70925	17:09:18.26	45.3854	73.0605	8.17	2.267	24	2.9	111	0.03	088.4/35.2	0.22	169.4/-12.4	0.36	0.69
70926	20:14:24.44	45.373	72.9138	6.96	2.400	20	5.93	145	0.03	089.2/6.5	0.16	177.2/-17.0	0.35	0.52
70929	02:29:59.43	45.3721	72.9747	8.96	1.950	20	4.03	138	0.04	091.0/13.4	0.19	175.6/-21.7	0.44	0.68
71005	20:31:15.41	45.1378	72.9751	10.55	3.963	28	22.37	160	0.06	052.2/3.8	0.41	142.2/-0.4	0.56	3.51
71006	08:12:21.26	45.1359	72.9733	8.02	3.723	28	22.62	160	0.07	066.3/3.8	0.44	156.2/-1.7	0.61	2.7
71006	13:12:13.97	45.4023	73.1343	8.31	2.579	26	3.48	236	0.05	260.2/-56.5	0.4	327.9/14.1	0.51	0.8
71007	08:04:25.29	45.1334	72.9707	8.02	2.622	26	30.55	166	0.06	222.1/-3.1	0.51	132.0/-1.9	0.57	3.26
71008	05:13:15.01	45.141	72.9696	8.37	1.698	26	22.23	159	0.04	214.5/-2.6	0.36	124.6/1.8	0.47	3.1
71009	21:18:01.38	45.1451	72.9709	7.25	2.439	26	21.77	158	0.06	252.2/-3.3	0.46	342.2/-0.3	0.7	3.43
71009	22:47:38.81	45.1425	72.9763	10.39	2.503	26	21.85	160	0.06	244.9/-4.2	0.43	334.8/1.2	0.65	3.47
71009	23:33:46.82	45.1372	72.9733	8.02	2.010	26	22.49	160	0.05	063.5/3.4	0.38	153.5/-0.8	0.57	2.71
71010	00:41:31.80	45.1378	72.9769	9.36	2.839	26	22.31	160	0.04	214.8/-2.5	0.37	124.8/1.7	0.5	3.39
71010	02:34:48.27	45.1365	72.9724	8.02	2.336	26	22.59	160	0.06	255.0/-3.6	0.43	344.8/3.2	0.72	2.88
71010	21:01:29.61	45.1384	72.9778	8.25	3.635	28	22.22	161	0.06	046.7/4.1	0.41	136.7/0.4	0.61	2.99
71010	22:02:45.02	45.1353	72.9742	8.02	2.406	28	22.66	160	0.06	069.4/3.3	0.41	159.2/-2.1	0.57	2.7
71011	00:17:15.00	45.1413	72.9746	9.69	2.679	26	22.03	160	0.07	245.8/-2.6	0.46	335.9/-1.0	0.67	3.86
71011	04:36:06.72	45.1346	72.9715	8.02	2.357	24	22.81	160	0.06	067.5/3.5	0.43	157.4/-1.7	0.68	2.82
71011	06:26:18.96	45.1359	72.9706	8.02	2.116	26	22.71	159	0.06	057.1/4.1	0.44	147.0/-1.2	0.59	3.06
71011	10:51:03.23	45.1289	72.969	8.95	2.669	26	23.47	183	0.06	070.9/3.3	0.44	160.7/-2.0	0.73	3.19
71011	12:37:23.79	45.1324	72.9657	11.61	1.885	21	23.22	159	0.04	258.7/-4.9	0.56	348.3/5.3	0.91	4.58
71011	21:22:32.71	45.1302	72.9698	10.03	3.128	28	23.31	160	0.06	047.8/5.2	0.41	137.6/-1.9	0.57	2.92
71011	22:30:56.45	45.1387	72.9674	10.33	1.852	20	22.53	158	0.05	246.7/-4.2	0.47	336.6/1.1	0.85	3.96
71012	04:24:23.26	45.1289	72.969	9.12	2.502	28	23.47	160	0.06	217.2/-4.2	0.42	127.1/-0.3	0.54	2.8
71012	15:38:38.23	45.3797	72.9187	6.9	2.312	21	5.16	139	0.03	089.5/7.4	0.15	177.4/-15.7	0.34	0.51
71013	10:50:30.01	45.3762	72.9786	5.39	1.772	24	3.62	61	0.05	084.0/21.6	0.18	174.2/0.7	0.34	1.32
71016	06:09:17.16	45.386	73.0587	7.84	2.650	22	2.97	147	0.04	253.4/-36.5	0.24	336.6/9.1	0.57	0.79
71019	21:49:15.53	45.3819	73.061	8.81	3.576	25	3.13	116	0.04	095.4/29.4	0.31	167.4/-28.8	0.49	0.84
71022	13:36:26.84	45.383	73.0441	10.27	2.334	12	20.19	313	0.03	133.3/-8.2	0.89	042.2/-7.3	0.93	3.1
71023	05:36:17.23	45.365	73.007	6.04	1.930	14	17.52	307	0.02	177.4/1.5	0.63	087.2/7.7	0.69	1.65

71025	15:21:57.37	45.3697	73.0956	8.03	2.171	6	24.3	321	0.02	193.3/1.8	3.85	261.0/-85.3	9.27	31.2
71026	12:04:01.97	45.3745	72.9167	7.03	2.563	14	10.41	295	0.02	015.5/2.3	0.41	104.5/-23.6	0.6	0.81
71029	00:17:05.42	45.3757	72.95	6.8	1.519	16	11.3	148	0.03	289.2/-6.5	0.16	019.2/0.2	0.45	1.23
71030	00:25:03.73	45.3738	72.9132	7	1.851	18	10.15	144	0.04	098.8/-1.3	0.23	008.8/3.0	0.41	0.75
71108	02:04:38.56	45.3681	72.9043	6.74	1.414	12	9.62	159	0.03	131.6/-4.8	0.43	039.4/-24.5	0.58	0.8
71108	15:14:29.72	45.4086	73.0964	13.66	1.741	10	1.27	224	0.04	301.4/-26.1	0.47	305.3/63.9	1.11	1.64
71109	10:02:13.58	45.3876	73.0564	7.17	2.422	24	3.75	129	0.05	296.5/-29.8	0.25	018.5/13.8	0.5	1.3
71110	07:37:10.92	45.3802	72.9851	6.36	1.661	15	9.36	129	0.03	094.7/18.1	0.22	182.4/-6.8	0.56	1.62
71112	23:38:51.59	45.9013	73.0288	5.24	2.729	14	47.25	292	0.09	119.9/-1.3	1.39	210.1/-7.1	2.85	9.56
71113	00:37:22.41	45.3813	72.9177	7.01	1.800	16	10.38	138	0.02	103.8/-0.1	0.17	013.8/-0.9	0.36	0.72
71113	04:38:30.76	45.2314	73.0587	8.22	1.760	18	10.26	259	0.05	243.9/-18.1	0.4	336.4/-7.4	0.87	1.85
71113	04:54:21.99	45.5314	73.1423	6.48	1.966	15	15.2	276	0.05	144.5/9.2	0.44	052.5/12.3	1.17	2.44
71113	11:48:03.81	45.3754	72.9703	6.43	1.607	8	10.95	174	0.02	303.2/-12.6	0.26	236.6/60.7	1.69	2.44
71113	15:21:11.49	45.5282	73.1423	6.45	2.290	12	14.85	279	0.04	146.0/11.1	0.45	054.0/10.4	1	2.34
71114	02:51:07.87	45.3903	73.0786	13.78	1.536	17	2.02	124	0.04	107.5/24.8	0.43	172.6/-42.4	0.91	1.45
71115	07:14:00.60	45.4102	73.4051	21.07	4.070	21	23.7	323	4.01	192.0/-37.7	4.07	349.7/-50.1	4.41	26.5
71116	01:53:12.82	45.2368	73.9551	15.07	3.300	21	68.36	312	0.13	296.9/-7.3	2.53	026.2/5.6	3.58	9.79
71116	08:06:34.71	45.1299	73.129	27.85	3.694	15	21.46	222	3.74	072.7/27.7	5.87	261.9/62.0	8.13	68.4
71116	15:30:22.12	45.4172	73.0958	8.64	1.483	6	2.19	233	0.02	187.0/14.2	5.21	061.5/66.5	7.11	16.8
71120	00:04:50.54	45.3764	72.9455	7.61	1.553	16	12.47	149	0.04	287.7/-7.2	0.2	017.2/3.8	0.54	1.32
71120	05:46:12.57	45.3852	73.0445	8.31	2.439	21	4.72	128	0.04	287.4/-24.5	0.28	013.8/8.0	0.59	1.38
71120	06:49:32.40	45.7962	72.7057	14.03	1.517	10	28.86	347	0.03	237.0/-3.1	1.88	330.2/-46.0	6.7	21.3
71120	10:27:02.49	45.5425	73.1552	5.97	2.428	18	16.63	278	0.07	145.7/10.3	0.55	052.2/18.8	1.12	2.9
71120	13:15:07.41	45.5437	73.1588	6.14	1.861	14	16.85	284	0.08	138.8/9.3	0.61	047.8/6.4	1.33	3.3
71121	02:22:29.96	45.389	73.0877	8.75	2.936	23	1.5	131	0.05	296.2/-18.6	0.51	020.1/17.6	0.85	1.44
71121	07:37:20.02	45.3746	72.9494	6.88	1.535	17	12.22	140	0.03	282.9/-6.3	0.23	013.2/-2.7	0.48	0.96
71126	07:55:19.37	45.3871	73.0372	6.01	2.529	18	5.21	132	0.04	101.2/30.5	0.23	187.3/-6.4	0.49	1.41
71128	05:44:03.53	45.482	73.1168	7.76	2.544	21	9.43	266	0.06	136.8/17.0	0.37	044.3/7.9	0.92	1.3
71130	05:10:32.87	45.3889	73.0564	6.79	2.472	21	3.71	131	0.04	289.4/-33.1	0.24	011.8/11.6	0.47	1.3
71204	10:39:11.56	45.3851	73.0325	6.4	1.731	14	5.62	130	0.03	290.4/-27.8	0.21	015.8/8.6	0.48	1.4
71205	10:37:37.10	45.3821	73.0607	9.94	1.888	14	3.69	118	0.05	292.5/-26.2	0.38	012.3/19.9	0.78	1.72
71206	03:01:42.71	45.3889	73.0482	6.18	2.232	22	4.32	133	0.05	302.3/-29.8	0.24	024.4/13.6	0.56	1.54
71208	13:24:26.51	45.9203	73.0449	3.43	4.421	21	49.71	295	0.18	299.4/-0.3	2.01	029.4/12.1	2.92	10.4
71210	11:13:09.90	45.3906	73.0511	6.61	2.583	16	4.06	135	0.03	298.6/-30.5	0.22	020.7/13.2	0.49	1.49
71211	23:55:04.37	45.3775	72.9656	8.46	2.398	17	10.91	124	0.02	283.2/-9.1	0.19	013.1/0.5	0.45	1.12
71212	10:28:04.62	45.4143	73.0728	6.53	2.071	14	2.9	192	0.04	303.0/-35.2	0.25	012.8/26.1	0.64	1.71
71212	18:38:39.29	45.389	73.0561	7.38	2.548	20	3.72	132	0.04	294.9/-28.3	0.26	016.7/14.9	0.52	1.31
71214	06:00:43.44	45.3884	73.0588	7.7	1.854	14	3.54	130	0.03	293.1/-30.5	0.26	014.9/13.6	0.52	1.62
71217	17:21:33.49	45.303	73.0504	4.93	2.216	13	3.61	225	0.05	273.9/-40.7	0.45	013.9/-11.5	1.09	1.68
71219	14:03:37.69	45.3055	73.0449	4.35	1.907	15	3.83	202	0.04	095.0/41.1	0.43	189.5/5.2	0.83	1.61
71221	05:09:19.93	45.3909	73.0804	13.46	1.906	20	1.86	125	0.08	108.9/10.5	0.55	023.1/-21.7	1.07	1.2
71221	19:45:57.22	45.3835	72.9398	6.74	2.095	12	12.78	145	0.09	291.6/-5.9	0.16	020.9/6.7	0.46	1.26
71222	06:38:49.37	45.4033	73.0924	12.72	1.572	14	0.95	191	0.12	122.4/19.2	0.44	048.4/-38.3	1.07	1.38
71222	07:38:43.19	45.9114	73.0359	0.12	3.024	17	48.51	293	0.19	092.7/4.0	2.73	181.8/-12.7	3.63	9.32
71224	15:34:34.04	45.414	73.0823	8.67	2.216	16	2.35	203	0.05	306.0/-25.0	0.4	028.3/15.9	0.88	1.44
71226	19:13:54.03	45.3776	72.977	6.13	1.962	10	10.03	141	0.03	280.9/-16.1	0.21	008.8/7.4	0.57	1.65

71227	19:49:02.97	45.3841	72.9199	6.85	2.595	18	10.52	125	0.05	097.6/-3.5	0.36	007.9/4.2	0.44	0.89
71228	08:28:31.66	45.3822	72.9141	6.77	2.013	14	10.09	138	0.04	283.1/0.3	0.2	193.1/0.8	0.42	1.01
71229	08:25:14.96	45.3741	72.9487	6.66	1.561	17	12.28	138	0.05	098.6/8.3	0.21	187.7/-5.7	0.53	1.53
71230	05:48:40.31	45.3813	72.9146	6.76	2.060	16	10.13	138	0.05	092.6/-1.0	0.26	002.8/13.5	0.48	0.86
71230	19:40:14.54	45.4855	73.2138	4.69	2.907	21	13.14	271	0.09	172.2/17.0	0.81	066.7/41.1	1.17	2.77
80103	07:52:02.54	45.8798	72.9801	5.41	2.529	18	43.3	288	0.13	296.2/0.2	1.28	026.3/10.1	2.4	8.55
80105	00:57:22.32	45.3828	72.924	6.69	1.936	13	10.85	125	0.04	292.6/-1.8	0.21	022.5/3.0	0.57	1.07
80105	01:08:05.00	45.3821	72.9238	6.74	1.805	10	12.89	148	0.04	297.3/-2.9	0.22	026.8/10.3	0.67	1.49
80107	18:43:42.74	45.3865	73.0553	7.09	4.031	21	3.87	127	0.04	287.4/-31.6	0.25	011.0/10.2	0.51	1.44
80108	02:58:17.17	45.3859	73.0508	7.06	2.155	12	4.23	128	0.04	305.8/-25.8	0.29	030.7/10.5	0.63	2.06
80108	05:07:57.21	45.3624	73.0548	4.93	2.124	15	5.25	108	0.03	292.7/-37.5	0.28	019.7/3.9	0.54	1.64
80108	14:08:52.82	45.3909	73.0561	6.85	2.594	18	3.67	135	0.03	291.9/-31.2	0.22	012.6/14.9	0.43	1.25
80109	04:45:25.75	45.4289	73.0636	5.69	1.805	16	4.54	204	0.06	297.0/-33.9	0.3	017.1/14.4	0.89	1.53
80111	09:19:16.45	45.3846	73.0526	8.4	1.559	10	4.14	125	0.03	100.1/29.9	0.31	180.6/-16.1	0.75	1.75
80111	14:33:54.28	45.3628	73.0534	4.8	1.829	11	5.33	120	0.04	309.3/-35.1	0.25	035.8/5.0	0.79	2.07
80113	18:21:47.22	45.5108	73.0798	2.82	2.275	14	21.07	262	0.06	141.2/4.7	0.65	049.8/16.1	1.33	5
80113	22:25:49.69	45.3897	73.0651	9.21	2.210	14	3.03	130	0.05	297.3/-24.9	0.35	020.9/13.5	0.8	1.32
80114	17:50:13.48	45.3859	73.0553	6.85	2.964	20	3.9	126	0.05	292.1/-26.7	0.33	018.6/7.0	0.67	1.65
80114	23:31:56.96	45.3903	73.057	7	2.419	18	3.62	134	0.06	098.4/33.0	0.33	181.9/-9.9	0.7	2.1
80115	10:35:58.53	45.4055	73.0802	8.16	2.348	18	1.89	178	0.05	301.9/-25.6	0.33	019.9/23.5	0.66	1.15
80116	13:05:00.80	45.3049	73.0566	5.51	1.913	13	3.09	211	0.04	080.6/37.6	0.51	182.3/14.8	0.87	1.76
80118	05:38:39.94	45.3873	72.9248	6.85	1.267	14	10.88	145	0.04	111.7/0.7	0.2	021.7/-3.0	0.53	0.95
80118	16:37:07.88	45.4175	73.08	7.17	2.590	20	2.76	206	0.05	310.6/-25.7	0.31	027.8/24.8	0.72	1.49
80118	18:12:46.35	45.0267	72.383	8.09	1.906	8	27.51	282	0.08	086.0/-11.7	2.01	356.4/2.0	3.37	10.4
80119	05:35:27.76	45.9532	72.9788	0.06	3.190	18	50.63	295	0.18	090.5/9.3	2.79	177.8/-16.2	3.73	7.9
80120	04:50:42.23	45.3093	73.035	3.59	2.312	22	4.39	113	0.07	267.7/-40.2	0.3	000.3/-3.0	0.74	1.25
80120	05:48:36.40	45.308	73.053	5.25	1.587	16	3.14	203	0.05	090.7/41.9	0.4	187.7/7.8	0.97	1.85
80126	13:31:11.37	45.8924	72.969	5.65	2.047	12	44.16	311	0.11	093.8/1.9	1.87	183.4/-11.3	2.72	9.37
80129	08:10:45.83	45.3764	72.9527	8.28	1.222	12	11.92	147	0.04	285.0/-6.0	0.26	015.0/0.6	0.64	1.47
80130	04:53:15.40	45.8899	72.9726	4.13	2.462	20	44.03	288	0.1	291.8/-0.3	1.18	021.8/9.4	2.32	9.48
80130	07:45:26.16	45.4118	73.0972	8.02	1.511	13	1.59	231	0.04	132.3/25.2	0.42	043.1/-1.7	0.99	1.32
80131	09:28:24.70	45.9317	73.0501	27.82	1.969	10	51.02	296	0.13	129.1/1.5	2.13	039.2/-6.0	3.67	16.5
80201	10:29:56.33	45.9823	72.9691	13.15	2.434	12	53.33	316	0.12	098.1/0.2	2.09	188.1/-2.7	3.46	12.7
80203	08:45:28.69	45.3833	73.0652	8.57	1.694	20	3.31	117	0.05	293.5/-29.7	0.27	015.2/14.3	0.53	1.33
80205	12:25:03.18	45.4896	73.1086	6.56	2.383	20	10.21	263	0.07	321.0/-18.2	0.4	040.5/29.1	1.05	1.59
80207	17:25:20.14	45.5156	73.1524	6.33	2.133	12	13.7	277	0.05	147.5/13.2	0.49	053.8/15.4	1.23	2.24
80207	20:34:00.71	45.8823	73.0201	7.39	2.264	14	45.08	290	0.1	293.2/-0.4	1.49	023.1/3.7	2.66	10
80210	06:57:18.68	45.3876	73.0636	9.12	2.406	18	3.22	127	0.04	291.3/-26.7	0.27	013.1/15.9	0.54	1.08
80211	01:53:34.37	45.5184	73.1501	5.62	1.850	16	13.95	277	0.06	147.6/18.0	0.58	049.5/23.5	1.12	2.51
80211	03:33:12.21	45.8848	72.94	0.06	1.927	16	42.43	286	0.15	175.8/-11.1	2.58	087.3/7.6	2.76	9.99
80212	11:35:26.19	44.9356	73.3439	16.24	2.979	22	47.12	218	0.25	091.0/5.6	1.86	180.6/-3.9	2.72	10.2
80215	10:21:22.87	45.3726	72.9789	6.53	1.528	14	10.04	133	0.05	283.1/-13.9	0.23	012.6/2.1	0.55	1.7

APPENDIX C

Examples of data quality and phase picking for events processed in Chapter 4.

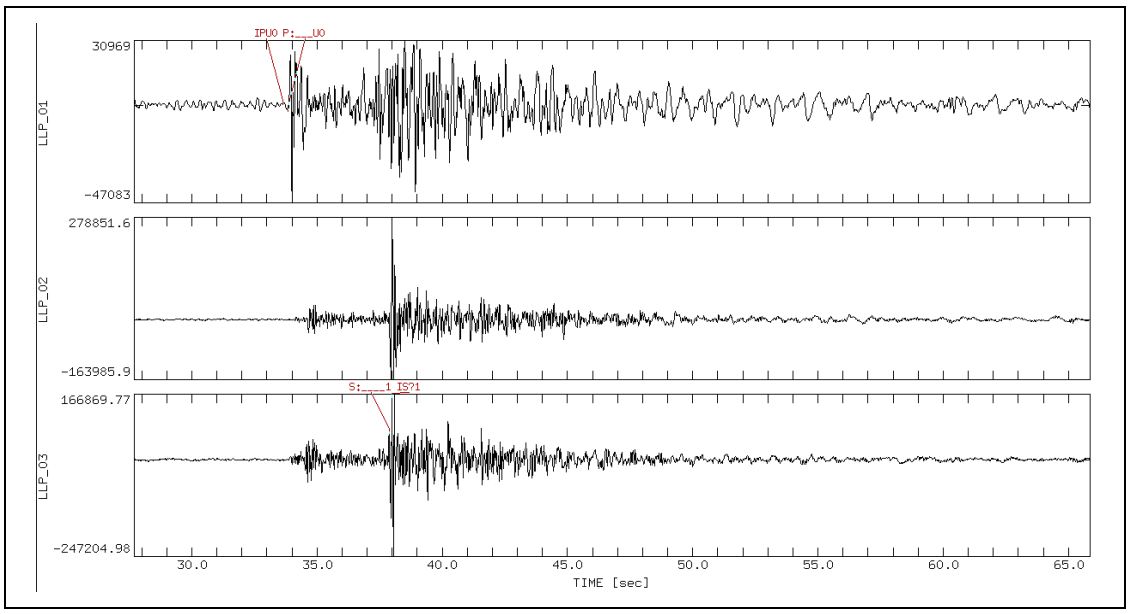

Figure C.1. Sample of the obtained data (vertical, N-S and E-W components) showing one event with both P and S arrivals picked. Bandpass filter 0.5-15 Hz.

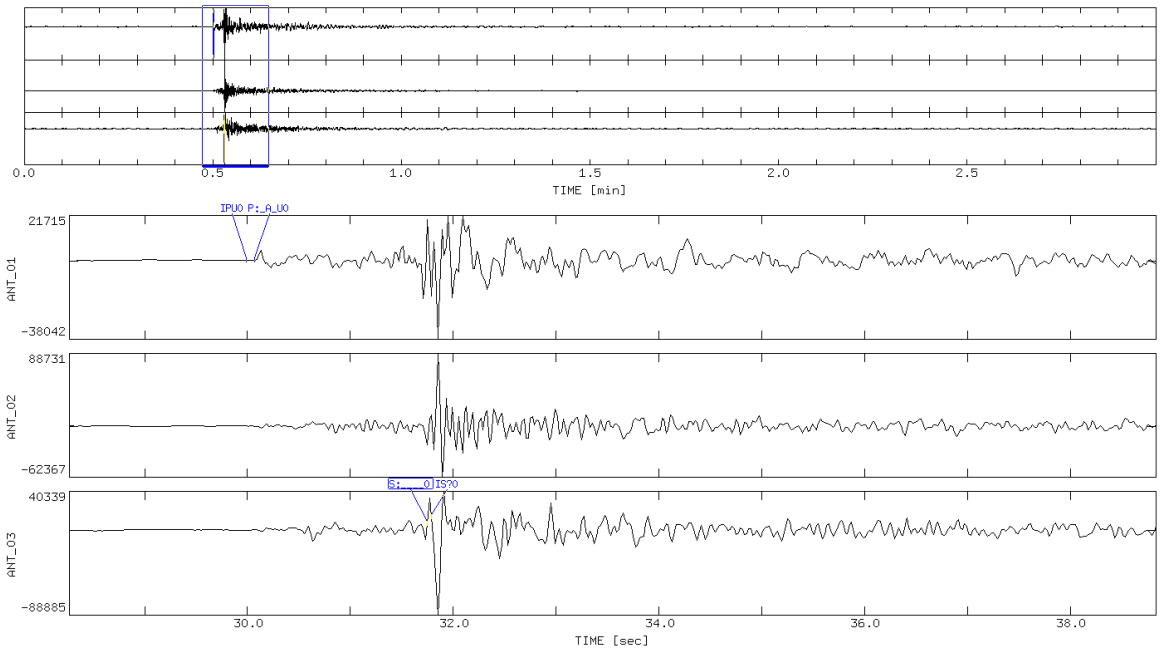

Figure C.2. Phase picking. Weights P=0, S=0.

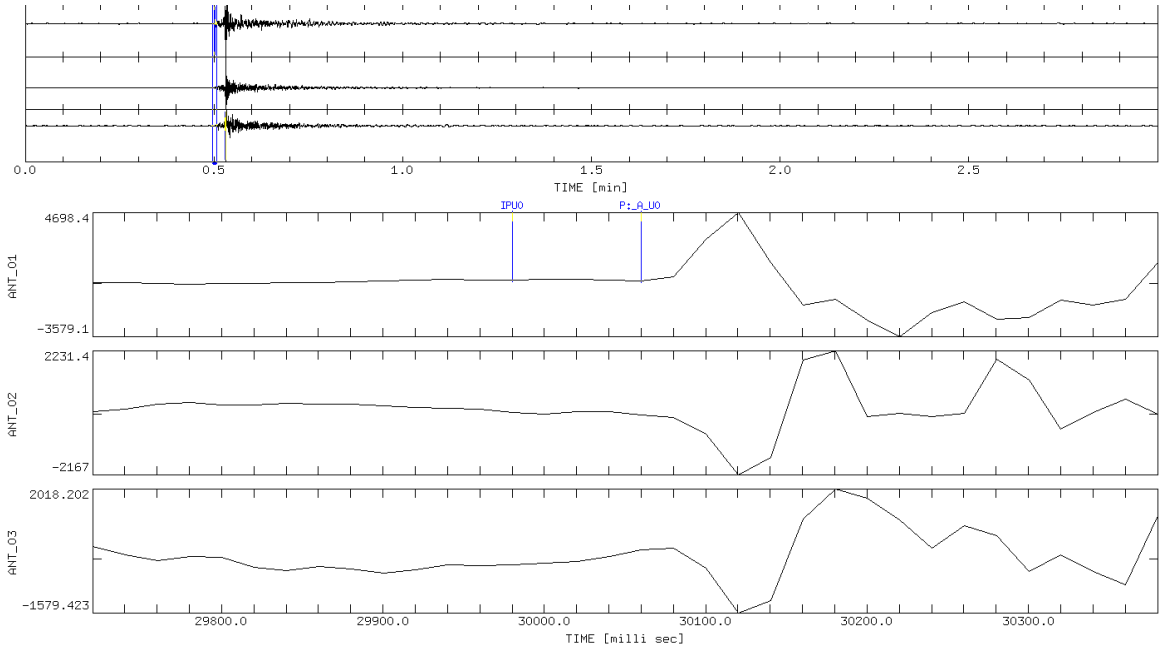

Figure C.3. Zoom-in of P arrival (P:_A_U0) of previous example (Figure C.2).

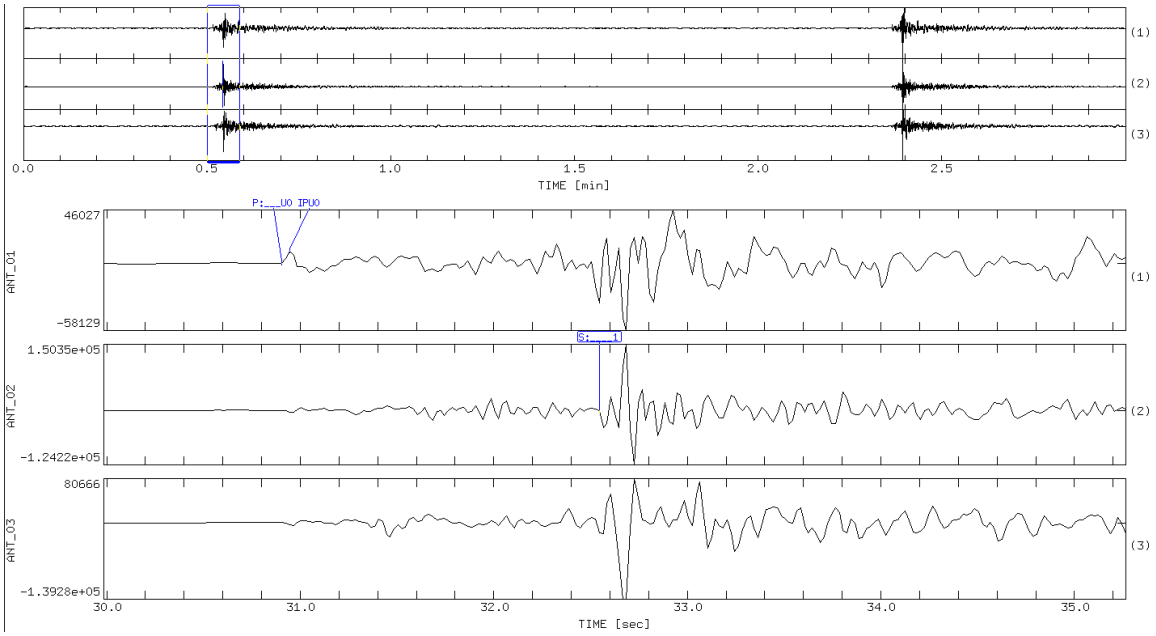

Figure C.4. Phase picking. Weights P=0, S=1.

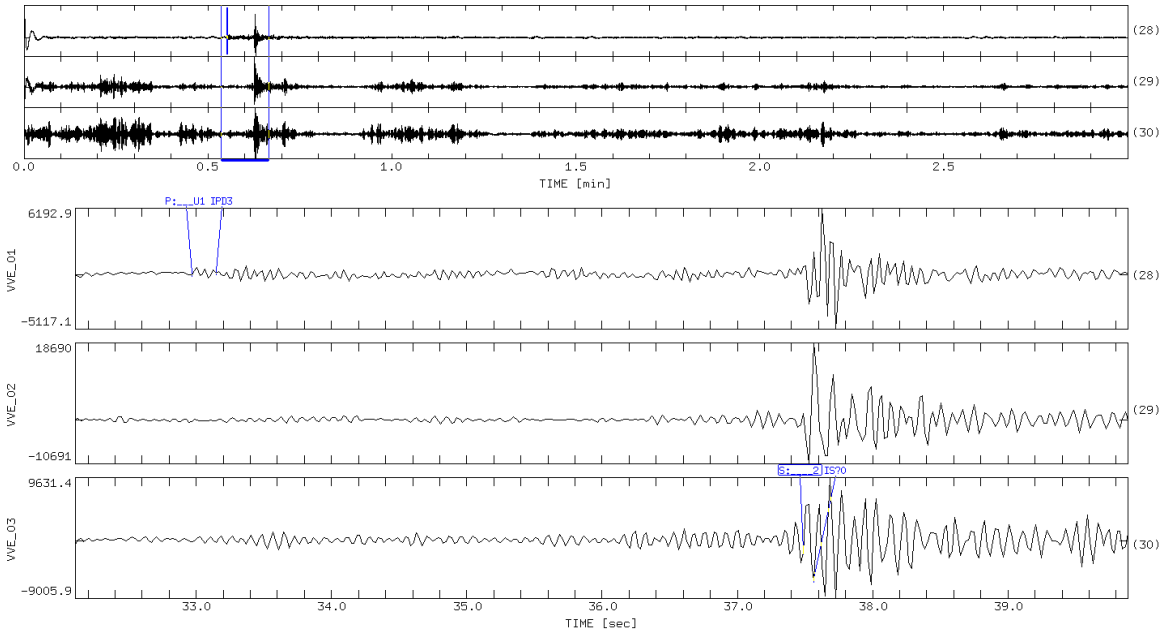

Figure C.5. Phase picking. Weights P=1, S=3.

APPENDIX D

SUPPLEMENTARY INFORMATION FOR CHAPTER 5

Supplementary Data and Methods

We employed data from the International Maule Aftershock Dataset (IMAD; http://www.iris.edu/mda/_IMAD), which is the result of combined international efforts orientated to the recording of the aftershock sequence of the 2010 Chile earthquake from as early as mid March 2010 onwards. Seismograms from a total of 126 stations, most of them broadband seismometers, were used for this research.

RMT inversion. We derived moment tensor solutions from full waveform inversions by using the software package ISOLA [Sokos and Zahradnik, 2008] which is especially designed for the processing of stations located at regional to local distances and considers full Green's functions for a 1D velocity model. For each event a corresponding 1D model based on a regional 2-D velocity model [Haberland et al., 2009] was constructed. Moment tensors are calculated by least squares minimization of the difference between observed and synthetic data, while best position (depth) and time are grid-searched in terms of the absolute value of the correlation coefficient between the data and synthetics. For each event, we used its epicentral coordinates and origin time from the catalogue of aftershocks published by Rietbrock et al. [2012], who also used IMAD data to derive hypocentral locations. We selected only events M>4.5, located with a minimum of 20 P-phase observations. Depending on the event magnitude, we used stations located 20-200 km from the epicentre location to assure both a good signal/noise ratio and the validity of the point source assumption. Waveforms were band-pass filtered mostly in the frequency range 0.05-0.09 Hz, but we also used lower frequencies down to 0.01 Hz for some of the large magnitude events. For a given event, we usually started the inversion at a fixed depth from the

location given by the local catalogue. We then inverted for a range of depths around this initial depth, in steps of e.g. 5 km each. Finally, we performed the inversion in depth steps of 1 or 0.5 km within the depth range that presented the largest correlation values. All events were inverted for a deviatoric moment tensor inversion, i.e., each solution is composed of a double couple (DC) and a compensated linear vector dipole (CLVD) part.

GCMT events relocation. Additionally, we relocated early (before April 2010) and late (after 2010 until March 2012) aftershocks included in the Global Centroid Moment Tensor (GCMT) catalogue that occurred either before the deployment of the IMAD network or after its removal, by moving their positions to an averaged shift. This shift was calculated by averaging the differences in location for those events included in both the GCMT and Rietbrock et al.'s [2012] location catalogue (Sup. Fig. D.1). Only horizontal (latitude and longitude) shift was considered, as teleseismic depths are poorly resolved and do not show any bias tendency regarding the local network locations.

SRA model. In order to calculate the fault slip of each event, we used equations from scaling relations for subduction zones [Blaser et al., 2010] and obtained the slip by solving the equation for seismic moment [Aki, 1966] considering an average shear modulus μ=39 GPa. The average μ was calculated from solving the equation for S-wave velocity, considering an average S-wave velocity of 3.58 km/s at megathrust seismogenic depths [Haberland et al., 2009] and a density of 3050 kg/m^3 for the seismogenic slab [Tassara et al., 2006].

For instance, the scaling relations for length and width of a thrust fault in a subduction environment are [Blaser et al., 2010]:

$$\log_{10} L = -2.37 + 0.57Mw \qquad \text{and} \qquad \log_{10} W = -1.86 + 0.46Mw$$

where L and W are the length and width of the fault respectively and Mw is the moment magnitude of the earthquake calculated through the moment tensor inversion.

Now, with the obtained length and width, we can calculate the area of the rupture, which is then replaced in the seismic moment equation [Aki, 1966]:

$$s = \frac{M_0}{\mu A}$$

where *s* is the slip of the fault, *Mo* is the seismic moment (calculated from the moment magnitude), μ is the shear modulus and A is the area of the rupture.

Distribution of aftershocks. To quantify the spatial distribution of aftershocks relative to the areal distribution of coseismic slip, we defined the ratio R_{ds} (see main text), which measures the normalized seismicity relative to the areal density of ranges of coseismic slip. This quantification method is proposed by Hauksson [2011] to determine the distribution of seismicity in southern California relative to several geophysical parameters. We determined the value of coseismic slip from the model proposed by Moreno et al. [2012] at the epicentre of each aftershock by bicubic interpolation [Wessel and Smith, 1998]. We then counted the number of aftershocks located at a given range of coseismic slip, in this case, every 1 m. The more the resolution of the slip model, the smaller the ranges that can be used. Finally, we calculated the area covered by every considered range of slip (e.g. the area contained between the 3 and 4 m contour lines for the range between 3-4 m of slip) and computed the ratio R_{ds} with the obtained values (green lines in Figures 5.4a and 5.4b).

We also determined the cumulative distribution of aftershocks relative to the distribution of slip (black lines in Figures 5.4a and 5.4b), in a similar way to the aftershock distribution histograms proposed by Woessner et al. [2006].

Lastly, we created a set of 1000 randomly distributed catalogue of events to test the R_{ds} values of a random distribution of aftershocks. We then plotted the 1 standard deviation values (red circles in Figures 5.4a and 5.4b) above and below R_{ds}=1 (i.e. above and below average).

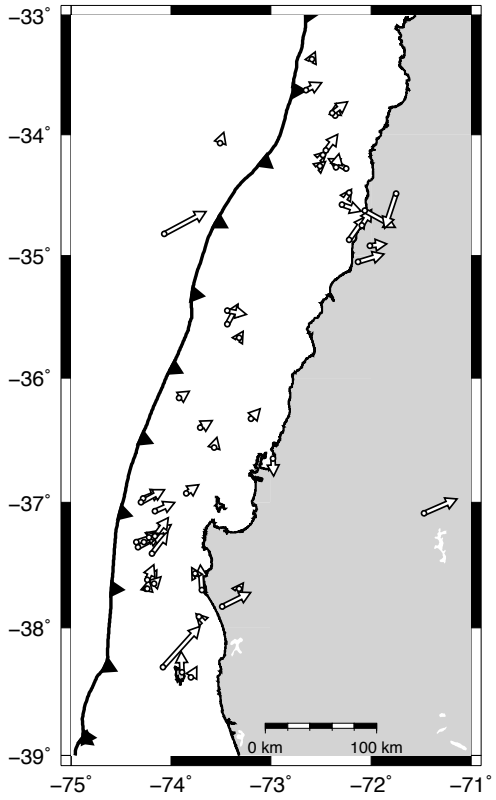

Supplementary Figure D.1. Relocation of GCMT events. Arrows start at GCMT position and end at relocated position showing GCMT solutions present a bias of 16 km in average towards SW direction.

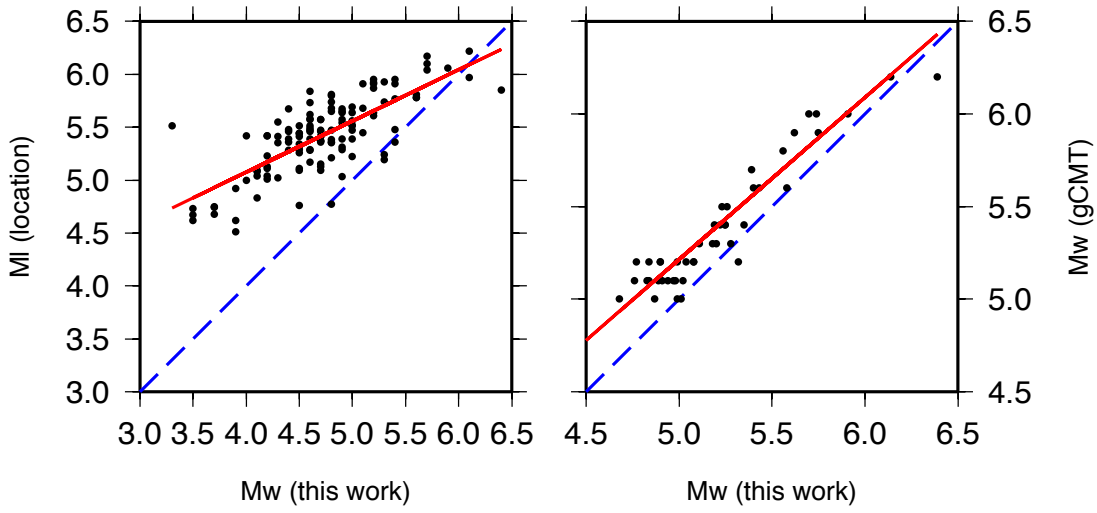

Supplementary Figure D.2. Comparison of obtained magnitudes. Left plot shows local magnitudes [Rietbrock et al., 2012] versus M_W obtained in this work. Right plot shows GCMT magnitudes versus this work's magnitudes.

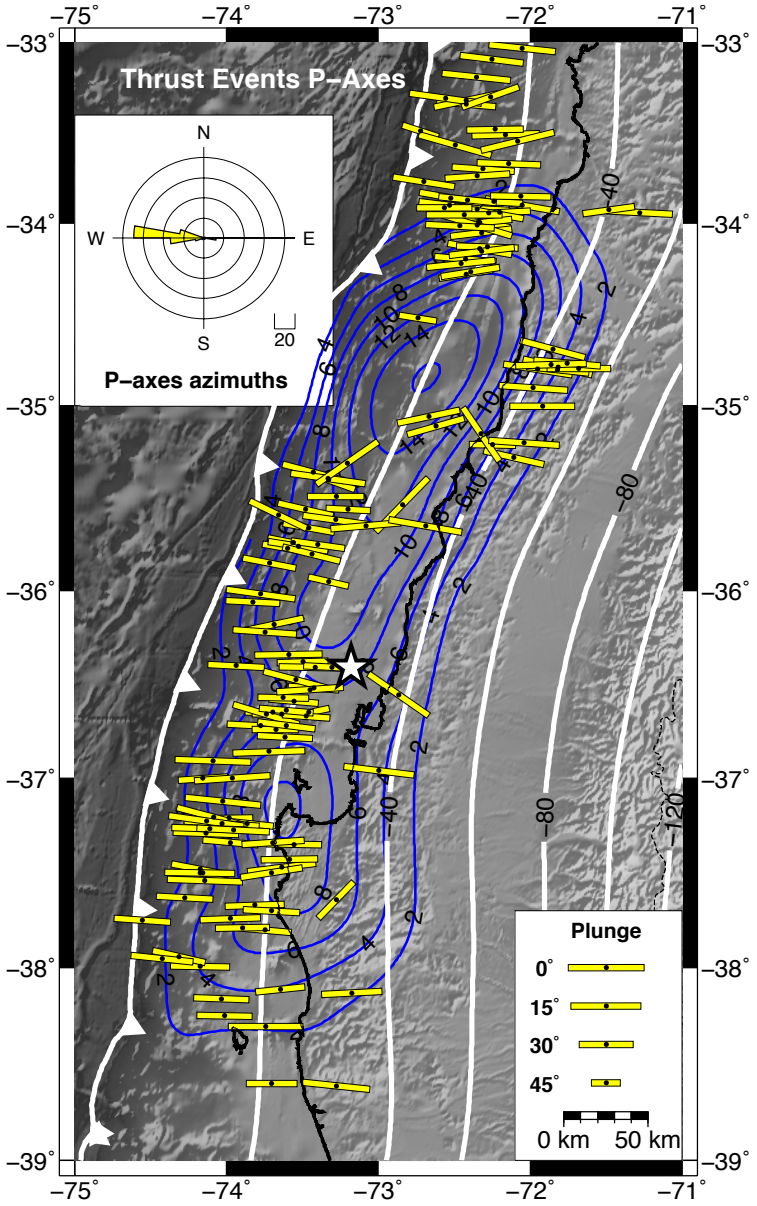

Supplementary Figure D.3. P-axes of interface thrust events. Inset contains rose histogram showing frequency of P-axes azimuths in bins of 10º.

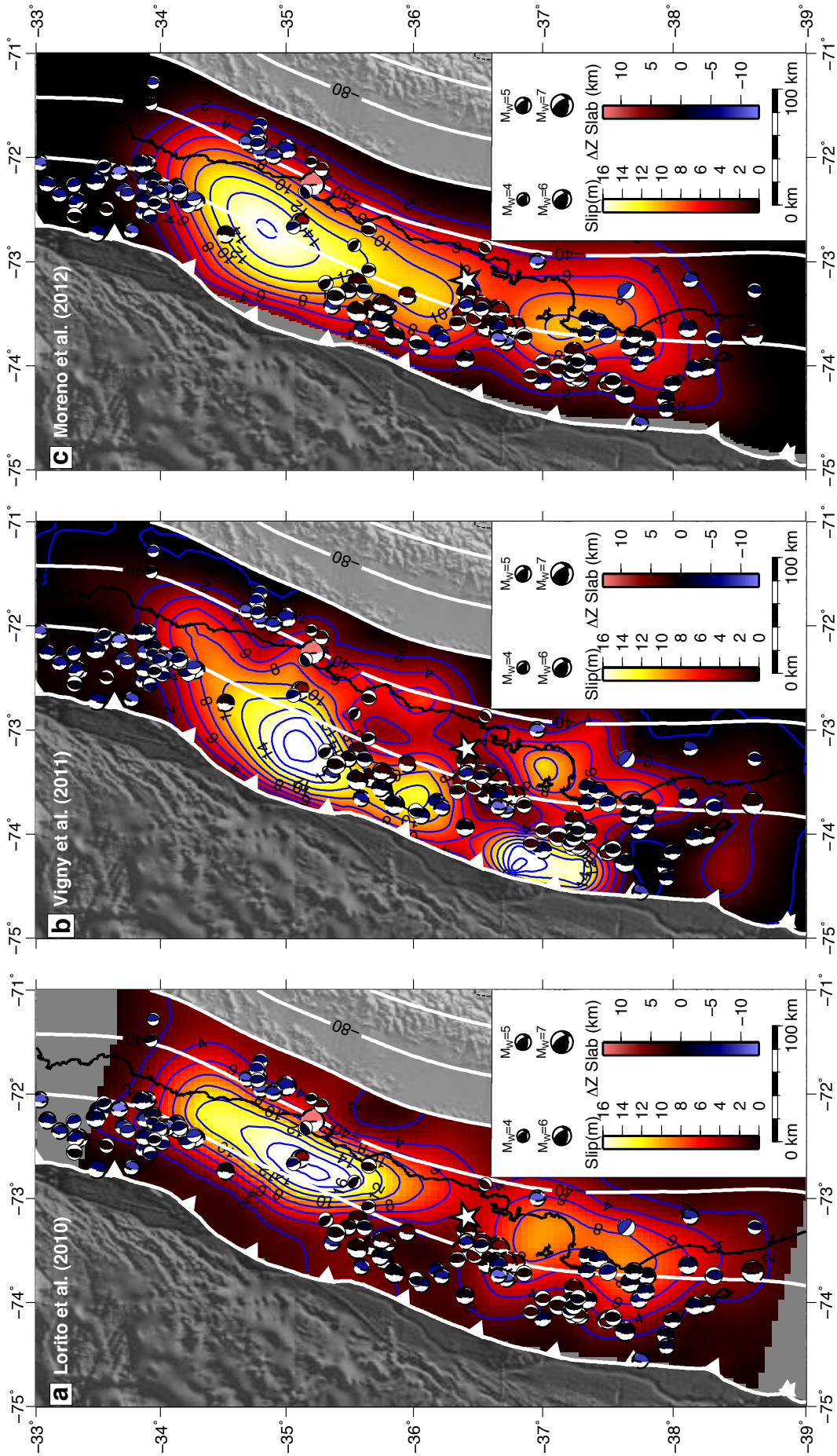

Supplementary Figure D.4. Interface thrust events plotted together with published coseismic slip models. Features are same of Figure 5.3a.

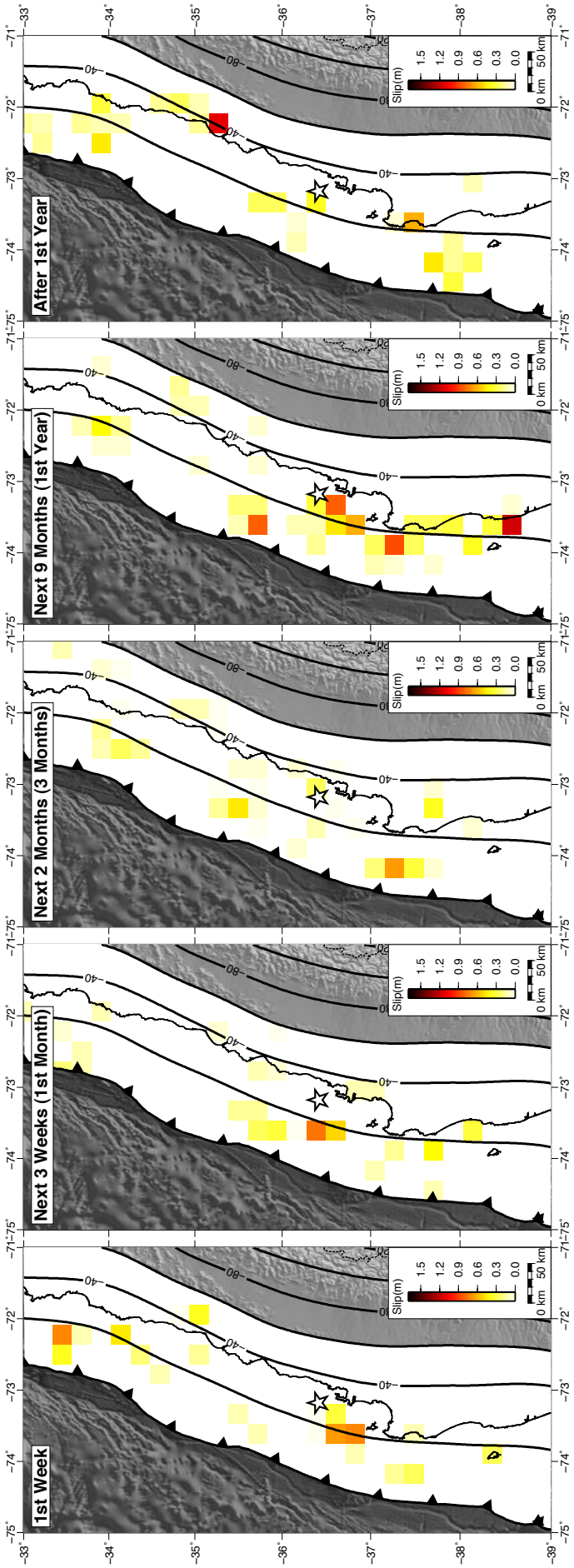

Supplementary Figure D.5. Temporal evolution of non-cumulative SRA.

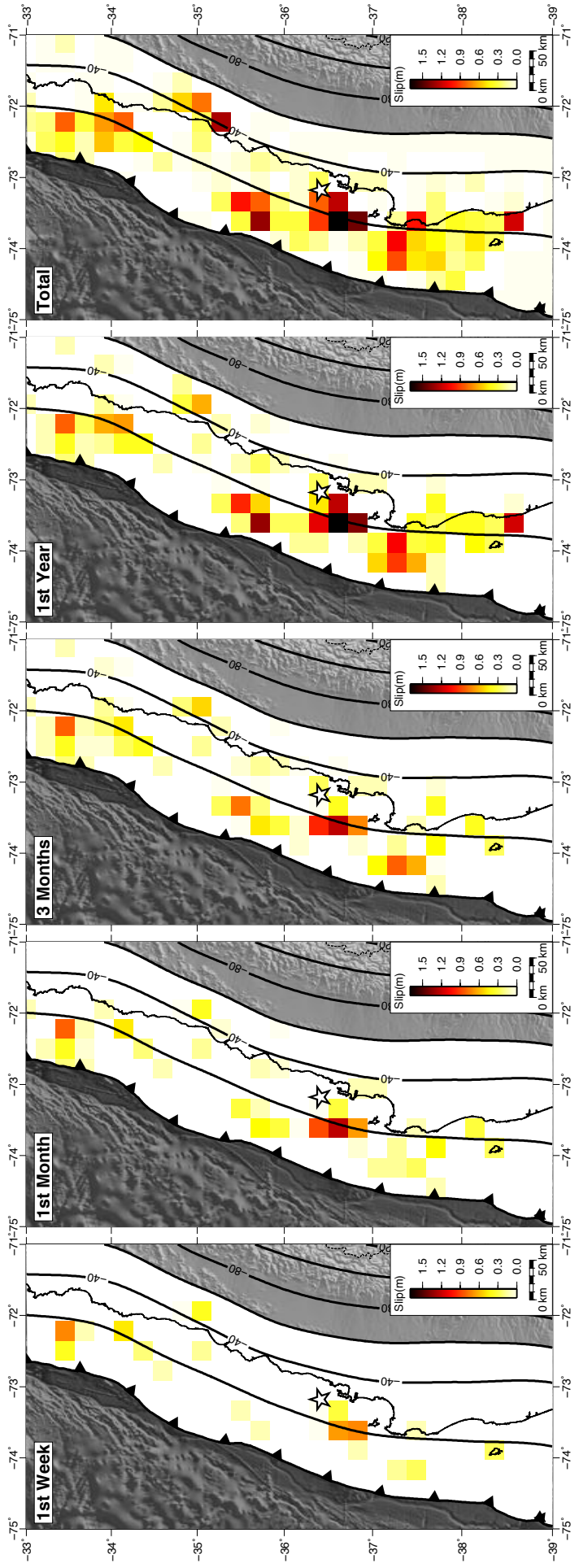

Supplementary Figure D.6. Temporal evolution of cumulative SRA.

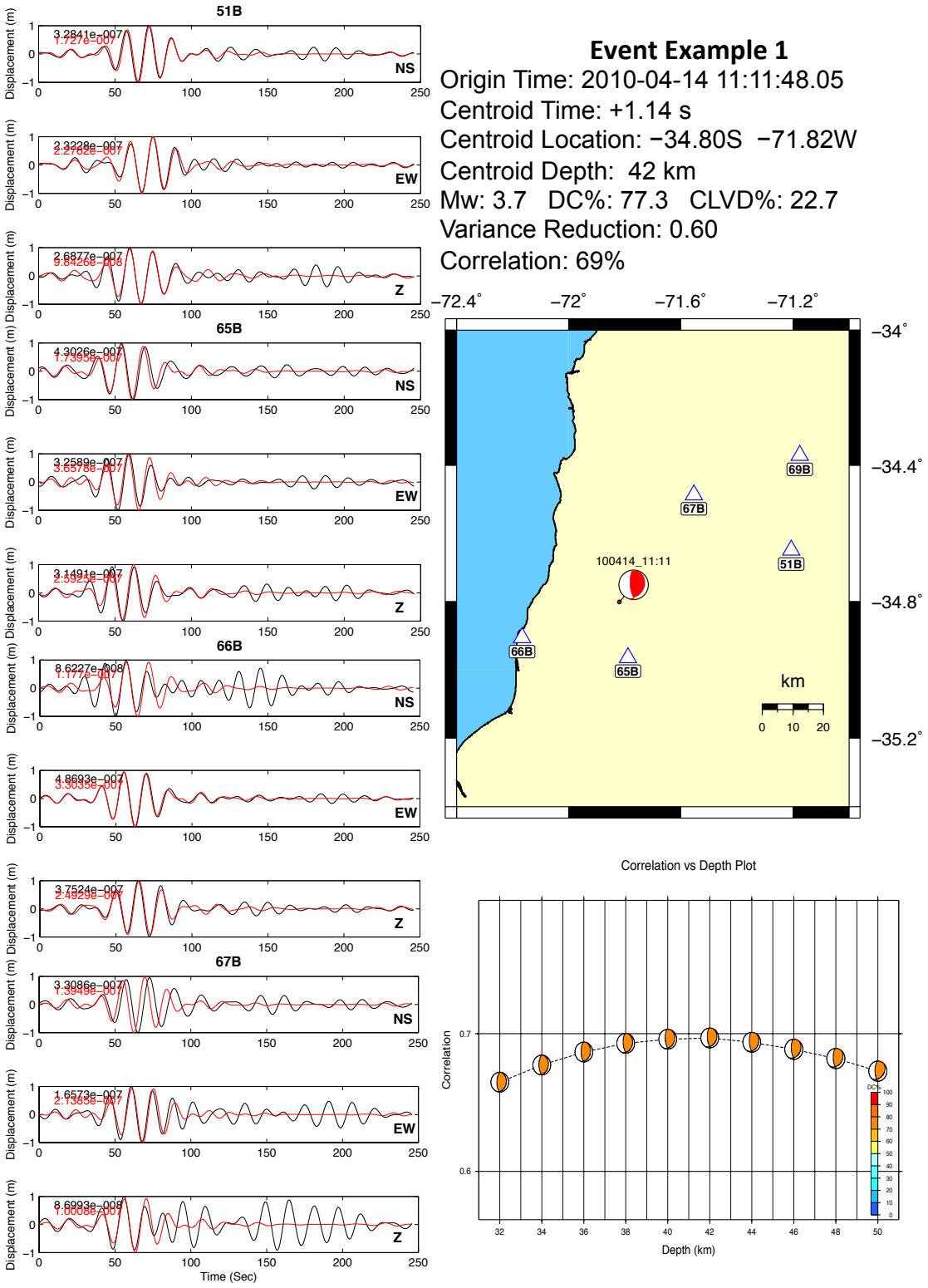

Supplementary Figure D.7. Event example 1. Red seismogram is synthetic, black is real data.

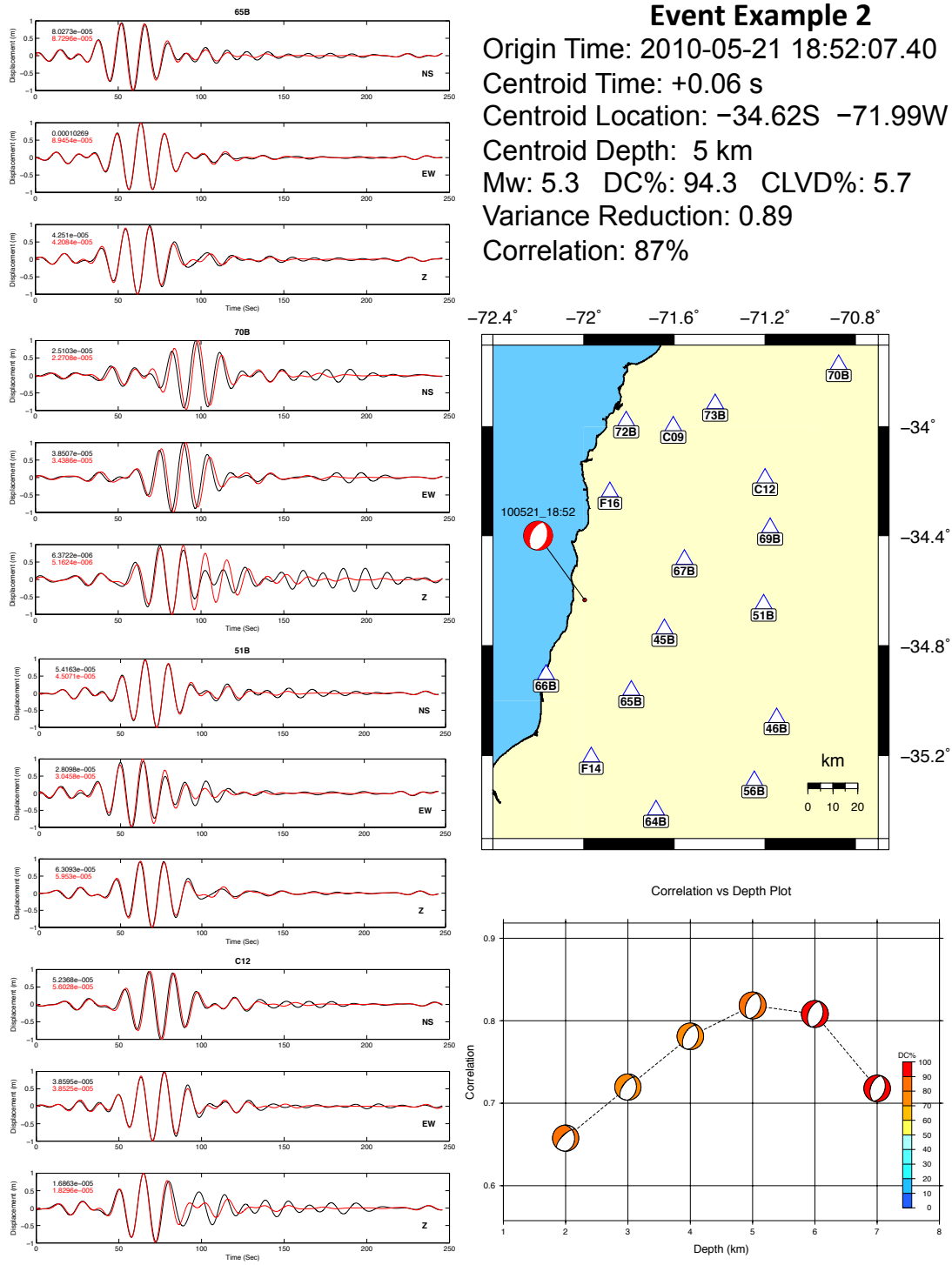

Supplementary Figure D.8. Event example 2. Red seismogram is synthetic, black is real data.

APPENDIX E

Catalogue of Regional Moment Tensor solutions obtained in Chapter 5.
Columns: **Origin Time** of event occurrence, **Longitude** west in degrees, **Latitude** south in degrees, **Depth** in km, **Moment magnitude, Strike** of nodal plane 1, **Dip** of nodal plane 1, **Rake** of nodal plane 1, **Variance** reduction of the inversion in percentage, **Number of stations** used for the inversion, **Double Couple** component percentage of solution, **Correlation** of synthetic and real seismograms after inversion in percentage.

Origin Time yyyymmdd_hh:mm:ss.ss	Lon.	Lat.	Dep (km)	Mw	Str	Dip	Rake	% Var	No Sta	% DC	% Corr
20100318_01:57:32.19	-72.9733	-36.7882	36	4.8	196	81	110	0	12	95.9	99.0
20100319_02:55:49.34	-72.4937	-33.5670	11	4.9	186	51	77	46	9	92.9	68.6
20100319_14:20:43.71	-72.5565	-33.3082	11	5	201	35	108	36	8	92.5	53.0
20100319_17:10:44.27	-72.1645	-34.4140	24	4.8	320	10	-57	77	7	61.1	15.4
20100320_10:04:32.16	-71.9625	-34.4650	7	4.7	5	51	-57	77	6	96.9	33.7
20100321_18:30:59.81	-73.5425	-36.4772	15	5.3	162	34	42	52	5	90	49.4
20100322_01:24:05.81	-72.8848	-35.9375	28	4.2	162	81	69	11	3	57.5	95.4
20100324_00:05:12.05	-74.0028	-37.1783	14	4.8	194	54	88	4	17	99.4	71.9
20100324_14:14:57.52	-72.9143	-35.6597	23	4.5	32	16	151	13	3	79.1	4.3
20100325_12:59:35.13	-72.2095	-34.2342	11	4.5	346	37	-77	15	8	63.8	23.7
20100325_13:57:52.14	-72.8373	-35.9915	19	4.6	165	50	86	34	4	59.3	65.5
20100326_10:30:41.33	-72.1068	-35.2803	42	4.7	179	71	72	71	9	83.9	88.0
20100327_04:37:53.44	-72.0835	-33.5467	21	4.6	162	49	85	61	4	97.7	64.0
20100328_14:36:27.67	-73.8160	-36.1043	1	5.3	346	87	-92	1	6	49.2	72.0
20100328_21:38:28.04	-73.3327	-35.3950	13	5.9	173	53	70	76	14	90.9	69.5
20100328_21:43:11.13	-73.2472	-35.4808	7	5.4	197	84	90	56	6	93	102.0
20100329_03:07:34.35	-74.0872	-37.2063	17	4.7	197	50	94	51	12	32.5	68.0
20100329_07:35:06.65	-71.8433	-34.9040	41	5.1	172	67	77	79	13	87.6	83.2
20100329_14:10:38.99	-72.3104	-35.3289	12	3.5	269	64	-21	60	6	84.7	71.2
20100330_07:07:06.22	-73.6147	-35.7712	6	4.5	203	28	114	66	4	83	46.0
20100330_08:12:56.99	-73.0000	-36.9457	13	3.9	218	77	-96	53	6	60.5	94.1
20100401_12:53:06.49	-72.0563	-34.6795	4	5	209	58	-111	93	15	57.3	75.8
20100401_19:42:58.74	-72.4272	-34.1973	17	4.9	196	21	104	45	11	46.4	39.0
20100402_06:48:20.00	-71.6877	-34.7175	19	3.5	214	52	-7	12	5	82.8	69.5
20100402_10:38:21.84	-73.5177	-36.6762	24	4.4	150	68	64	27	13	71.5	80.3
20100402_19:34:09.37	-72.8702	-36.1203	30	4.6	122	50	43	6	12	47.5	56.1
20100402_22:58:07.40	-73.1098	-36.2502	19	5.7	200	74	99	68	7	96.8	92.0
20100403_02:12:39.76	-73.1262	-36.2752	30	4.2	160	52	75	1	10	81.7	66.7
20100405_03:32:15.14	-71.0496	-33.4382	66	5	236	47	119	4	3	75.6	62.1
20100406_13:04:40.33	-72.8857	-35.0447	8	4.9	274	37	-59	73	14	61.2	44.6

20100407_02:18:35.64	-72.8427	-35.5360	25	4.3	119	53	69	48	3	45.9	58.0
20100407_02:29:46.09	-72.8463	-35.5747	20	4.6	146	31	66	70	14	48.7	44.0
20100407_17:50:39.76	-73.2369	-37.0348	21	4.2	252	56	-3	1	9	56.3	67.8
20100408_08:03:00.50	-72.3254	-35.1531	37	4.4	50	66	82	86	10	60.3	51.0
20100410_04:36:01.83	-71.8235	-34.1642	33	4	72	33	62	12	3	31	26.0
20100411_09:58:46.15	-73.8140	-38.0367	17	4.7	6	70	-110	64	11	97.4	52.5
20100411_10:28:07.29	-71.8185	-34.7887	47	4.6	175	62	65	56	18	97.3	78.6
20100412_10:45:55.82	-72.0428	-35.2009	46	3.9	170	61	72	41	9	69.5	77.0
20100412_20:59:35.62	-73.2524	-36.6037	15	4.5	200	78	103	45	15	94.8	96.0
20100413_15:10:37.18	-72.2723	-33.9430	21	4.3	179	61	76	79	13	96.9	78.0
20100414_04:46:54.27	-73.2048	-35.3104	15	4.7	125	45	60	80	13	63.9	52.2
20100414_11:11:48.55	-71.8190	-34.8016	42	3.7	175	69	76	60	5	77.3	85.6
20100414_23:02:28.02	-72.5651	-33.9151	17	4.6	216	21	136	73	6	51	38.6
20100415_10:13:11.32	-72.0000	-34.6980	6	4.1	160	77	-164	57	5	47.5	91.1
20100415_12:12:45.88	-72.8653	-36.5563	35	4.2	206	36	76	57	11	52.4	53.9
20100416_22:41:33.52	-74.1433	-37.5420	13	5.4	173	50	78	62	13	77.1	66.5
20100416_23:15:33.48	-74.1753	-37.5000	7	5.4	182	30	91	68	15	57.9	47.5
20100417_09:47:59.93	-73.6527	-38.0627	34	4.7	182	81	86	68	6	92.6	98.2
20100417_10:09:49.86	-71.2787	-33.9425	57	4.1	172	66	76	32	6	92	82.2
20100418_01:49:35.69	-74.0312	-37.2395	14	5.6	182	51	88	76	19	81.8	68.4
20100418_02:52:16.77	-74.1337	-37.2260	12	4.9	187	47	90	73	15	84.4	64.7
20100419_07:21:30.64	-72.4657	-35.7191	21	4.2	207	57	99	6	5	49.8	74.9
20100420_07:41:17.74	-71.3937	-34.0087	40	4.2	177	65	83	2	5	87.2	81.8
20100422_15:46:12.61	-71.9317	-34.6979	2	3.7	40	53	-86	83	5	92.8	36.6
20100423_08:51:39.78	-71.8659	-34.5443	7	3.7	37	41	-28	87	6	95.7	24.4
20100423_10:03:04.76	-73.2785	-37.6442	39	5.7	129	77	85	64	14	88.9	83.6
20100425_15:42:21.55	-73.1903	-37.6490	36	4.7	125	79	80	23	13	90.8	84.4
20100427_05:37:17.61	-72.0820	-34.3440	11	4.3	56	69	-3	44	16	93.4	55.2
20100428_04:26:30.37	-72.8202	-35.7142	29	4.1	126	68	85	5	19	70.2	74.2
20100429_07:56:30.45	-74.0887	-36.9093	9	4.9	182	46	91	76	10	65.2	63.4
20100430_09:47:33.74	-71.1398	-36.3583	6	3.5	283	72	30	34	4	86.9	74.7
20100501_14:41:05.63	-72.2612	-33.3017	21	4.7	170	71	103	34	11	69.6	86.9
20100502_14:52:41.98	-72.1972	-34.4513	12	5.7	357	43	-73	59	17	94.8	27.0
20100502_19:22:58.38	-72.1678	-34.2799	11	4.5	356	31	-75	84	10	88.5	15.9
20100503_06:49:26.12	-72.1807	-34.2895	18	4.5	13	31	-47	1	11	92.1	13.2
20100503_18:39:40.80	-74.1112	-37.2672	10	5.3	191	45	102	76	17	79.5	62.9
20100503_23:09:46.14	-73.7093	-37.9870	1	6.4	194	89	91	48	19	89.2	106.9
20100504_13:55:04.88	-72.4433	-34.1403	30	5.1	181	67	82	73	16	70.7	84.2
20100505_15:24:07.02	-73.2807	-35.6177	18	5.2	185	64	86	80	8	39.4	81.5
20100505_17:05:42.02	-70.3097	-34.9855	25	3.9	354	40	-175	3	5	75.3	24.7
20100508_21:52:49.58	-73.7767	-36.0173	13	4.9	213	33	125	47	3	64.9	50.6
20100509_03:29:35.83	-72.3317	-33.9962	22	4.9	161	69	74	75	17	85.1	83.5
20100509_06:54:26.74	-73.5381	-34.3612	40	4.8	114	86	84	38	2	54.1	87.7
20100509_13:42:58.60	-74.5451	-36.5862	6	4.5	341	27	-148	45	4	91.7	16.7

20100511_13:04:52.66	-73.0817	-35.6498	20	4.4	158	63	67	82	11	8.1	77.1
20100513_03:56:03.52	-73.0255	-35.1342	23	4.5	201	71	85	21	18	59	89.0
20100513_07:13:00.90	-74.0907	-37.2012	16	4.4	183	46	94	4	18	76.8	63.4
20100513_20:39:11.15	-72.4543	-34.2227	22	5	160	64	71	80	14	88.9	78.4
20100518_10:11:20.21	-72.8475	-34.8650	23	4.8	0	90	-70	72	16	83.7	73.0
20100519_09:38:48.40	-72.3938	-34.2672	28	4.8	170	71	90	88	10	97.7	86.9
20100519_10:48:04.45	-72.5867	-34.6595	21	4.3	357	72	-93	67	10	89.1	55.5
20100520_16:53:39.80	-73.0513	-35.6193	21	4.2	13	60	-93	78	16	57	42.1
20100521_18:52:07.40	-71.9930	-34.6197	5	5.3	17	40	-95	89	19	94.3	22.0
20100524_19:12:14.08	-72.9618	-35.7322	24	4.6	74	83	-133	68	16	58.2	73.0
20100524_23:57:32.73	-73.5908	-36.3432	16	5.2	173	63	83	74	16	87.8	79.4
20100525_13:09:24.81	-73.2047	-37.7177	36	5.2	161	68	83	1	18	77.7	82.5
20100530_02:27:44.24	-71.6803	-34.7953	57	4.7	174	67	83	49	8	83	83.5
20100601_16:05:29.21	-73.7232	-36.8593	17	5	178	57	90	59	17	75.1	74.0
20100606_08:26:48.75	-71.8925	-34.7757	5	4.6	348	78	-178	47	15	94.3	62.8
20100611_08:54:14.17	-72.1613	-34.7287	8	4.6	10	48	-146	68	16	80.7	30.3
20100616_09:19:07.92	-71.1198	-36.3155	130	4.6	328	86	-108	9	6	52.2	74.9
20100621_14:51:00.22	-72.3487	-34.0108	15	4.7	207	57	104	79	7	61.4	74.9
20100622_08:24:27.71	-71.6785	-34.2995	41	4	69	36	176	23	9	93.7	27.6
20100623_16:29:45.29	-73.0297	-34.6747	13	4.4	33	56	-93	71	6	45.3	38.7
20100624_13:24:05.78	-73.9620	-36.9998	12	5	185	46	103	68	8	34.2	63.6
20100627_07:15:47.63	-74.0632	-36.8980	5	4.7	183	33	88	35	11	60.6	50.5
20100628_00:59:49.42	-74.6752	-37.7415	3	5.4	21	15	-108	34	5	94.4	3.1
20100629_01:39:59.67	-73.7498	-37.8852	15	5.2	108	66	71	20	9	98.4	66.9
20100629_12:49:10.60	-73.6390	-36.2968	8	4.6	161	45	91	11	3	86.4	60.0
20100701_20:58:22.87	-72.6902	-35.6495	31	4.8	182	37	78	86	7	49.9	54.4
20100703_00:05:07.09	-71.7573	-34.7672	54	5	176	65	79	34	16	80.5	81.7
20100706_13:54:02.46	-72.1190	-35.6518	44	4.6	175	64	75	54	6	87.9	80.6
20100707_18:02:17.61	-73.1168	-34.9862	30	4.3	345	9	128	51	7	73.7	11.6
20100708_05:49:38.33	-72.2138	-34.4797	2	4.6	318	41	167	67	13	92	35.3
20100714_08:32:18.81	-73.8983	-38.1852	31	6.1	183	80	96	57	7	72.7	97.3
20100714_15:05:48.15	-73.7415	-38.3060	25	5.6	194	55	110	61	8	90.2	72.9
20100715_00:36:02.88	-72.3203	-34.1555	23	5.2	162	66	76	86	8	47.2	80.7
20100715_22:57:01.80	-72.8659	-35.2107	13	4.5	10	56	-95	3	11	39.7	38.3
20100724_21:46:36.30	-72.4625	-34.0153	20	4.8	191	28	100	70	10	99.3	45.9
20100805_06:01:46.43	-73.7052	-37.5010	26	5.6	169	68	88	75	17	95.4	83.8
20100805_06:27:13.46	-73.7940	-37.5232	35	5.4	174	73	87	55	12	53.1	89.4
20100806_15:15:50.73	-72.6675	-35.0587	28	4.5	154	69	72	77	15	96	82.1
20100809_12:13:43.03	-73.2782	-38.6150	33	4.7	192	63	99	58	9	52.2	80.9
20100815_07:50:33.62	-71.1413	-36.9752	5	5.1	206	74	-161	84	13	68.9	91.9
20100822_03:50:02.09	-73.4500	-36.5292	24	4.9	169	64	81	80	16	42.8	79.8
20100906_03:20:46.71	-73.9562	-37.2760	16	5	165	36	64	66	11	96.8	51.8
20100909_07:28:00.39	-74.0255	-37.1212	12	6.1	185	42	88	75	19	79.8	59.6
20100910_07:44:43.40	-72.4342	-33.9532	16	4.4	172	47	80	75	13	66.3	63.4

20100912_19:16:22.92	-71.4833	-33.9270	41	4.3	162	77	79	48	12	92.4	91.5
20100914_03:23:34.44	-74.0607	-37.2562	6	4.8	188	42	90	32	15	57.7	59.7
20100917_06:52:39.69	-74.1020	-37.5955	13	4.5	188	56	102	27	17	50.8	73.7
20100920_05:42:53.60	-72.3487	-33.7398	23	4.8	172	66	85	79	13	89.3	82.2
20100923_16:36:17.96	-71.8710	-34.9857	41	5.2	171	65	79	8	16	94.5	81.1
20100928_04:29:22.10	-72.0878	-34.5002	12	4.4	152	77	-125	31	10	92.8	89.5
20100929_16:29:50.41	-71.8648	-34.7763	48	4.8	170	60	80	45	4	75.4	76.0
20101201_10:01:43.25	-71.7865	-33.7367	34	3.3	324	68	-156	0	4	29.4	58.6

APPENDIX F

Catalogue of relocated GCMT moment tensor solutions used in Chapter 5. Longitude and Latitude columns show relocated positions; rest of columns show data from GCMT catalogue.

Origin Time yyyymmdd_hh:mm	**Longitude** degrees	**Latitude** degrees	**Depth** km	**Mw**	**Strike** degrees	**Dip** degrees	**Rake** degrees
20100227_06:34	-73.0183	-35.8711	23.2	8.8	19	18	116
20100227_19:00	-72.1620	-33.5111	24.2	6.2	3	27	97
20100227_23:02	-73.1949	-37.8310	53.4	5.9	349	27	90
20100228_01:08	-72.3311	-34.1411	31.5	5.9	13	24	95
20100228_11:25	-71.9198	-35.0011	53.5	6.2	17	25	113
20100228_19:48	-74.0141	-38.2510	15.1	5.8	1	16	91
20100301_01:10	-72.1993	-35.2911	57.8	5.2	34	33	130
20100301_02:44	-72.6196	-35.1111	18.9	5.6	302	29	32
20100301_05:30	-73.7504	-34.6111	16.5	4.9	234	44	-67
20100301_07:49	-73.4004	-34.6211	12.0	5.3	208	35	-65
20100301_08:46	-73.3291	-35.4011	15.1	5.3	26	17	98
20100301_08:58	-74.8250	-37.8010	18.8	5.0	204	41	-79
20100301_12:20	-73.8806	-34.4611	12.0	5.1	41	40	-91
20100301_14:36	-73.8307	-34.4211	12.0	5.2	46	39	-89
20100301_15:52	-73.7769	-36.7211	27.2	5.1	13	27	104
20100301_16:56	-72.5676	-36.2911	67.6	5.0	43	35	125
20100301_22:40	-74.1401	-34.7911	18.0	5.0	32	37	-88
20100302_02:09	-71.3312	-39.7510	15.6	5.1	176	65	-168
20100302_04:09	-73.5985	-35.7711	15.0	5.4	359	13	78
20100302_04:28	-73.6769	-36.7411	15.2	5.5	17	11	110
20100302_06:10	-72.7405	-34.5211	14.7	5.3	3	5	84
20100302_11:30	-72.8592	-35.3411	12.0	5.0	198	67	-163
20100302_12:16	-73.6970	-36.6511	18.4	5.2	5	16	95
20100302_14:07	-74.2915	-39.6110	34.7	5.1	16	28	112
20100302_19:12	-72.4209	-34.2811	19.1	5.6	14	17	119
20100302_21:44	-73.7173	-36.5011	37.0	5.1	44	26	115
20100303_04:35	-74.1555	-37.5011	15.0	5.3	350	12	66
20100303_04:42	-74.1359	-37.2911	20.9	5.1	13	26	105
20100303_06:16	-72.3118	-33.7011	23.5	5.2	10	22	99
20100303_17:44	-73.5571	-36.5911	16.3	6.1	15	12	103
20100303_19:58	-72.2321	-33.4811	19.1	5.8	2	17	94
20100304_01:59	-72.4223	-33.3411	12.8	6.0	10	19	97
20100304_09:03	-74.8253	-37.6110	16.8	5.0	217	45	-56

20100304_17:37	-72.2811	-34.1311	23.5	5.4	14	22	106
20100305_03:34	-71.8104	-34.5611	12.0	5.4	1	38	-77
20100305_03:55	-71.8205	-34.5211	26.1	5.3	319	75	177
20100305_07:36	-73.2794	-35.2411	36.2	5.1	266	50	-3
20100305_09:19	-73.4570	-36.6511	15.0	6.1	11	8	116
20100305_10:31	-73.6356	-37.4711	26.0	5.2	358	28	97
20100305_11:47	-73.6168	-36.7811	14.9	6.6	9	16	98
20100306_15:19	-74.1756	-37.4811	14.3	5.2	28	19	112
20100307_04:46	-72.0527	-33.0311	29.1	5.1	7	26	92
20100307_15:59	-73.6444	-38.1110	25.0	5.9	348	12	84
20100307_18:36	-72.0905	-34.5411	47.0	5.3	24	27	114
20100307_22:00	-72.0515	-33.9011	34.4	5.2	26	42	113
20100307_23:46	-73.2280	-36.0611	29.4	5.1	26	21	-119
20100308_13:03	-73.8406	-34.4311	12.0	5.1	38	41	-97
20100308_17:50	-71.9131	-32.7711	16.5	5.3	360	28	108
20100308_18:08	-71.9833	-32.6711	16.0	5.3	353	26	89
20100309_22:10	-72.7017	-33.7711	20.3	5.1	358	22	76
20100310_02:41	-72.9965	-36.9611	48.5	5.2	19	32	107
20100310_04:01	-73.9860	-37.2111	15.0	5.1	15	12	109
20100310_08:45	-74.1597	-35.0511	17.9	5.1	48	34	-59
20100310_12:20	-72.7221	-33.4911	15.0	5.6	47	6	122
20100311_10:51	-72.1608	-34.3011	16.8	4.9	319	31	-99
20100311_14:39	-71.9806	-34.4311	12.9	6.9	324	35	-90
20100311_14:55	-72.0007	-34.4211	16.3	7.0	16	6	-53
20100311_20:11	-71.9505	-34.5111	19.3	5.6	3	44	-61
20100311_22:34	-73.9751	-37.7410	22.5	5.3	351	20	82
20100312_10:32	-74.5551	-37.7510	17.9	5.1	348	18	71
20100312_16:50	-72.0508	-34.3011	12.0	5.7	342	40	-87
20100313_03:15	-73.8871	-36.5811	31.4	5.3	2	23	88
20100313_03:19	-73.6370	-36.6611	23.7	5.4	10	19	102
20100313_07:12	-71.8405	-34.5411	18.9	5.1	345	45	-81
20100313_10:34	-73.8152	-37.6710	20.0	5.8	7	19	102
20100313_15:22	-71.9406	-34.4611	15.6	5.2	10	29	-75
20100313_20:20	-74.1564	-37.0011	15.0	5.3	346	12	79
20100314_07:31	-71.9708	-34.3111	16.4	5.2	341	34	-116
20100314_13:52	-73.7135	-38.6010	19.3	5.5	281	25	-26
20100314_20:04	-73.7135	-38.5710	13.3	5.4	228	23	-60
20100315_11:08	-73.7184	-35.8511	12.0	6.2	21	15	103
20100316_02:21	-73.4975	-36.3811	13.4	6.6	12	14	107
20100316_03:04	-73.6272	-36.5711	17.2	5.9	19	14	112
20100317_18:29	-73.4292	-35.3611	20.5	5.1	27	24	106
20100318_03:18	-72.2907	-34.3811	30.6	5.1	35	21	-54
20100319_08:54	-73.1988	-35.5611	15.0	5.5	27	10	118
20100325_11:10	-73.5586	-35.7411	15.0	5.3	21	14	103
20100913_16:44	-70.3346	-31.7111	0.0	5.1	260	68	15

20100914_03:37	-74.1187	-37.2597	27.8	5.1	352	19	76
20100926_05:29	-72.9998	-40.4710	73.9	5.0	126	43	103
20100930_00:26	-73.9374	-36.4011	12.4	5.6	9	17	98
20101021_02:49	-73.6527	-34.6360	71.3	5.9	2	45	-136
20101023_05:58	-73.7450	-37.8010	21.2	5.5	31	16	123
20101023_10:57	-73.7370	-36.6611	28.5	5.1	31	29	110
20101031_07:10	-72.2352	-33.7247	33.3	5.3	4	20	94
20101110_01:23	-73.4174	-36.4111	28.8	5.0	359	33	88
20101128_08:19	-72.0967	-34.6337	26.4	5.2	40	24	-70
20101213_18:51	-73.4730	-33.9795	42.4	5.2	38	28	-89
20110102_20:20	-73.7035	-38.6010	19.4	7.1	5	13	97
20110107_09:42	-73.5285	-35.7611	12.3	5.4	22	21	107
20110107_14:05	-73.5988	-35.6111	34.8	5.1	26	37	90
20110110_06:02	-73.4587	-35.6611	12.1	5.9	22	14	105
20110111_01:05	-73.6588	-35.5911	18.4	5.0	29	23	95
20110111_05:33	-71.9494	-35.2211	12.0	5.1	138	15	60
20110121_15:36	-72.3514	-33.9211	27.6	5.0	347	25	69
20110205_16:11	-73.7052	-37.7010	21.0	5.7	9	17	98
20110211_20:05	-73.4272	-36.5211	17.8	6.8	15	13	104
20110211_23:39	-73.9758	-37.3411	16.4	6.0	11	16	98
20110212_01:17	-73.8660	-37.2411	14.1	6.0	12	15	98
20110213_08:51	-73.4770	-36.6711	16.2	5.9	13	11	101
20110213_10:35	-73.6069	-36.7211	14.1	5.9	12	18	97
20110213_13:44	-73.6070	-36.6411	17.8	5.6	9	15	95
20110214_03:40	-73.4788	-35.5611	12.0	6.6	25	17	105
20110214_10:21	-73.2790	-35.4911	14.9	5.2	13	18	107
20110214_12:18	-71.4089	-35.5411	12.8	5.2	211	21	-33
20110218_17:01	-72.2415	-33.8811	27.3	5.3	14	20	105
20110219_06:26	-72.2014	-33.9411	20.8	5.2	360	21	94
20110224_04:36	-73.6878	-36.1811	20.5	5.1	24	27	139
20110228_01:29	-73.5558	-37.3511	25.3	5.8	6	16	97
20110303_07:58	-73.6958	-37.3411	23.3	5.2	1	22	97
20110316_22:36	-71.7636	-32.4611	36.8	5.5	15	28	105
20110317_11:14	-71.8734	-32.5611	35.0	5.2	6	28	101
20110328_06:10	-71.9501	-34.8011	51.1	5.2	29	32	119
20110328_23:57	-72.2319	-33.5811	32.8	5.1	2	33	96
20110410_20:24	-73.8280	-36.0611	18.0	5.2	357	15	83
20110413_15:14	-72.1418	-33.6711	31.2	5.4	9	23	100
20110419_00:57	-72.3525	-33.1911	20.6	5.1	355	29	76
20110419_05:50	-72.5215	-33.8611	21.4	5.1	23	24	108
20110422_05:12	-74.1746	-37.9910	13.8	5.3	359	19	88
20110427_04:57	-72.5315	-33.9011	20.2	5.1	17	21	103
20110507_06:57	-72.6915	-33.8711	29.1	5.0	17	25	93
20110519_17:05	-71.8205	-34.5211	53.2	5.2	19	32	118
20110601_12:55	-74.2753	-37.6310	12.0	6.3	1	17	88

20110601_13:47	-74.1659	-37.2611	27.0	5.4	9	23	77
20110605_10:25	-71.9799	-34.9011	50.1	5.3	24	31	118
20110629_05:36	-72.4115	-33.8711	18.9	5.5	13	18	100
20110713_02:01	-73.7478	-36.2211	21.0	5.0	6	23	93
20110716_00:26	-72.0615	-33.8511	23.9	6.0	14	21	108
20110725_11:15	-73.8950	-37.7910	20.5	5.4	3	15	95
20110728_16:05	-73.4385	-35.8011	12.6	5.2	24	19	103
20110728_19:50	-73.3985	-35.7511	13.2	5.6	344	17	61
20110806_13:22	-73.3282	-35.9511	15.0	5.5	49	9	131
20110828_04:30	-72.2527	-33.0911	19.7	5.4	7	23	90
20110903_16:20	-74.0343	-38.1610	18.3	5.8	4	16	93
20110907_11:21	-72.4223	-33.3211	18.9	5.2	338	24	78
20110910_03:17	-72.3413	-33.9911	28.6	5.0	27	25	112
20110914_07:03	-71.7532	-32.6911	26.2	5.9	359	16	84
20110928_22:40	-74.3147	-37.9410	12.0	5.5	6	15	82
20110929_15:40	-74.4247	-37.9510	12.0	5.2	3	22	87
20111108_17:18	-72.3212	-34.0511	28.9	5.3	6	22	108
20111111_08:08	-73.1744	-38.1310	41.3	5.2	346	20	76
20111122_07:41	-71.8502	-34.6911	52.6	5.1	43	31	129
20120123_16:04	-73.3074	-36.4111	21.0	6.2	15	17	105
20120211_02:58	-73.5856	-37.4311	26.8	5.7	2	17	94
20120325_22:37	-72.2494	-35.2111	26.6	7.2	21	11	114